MANIPULATION OF MATTER WITH LIGHT: FROM ATOMS TO BUBBLES

Harry E. Saunders-Singer

A thesis submitted in partial fulfilment of the
requirements for the degree of Doctor
of Philosophy at University College London

Laser Cooling Group

Department of Physics

University College London

UMI Number: U602703

All rights reserved

INFORMATION TO ALL USERS
The quality of this reproduction is dependent upon the quality of the copy submitted.

In the unlikely event that the author did not send a complete manuscript
and there are missing pages, these will be noted. Also, if material had to be removed,
a note will indicate the deletion.

UMI U602703
Published by ProQuest LLC 2014. Copyright in the Dissertation held by the Author.
Microform Edition © ProQuest LLC.
All rights reserved. This work is protected against
unauthorized copying under Title 17, United States Code.

ProQuest LLC
789 East Eisenhower Parkway
P.O. Box 1346
Ann Arbor, MI 48106-1346

To my Grandmother, Evelyn Gwendoline Saunders-Singer

June 1918 – May 2004

Scientific Instrument Maker

"Most people say that it is the intellect which makes a good scientist.
They are wrong: it is character."

Albert Einstein

ABSTRACT

Manipulation of Matter with Light: From Atoms to Bubbles

Harry E. Saunders-Singer, University College London, London

PhD. Thesis, June 2004

This thesis concerns the interaction between matter and light, in particular the coherent manipulation and directed motion of cold atoms in a Hamiltonian system in the fully chaotic regime. The system under scrutiny is the cold atom realisation of the delta kicked rotor, a paradigm system for the study of quantum chaos in which ultra-cold caesium atoms are periodically 'kicked' by a symmetric (and in this case far-detuned) optical lattice. Experiments demonstrate quantum features such as dynamical localisation, and asymmetric diffusion is achieved as a result of mixed (chaotic and regular) classical dynamics. Further experiments make an exploration of phase space past the momentum boundary, a manifestation of finite-width kicks, and by reducing system symmetries it is shown that directed atomic motion in this Hamiltonian system can result from purely chaotic dynamics alone.

The second part of this thesis describes the design and construction of a computer-controlled scanning-beam laser tweezers for the manipulation of dielectric microspheres and micron-sized protein-coated bubbles. Evidence

for the three-dimensional trapping and the automated two-dimensional manipulation of these neutral particles in time-shared optical traps is presented. The preparation and plans for biological research applications is also detailed, the work of which marks the beginning of future biophysical collaborations.

ACKNOWLEDGEMENTS

First and foremost my deepest thanks goes to my parents who have been fantastically supportive with everything I have done throughout my academic career. They are an infectiously happy and simple couple, surviving mostly on Somerset vegetables, seeds, and rye bread.

Secondly I have to thank Dr. Phil Jones, without whom I can not imagine the laser cooling experiment to have ever worked in the first place. Although his engineering skills are somewhat lacking (especially with regard to drilling holes in a straight line), he is a very good experimentalist and has taught me a great deal. Next is Malika Goonasekera, for her superb skills of laser alignment and data-collecting expertise, and for the entertainment provided by her electronics misfortunes.

I must also thank my first supervisor, Dr David Meacher, who was friendly enough to recruit me in the beginning, and who is going to be kind enough to accommodate and feed me when I invite myself to Munich for snowboarding next year. My new supervisor, Dr Ferruccio Renzoni, has also been a great help in the short time he has been here so far. People obey him and hold the utmost respect for his students because he is in the Italian Mafia and can easily have your kneecaps removed or your extended family taken out without a trace.

Then there's everyone else who has passed through the doors of the laser cooling lab, particularly Dr. Stephan Winklbauer for sorting out computer problems, both Steph and my rich friend Matthew Isherwood for theoretical

work, and Dr. Silvia Bergamini for writing a fantastic control program that has lasted the test of time.

Other essential souls have been Ivan and Ted from the Physics Workshop, Brian Anderson and Tim Phillips from the Physics Stores, Derek Thomas and Martin Postranecky from the undergraduate laboratories, the guys from the MAPS Workshop in the Chemistry Department, and the kindest characters in the Physics department: Dr Moores, Trea Saint and Dr Harker.

The penultimate thankyou goes to my flatmates and the rest of my close friends for support and for putting up with my dweeby antisocial behaviour.

Finally, on the financial side I would like to thank the EPSRC for a studentship, WCSIM for generously awarding me the Beloe Fellowship and Singer Instruments for generous sponsorship.

CONTENTS

List of Figures

CHAPTER 1

Introduction

The exciting and relatively new field of laser trapping and manipulation has been found to apply over a vast range of particle types, from matter as small as single atoms and ions, to molecules, living biological cells and even macroscopic dielectric particles hundreds of micrometers in size. It is being used across the scientific disciplines and has opened up many new ways of studying a large variety of topics, from fundamental physics research to exciting biological applications.

For example, in biological sciences and chemistry the use of "laser tweezers" has led to the trapping and manipulation of all manner of biological matter such as organelles within cells, biological molecules, proteins, viruses, and bacteria. With the ability to measure small forces some important applications have been the study of molecular motors responsible for functions such as muscle action, and the study of the physical properties of DNA.

In atomic physics, laser trapping and cooling techniques have led to the optical trapping of single atoms and ions, to atom cooling down to the lowest temperatures in the universe, and to Bose-Einstein condensation. The versatile structures that are "optical lattices" have provided a rich environment to help understand such phenomena as quantum transport and tunnelling. Practical applications of laser cooling and trapping in atomic physics include the latest generation of atomic clocks, potential uses in atom lithography, and the new field of atom optics: the manipulation of matter waves analogous to that of light by conventional optics.

A particular use of cold atoms of interest in this thesis is to model the system known as the delta-kicked rotor. This is familiar from classical chaos because the seemingly simple model actually has very complex dynamics. The quantum system, which in the classical limit exhibits chaos, is realised in this context by cold atoms subjected to a pulsed, sinusoidal potential surface created by a far-detuned standing wave of light. When the potential is pulsed on, the atoms feel a 'kick' and their momenta change by an amount that is dependent on the position of the atom in the periodic potential at the time the kick occurs. We are specifically interested in investigating the effects of broken symmetries on this fully-chaotic, dissipation-free system in order to generate directed atomic motion.

The latter part of this thesis describes the construction of an optical tweezers apparatus for the trapping and manipulation of neutral micron-sized objects with a laser beam. Future plans are to use this apparatus to conduct research in areas of biophysics. One such plan is to study the properties of 'bubbles', protein-coated gaseous microspheres primarily used

as a contrast agent in ultrasound imaging. Another is to use the tweezers as a sensitive force transducer for the study of the forces involved in the important mechanisms behind cell migration. However, the primary motivation behind constructing the tweezers is to complement the experiments with cold atoms. While the latter will be shown to demonstrate directed atomic diffusion in a fully chaotic, deterministic and non-dissipative system, the optical tweezers can be used to generate directed motion of micron-sized particles in a heavily-damped, Brownian system. The important feature of interest for both models is that directed motion results despite the potential being macroscopically flat and there being zero net force.

A simple example of extracting useful work from *random* motion is the self-winding wrist watch. An internal ratchet and pawl mechanism allows the unbiased motion of the gesticulating carrier to load the spring. However, the issue becomes more subtle on a smaller scale for systems in which microscopic fluctuations of a classical or quantum Brownian nature are involved. In the presence of dissipation, this area of research is known as *ratchet devices*, *Brownian motors*, and in the biological domain as *molecular motors* (for reviews see [1–5]). In fact much of the early work in the field was motivated by the need to understand how various biological processes occur. For example, the molecules kinesin and myosin have the ability to move unidirectionally along structural filaments such as microtublin and actin for, among other essential physiological functions, the transportation of organelles and muscle contraction respectively [6].

The ratchet effect is most commonly defined as the rectification of ran-

dom fluctuations into useful work.[1] However, useful work cannot be achieved without cost. As argued by Smoluchowski and later by Feynman [7], gaining useful work from a system which exerts no force in a particular direction without the input of energy, for example a spatially periodic system in contact with a single thermal heat bath, is ruled out by the second law of thermodynamics. In order to produce a ratchet effect or directed motion it has been demonstrated, theoretically and experimentally with many different examples (see cited reviews), that thermal equilibrium must be broken and system symmetries must be lowered: thermal equilibrium can be driven away from by an unbiased deterministic or stochastic perturbation, the breaking of time symmetry is most commonly met in systems with thermal noise, and spatial symmetry is usually broken with an antisymmetric periodic potential. These requirements are achieved through one of the following basic schemes: pulsed ratchets, rocking ratchets or fluctuating state ratchets. Definitions and examples of each can be found in the cited reviews, but this context will mostly be concerned with the pulsed scheme.

One example of the pulsed ratchet can be experimentally realised by a Brownian particle diffusing in a pulsed one-dimensional asymmetric sawtoothed periodic potential [8]. If the potential height is much larger than the thermal noise the particle rolls down the potential slope and becomes localised at a potential minimum. When the potential is flattened the particle diffuses freely. Because the length scales that constitute one period of the

[1]Some extend this definition to the rectification of random *or* anti-symmetric fluctuations into useful work, such that the term may also be applied to systems in which the fluctuations are from processes that are not random. However, to avoid controversy we shall adopt the former definition and simply refer to directed motion or asymmetric diffusion when relating to that of deterministic (or dissipation-free) systems.

ratchet surface are unequal, the probability of the particle to diffuse into the domain of the adjacent ratchet period is anisotropic. When the potential is turned back on the particle will then fall to the minimum of a neighbouring potential well with directional preference and the net result is motion in one direction: rectification of the Brownian fluctuations.

Given the tiny scale of this experimental realisation and other, natural Brownian motors, it is an obvious progression to take quantum mechanical effects into account [5, 9, 10]. This can lead to surprising new dynamics in comparison to the purely classical approach as tunnelling and other quantum effects can become important for the transport properties.

To reduce models further, the next step was to replace the random noise with deterministic chaos. Ratchet effects were accomplished in damped systems [11], and the extent to which deterministically induced chaos mimics the role of noise was investigated. An ideal experimental testing ground for quantum chaos was found to be the atom-optics realisation of the kicked rotor: cold atoms in a pulsed periodic potential [12, 13]. In the course of this thesis it will be seen that this system is very versatile: it enables full control over the dynamics of the system, including the ability to set the level of quantum behaviour and the amount of dissipation. Among other examples, experimental realisations of directed atomic diffusion in this system with dissipation are presented in [14, 15].

In the final reduction to a conceptual skeleton we will abandon dissipation in our system entirely. In doing so, the most natural mechanism for the breaking of time-reversal symmetry is lost. However, it can be replaced by choosing the driving function asymmetric in time (in other words, by using a

syncopated pulsed potential). At this stage, the study of such systems[2] begins to overlap strongly with chaos and quantum chaos in Hamiltonian systems, shifting attention from directed diffusion to the detailed features of nonlinear dynamics responsible for it. However, to date there has been very little work on directed motion in chaotic Hamiltonian systems. Notable exceptions are the theoretical works by Flach *et al.* [16] and Schanz *et al.* [17,18]. Although different, the theories that each group use to explain directed diffusion rely on mixed (chaotic and regular) classical dynamics.

In contrast, in this thesis experimental evidence is presented to prove that directed motion can be generated in a fully chaotic Hamiltonian system with appropriately reduced symmetries.

1.1 Breakdown

The research presented in this dissertation starts in **chapter 2** with an introduction to the ways in which light exerts force on matter. This leads into the concepts behind laser cooling - Doppler cooling, the magneto-optical trap, and optical lattices - as well as the application to laser tweezers.

Chaos and quantum chaos is introduced in **chapter 3** using as the exemplar system the kicked rotor.

In **chapter 4** the cold atom realisation of the kicked rotor is described, effects due to deviations from the ideal case in real experimental scenarios are calculated, and the principal points behind the theory of momentum diffusion in the system with broken spatial and temporal symmetry are discussed.

[2]Note that Schanz *et al.* refer to these systems as Hamiltonian ratchets, while Flach *et al.* do not.

Details of the experimental set-up and procedure necessary to realise the quantum chaos experiments with ultra-cold atoms are given in **chapter 5**. The chapter continues to present results of preliminary experiments to show known phenomena, to test the operation and flexibility of the experiment and to demonstrate new techniques. Also shown here are data that result from utilising the new techniques in a partly chaotic system.

Demonstrated in two different ways, the results in **chapter 6** present an experimental realisation of directed atomic transport in a Hamiltonian system due to chaotic dynamics alone.

Proposals and experimental preparation for future experiments to produce directed transport in a fully chaotic Hamiltonian system are drawn up in **chapter 7**. Also highlighted are the experimental challenges these experiments present and the work done so far to solve them.

Changing theme, **chapter 8** details the design and construction of a scanning optical tweezers.

Evidence of trapping, multiple trapping, and the manipulation of dielectric microspheres and micro-bubbles of ultrasound contrast agent is shown in **chapter 9**. This should prove to be a very useful tool for future experiments, and proposals for research in exciting interdisciplinary fields of biophysics are made.

Finally, **chapter 10** concludes.

CHAPTER 2

Light forces, laser cooling and optical trapping

The purpose of this chapter is to provide a little historical background and to review some of the highlights in neutral particle manipulation with emphasis on the relevant techniques for laser cooling and optical trapping.

2.1 A brief history

The concept of light exerting a mechanical force on matter was realized early on in Astronomy. Kepler correctly suggested in 1619 that it was the pressure of sunlight that made the tail of a comet stream away from the Sun [19]. It was about 250 years later that Maxwell's theory of electromagnetism quantified radiation pressure, and in 1901 Nicholas and Hull were the first to detect

it [20]. Despite excitement, the discovery was considered to have no practical application because the magnitude of the measured forces were so minute. The force of light was observed on individual atoms by Frisch in 1933 (see [21] and references therein) by deflecting a beam of sodium atoms by bombarding with light from a sodium lamp, but it was not until the advent of lasers in 1960 [22] that much progress was made in this field. The monochromatic laser beams enabled light to be focussed down to small, highly intense spots. Basic calculations by Ashkin led him to believe that tightly focussed beams of laser light could accelerate small particles by a colossal amount[1]. Indeed, simple experiments using just milliwatts of laser power, weakly focussed into a suspension of small dielectric spheres, showed the particles moving in the direction of the laser light with a velocity in approximate agreement with the crude estimations. However, it was found that not only was this 'scattering force' observed in the direction of the beam, but an unforeseen effect was causing another component of force directed toward the beam axis. It will be shown in section 2.2 that this separate transverse component also originates from radiation pressure, and is due to the gradient in light intensity across the cross-section of the Gaussian beam. Having understood the origin and magnitude of the two force components (using a ray-optics approach) made it possible for Ashkin to trap the neutral dielectric particles in three-dimensions using weakly diverging counterpropagating beams [23]. He also demonstrated that particle levitation was possible by suspending a neutral dielectric microsphere in a slightly diverging, upward pointing beam. The

[1]For example, as a rough calculation a 100mW beam focussed to a spot comparable in size to the wavelength $\approx 1\mu$m will exert a force on a particle of diameter $\approx 1\mu$m (treated as 100% reflective, with a density of 1gcm^{-3}) such that the acceleration experienced is approximately 2×10^5 times the acceleration due to gravity!

particle is trapped in the vertical/axial direction by the balance between the scattering force and gravity, and confined in the transverse direction by the gradient force. It was later realised that just a single, tightly focused laser beam could be used to capture particles in three dimensions. This configuration, the simplest of all traps, is axially stable because of the dominance of the backward axial gradient force over the forward scattering force. The particles could be manipulated by moving the beam, and this work has developed into what is now known as optical tweezers, whereby the light is typically focussed through a microscope objective. This is exactly the approach discussed in this thesis for the manipulation of micron-sized particles.

The success of the experiments on macroscopic particles prompted more thought about the trapping of atoms using laser light tuned to specific optical transitions [23]. It was shown that a scattering force in the direction of the incident light should exist due to the process of absorption and subsequent isotropic emission of resonant photons. The first proposals for what is now commonly known as laser-cooling were made independently in 1975 by Wineland & Dehmelt [24] for the cooling of trapped ions (which will not be discussed further in this context) and Hänsch & Schawlow for the cooling of free atoms [25]. They made the important suggestion that it was possible to exploit the Doppler effect to produce a strong velocity-dependent scattering force, reminiscent of that experienced by an object moving through a viscous liquid.

A big experimental step on the way to atom trapping was the gross slowing of atomic beams using the scattering force of an opposing laser beam by Phillips *et al.* [26, 27]. The large Doppler shifts that occur as the atoms are

slowed were accounted for by magnetically tuning the resonant frequency of the atoms with a tapered magnetic field to keep the peak of the distribution resonant with the laser light. Although this 1D technique could slow axial velocities there was still no transverse cooling and lowest average temperatures were around 0.1K.

In 1985 Chu *et al.* [28] used three pairs of opposing beams to damp atomic motion in 3D. However, the atoms were not 'trapped' as they underwent a diffusive-type motion through the "optical molasses", and could eventually reach the edge of the light field and escape. The same group reported the first optical trapping of atoms in 1986, transferring the optical molasses to a dipole force (gradient force) optical trap created by a strongly focussed laser beam tuned far below resonance. Large gradient forces with detuned light were also used to focus an atomic beam [29], marking the beginning of the field of atom optics whereby atoms are guided by light.

It was in 1987, however, that atomic physics was revolutionised by the addition of a magnetic field to an optical molasses. Working on a suggestion of Jean Dalibard, the group of Raab demonstrated the magneto-optical trapping of atoms from an atomic beam [30]. The magneto-optical trap (MOT) uses optical molasses to cool atoms, while simultaneously utilising the Zeeman shift of the atomic energy levels in a magnetic field to introduce a spatial dependence on the radiation pressure and thus confine the atoms to the centre of the magnetic field. The MOT was considerably simplified when it was demonstrated that atoms could also be trapped directly from an ambient atomic vapour [31]. The MOT has become one of the most powerful tools in atomic physics, as it provides a cold sample of atoms that can be

used as the starting point for a very wide range of experiments [32]. Indeed, all of the experiments with cold atoms discussed in this thesis are performed with a caesium MOT loaded from atomic vapour, as described in [33].

In 1988, Lett *et al.* reported seemingly anomalously low temperatures of a sodium optical molasses [34]. The observed temperature of $43\pm20\mu$K was well below the 'Doppler temperature' (240μK for sodium), which was thought to be the lowest obtainable by laser cooling. The explanation for the 'sub-Doppler' temperatures was soon found in the optical pumping, light shift and polarisation gradient effects that were neglected in the simple Doppler cooling model. (For a more detailed account of the history and ideas behind laser cooling, see references [21, 32, 35–41]). The new theories were successful in accounting for the low temperatures observed experimentally. Furthermore, the mechanism proposed by Dalibard and Cohen-Tannoudji [42,43] (the fantastically intuitive picture of Sisyphus cooling, which has since become the standard model for sub-Doppler cooling - see section 2.5) highlighted the possibility of trapping atoms in an array of sub-wavelength sized potential wells. Unsurprisingly, these structures were termed optical lattices, and several schemes have been devised to extend them to higher dimensions [44]. Optical lattices have proven to be a very useful tool and a testing ground for many different experiments. By tuning the lattice beams far from atomic resonance such that spontaneous scattering (and hence dissipation and decoherence) are negligible, a large proportion of the atoms can be prepared in the ground state [45,46]. As a result, optical lattices provide an excellent setting to perform experiments where the absence of dissipation is essential, such as demonstrating phenomena in chaos, as will be shown later.

The breadth of research involving the interaction of matter with light is now enormous. Experiments and practical applications using optical tweezers, let alone magneto-optical trapping, optical lattices, atom optics and Bose-Einstein condensates, are far too numerous to mention in this short introduction. It will have to suffice to say that theoretical and technological advances that have been made using the interaction of matter and light since the birth of the laser have been immense. To recognise only the most highly awarded achievements, the Nobel Prize was given to Hans G. Dehmelt and Wolfgang Paul "for the development of the ion trap technique" along with Norman Ramsey for his contribution to, among other examples, time stadards and atomic clocks. It was also awarded to Claude Cohen-Tannoudji, William Phillips and Steven Chu in 1997 for the development of methods to cool and trap atoms with laser light, and to Eric Cornell, Carl Weimann and Wolfgang Ketterle in 2001 for the achievement of Bose-Einstein condensation in dilute gases of alkali atoms, and early fundamental studies of the properties of the condensates.

2.2 Light forces

Light can exert force on matter because photons carry momentum. The basic mechanism for radiation pressure is the conservation of this momentum as it is exchanged with atoms or particles. This can either occur coherently, by the re-distribution of the incident field, or incoherently, by the absorption and spontaneous re-emission of photons.

The force that arises from the coherent interaction with light is also called

the *dipole force.* It is coherent because it does not involve dissipation or diffusion. It occurs because atoms placed in an electric field become polarised, acquiring an induced electric dipole moment in the direction of the field. This dipole moment results from the perturbation of the motion of the electrons produced by the applied electric field. Molecules may also acquire an induced electric dipole moment in the direction of the external field. Therefore if an insulator is placed in an electric field, its atoms or molecules become electric dipoles oriented in the direction of the applied field.

The dipole interaction energy has the form $-\mathbf{d} \cdot \mathbf{E}$, where $\mathbf{d}$ is the dipole moment and $\mathbf{E}$ is the electric field. Because the induced dipole moment is proportional to the applied field, the optical potential (due to the ac Stark shift) is proportional to the field intensity, and thus the dipole force is proportional to the gradient of the field intensity. Hence this force is also commonly referred to as the *gradient force.*

For an atom in its ground state, the polarisability is positive for laser frequencies up to the first resonance. Ashkin proposed that atoms could be trapped by a strongly focused laser beam tuned below the atomic resonance [23, 47]. Unfortunately, the dipole moments that can be induced on an atom under experimentally realisable conditions are extremely weak. The trapping potential is thus rather shallow - equivalent to a temperature on the order of mK - and so optical trapping of atoms is only feasible in conjunction with suitable cooling schemes. However, in the case of small, dielectric particles ranging from 100μm down to approximately 20nm, the particles are polarizable enough to be trapped by a reasonable light intensity gradient in a suitable medium. This forms the basis for optical tweezers, which shall be

discussed further in section 2.6.

The dissipative force that arises from the incoherent interaction with light, namely spontaneous photon scattering events, is called the *scattering force.* It is very easy to understand the physical origin of radiation pressure. Every time an atom scatters a photon it experiences a small change in momentum. This momentum is precisely equal to the difference in the photon momentum before and after the interaction with the atom. In the case of incoherent scattering due to the absorption and spontaneous emission of a photon, the atom experiences a recoil in the direction of the incident light on absorption and then another recoil in the opposite direction to the emitted photon. Because spontaneous emission has no preferred direction, it does not contribute to the net change in momentum when averaged over many absorption/spontaneous emission cycles, and the average change of velocity per scattered photon is $\Delta v = p/m = h/m\lambda$, where m is the mass of the atom.

As a sense of scale we shall calculate this for caesium - the atomic species used in our laser cooling experiment. A group one alkali metal it has a mass of $m = 133\text{au} = 2.21 \times 10^{-25}\text{kg}$. The infra-red D2-line transition is $6^2S_{1/2} \leftrightarrow 6^2P_{3/2}$ with wavelength 852.3nm, and so $\Delta v \approx 4\text{mms}^{-1}$. This appears insignificant in comparison to typical atomic thermal velocities of around 10^5mms^{-1}. However, the transition has a lifetime of 30.5ns [48]. A saturated caesium atom has 50% probability to be excited, so on average it absorbs, and emits, one photon every 61ns or approximately 2×10^7 photons s^{-1}. The corresponding acceleration of the atom is thus $(2 \times 10^7)h/m\lambda \approx 10^5\text{ms}^{-2}$, which is approximately ten thousand times the acceleration due to gravity! A beam of laser light thus has a substantial, albeit unidirectional,

effect on atoms. The following section describes a way of harnessing the scattering force to cool an atomic sample.

2.3 Doppler cooling

The Doppler cooling scheme exploits the Doppler effect to generate a velocity dependent scattering rate such that faster moving atoms feel a larger force opposing their direction of motion. For simplicity, consider a two-level atom illuminated by counter-propagating laser beams tuned below atomic resonance. An atom moving against the direction of a laser beam will see the beam Doppler-shifted into resonance, while the beam co-propagating with the atom will be Doppler-shifted further away from resonance. Thus the atom will preferentially scatter photons from the counterpropagating beam and the result is a net momentum transfer opposing the motion of the atom. For small velocities and suitable detuning this force is proportional to the velocity and resembles the drag force experienced by an object moving in a thick, viscous liquid. This arrangement was hence termed *optical molasses.*

There is a limit to the temperature achievable by Doppler cooling - the *Doppler limit* - which corresponds to the equilibrium of cooling and heating processes. The cooling mechanism has already been discussed. The heating originates from the random walk in momentum space caused by the random momentum associated to spontaneous emission. This random walk leads to a broadening of the atomic momentum distribution (heating). By equating the rates of these competing processes, the Doppler Temperature, T_D, can

be shown to be given by the following simple equation:

$$T_D = \frac{\hbar\Gamma}{2k_B} \tag{2.1}$$

where Γ is the natural linewidth of the excited state. For caesium, $\Gamma = 2\pi \times 5.22\text{MHz}$, and so $T_D = 125\mu\text{K}$. Rather intuitively, this shows that the limit to the Doppler cooling mechanism is determined by the linewidth of the cooling transition.

2.4 The magneto-optical trap

An obvious extension to the above scheme is to consider pairs of counterpropagating laser beams along three orthogonal axes to cool an atomic sample in three dimensions. However, although the 3D optical molasses cools the atoms, they are not trapped. The atoms are still free to diffuse within the region defined by the intersection of the laser beams and they will eventually escape. Atoms can be trapped by applying a magnetic field gradient which increases linearly from zero with distance from the trap centre. The resulting configuration is called the Magneto-Optical Trap (MOT).

To explain the principle of operation of a MOT consider a (fictitious) two-level atom with ground state angular momentum $|J_g = 0\rangle$, excited state $|J_e = 1\rangle$, and three Zeeman sub-levels. An applied magnetic field produces a shift in the potential energy of

$$\Delta V_{Zeeman} = g_J \mu_B m_J B \tag{2.2}$$

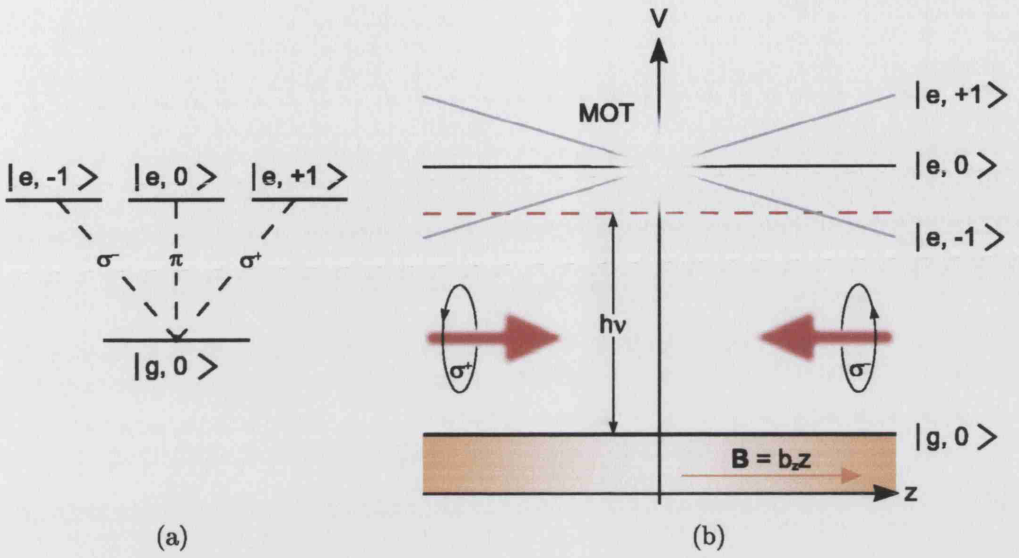

Figure 2.1: Principle of magneto-optical trap (MOT) operation. The scheme is easily extended to 3D using a spherical quadrupole magnetic field and 3 orthogonal $\sigma^+\sigma^-$ standing waves (polarisation defined with respect to the direction of propagation of the laser beams).

where g_J is the Landé g-factor and μ_B is the Bohr magneton. As illustrated in figure 2.1, the inhomogeneous magnetic field varies as $\mathbf{B} = b_z\mathbf{z}$. This results in a position-dependent energy shift of the $|J_e, m_j = \pm 1\rangle$ sub-levels. By subjecting the atom to red-detuned laser light from a counterpropagating pair of beams, the velocity dependent scattering rate, as discussed previously, is now supplemented by a spatially dependent scattering rate. The result is that the larger the distance of the atoms from $B = 0$, the closer the $|J_e, m_J = -1\rangle$ level is shifted into resonance and the greater the scattering force pushing the atoms towards the centre of the MOT by one of the circularly polarised beams. In this way atoms accumulate around the position of zero magnetic field.

A real atom such as caesium has a more complicated level structure, as

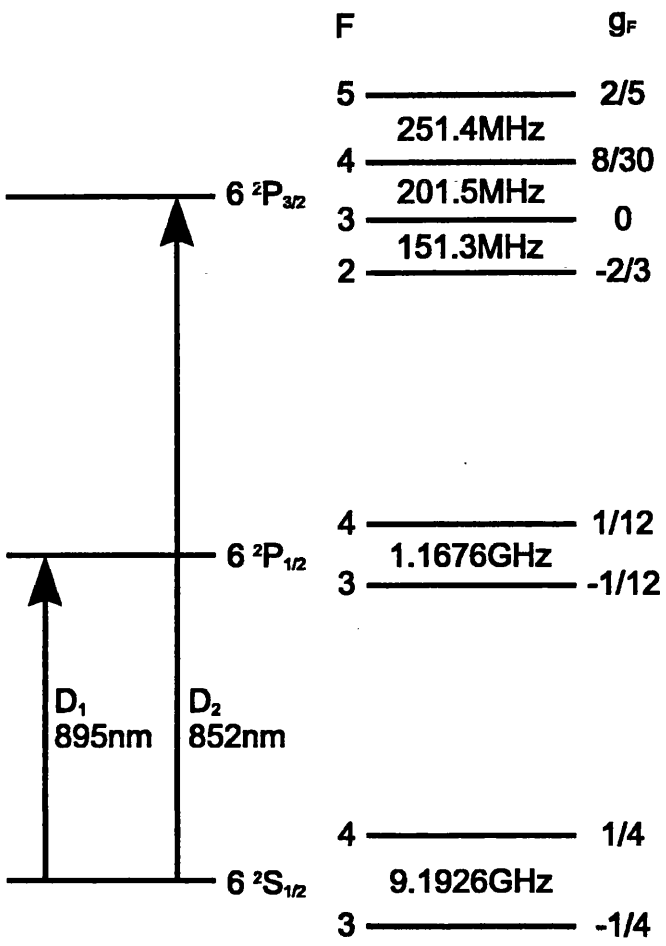

Figure 2.2: Caesium energy level structure showing the hyperfine splittings and Landé g-factors for the D_1 and D_2 lines.

shown in figure 2.2. The ground state has hyperfine components with angular momentum $|F_g = 3, 4\rangle$, and the excited state $|F_e = 2, 3, 4, 5\rangle$. The cooling transition is the closed $6^2S_{1/2}(F_g = 4) \rightarrow 6^2P_{3/2}(F_e = 5)$ transition.

Optical pumping may cause losses due to off-resonant excitation. This is because any off-resonant excitation to a state other than $|F_e = 5\rangle$ can be followed by decay into $|F_g = 3\rangle$ where an atom is lost from the cooling cycle. To solve this a 'repumper' beam is usually used in a MOT, in this case tuned

to the $6^2S_{1/2}(F_g = 3) \rightarrow 6^2P_{3/2}(F_e = 4)$ transition.

The MOT in our experiment is loaded directly from the background vapour in a large optically-accessible cell [31, 49]. The vapour in the glass cell needs to be at a very low pressure to minimise losses from the trap due to collisions with untrapped atoms. Extending the cooling scheme to 3D is straightforward. The three orthogonal $\sigma^+\sigma^-$ standing waves are created with three circularly polarised retroreflected beams (from frequency-locked grating-stabilised lasers) that make a double pass through a $\lambda/4$ waveplate before returning through the cell. The configuration is shown in figure 2.3 with the mirrors and waveplates omitted.

The MOT requires a magnetic field gradient of around ten Gauss per cm across the trapping region. This is generated by a pair of water-cooled anti-Helmholtz (trap) coils (whereby the current flows in opposite directions in each) around the cell. The field is zero at the midpoint on axis between them and increases linearly in all directions (a spherical quadrupole) [50]. For such a field the radial field gradient is equal to half the axial gradient and in opposite sign. This is the reason why the polarisation of the +z beams are opposite in sense to that of the +x and +y beams.

In addition to the trap coils, three much larger pairs of Helmholtz coils, each with their axis orthogonal to that of the other two, are necessary. After cooling, the atoms are very sensitive to magnetic fields and these coils are to compensate for the terrestrial field of a few hundred mG. The size of the coils is to allow optical access to the cell and so that the resulting magnetic field at the trap due to these coils is uniform.

The MOT is the starting point for all of the chaos experiments described

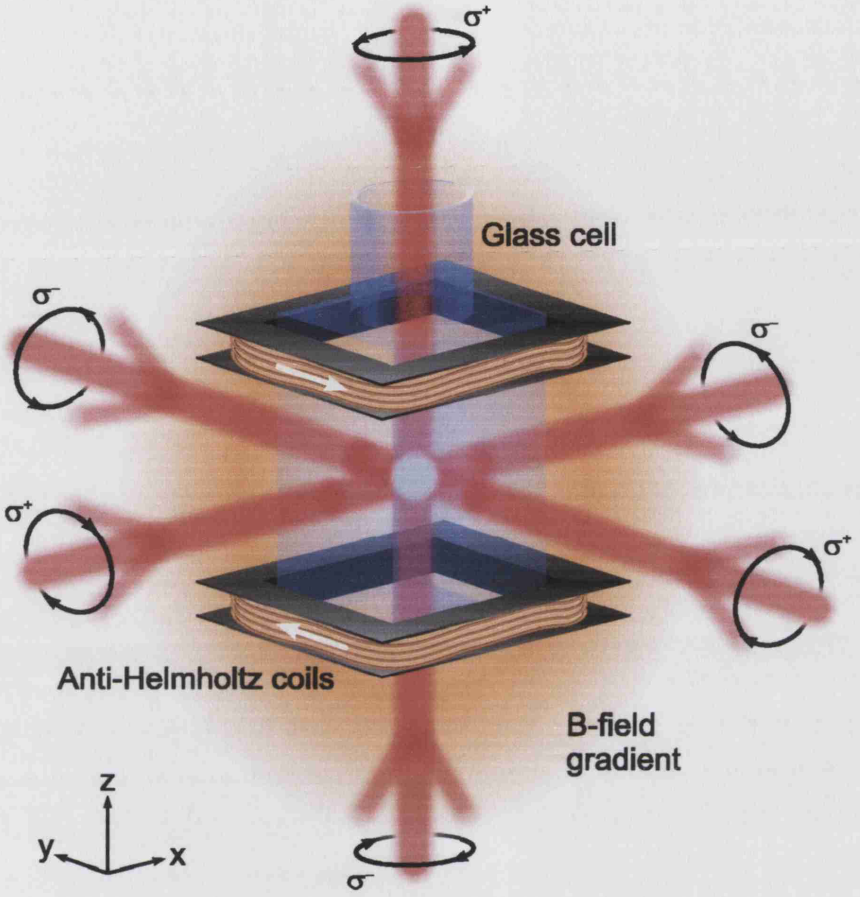

Figure 2.3: MOT configuration. The white arrows indicate the direction in which the current flows around the coils. The orange shading is an impression of the resulting magnetic field which is zero at the centre of the trap.

in this thesis and the cold atom and atom-optics experiments of many other research groups. It is relatively easy to operate and surprisingly robust, being fairly insensitive to imbalances in laser beam intensities, misaligned trapping beams and impure circular polarisations. Full details particular to our experiment: the design of the grating stabilised lasers, their frequency locking, the setup procedure and vacuum system necessary to prepare the

glass cell, the necessary magnetic fields, and the characterisation of the trap can all be found in [33,51].

2.5 Sisyphus cooling and optical lattices

It transpires that the multi-level nature of any real atomic species used for optical trapping and cooling experiments is of great significance. After it was reported that temperatures far lower than the Doppler limit could be attained it was soon realised that a more sophisticated understanding, including consideration of a multi-level ground state, was necessary. For this, consider another fictitious atom with ground state $|J_g = 1/2\rangle$ and excited state $|J_e = 3/2\rangle$. This energy level scheme and the associated Clebsch-Gordan coefficients are shown in figure 2.4. Also consider the

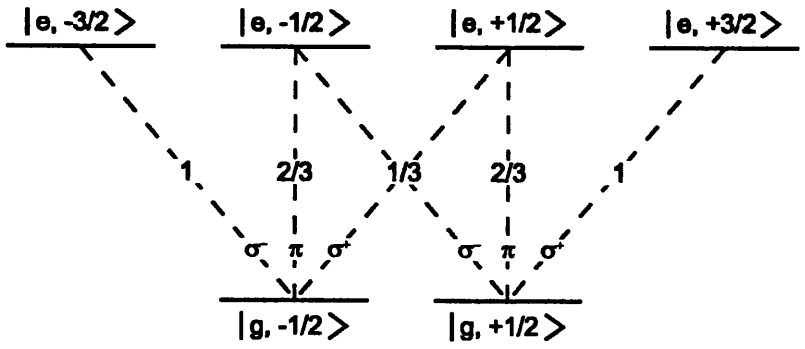

Figure 2.4: Squares of the Clebsch-Gordan coefficients for a $|J_g = \frac{1}{2}\rangle \rightarrow |J_e = \frac{3}{2}\rangle$ transition.

fictitious atom being illuminated by counter-propagating laser beams that this time have orthogonal *linear* polarisations[2]. The light fields form a po-

[2]New sub-Doppler cooling mechanisms also arise for a $\sigma^+\sigma^-$ configuration. However, these mechanisms do not produce atomic localisation, and therefore will not be discussed in the present context.

larisation gradient as shown in figure 2.5. The polarisation changes from linear (+45°) to σ^- to linear (−45°) to σ^+ and back to linear (+45°) in half the laser wavelength. This has a profound effect on the relative magnitude of the light-shifts (the A.C. Stark shift) of the $m_J = \pm 1/2$ components of the ground state. For example, take the point at $z = \frac{\lambda}{8}$ in figure 2.5 where the polarisation is purely circular (σ^-). From figure 2.4 it can be seen that of the favoured transitions for σ^- polarisation, the one from $|J_g, m_J = -1/2\rangle \rightarrow |J_e, m_J = -3/2\rangle$ has a Clebsch-Gordan coefficient three times greater that that from $|J_g, m_J = +1/2\rangle \rightarrow |J_e, m_J = -1/2\rangle$. Consequently, the light-shift of $|J_g, m_J = -1/2\rangle$ is three times greater than that of $|J_g, m_J = +1/2\rangle$. The scenario is reversed at $z = \frac{3\lambda}{8}$ where the polarisation is purely σ^+. Therefore, the spatially dependent polarisation leads to a spatial dependence of the relative light-shifts of $|J_g, m_J = \pm 1/2\rangle$ as illustrated in figure 2.6.

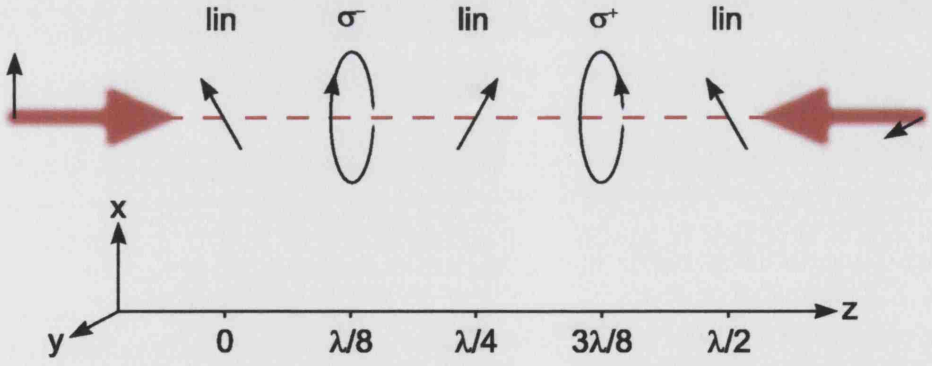

Figure 2.5: Polarisation gradients in a 1D lin⊥lin configuration. The polarisation changes from linear (+45°) to σ^- to linear (−45°) to σ^+ and back to linear (+45°) in half the laser wavelength.

In this simple case there is a sinusoidal variation in the light-shifts whereby the potential minimum of one sub-level coincides with the maximum of the

other. The variation of the light-shifts is given by

$$V_{\pm}(z) = \frac{V_0}{2}(-2 \pm \cos(2kz)) \tag{2.3}$$

where k is the wavevector of the laser beam and V_0, the average light-shift is given by

$$V_0 = -\frac{\hbar\Delta}{3}\frac{\Omega_R^2}{\Delta^2 + \Gamma^2/4} \tag{2.4}$$

In equation 2.4, Δ is the detuning of the laser from resonance and Ω_R is the Rabi frequency for a transition with a Clebsch-Gordan coefficient equal to one. It is given by $\Omega_R = -D\mathcal{E}_0/\hbar$, where D the dipole matrix element and $\mathcal{E}_0$ the electric field amplitude, and hence Ω_R^2 is proportional to the laser light intensity. Writing the Rabi frequency as $\frac{\Omega_R^2}{\Gamma^2} = \frac{I}{2I_{sat}}$, where $I_{sat} = \frac{\pi h \Gamma c}{3\lambda^3}$ is the saturation intensity, and for a detuning not too close to resonance the potential well depth can be re-written:

$$V_0 = -\frac{I}{I_{sat}}\frac{\hbar\Gamma^2}{6\Delta} \tag{2.5}$$

The potential depth is thus inversely proportional to the detuning, $V_0 \propto \frac{I}{\Delta}$.

Now consider the effects of optical pumping on an atom traversing the potential surface. As an example, starting in the $|J_g, m_J = +1/2\rangle$ state at $z = -\frac{\lambda}{8}$ the atom climbs the potential "hill" as it moves in the positive z direction. As the dominant circular polarisation changes from σ^+ to σ^-, the probability of absorbing a σ^- photon increases. This is most likely near the "top" of the hill where the local polarisation is pure circularly polarised, and the atom is excited to $|J_e, m_J = -1/2\rangle$. The atom then decays back to

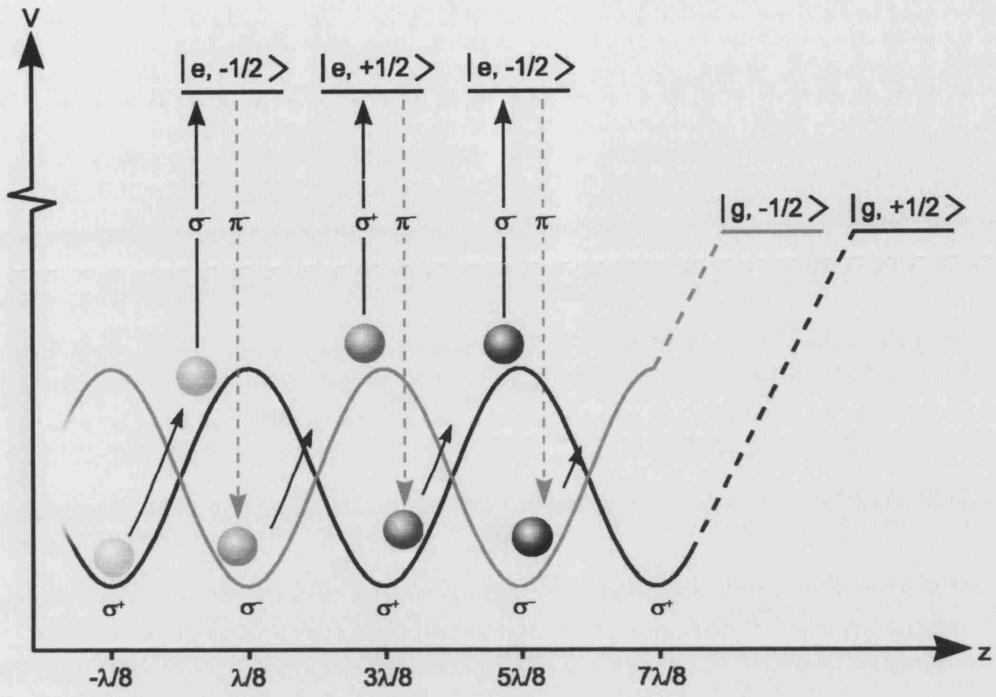

Figure 2.6: Intuitive picture of Sisyphus cooling. Repeated optical pumping between the sublevels reduces the atomic kinetic energy.

$|J_g, m_J = +1/2\rangle$ to be re-excited, or to the "valley" of $|J_g, m_J = -1/2\rangle$. As the atom climbs the potential hill it expends kinetic energy. Then, after a few absorption/emission cycles, the atom will end up in the $|J_g, m_J = -1/2\rangle$ state, but not regaining the kinetic energy as it is optically pumped into the valley without descending the slope. This mechanism has been termed 'Sisyphus cooling' because it recalls the fate of Sisyphus in Greek mythology, doomed for ever to roll a boulder up a hill, only to see it roll down and have to start again [52].

The atoms eventually lose enough kinetic energy through this repeated process that they can no longer climb the hill. For this simple $|J_g = 1/2\rangle \rightarrow |J_e = 3/2\rangle$ system the atoms thus become localised in space at the minima of

a periodic potential, i.e. they become trapped in the potential well, leading to a spatially periodic density. The resulting structure is termed an 'optical lattice'.

For a more complicated, real energy level structure such as that in caesium with nine Zeeman sub-levels in the ground state, there are nine potential surfaces, and a local 'intra-well' Sisyphus-type mechanism has been proposed which leads to further cooling and localisation [53]. The important result is that there is a correlation between the positions of maximum light shift and maximum optical pumping rate which results in the atoms being pumped towards the lowest lying potential surface. As for Doppler cooling, by considering the competition of heating and cooling effects, a temperature limit at the point of equilibrium for Sisyphus cooling has been shown to be

$$T \approx \frac{\hbar\Omega_R^2}{8k_B|\Delta|} \tag{2.6}$$

In summary, this section described the sub-Doppler cooling mechanism associated with the 1D lin⊥lin configuration, and mentioned that sub-Doppler cooling is also present in the $\sigma^+\sigma^-$ configuration when multi-level atoms are considered. It should be noted that in a real (multi-level) atom, both types of cooling mechanisms are present [54].

2.5.1 Far-detuned optical lattices

It shall be seen later that for the chaos experiments the atoms must be subjected to a coherent interaction with a 1D sinusoidal optical lattice. For

this reason any decoherence must be eliminated by reducing the spontaneous scattering. The scattering rate Γ' is given by the following equation:

$$\Gamma' = \frac{s}{2(1+s)}\Gamma \tag{2.7}$$

where s is the saturation parameter, given by:

$$s = \frac{I/I_{sat}}{1+(2\Delta/\Gamma)^2} \tag{2.8}$$

So the scattering rate is proportional to the inverse-square of the detuning Δ, and to reduce the scattering the optical field must be tuned sufficiently far from the nearest atomic resonance. However, it was seen in equation 2.5 that for detuned laser fields the potential depth is inversely proportional to the detuning. High laser powers are therefore necessary to achieve viable potential depths at negligible scattering rates. This is discussed further in section 5.1.3. To compensate for the loss of potential depth with increased detuning, a powerful titanium-sapphire (Ti:sapphire) laser is used.

For far-detuned lattices the interaction is dominated by the dipole force, a coherent interaction, but because this is nondissipative the experiments with atoms in far-detuned lattices must first pre-cool the atoms with near-resonant light. The cold atom cycle to achieve this is discussed in section 5.1.1.

The final point to note is that to produce a single sinusoidal optical potential, all of the Zeeman states of the atom must have the same light shift. This is easily achieved by creating the simplest possible lattice from counterpropagating beams with linear parallel polarisation, the so-called lin||lin

configuration.

2.6 Laser tweezers

Laser tweezers are three-dimensional traps that use a focused laser to trap and manipulate microscopic, neutral objects such as small dielectric spheres. High spatial light intensity gradients are most commonly created by focussing laser light to a diffraction-limited beam waist using a microscope objective.

The *numerical aperture* (N.A.) of an objective is a quantity used to express its light-gathering ability. It is a measure of the number of highly diffracted image-forming light rays that are captured by the objective. Higher values of numerical aperture accept increasingly oblique rays to enter the front lens of the objective, producing images with better resolution. Conversely, as has been mentioned, objectives are also used to focus laser light onto the specimen plane, and objectives with the highest numerical aperture focus light more sharply. To form the smallest possible beam waist (the diffraction-limited beam waist), and hence maximise the intensity gradient therefore maximising the gradient trapping force, a microscope objective with a high magnification and high numerical aperture is necessary. It is also necessary for the incident laser light to fill (or even slightly overfill) the back aperture of the objective. This will be discussed in sections 2.6.1 and 8.2.1.

The efficiency of a particular laser tweezers setup is customarily quantified in terms of a dimensionless quantity Q, whereby the trapping force on the object is given by

$$F_{obj} = Q\frac{n_m P}{c} \tag{2.9}$$

where n_m is the index of refraction of the suspending medium, c is the speed of light and P is the incident laser power. Q can also be considered as the fraction of the power from the light that is utilized to exert force on the object. The efficiency parameter includes the effect that the laser beam has on the trap performance through parameters such as convergence angle, spot size, wavelength, polarisation, and beam profile. It also takes into account the optical properties of the trapped object, including size, shape, and relative refractive index with respect to the surrounding medium.

Two distinct approaches may be adopted when trying to understand the origin of the forces acting within optical tweezers. For particles in the Mie regime, where the diameter of the particle is large compared to the wavelength of the trapping light, a ray optics approach is used. For particles in the Rayleigh regime, where the particle is much smaller than the wavelength of the trapping light, the dipole model is used.

Presented here are both the qualitative ray optics description (for a comprehensive quantitative calculation see [55]) and the dipole force description of the operation of laser tweezers. Unfortunately our area of concern, and the majority of biological work, falls in between the Rayleigh and Mie regimes where the dimensions of the particle approximates the wavelength of the trapping light. Here, experimental data is not consistent with previous calculations [56] and optical trapping theory is relatively immature. Although considerable work has gone into predicting optical forces, the agreement between theory and measurement is unsatisfactory. A good review of trapping theories in both regimes, and possible considerations for future models in between the Rayleigh and Mie regimes, is discussed by Svodboda and Block [56].

2.6.1 The Mie Regime - Ray Optics Model

This is a remarkably accurate description of laser tweezers for objects that are larger than the wavelength of the laser. Core to this approach is the understanding that, since light carries a linear momentum of h/λ per photon, the refraction of light by a transparent object results in a change in photon momentum and a corresponding reaction force acting on the object.

Figure 2.7 shows the refraction of light rays at the surface of a dielectric sphere and the resulting forces acting on it. The counter-intuitive aspects are immediately apparent. The (Gaussian) intensity profile of the beam cross-section results in a lateral force on the object acting towards the centre of the beam. The tight focus of the beam generates an axial force that acts in the direction of the center of focus. This resultant force is called the gradient force. The stability of the trap is the result of the dominance of the gradient force pulling particles toward the high focus of the beam over the scattering force trying to push particles away from the focus in the direction of the incident light. The trap position depends on the competition between these two forces and is usually just a little distance away from the beam focus in the direction of propagation of the light.

Quantitative calculations of trapping forces in the Mie Regime [55] model a known distribution of parallel rays entering the back focal plane of an objective, which is assumed to focus all rays to a point. In this limit, by definition, diffraction effects are neglected. Taken into account is the reflection and refraction both internally and at the surface of the sphere, so it is exact within the ray optics approximation. The overall force exerted by a beam with a given profile is the vector sum of the forces resulting from the ensemble of

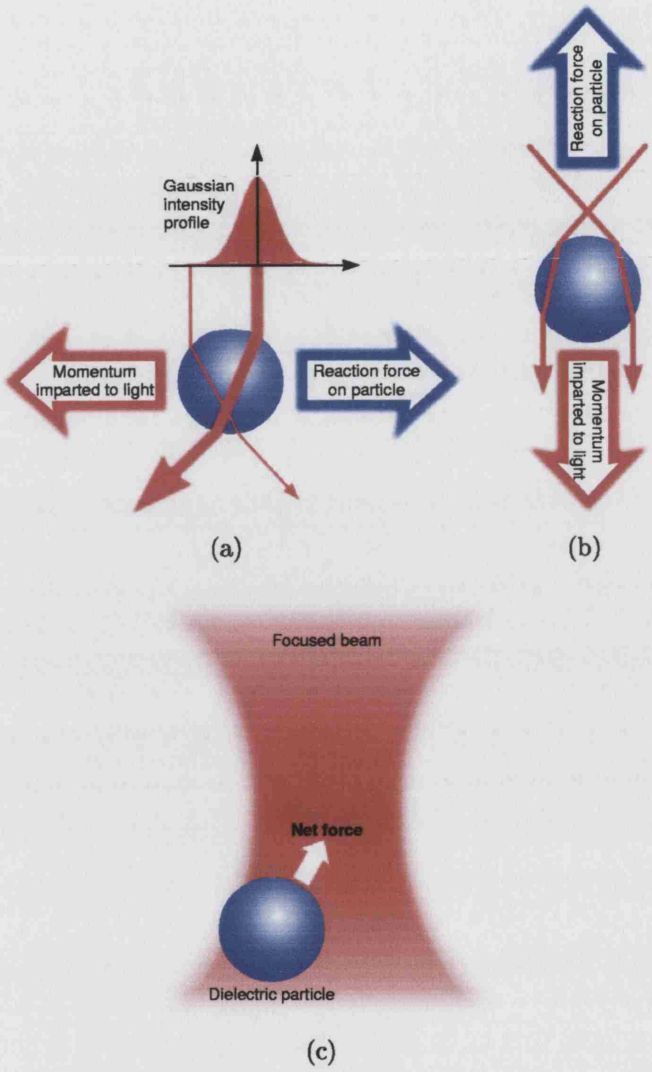

Figure 2.7: Qualitative view of the trapping of dielectric spheres. Figure (a) shows the lateral trapping force, (b) the axial trapping force, and (c) the overall trapping force, the gradient force.

rays that comprise the beam. The gradient and scattering components of the force, $\mathbf{F}_{grad}$ and $\mathbf{F}_{scat}$, due to a single ray of power, P, are given by

$$\mathbf{F}_{grad} = \frac{n_m P}{c}\left\{R\sin 2\theta - \frac{T^2[\cos(2\theta - 2\epsilon) + R\cos 2\theta]}{1 + R^2 + 2R\cos 2\epsilon}\right\}\hat{\mathbf{k}}$$
$$\mathbf{F}_{scat} = \frac{n_m P}{c}\left\{1 + R\cos 2\theta - \frac{T^2[\sin(2\theta - 2\epsilon) + R\cos 2\theta]}{1 + R^2 + 2R\cos 2\epsilon}\right\}\hat{\mathbf{i}} \qquad (2.10)$$

where θ and ϵ are the angle of incidence and refraction, $\hat{\mathbf{k}}$ and $\hat{\mathbf{i}}$ are unit vectors parallel and perpendicular to the direction of the incident ray, and R and T are the Fresnel reflection and transmission coefficients. Because these coefficients are polarisation dependent, so are the trapping forces.

The smallest forces occur in the axial direction where, as has previously been noted, the gradient force must overcome the scattering force. For this reason, the strongest trap is achieved by maximising the restoring force in this direction, even at the expense of the transverse force components. The ray optics theory predicts that *overfilling* the back aperture of the objective leads to stronger trapping than just filling the back aperture [55]. This results because highly converging rays contribute disproportionately to the axial intensity gradient. In addition, discussions of the possible advantages of filling/overfilling the back aperture with laser modes *other* than TEM_{00} are discussed by Ashkin [55].

2.6.2 The Rayleigh Regime - Dipole Model

For particles smaller than the wavelength of the laser light, the ray optics approach is less satisfactory. Instead it is better to consider the forces in terms of the electric field near the trapped particle. In this regime, trapping forces naturally split into two components and, given that the electromag-

netic field is uniform across the dielectric, particles are treated as induced point dipoles [57]. The scattering force, proportional to the optical intensity and in the direction of propagation of the laser light, is given by [58]

$$\mathbf{F}_{scat} = n_m \frac{\langle \mathbf{S} \rangle \sigma}{c} \tag{2.11}$$

where

$$\sigma = \frac{8}{3}\pi (kr)^4 r^2 \left(\frac{m^2 - 1}{m^2 + 2} \right)^2 \tag{2.12}$$

is the scattering cross section of a Rayleigh sphere of radius r. The relative refractive index of the particle is given by $m = n/n_m$ where n is the refractive index of the particle and n_m the refractive index of the medium, $\langle \mathbf{S} \rangle$ is the time-averaged Poynting vector, and $k = 2\pi n_m/\lambda$ is the wave number of the light.

As the object is polarised by the laser, the object experiences a dipole induced Lorentz force. The force is proportional to the gradient of the electromagnetic field intensity. It is given by

$$\mathbf{F}_{grad} = \frac{\alpha}{2} \nabla \langle \mathbf{E}^2 \rangle \tag{2.13}$$

where the polarisability of the object is

$$\alpha = n_m^2 r^3 \left(\frac{m^2 - 1}{m^2 + 2} \right) \tag{2.14}$$

So, the gradient force, as before, will push a dielectric object, with a higher refractive index than that of the suspending medium, towards the beam focus. As long as the gradient force in the axial direction is greater than the

scattering force, stable trapping is achieved. Again, for a trapped object the equilibrium position is slightly down-beam from the laser focus as a result of these forces.

2.6.3 Trapping low-index particles

The theory above has been concerned with trapped objects with a refractive index higher than that of the suspending media. However, there is another class of particles for which the gradient force is reversed and the particles are pushed out of the high intensity region of the beam. Included in this class are transparent hollow dielectric spheres [59], coated bubbles (see section 9.2) and highly reflecting metals [60]. In a ray-optics picture, this is because the deflection through the particle reverses in the case of the low index dielectric spheres and bubbles [23], and the transverse force is dominated by reflected rays for metals. All such particles can be levitated or trapped by using a TEM_{01} laser beam mode, which has an intensity minimum on the beam axis. An obvious alternative solution will be presented in section 9.2.

2.7 Conclusion

Having thus presented a brief account of neutral particle manipulation and laser cooling mechanisms, the next chapter introduces the relevant background material in a different field: chaos.

CHAPTER 3

Chaos

The purpose of this chapter is to introduce the basic notions about chaos and to describe the delta-kicked rotor, a very simple but important model system to study chaotic dynamics.

3.1 A brief history

The study of chaos in dynamical systems began close to the end of the 19th century [61, 62]. An accurate description of two-body interaction in the solar system may be given by Newtonian mechanics. However, the problem of the dynamics of three or more gravitationally interacting bodies was not (and still is not) analytically solvable in general. Nevertheless, much headway was made in the prediction of planetary locations. This was done by first considering the interaction of each planet with the sun and then taking into account the perturbations due to the interactions of the planets with

each other. In fact, Neptune was discovered as a result of this! However, the long-term accuracy with which the planetary motion could be calculated provoked great concern over the stability of the solar system by scientists worldwide. So much so that it was proposed as a prize question in a contest, "The Three Body Problem", won by Henri Poincaré's second submission, a complex and innovative entry that concluded that the stability of the solar system could not be guaranteed. A disturbing discovery in this work later prompted Poincaré to make the famous statement that minute differences in the initial conditions of a system can lead to wildly different outcomes. This exponential sensitivity to initial conditions is fundamental to chaotic dynamical systems and consequentially, small inescapable errors in the knowledge of the state of a system make long-term predictions of the system's evolution impossible. Thus, regardless of the deterministic nature of chaotic systems, their dynamics are intrinsically unpredictable.

Despite the early achievements of Poincaré, the study of chaos did not really take off for several decades. The next important result was obtained in stages around the 1950s and 60s by Kolmogorov, Arnol'd and Moser in the acclaimed KAM theorem (see [63] and references therein). This revived the three-body problem and restored the stability of the solar system in the sense that it proved that certain configurations are stable if the aforementioned perturbations are small. This resulted in the important recognition of the possibility of chaos, the study of which did not really begin in earnest until the arrival of the computer.

The prediction of the weather has always been a problem for mainstream science, because every effort to accurately forecast it has produced very mixed

results. So when digital computers began to come on line in increasing numbers, meteorologists were hopeful that they could now build models sophisticated enough to take into account the many variables involved in weather forecasting. However, despite the employment of intricate computer models weather prediction showed little improvement. Nevertheless an interesting discovery was (somewhat serendipitously) made by Lorenz when he found a peculiarity in the weather model he was testing on his new computer. The basic model of his hydrodynamic system [64], a completely deterministic system of differential equations, gave values for a month or so of simulated weather that were *completely* different from those calculated on his old computer. Eventually discovering that this was due to minute differences in the starting parameters due to the numerical precision of the computers, Lorenz rediscovered Poincaré's "sensitivity to initial conditions". Lorenz called it the *Butterfly Effect*, because it implied that if a butterfly in Brazil flapped its wings it could set off a chain reaction in weather patterns that could lead to a hurricane in Hertford, Hereford and Hampshire a few weeks later[1]. Since then, chaos has been found to be ubiquitous, having found applications in all manner of diverse, and often surprisingly simple, systems. The term "chaos" was coined by Li and Yorke in 1975 [66] to refer to this "deterministic randomness" and the exponential sensitivity to initial conditions of dynamical systems, where it is now understood as the rule rather the exception.

[1]It is, however, widely acknowledged that in these locations hurricanes hardly ever happen [65].

3.2 The classical delta-kicked rotor

The standard system that is used in the investigation of the dynamics of chaotic systems with time dependent Hamiltonians is the kicked rotor. As shown in figure 3.1 the set-up is simple, there are no complicated boundary conditions and noise effects are neglected. However, simple as it may seem, the dynamics of such a system is complicated and cannot be solved analytically in the presence of a strong driving force.

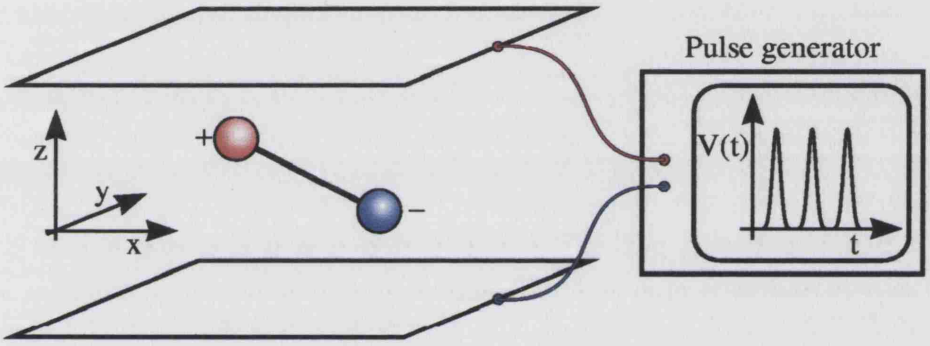

Figure 3.1: The kicked rotor: a diatomic molecule kicked by an electric field. The kicking field is generated by an applied voltage $V(t)$ across the two plates.

A pendulum is often used as the example, but consider here a molecule which is periodically kicked by a uniform electric field. The molecule is simplified to a two-dimensional dipole that is free to rotate in one plane and the sequence of finite-width pulses, as provided by any real function generator, is simplified to a train of n zero-width δ-function kicks. If ε_0 is proportional to the field strength and T is the time between kicks, then a

regular sequence of electric field pulses can be written as

$$E(t) = \varepsilon_0 \sum_{n=-\infty}^{\infty} \delta(t - nT) \tag{3.1}$$

Since we are heading towards a discussion of quantum systems, we use the Hamiltonian formalism to describe the classical *delta-kicked rotor* (CDKR). If L is the angular momentum of the rotor, I the moment of inertia and μ the dipole moment, the sum of kinetic and potential energies give the Hamiltonian:

$$H(L, \theta, t) = \frac{L^2}{2I} + \mu\varepsilon_0 \cos\theta \sum_n \delta(t - nT) \tag{3.2}$$

where θ is the angle of the dipole with respect to the z-axis as shown in figure 3.2. Differentiating equation 3.2, Hamiltonian's equations of motion are

$$\begin{aligned} \dot{L} &= -\frac{\partial H(L,\theta,t)}{\partial \theta} = \mu\varepsilon_0 \sin\theta \sum_n \delta(t - nT) \\ \dot{\theta} &= \frac{\partial H(L,\theta,t)}{\partial L} = \frac{L}{I} \end{aligned} \tag{3.3}$$

The rotor has periods of free motion, during which the electric field is turned off, followed by a kick whereby its angular momentum changes abruptly by an amount that is dependent on the value of the angle θ at the moment at which the kick occurs. Let us call the values of L and θ immediately before the n^{th} kick L_n and θ_n. The solution of equations 3.3 can then be stated in the form of a mapping that relates L_n and θ_n to L_{n+1} and θ_{n+1},

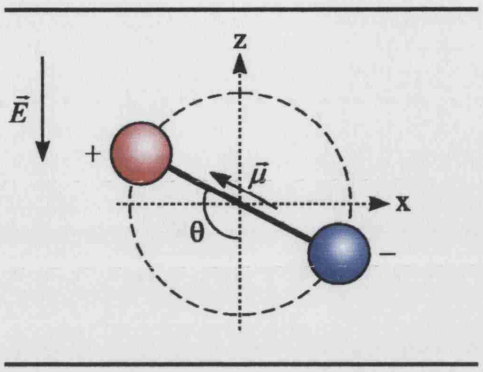

Figure 3.2: The kicked rotor: a dipole with planar rotational freedom, periodically kicked with an electric field $\vec{E}$

the values immediately before kick number $n+1$. If the mapping is known, and the starting conditions L_0 and θ_0 at kick number 0 are given, then the values of L and θ at kick number n can be calculated by simply iterating the mapping. To derive the explicit form of the mapping one must integrate equations 3.3. Using ϵ as an infinitesimally short time interval, integrate the equation for L,

$$\int_{t_n-\epsilon}^{t_{n+1}-\epsilon} \dot{L}(t)dt = \int_{t_n-\epsilon}^{t_{n+1}-\epsilon} \mu\varepsilon_0 \sin\theta \sum_n \delta(t-nT)dt \tag{3.4}$$

where $t_n = nT$ is the time of the n^{th} kick. This equation becomes

$$L(t_{n+1}-\epsilon) - L(t_n-\epsilon) = \mu\varepsilon_0 T \sin\theta_n \tag{3.5}$$

Similarly, integrate the equation for θ,

$$\int_{t_n-\epsilon}^{t_{n+1}-\epsilon} \dot{\theta}(t)dt = \int_{t_n-\epsilon}^{t_{n+1}-\epsilon} \frac{L}{I}dt \tag{3.6}$$

which becomes,

$$\theta(t_{n+1} - \epsilon) - \theta(t_n - \epsilon) = \frac{TL_{n+1}}{I} \tag{3.7}$$

As $\epsilon \to 0$ the following mappings are obtained as a solution to the dynamics defined by 3.3

$$\begin{aligned} L_{n+1} &= L_n + \mu\varepsilon_0 T \sin\theta_n \\ \theta_{n+1} &= \theta_n + TL_{n+1}/I \end{aligned} \tag{3.8}$$

Now define a scaled angular momentum $l_n = TL_n/I$ and introduce a control parameter called the *stochasticity parameter*, or kick strength, $K = \mu\varepsilon_0 T^2/I$, to convert the mapping equations to the conventional scaled dimensionless form. The resulting coupled equations are known as the *Standard Map* [67] (or the Chirikov-Talyor map), so called because of its broad importance in the study of Hamiltonian chaos:

$$\begin{aligned} l_{n+1} &= l_n + K\sin\theta_n \\ \theta_{n+1} &= \theta_n + l_{n+1} \end{aligned} \tag{3.9}$$

Re-writing the Hamiltonian in terms of the new scaled dimensions, $\mathcal{H} = HT^2/I$ gives

$$\mathcal{H} = \frac{l^2}{2} + K\cos\theta \sum_n \delta(t - nT) \tag{3.10}$$

This will be a useful reference for comparison in chapters to follow.

3.2.1 Poincaré surfaces of section

The standard map cannot in general be solved explicitly, for example it is impossible to derive an analytical expression to predict l_n and θ_n for all n and all initial conditions l_0 and θ_0. Information about the system evolution for a particular starting condition is obtained by iterating the mapping and plotting each value of l against θ. By doing this for various values of the starting conditions one may build up a picture known as a Poincaré surface of section: a concise, visual summary of the possible dynamics of the system. Understand that this is not the same as, for expample, plotting θ vs l continuously for an unkicked rotor or a swinging pendulum. Although plots for the kicked rotor at low kick strength look very similar to that of a pendulum, here we are not looking at the continuous evolution of trajectories but rather each point is a snapshot of the trajectory before each kick.

Portions of the two-dimensional (θ, l) phase space are shown in figure 3.3 for various values of the kick strength. The portraits were generated by plotting 300 iterates from the starting conditions ($\theta_0 = \pi$, $l_0^m = -2\pi + m\pi/20$), with $m = 0, 1, \ldots, 80$, for $K = 0.5$, $K = 1$, $K = 2$ and $K = 5$. Highlighted within each phase portrait are a number of trajectories with different starting positions, the successive iterations of which are linked by coloured lines to show the order of time evolution, and the values are marked with oversized points. Note that these lines do not represent a path in phase space by which the trajectories travel but are just intended as a guide from kick-to-kick. Each pair of highlighted trajectories are started very close to each other about an arbitrary point in phase space: $(\theta, l) = (0.75\pi, \pi)$, separated by $\Delta\theta = 0.0005\pi$. The only exception to this are the additional black and

white trajectories plotted for $K = 0.5$ that start at $(\theta, l) = (\pi, 0.4\pi)$, also separated by $\Delta\theta = 0.0005\pi$. The trajectories are intended to demonstrate how the different parts of phase space are built up and how the divergence of the closely starting trajectories changes with kick strength.

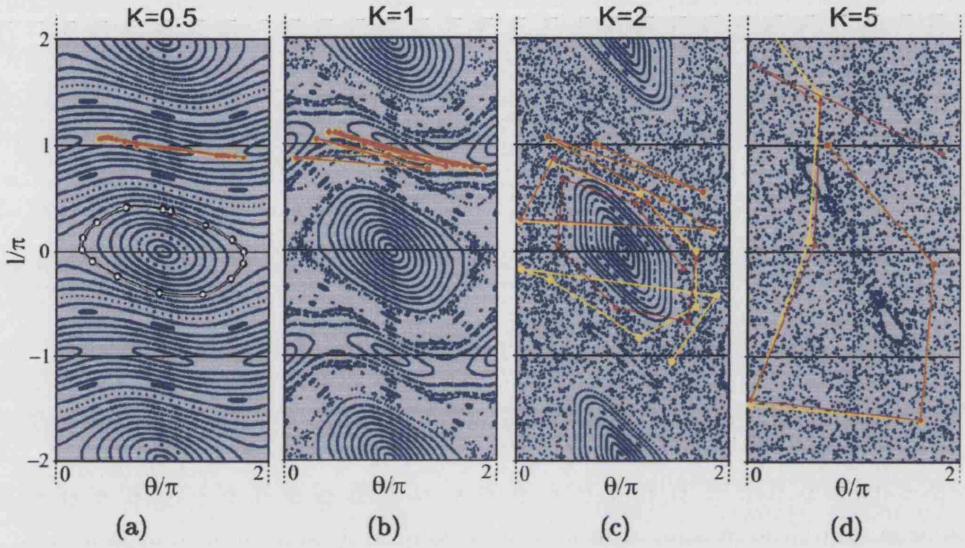

Figure 3.3: Phase-space portraits (Poincaré surface of sections) of the classical kicked rotor for the following kick strengths: (a) $K = 0.5$, (b) $K = 1$, (c) $K = 2$ and (d) $K = 5$

One can see from the phase space portraits, and it can easily be proved from the mapping equations 3.9, that they are periodic in θ with a period of 2π. Although the features in phase space are also 2π periodic in momentum the system is unbounded in l. The portraits can thus be thought of as cylindrical surfaces. Obvious features of the portraits at low kick strength are the solid curves, or tori, running across the phase space, and elliptical curves, or islands. These stable trajectories, which represent stable motion of the kicked rotor, are called *invariant curves* because all subsequent iterations of an initial condition selected from the curve will always be mapped back

onto the curve. As the kick strength gets larger, more and more of the invariant curves break up and yield to an irregular pattern. It shall soon be seen that this represents chaotic motion.

In figure 3.3(a) there are additional black and white trajectories that run around within the central stable island. These trajectories only show the first 15 successive points of an iteration to demonstrate how they build up to form a regular elliptical pattern like those inside it. The invariant ellipses in the portraits with higher kick strengths are built up in a similar way.

The orange and yellow trajectories in figure 3.3(a) jump back and forth between points that would eventually build up an invariant curve circling around the phase space cylinder. There is a similar pattern forming from the highlighted trajectories in figure 3.3(b). As has been said, the starting points of the trajectories within each highlighted pair are separated by a small angle. Because the kick strength is low and the trajectories are stable, after 15 iterations the points that have evolved from slightly perturbed starting positions are still very close together for both $K = 0.5$ and $K = 1$.

The highlighted trajectories in figures 3.3(c) and 3.3(d) exhibit completely different behaviour to those that have been looked at already. The kick strength has increased and the previously regular phase space around the starting position has broken up into an irregular dotted region. The pair of trajectories in figure 3.3(c) do not form part of a stable pattern but dot from position to position about the irregular area. The trajectories remain fairly close to each other for five iterations. They then noticeably start to diverge by increasing amounts until around ten kicks at which point they start to take on completely different paths. Both of the trajectories seem affected

by the central stable island and while the orange one appears stuck in an elliptical path, the yellow one has broken free to roam elsewhere.

The divergent behaviour of closely starting pairs of trajectories is even more pronounced in figure 3.3(d) for $K = 5$. The kick strength is higher and the average distance between successive iterations is now noticeably larger. At this scale the divergence of the two trajectories is noticeable after only three iterations, and only another three iterations later they have become very widely separated in phase space. The small, quasi-stable regions in phase space do not have an obvious effect on the direction of the seemingly random walk of the trajectories about phase space. It is the "deterministic randomness" that is observed here, and in other systems like the kicked rotor, that invoked the term "chaos" to be introduced. The highlighted trajectories in figures 3.3(c) and 3.3(d) are very good demonstrations of the sensitivity to initial conditions that is evident in all chaotic systems. Dynamical instability such as this leads to the unpredictability that is a central characteristic of chaos. Furthermore, the instability of a chaotic system should be exponential rather than linear in time, since in the exponential case no additional predictive power is gained by knowing the system history beyond the initial condition [68]. Predictability in a linear case is possible even in the presence of a small uncertainty if a sufficiently long history of the system is known. These properties are more formally quantified using the Lyapunov exponent and the Kolmogorov-Sinai entropy [69, 70] which give a measure of the rate of exponential divergence from perturbed initial conditions.

Chaotic trajectories should also be *ergodic*, so that they eventually wander throughout the possible range of chaotic phase space (although it is possible

to find disconnected regions of chaos in weakly perturbed Hamiltonian systems, as can be seen in figure 3.3(b) for $K = 1$). In the next section we will relate the roaming ability of trajectories and the structure of the patterns in phase space to the growth of energy in the system.

3.2.2 Classical transport

Because two distinct "futures" may not have the same past, distinct classical trajectories, such as the invariant lines discussed in relation to figure 3.3, will never cross. The consequence of this, for $K = 0.5$, is that the rotational energy of the kicked rotor is bounded and cannot grow indefinitely. The proof of this is as follows. With energy in units of I/T^2, the kinetic energy of the kicked rotor $E_{kin} = l^2/2$. Hence the energy of the rotor may only increase if the magnitude of the angular momentum increases. However, as can be seen from figure 3.3(a), a large increase in momentum ($\Delta l/\pi > 1$) is impossible without crossing invariant curves. The angular momentum, and therefore the kinetic energy of the kicked rotor, do not grow as a function of the number of kicks but remain bounded no matter how large n becomes. For this reason, the invariant curves that circle about the phase space cylinder are called *sealing curves* because they act as a boundary, dividing phase space into dynamically disconnected areas.

As the rest of the figures in 3.3 show, as K increases chaotic regions begin to appear and the sealing curves break up. As the last sealing curve (the Golden Torus) fractures at a critical value of K, $K_c \approx 1$ [70], the angular momentum becomes unbounded because there are no invariant tori that prevent trajectories in the main chaotic region from obtaining arbitrarily large

momenta. At this point the system is called "globally chaotic". As K is further increased the remaining cantori (broken tori) are progressively weakened and more and more islands in phase space disappear.

The sealing lines are all obviously broken for $K = 2 > K_c$ and the trajectories are free to roam about the chaotic sea uninhibited in the l direction. The rotor is thus able to absorb energy from the external driving field as it makes this random walk about momentum space, and its kinetic energy grows diffusively and without limit. It does so with a quasi-linear energy diffusion rate given by [71]:

$$D \sim \frac{K^2}{4} \tag{3.11}$$

where the energy $\bar{E}_n = Dn$ for kick number n. This quasi-linear form is a first order approximation to the actual diffusion constant and is only valid in the limit of arbitrarily large K, but nonetheless useful for discussing general trends. Higher order corrections arise from kick-to-kick correlations. The result from [71,72] is

$$D = \frac{K^2}{2}\left[\frac{1}{2} - J_2(K) - J_1^2(K) + J_2^2(K) + ...\right] \tag{3.12}$$

to second order in the Bessel functions, $J_{1,2}(K)$, of the stochasticity parameter K. These correlations will become important later.

It is seen in figure 3.3(d) that for $K = 5$ the phase space for the kicked rotor is almost entirely chaotic. In fact for $K > 4$ the primary resonances (the stable islands about $2\pi n$, where n is any integer) become unstable, phase space is completely chaotic with the exception of only a small number of regular islands, and the system is referred to as being "predominantly

chaotic".

3.2.3 Summary

The dynamics of the classical delta-kicked rotor is heavily influenced by the nature of the phase space of the system. Poincaré surfaces of section are used to display the characteristics of the Standard Map in a very straightforward fashion. Thus when talking about other chaotic systems the Standard Map can be referred to as a useful comparative example. From the phase portraits it has been seen that the kicked rotor is highly dependent on the kick strength K which governs the transition from regular, stable behaviour to unstable, chaotic motion. The important part to take away from this paradigm of chaos is that for a globally chaotic system, when $K > K_c \approx 1$, there is a strong absorption of energy from the external driving field and the kinetic energy is able to grow diffusively and without limit. For $K < K_c$ the rotor cannot absorb any considerable amount of energy from the driving field, no matter how long it is exposed to the field. Bearing these points in mind, we will now take a look at the dynamics of the analogous *quantum* system.

3.3 Quantum chaos

The field of quantum chaos, which unites the study of classical chaotic dynamics and quantum-mechanical systems, is a relatively new area of study, especially given how long the fundamental ideas of the two parent fields have existed. Most of the progress in the field of quantum chaos has been made only during the last 25 years.

It is very difficult to define chaotic behaviour in the context of quantum mechanics. As we have discussed, the classical picture of chaos relies upon the ideas of sensitive dependence on initial conditions and exponentially diverging trajectories. This type of definition is simply not possible in quantum mechanics because the Uncertainty Principle restricts our knowledge of initial conditions. Furthermore, the probablalistic nature with which quantum particles are described restricts us from even considering trajectories in quantum mechanics. On top of this, as will be shown later, in a surprising phenomenon that has come to be known as *dynamical localisation*, the effects of classical chaos are suppressed in quantum systems. Even so, there are still some manifestations of the underlying classical disorder and almost all conservative dynamical systems are at least partly chaotic in the range of their behaviour. The general consensus is that quantum theory does permit chaos, but just for a while. Until the "break time", a quantum system will mimic its chaotic classical counterpart. This applies to molecules, atoms, quantum dots, acoustics, microwaves, and dozens of other systems.

The attention to quantum chaos has, aided to a large extent by the renewed interest in classical nonlinear dynamics, grown due to quantum experiments bordering on the macroscopic size regime where the laws of classical

mechanics are expected to emerge. A central question in quantum mechanics is how to obtain the laws of classical mechanics as limiting cases of the more fundamental laws governing the microscopic constituents of matter. This connection between the quantum and classical worlds is known as the *correspondence principle.* However, it is argued that when there is chaos, the correspondence principal fails in that it connects quantum mechanics not to all of classical physics but only to the remnants of order within it. A few scientists with heretical viewpoints have even questioned the validity of quantum mechanics (Joseph Ford, Giorgio Mantica and Gerald Ristow of the Georgia Institute of Technology). However, quantum theory has never failed an observational test, and has beaten off innumerable challenges.

One approach to the enigma of quantum chaos is not to attempt to define chaos in quantum mechanics but concentrate instead on identifying features of a quantum system that correspond to chaos in a classical system. In light of the suppression of chaos in quantum systems, the term *quantum chaology* has been introduced [73] to refer to the study of these "signatures" of classical chaos in their quantised counterparts. This is exactly the approach to quantum chaos adopted in this work, as we embark on an investigation of quantum transport phenomena in classically chaotic systems.

In trying to solve a problem, physicists seek to find the simplest model possible that properly explains the unknown phenomenon. Because of the simplicity of its equation of motion and the wealth of knowledge available on the classical system, the delta-kicked rotor has become the paradigm for quantum chaos. The kicked rotor can be realised experimentally in many different ways. In our experiment we study a realisation of the quantum

kicked rotor in which cold caesium atoms are "kicked" by a periodically pulsed standing wave of far-detuned light. Early work with sodium atoms established this system as an excellent setting for the study of quantum chaos [12,13,74]. It will be seen how the high degree of control over the experimental parameters enables detailed comparisons with theoretical predictions and provides a unique testing ground for quantum chaos.

3.3.1 The quantum delta-kicked rotor

The quantum Hamiltonian of the classical kicked rotor, defined by the classical Hamiltonian (3.2), is found by replacing the classical angular momentum L by the quantum angular momentum operator $\hat{L}$:

$$L \rightarrow \hat{L} = -i\hbar\partial/\partial\theta, \tag{3.13}$$

which gives

$$\hat{H} = \frac{\hat{L}^2}{2I} + \mu\varepsilon_0 \cos\theta \sum_n \delta(t - nT) \tag{3.14}$$

Using a procedure similar to that used in the derivation of the classical standard map, the quantum dynamics of 3.14 can be solved by way of a quantum mapping [75]. The mapping operator is the time evolution operator of the rotor over one period of the driving force. Although the derivation of the quantum mapping will not be shown here, it is necessary to introduce the parameters used to scale the mapping into its dimensionless form. These

are the dimensionless angular momentum $\hat{l}$ according to

$$\hat{L} = \hbar\hat{l} \tag{3.15}$$

and the dimensionless control parameters

$$\begin{aligned} \alpha &= \hbar T/I \\ k &= \mu\epsilon_0 T/\hbar \end{aligned} \tag{3.16}$$

The classical analogue of the quantum mapping is then obtained by simple substitution of equations 3.15 and 3.16 into equations 3.9 to obtain

$$\begin{aligned} l_{n+1} &= l_n + k\sin\theta_n \\ \theta_{n+1} &= \theta_n + \alpha l_{n+1} \end{aligned} \tag{3.17}$$

where, in this classical context, l is no longer an operator. Rescaling the angular momentum according to $\tilde{l} = \alpha l$ the mapping (3.17) can be written in the form of equation 3.9:

$$\begin{aligned} \tilde{l}_{n+1} &= \tilde{l}_n + K'\sin\theta_n \\ \theta_{n+1} &= \theta_n + \tilde{l}_{n+1} \end{aligned} \tag{3.18}$$

where $K' = \alpha k$. This allows us to compare and associate a classical kicked rotor characterised by the control parameter K with a quantum kicked rotor characterised by the two control parameters α and k. This comparison will be made in the next section where we will reveal a surprising phenomenon and

show α to be an essential independent parameter on which the dynamics of the QDKR decisively depend. Because K' is still a measure of how classically chaotic the system is, we will henceforth drop the prime.

3.3.2 Dynamical localization

For the CDKR we have seen how the dynamics are highly dependent on the stochasticity parameter K. As K is increased from zero, stable trajectories start to break up: at $K \approx 1$ the last stable trajectory that inhibits momentum diffusion is broken and the system becoms globally chaotic. For $K > 4$ the phase space is predominantly chaotic and the momentum grows diffusively and without limit. However, the quantum dynamics of this simple system show some different and surprising results. Figure 3.4 compares the energy growth between simple numerical computations for the classical and quantum kicked rotor. Classical and quantum simulations were run with equivalent starting conditions. The values of the quantum control parameters correspond to classical $K = 5$, well within the chaotic regime.

The red plot in figure 3.4 is a numerical simulation for classical diffusion (labelled $\alpha = 0$) which closely follows the expected quasi-linear diffusion rate $D \sim K^2/4$ (see section 3.2.2). However the blue and green plots, for $\alpha = 0.25$ and $\alpha = 1$ respectively, grow as the classical energy does but only up to a short, α-dependent time called the quantum *break time* before abruptly breaking away and remaining bounded. The quantum break time, t^*, is commonly taken at the crossing of an asymptote to the saturated quantum energy and the classical linear growth, as demonstrated by the dashed lines for the blue plot. The effect is called *dynamical localisation* [76–78] and

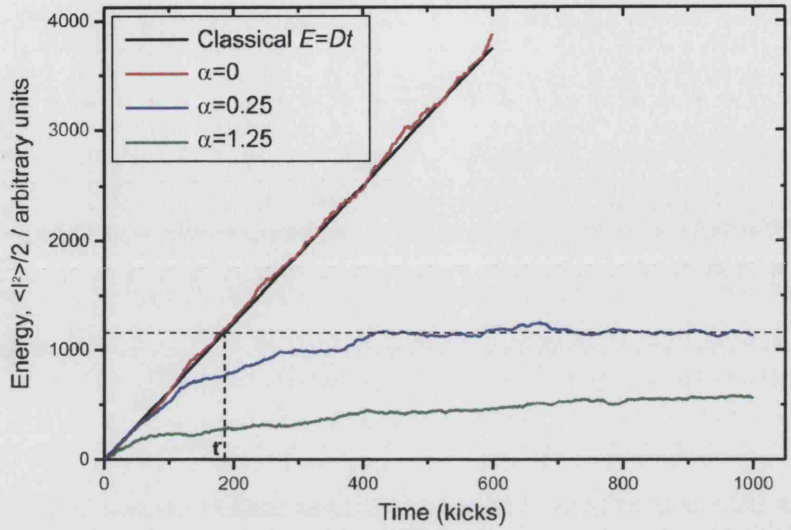

Figure 3.4: Comparison between classical and quantum energy growth in the classically chaotic regime for $K = 5$. The black plot shows the classical energy growth according to the quasi-linear diffusion rate. The red plot, a numerical simulation for classical diffusion (labelled $\alpha = 0$) follows the expected quasi-linear diffusion rate. The blue and green quantum simulations, for $\alpha = 0.25$ and 1.25 respectively, demonstrate quantum localisation whereby energy growth is suppressed by localisation of the wavefunction in momentum space.

was first noted by Casati and collaborators [79]. It was formally described in terms of Anderson localisation [80, 81] as observed in the conductance in disordered solids [77]. In the Anderson description, dynamical localisation is explained as a destructive interference effect that limits the spread of the rotor wavefunction over the available angular momentum space. This results in the quantum energy diffusing as the classical energy until the quantum interference effects arrest the diffusion of the wavefunction. Notice that the smaller the value of α for the system, the more classical the system is, and the longer the quantum dynamics follow their classical counterpart. In this way α acts as an effective $\hbar$ for the system, and from henceforth we will label it $\hbar_{eff}$. Even for small $\hbar_{eff}$ the quantum interference effects eventually

dominate. The ability to control the magnitude of $\hbar_{eff}$, by means that will be shown later, makes the QDKR an important system in the study of chaotic dynamics.

Theoretically it can be shown that dynamical localization manifests itself as a momentum profile with an exponential signature, as illustrated by the results of a numerical simulation shown in figure 3.5 [82]. The graph is a result of plotting the occupation probabilities P_l (the absolute squares of the time averaged expansion amplitudes of the rotor wavefunction) of the rotor in the angular momentum states $|l\rangle$. The simulation shows the resulting distribution for $K = 5$ and 1000 kicks. Given that the data is plotted against a $\ln[N(l)]$ scale, an exponentially (dynamically) localized distribution is immediately evident from the straight wings of the plot. This exponential localisation takes the form $N(l) \sim exp(-l/L)$ where L is known as the localization length. The localisation length is therefore equal to the reciprocal of the gradient of the wings of the logarithmic plot.

So, it has been seen that dynamical localization in the quantum kicked rotor is characterised in terms of the *localization length*, L, and the quantum *break time*, t^*, estimations of which are as follows [76,82]:

$$L \approx \frac{K^2}{2\hbar_{eff}} \tag{3.19}$$

$$t^* \approx \frac{L}{\hbar_{eff}^2} \tag{3.20}$$

Note that the quantum break time must therefore vary with the momentum diffusion constant since $t^* \propto K^2 \propto D$. To recap, the quantum break time defines when the energy of the quantum system breaks away from the classical

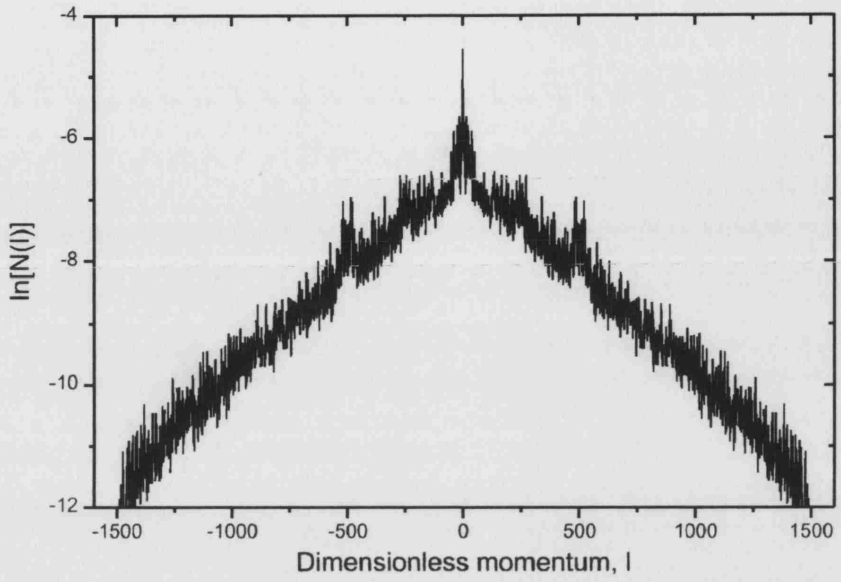

Figure 3.5: Simulation to show the signature of dynamical localisation: exponential localisation of the wave function of the quantum kicked rotor in the classically chaotic regime.

energy. The localization length defines how fast the momentum falls away after the wavefunction becomes frozen in momentum space.

3.3.3 Summary

The dynamics of the quantum kicked rotor is completely different to that which one would naïvely expect on the basis of the classical results. In the classically chaotic regime, the quantum kicked rotor only follows the diffusive energy growth of the classical kicked rotor until the quantum break time at which the quantum interference phenomenon of dynamical localisation suppresses further increase. Experimentally we should see dynamical localization manifest itself with a characteristic exponential signature. The dynamics are very sensitive to the effective Planck's constant $\hbar_{eff}$ which is a measure of

the strength of the quantum effects of the system, and the kick strength K which defines how classically chaotic the system is. The next chapter will describe how the delta-kicked rotor can be realized experimentally with laser cooled atoms.

CHAPTER 4

The cold atom realization of the quantum delta-kicked rotor

In this chapter we show how a quantum delta-kicked rotor may be realised using laser-cooled atoms in a pulsed sinusoidal optical potential. We will also look at an effect that arises due to deviations from the ideal case in a real experiment - finite width kicks - and demonstrate that this results in a boundary in phase space that restricts atomic momentum growth. Following that we examine the response of the system to a series of kicks that have been made asymmetric in time and show that this induces a momentum dependence in the energy diffusion of the system. The penultimate section demonstrates that this momentum dependence can be exploited to generate asymmetric atomic momentum diffusion in a fully chaotic Hamiltonian system. In the final section, one way of breaking the spatial symmetry is presented as a useful example and for later reference.

4.1 Cold atoms in a pulsed optical lattice

Consider a cold atom trapped in a one-dimensional optical lattice, a standing wave of light created by two counter-propagating laser beams with parallel linear polarisations. To re-iterate a few points made in chapter 2, the internal structure of the atom can be neglected if the laser detuning $\Delta_L = \omega_L - \omega_0$ of the laser light at frequency ω_L from the atomic resonance frequency ω_0 is large in comparison to the natural linewidth Γ. It can then be treated as a point particle in a sinusoidal optical potential that arises from the spatial variation of the ac Stark shift. The beams must have parallel polarisation so, in contrast to Sisyphus cooling, all of the Zeeman states of the atom have the same light shift. This means that any atom would be affected by the same sinusoidal potential surface. Assume for now that by creating the lattice with short laser pulses the delta-function kicks are realizable. The Hamiltonian, H, describing the motion of the atom in this potential is very similar to that of the kicked rotor or a pendulum, but is now expressed as a function of position x, which is not limited to $0 \rightarrow 2\pi$, and momentum p rather than angle and angular momentum. It is given by:

$$H = \frac{p^2}{2M} + V_0 \cos(2k_L x) \sum_n \delta(t - nT) \tag{4.1}$$

where M is the atomic mass and $k_L = 2\pi/\lambda$ is the laser wavevector. The potential depth V_0 of the lattice is given by equation 2.5. Scaling dimensions is, as usual, a useful way of making the maths more intuitive. The scaled

position and momentum are defined as follows

$$\begin{aligned} \phi &= 2k_L x \\ \rho &= \frac{2Tk_L p}{M} \end{aligned} \tag{4.2}$$

Then, bearing in mind that $[x,p] = i\hbar$ it can easily be shown that the commutation relation $[\phi,\rho] = i8\omega_R T = i\hbar_{eff}$, where $\omega_R = \hbar k_L^2/2M$ is the recoil frequency. So in this case $\hbar_{eff} = 8\omega_R T$, which is, as was mentioned before, a measure of the action scale of the system. The scaled momentum can thus be written as:

$$\rho = \frac{\hbar_{eff} p}{2\hbar k_L} \tag{4.3}$$

If we now define

$$\begin{aligned} \tau &= t/T \\ K &= \hbar_{eff} T V_0/\hbar \\ \mathcal{H} &= \hbar_{eff} T H/\hbar \end{aligned} \tag{4.4}$$

then the kicked rotor Hamiltonian can be rewritten as

$$\mathcal{H} = \frac{\rho^2}{2} + K\cos(\phi)\sum_n \delta(\tau - n) \tag{4.5}$$

and the standard map becomes:

$$\begin{aligned} \rho_{n+1} &= \rho_n + K\sin\phi_n \\ \phi_{n+1} &= \phi_n + \rho_{n+1} \end{aligned} \tag{4.6}$$

Again, the striking similarity of this Hamiltonian and the classical one elucidates the close resemblance of this system with the classical kicked rotor. By re-scaling the Hamiltonian the classical system has been reduced to a single parameter K, and the quantum system to two parameters $k = V_0T/\hbar$ and $\hbar_{eff}$. The corresponding classical kick strength for the quantum system ($K = k\hbar_{eff}$) then allows one to use the Standard Map as a guide to atomic motion. Remember that $\hbar_{eff}$ is a measure of how classical the system is and which, for delta-kicks, can be controlled with the period of the kicking sequence. In the next section we consider the effect of deviations from δ-kicks that are unavoidable in a real experiment.

4.2 Finite-width kicks and the momentum boundary

Delta-function pulses cannot be achieved in a physical experiment and one can only strive to come as close to possible to this limit by using short laser pulses. In this section we will look at the effect that kicks of finite width has on the scaled stochasticity parameter and on the diffusion constant, and show how finite-width kicks introduce momentum boundaries. These are values of momentum where the diffusion constant drops to zero. The momenta of atoms at a boundary thus cannot change and we shall see this manifested in phase space as invariant tori that trajectories cannot cross.

To describe the sequence of real kicks the delta function is replaced with the square pulse function $F(t)$ of unit height, centred at $t = 0$ with duration

t_p and period T. This can be written as follows:

$$\sum_n F(t - nT). \tag{4.7}$$

The suitability of assuming a square pulse function will be discussed in section 5.1.3.

To scale the pulse function define a pulse integral, or "duty cycle", η such that $f(\tau) = F(t)/\eta$ and $\eta = T^{-1}\int_{-\infty}^{\infty} F(t)dt = t_p/T$ (so that $\int_{-\infty}^{\infty} f(t)dt = 1$). As a result, it is easy to show that the scaled kick strength for square pulses becomes

$$K = \frac{V_0}{\hbar} t_p \hbar_{eff}. \tag{4.8}$$

So the kick strength is now dependent on the pulse time and the effective Planck's constant. The scaled Hamiltonian for finite-width kicks can be written as follows

$$\mathcal{H} = \frac{p^2}{2} + K\cos(\phi)\sum_n f(\tau - n). \tag{4.9}$$

From equation 4.8 it would appear that the transition to global chaos that occurs with increasing $K \propto t_p$ may be studied by simply increasing the duration of the pulses. However, outside the limit $t_p << T$ the finite width of the pulses has a significant effect on the momentum diffusion. This can be understood with the semiclassical picture of an atom moving a finite distance along a one-dimensional lattice during the time t_p when the potential is switched on. This is illustrated in figure 4.1. The momentum kick recieved by the atom is then the average kick strength over the duration of the kick,

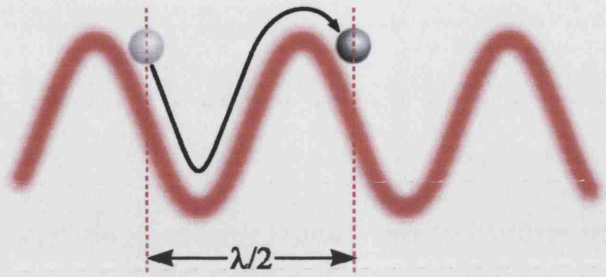

Figure 4.1: Atomic motion in a 1D optical potential to illustrate the effect of finite-width kicks.

such that for all momenta greater than zero the kick is on average less than that imparted by a delta-function pulse. Consequentially, for a particular momentum at which the atom travels one period of the potential during t_p, the momentum transferred averages out to zero and the atom is said to have reached the *momentum boundary*. In the frame of reference of the lattice, the momentum at which this occurs is thus $p_b = \pm M\lambda/2t_p$, where M is any non-zero integer. In scaled units this is written as:

$$\rho_b = \pm\frac{M\lambda^2}{8\pi\hbar t_p}\hbar_{eff} = \pm 2\pi\frac{T}{t_p} = \pm 2\pi/\eta. \tag{4.10}$$

In other words, at the momentum boundary the "kick" received at $t = t_p/2$ is very strongly correlated with the "kick" received at $t = 0$ and the effects of the kicks cancel out. Similarly, for an infinitesimal time interval later the "kick" at $t = t_p/2+\epsilon$ cancels out the effect of the "kick" at $t = \epsilon$ etc. This is analogous with the broad-slit diffraction pattern, and it has in fact been shown that the resulting stochasticity parameter becomes momentum dependent with the form of a sinc function: $K_{eff}(\rho)$ is related to the shape of the pulse through a Fourier transform [83, 84], and for the square pulse

$f(\tau)$ considered above the effective kick strength becomes:

$$K_{eff}(\rho) = K\frac{\sin(\pi\rho/\rho_b)}{\pi\rho/\rho_b}. \tag{4.11}$$

The first zeroes of $K_{eff}(\rho)$ then occur when $\rho = \rho_b$, where ρ_b is given by equation 4.10.

Recall from section 3.2.2 the relationship between the kick strength and the classical diffusion constant, $D \propto K^2$. The correction to K, with the form of a sinc function, therefore results in an according correction to the diffusion constant, $D(K) \rightarrow D(K_{eff}) \propto K_{eff}^2$. Thus the diffusion constant also becomes momentum dependent, with the form of a sinc-squared function (like the intensity distribution of the single-slit diffraction pattern). Again this will have zeros at the momentum boundaries, and we will be exploring the induced momentum dependence on the diffusion constant due to finite kicks in sections 5.2.3 and 5.2.4.

Now take a brief look at some phase space portraits that result from finite-width kicks by iterating the well-known Standard Map of equation 4.6 but replacing K with $K_{eff}(\rho)$. For the two portraits shown in figure 4.2 the classical kick strength was set at $K = 5.3$, with $t_p = 1.42\mu s$, $T = 9.47\mu s$ so that $\rho_b = 42.5 = 13.5\pi$. The map was iterated through 120 kicks. Although just an example here, the choice of parameters make the plots useful for later reference.

Diagram 4.2(a) shows that trajectories starting within $\rho = \pm\rho_b$ remain bounded within this region. This is because once an atom reaches this momentum the stochasticity parameter, and hence the diffusion constant $D \propto K^2/2$, drops to zero and the momentum does not change. Totally

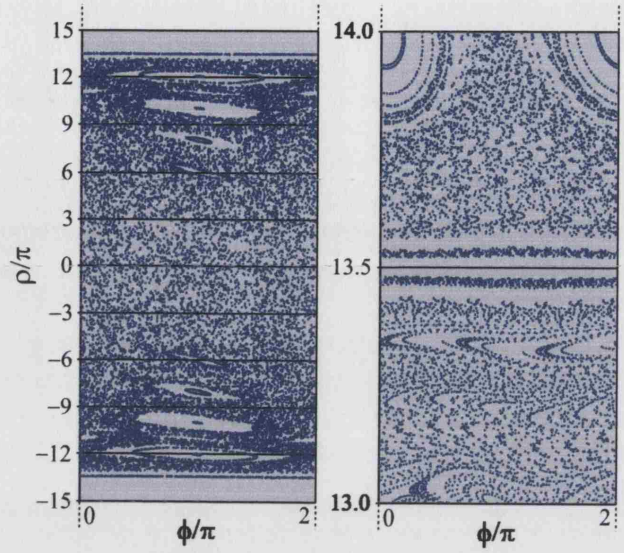

Figure 4.2: Phase-space portraits (Poincaré surface of sections) for $K(\rho = 0) = 5.3$, 120 kicks and $\rho_b = 13.5\pi$. Diagram (a): all trajectories start and remain within the momentum boundaries. Diagram (b): enlargement of the momentum boundary with trajectories starting on both sides stable motion at $\rho = \rho_b$

chaotic dynamics is observed around $\rho = 0$ where the kick strength is highest. As ρ increases, the kick strength falls and we see the first obvious sign of regions of regular motion, a small island or cantori, at $\rho = \pm 6$. The islands get wider in ϕ towards the momentum boundary, but they will not act as invariant curves or boundaries because they do not span the entire width of ϕ, although it is possible that they may slow diffusion. Diagram 4.2(b) illustrates in greater detail the region around $\rho = 13.5\pi$, but with trajectories starting both sides of the momentum boundary. The unbroken line at ρ_b represents a stable region at the boundary that corresponds to uniform motion at a constant momentum.

4.3 Breaking time symmetry

Here we introduce one way of breaking time symmetry for the cold atom kicked rotor. In the previous section we saw how the dynamics of the system showed various dependencies on the period and duration of the regular kicking pattern. Instead of using a time symmetric pulse sequence, now consider a simple, antisymmetric, two-period kicking cycle of periods $T_1 = T(1+b) : T_2 = T(1-b)$, where the chirp parameter $b << 1$. This cycle can be written as:

$$F_2(\tau) = \sum_{n=0}^{\infty} \sum_{M=1}^{2} f(\tau - nT_{tot} + \sum_{i=1}^{M} T_i) \tag{4.12}$$

where $T_{tot} = T_1 + T_2$. This means that the first kick after $\tau = 0$ is at $\tau = T_1$, the second kick at $\tau = T_1 + T_2$, the next one at $\tau = T_1 + (T_1 + T_2)$ and so on, so there is a small deviation from evenly-spaced kicks by the chirp parameter b.

The new kicking cycle is illustrated in figure 4.3. The Hamiltonian is now

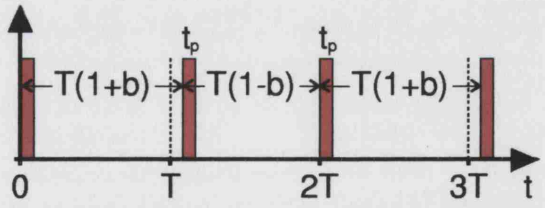

Figure 4.3: Two-period kicking cycle, $T(1+b) : T(1-b)$ where b is the chirp parameter

an extension of equation 4.9, which becomes:

$$\mathcal{H} = \frac{\rho^2}{2} + K\cos(\phi)F_2(\tau). \tag{4.13}$$

The mapping is now written

$$\rho_{n+1} = \rho_n + K\sin(\phi_n),$$
$$\phi_{n+1} = \phi_n + \rho_{n+1}(1 + b(-1)^n). \tag{4.14}$$

Now have a brief look at some phase space portraits to compare the Standard Map of equation 4.6 with this new mapping for the asymmetric kicking sequence. We choose the parameters $K = 3.5$ and $b = 0.2$ which will be useful for later reference. The portraits are shown in figure 4.4. The Standard Map has stable islands centred at 2π integer multiples of ρ, and the rest of phase space is chaotic. For $b = 0.2$, phase space is significantly more chaotic. There are still cantori about $\rho = 0$ but the 2π periodicity in ρ is gone. Displaying a larger range in ρ, figure 4.4(c) shows that the periodicity in momentum is π/b. Analytical proof of this can be found in [85,86]. This means that for $b < 1$, there are fewer stable islands in mixed phase space to hamper the atomic energy growth.

It was shown in [86], and a rigorous mathematical proof can be seen in [85], that the effect of chirping the kicks in this way modifies the correlations between next-but-one kicks (the "two-kick correlation", $C(2)$) such that the diffusion constant of equation 3.12 becomes:

$$D(K,\rho,b) = \frac{K^2}{4}(1 - 2J_2(K)cos(2\rho b) + ...) \tag{4.15}$$

where J_2 is, as previously, a second order Bessel function. The important feature is that the diffusion constant now varies with a cosine momentum

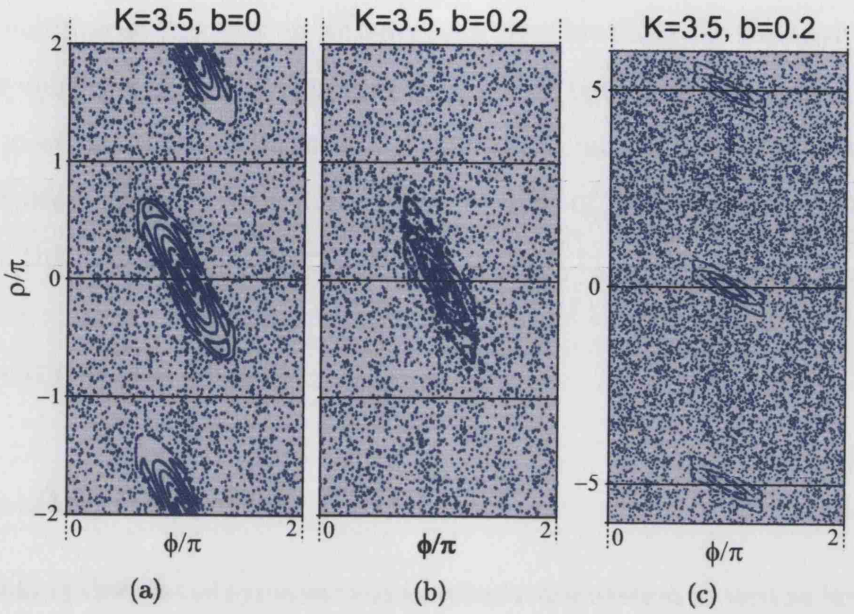

Figure 4.4: Phase-space portraits (Poincaré surface of sections) to illustrate the effect of an asymmetric kicking sequence. Figure (a): $K = 3.5$, $b = 0$ (Standard Map). The portrait has stable islands centred in ρ at integer multiples of 2π. The rest of phase space is chaotic. Figure (b) and (c): $K = 3.5$, $b = 0.2$. Reminiscent of the stable islands in the Standard Map, there is a feature at $\rho = 0$ but it is more chaotic. Figure (c) shows that the features are 5π periodic in momentum.

dependence of period π/b [85]. It is also shown in [85, 86] that this correction has a finite lifetime which has been termed the "ratchet time", t_r, beyond which the correction to the diffusion constant saturates. In an analytical derivation the ratchet time was found, for small b, to be related to the diffusion constant and the chirp parameter by

$$t_r \propto \frac{1}{Db^2} \tag{4.16}$$

In general, t_r is the time taken for the momentum to reach 95% of its saturation value [82].

To summarise this section we have seen that breaking the time symmetry by introducing a simple asymmetry to the kick pattern makes mixed phase space more chaotic and imposes a cosinusoidal momentum dependence on the diffusion constant for a finite time. Results of an investigation into the form of this momentum dependence can be seen in section 6.1.2, and in the following section we discuss a technique to exploit the dependence to achieve asymmetric atomic diffusion.

4.4 Asymmetric diffusion

By breaking the spatial symmetry of a kicked rotor system as well as breaking the temporal symmetry it is possible to produce asymmetric atomic diffusion in the fully chaotic regime. This has been termed a "chaotic ratchet" effect by some [87]. An experimental proof of principle of this effect may be demonstrated by cooling the atomic distribution to a non-zero mean momentum (the practicalities of this will be discussed in section 5.1.4, and an alternative way of breaking the spatial symmetry will be presented in the next section). Remember from the previous section that the diffusion constant varies cosinusoidally as a function of momentum with a period of π/b, and so with this technique the distribution can be centred at momenta where the diffusion constant is locally asymmetric. The *classical* diffusion rates for positive and negative momenta (D^+ and D^- respectively) are then different up to t_r, and for $t < t_r$ an asymmetry in the momentum distribution accumulates with kick number. We quantify the asymmetry, the "current", with the mean momentum $\langle p \rangle$ (in this case where the atoms are cooled to

a non-zero momentum the results would be measured in the rest frame of the initial distribution). Beyond the ratchet time the rates equalize and so $D^+ \approx D^- \approx D$ (where $D \sim K_{eff}^2/2$ is now the global diffusion rate) and the classical current saturates to a constant, non-zero value. Of course the energy continues to grow with time as $\langle p^2 \rangle \sim Dt$. The corresponding current in the quantum system depends on the competition between the ratchet time and the break time: if the break time is too short then effects due to broken time symmetry go unnoticed because dynamical localization, and hence the saturation of the momentum to a finite value, sets in before any asymmetry can accumulate. Conversely, if the break time is sufficiently longer than t_r the effects of the modulated, momentum dependent diffusion constant become diluted as the energy continues to grow symmetrically after t_r. In the case where $t^* \sim t_r$ the current is allowed to reach its maximum value before the asymmetry is 'frozen-in' to the distribution as the energy growth is limited beyond the break time. Indeed, the main conclusion of [87] is that this system will have the clearest experimental signature if this is the case. Recall from the previous section that $t_r \sim 1/Db^2$ and estimations of the ratchet time by [69,88] give $t^* \sim D/\hbar^2$, so to achieve maximum diffusion asymmetry would require $t^*/t_r \sim Db/\hbar_{eff} \sim 1$.

4.5 Breaking spatial symmetry

One way of breaking the spatial symmetry is to introduce to the potential a linear term, a potential gradient A, that alternates in sign with each succes-

sive kick:

$$V(\phi) = K\cos(\phi) + A\phi(-1)^n \tag{4.17}$$

where n is the kick number. Ways in which this may be implemented experimentally will be discussed later (see sections 6.2 and 7.2). As before, if temporal symmetry is broken by using a chirped sequence of kicks with chirp parameter b, then the dimensionless Hamiltonian can be written:

$$\mathcal{H} = \frac{\rho^2}{2} + (K\cos(\phi) + A\phi(-1)^n)\sum_{n=0}^{\infty}\sum_{M=1}^{2} f(\tau - nT_{tot} + \sum_{i=1}^{M} T_i). \tag{4.18}$$

The mapping is now written:

$$\begin{aligned} \rho_{n+1} &= \rho_n + K\sin(\phi_{n+1}) + A(-1)^n, \\ \phi_{n+1} &= \phi_n + \rho_n(1 + b(-1)^n) \end{aligned} \tag{4.19}$$

which can be regarded as a three-parameter extension of the standard map.

It was previously stated that by breaking time symmetry the diffusion constant becomes momentum dependent. However, as shown by [89] (for which a rigorous mathematical proof can be found in [82]), the corrections to the diffusion constant that arise from kick-to-kick correlations now include the potential gradient term A, such that the diffusion constant can now be approximated by:

$$D(K, \rho, b, A) = \frac{K^2}{4}(1 - 2J_2(K)cos(2\rho b - A) + ...) \tag{4.20}$$

Again, the important point is that the diffusion constant varies with a co-

sine momentum dependence of period π/b. The novel feature now is that this dependence can be made asymmetric about $\rho = 0$ by varying A, i.e. A introduces a phase shift. One may now expect an asymmetric diffusion of the kicked atoms with the magnitude and direction of asymmetry being proportional to the gradient of the diffusion constant. Given that A is effectively the phase of the cosinusoidal momentum depencence of the diffusion constant, the asymmetry in atomic diffusion should vary with 2π periodicity in A. For atoms centred at zero momentum, one would expect maximum diffusion asymmetries at values of $A = \pi(j + \frac{1}{2})$ and minima at $A = j\pi$, where j is any integer.

4.6 Summary

The quantum kicked rotor can be experimentally realised with cold atoms in a pulsed, far-detuned optical lattice. The dynamics of this system can be completely controlled by the effective Planck constant and the kick strength.

The effective Planck constant is essentially a handle with which one can control how classical or quantum the system is and it is related to the period of the kicks by $\hbar_{eff} = 8\omega_R T$. The kick strength is a control of how classically chaotic the system is. For delta-function kicks it is given by $K = \frac{V_0}{\hbar} T\hbar_{eff}$, but for finite-width kicks, approximated by square pulses of duration t_p, the effective kick strength becomes momentum dependent such that the maximum effective kick strength, transferred to atoms with zero momenta, is related to t_p by $K_{max} = \frac{V_0}{\hbar} t_p \hbar_{eff}$. For atoms with higher momenta the diffusion constant falls away as a sinc^2 function, at the zeroes of which mo-

mentum boundaries become apparent past which atoms can not diffuse. The momentum boundaries at lowest momenta are given by $p_b = \pm 2\pi T/t_p$.

The effect of introducing a simple asymmetry into the kick sequence by the chirp parameter b also introduces a momentum dependence into the diffusion constant. This modification, the 'two-kick correlation', takes the form of an additional cosinusoidal term which varies as $-K^2 J_2(K)\cos(2pb)$. In addition, introducing an alternating potential gradient A will modify the form of the diffusion constant so that the correction becomes $-K^2 J_2(K)\cos(2pb - A)$. A thus acts as a handle with which to control the phase and hence the symmetry of the cosinusoidal term about the mean momentum of the atomic sample. Depending on two independent timescales, the "ratchet time" t_r and the break time t^*, breaking both the temporal and the spatial symmetry can lead to asymmetric atomic diffusion. This asymmetry will have the clearest experimental signature if $t^* \sim t_r$.

In conclusion, full control over the dynamics of this system is enabled through easily accessible parameters such as the pulse duration and period and the potential depth of the optical lattice. This makes the cold atom realisation of the kicked rotor a very useful experimental tool in the study of chaotic dynamics.

CHAPTER 5

Experimental details and observations of quantum chaos

The first part of this chapter gives the details particular to our experiment. This includes the cold atom cycle, the generation of the sequences of short kicks, and the way in which the experimental data is processed. Also discussed is the experimental arrangement and apparatus necessary to prepare cold atoms with a non-zero initial momentum distribution: a very useful tool for exploring phase space and perfoming asymmetric diffusion experiments, as shall be seen later. In preparation for experiments with broken time symmetry, presented in the second half of this chapter are results that demonstrate dynamical localisation with a time-asymmetric kick sequence. Also presented are results from investigations of the momentum boundary and mixed phase space, to demonstrate the utility of a moving pulsed optical

lattice, and to show that these features can be used to generate preferential directional atomic diffusion.

5.1 Experimental details

5.1.1 The cold atom cycle

As a brief overview before going into detail, a laser cooling apparatus [33] is used to prepare an atomic sample of caesium with a narrow momentum distribution. A symmetric optical lattice, formed by laser beams derived from a Ti:Sapphire laser, incident on the cold cloud of atoms is then quickly pulsed on and off for the kicking sequence. Additional beams for fluorescence imaging and an infrared CCD camera are used to record the resulting spatial distributions.

The cold atom cycle for chaos experiments is illustrated in figure 5.1 and the timing details are shown in figure 5.2. A detailed description follows.

A cloud of caesium atoms is collected from the background vapour in our standard six-beam MOT for typically 2500ms. The atoms are cooled for a further 30ms in an optical molasses for which the magnetic field gradient is switched off, the detuning of the trap beams is increased and the intensity of the trap beams is decreased. This phase cools the sample to a temperature of around $(6.0 \pm 0.5)\mu$K, corresponding to an rms dimensionless momentum width of $\sigma_p = 2.8 \pm 0.3$ for $\hbar_{eff} = 1$.

The atoms are then released by switching off the molasses beams and the far-detuned, coherent kicking potential, formed from two counterpropagating beams from the Ti:Sapphire laser, is pulsed on with a pre-determined kicking

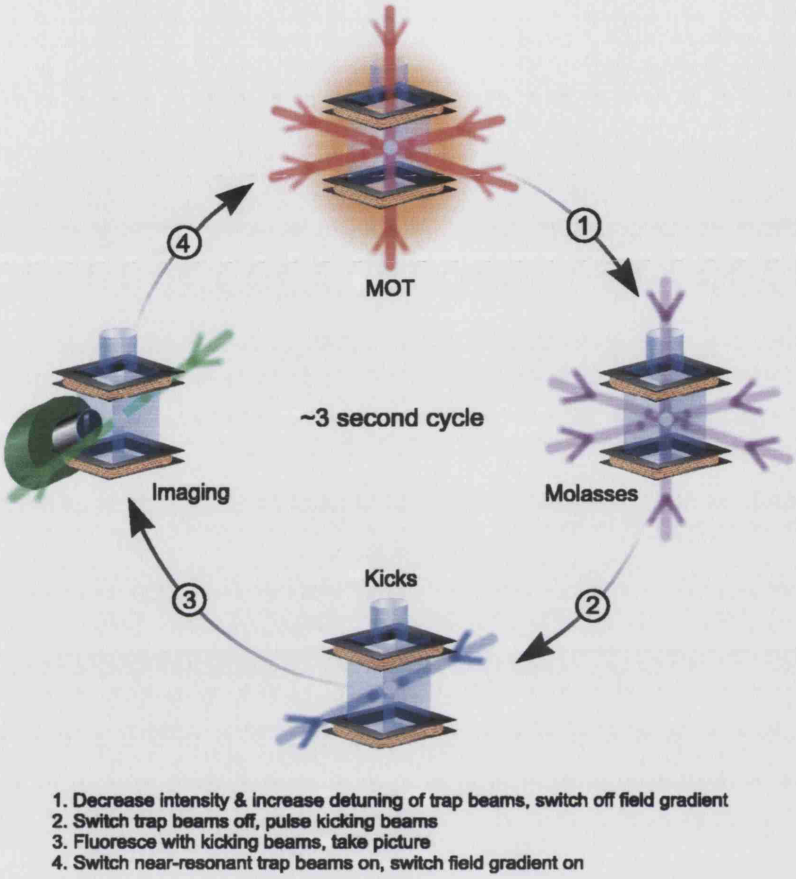

Figure 5.1: The cold atom cycle

pattern for typically 1ms (see section 5.1.3). The number of kicks is limited by the time taken for the cloud to fall out of the interaction region and the kicking pattern is experiment-specific. Unless an experiment is investigating the effect of the number of kicks, they are in general kicked for a time that is greater than the break time. This is to ensure that the energy growth has completely levelled out through dynamical localisation.

After the kicking, the cloud of atoms is allowed to expand ballistically for a 10-20ms drop-time before the near-resonance fluorescence beams are

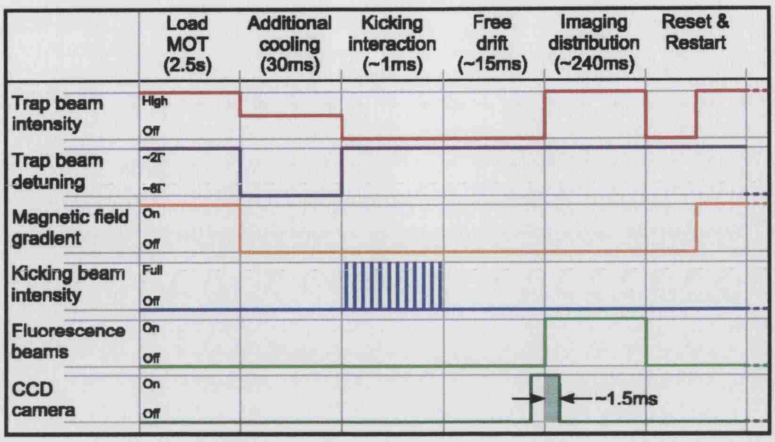

Figure 5.2: Timing for the cold atom cycle

switched on and the fluorescence is imaged with a Princeton Instruments cooled infrared CCD camera[1]. The minimum shutter time of the camera is 2ms. However, for an exposure to near resonant light of around 2ms, distortion of the atomic distribution due to the scattering of photons becomes noticeable. For this reason, the camera shutter is opened just before the fluorescence beams are turned on and closed just after, such that fluorescence is collected for around 1.5ms. The camera is linked to a computer with which the spatial distribution of the fluorescence is monitored and captured using a proprietary software package called WinView. The whole cycle takes approximately three seconds and a picture set of at least five measurement cycles are taken for each reading. The pictures are stored in a multi-frame 8-bit tiff format which can be read into a Matlab program for analysis.

[1]Princeton Scientific Intstuments Inc. MicroMax camera supplied by Roper Scientific Inc., www.roperscientific.com

5.1.2 Data processing

The first stage of the data analysis is to generate an average picture from the picture set taken for each reading. A Matlab program does this by converting the multi-framed images from the experiment from tiff format into a three-dimensional array and by averaging along the third dimension (number of frames) to leave a 768×512 two-dimensional array corresponding to the average intensity distribution. For the next stage the user defines a region of interest: a finite-width strip through the distribution along the x-axis (direction of propagation of the laser). The program then averages along the width of the strip (typically ±20 pixels) to produce a single column of data representing the spatial distribution of the fluorescence. The program then subtracts the background intensity which is taken from the extremities of each dataset. With the input of a suitable scaling factor, related to the drop-time, the mass of the atomic species and $\hbar_{eff}$, the pixel number is converted into dimensionless momentum. Assuming that there are an equal number of atoms involved in each measurement the distributions are then normalised by area to compensate for the automatic gain control of the camera. The normalised intensity distribution is then a measure of the number of atoms at a particular momentum, $N(\rho)$. The data is converted into ASCII format and saved in a file to be imported into Origin or Excel for analysis.

The program also calculates the mean and mean-squared scaled momentum for a each distribution. As mentioned in section 4.5, the mean momentum quantifies the asymmetry, or the 'current' I, of a distribution, and is

taken as the first moment of the atomic momentum distribution:

$$I = \langle \rho \rangle = \frac{\int \rho N(\rho) d\rho}{\int N(\rho) d\rho} \tag{5.1}$$

The energy of the atomic sample is taken from the second moment of the distribution:

$$E = \frac{\langle \rho^2 \rangle}{2} = \frac{\int \rho^2 N(\rho) d\rho}{2 \int N(\rho) d\rho} \tag{5.2}$$

Error values are taken as the standard deviation. Again, the results are converted into an ASCII format and saved in a file to be treated in Microcal Origin or Microsoft Excel for analysis.

5.1.3 Generating short kicks

As has been mentioned previously, delta-function pulses can not be achieved in a physical experiment and one can only strive to come as close to possible to this limit by using short laser pulses. The kicks can be provided by periodically pulsing a one-dimensional optical lattice. The counterpropagating beams forming this lattice are derived from the titanium sapphire laser. As explained in section 2.5.1, the laser beams, with a $1/e$ radius of (0.95 ± 0.05)mm, require parallel linear polarisations and the resultant one-dimensional lattice produces a sinusoidal spatial variation of the ac Stark shift proportional to the local intensity and independent of the Zeeman substate.

Figure 5.3 shows the apparatus necessary to create a pulsed one-dimensional optical lattice for quantum chaos experiments.

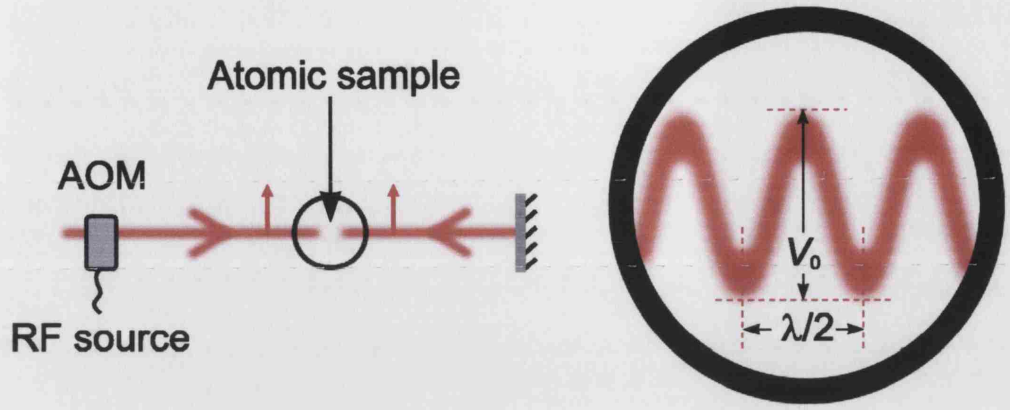

Figure 5.3: Experimental arrangement to generate a stationary pulsed optical lattice, the period of which is $\lambda/2$, where λ is the wavelength of the laser light . AOM is an acousto-optic modulator, used here to switch the lattice beam on and off. Parallel polarisations are necessary such that atoms in different Zeeman states are affected by the same potential.

The lattice is derived from laser light from the Coherent[2] MBR-110 Ti:Sapphire laser as previously mentioned. This is a tunable, CW, single-frequency ring system with a maximum output power of 1W at 852nm. It is pumped by a high power, CW, single-frequency Coherent V8-A1317 Verdi laser, a solid-state, diode-pumped, frequency-doubled Nd:YVO_4 laser providing 8W at 532nm. The output from the Ti:Sapphire laser (not shown in the figure) is passed through a 3080-112 acousto optic modulator (AOM) from Crystal Technology[3] which is driven by an SMY01 Rohde and Schwarz[4] radio-frequency (RF) synthesizer at a carrier frequency of $f = 80$ MHz. The first order beam from the AOM is retroreflected through the optical molasses with a mirror to create the optical lattice. The first order beam may be turned on and off by switching the RF to the AOM, and the power of

[2]Coherent Inc. 5100 Patrick Henry Drive, Santa Clara, CA 95054, USA, www.cohr.com
[3]Crystal Technology Inc., 1040 East Meadow Circle, Paulo Alto, CA 94303, USA
[4]Rohde and Schwarz GmbH & Co. KG, Mühldorfstraße 15, D-91671 München, www.rohde-schwarz.com

the beam may be controlled by varying the level of the RF input with an electronic attenuator. The detailed timing of the kicking sequence is specific to a particular experiment. To pulse the lattice with arbitrary kicking patterns, the RF synthesizer is controlled by a fast RF switch (Mini-Circuits[5] ZYSWA-2-50DR) that is triggered by a TGA1230 Thurlby Thandar waveform generator[6] that produces the kicks.

A package called WaveCad is used to draw the kick sequence, over a scale of 1024 pixels, after which it is downloaded to the waveform generator. While the duty cycle, $\eta = t_p/T$, is set by the drawing on WaveCad, the pulse duration, kick period and the number of kicks can be controlled by the waveform generator. The pulse duration and kick period are set by assigning a sample period to each pixel, the shortest period being 33.33ns/pixel. The waveform generator is triggered by the dedicated laser cooling control computer. The kicking sequence from the waveform generator is then used to trigger the fast RF switches that control the RF to the AOMs via an RF amplifier.

It is interesting to note that because the rise time of the AOM is around 100 ns, short pulse durations (around 200 ns) may be more suitably modeled by a Gaussian pulse function than the square pulse function assumed in section 4.2. This non-ideal pulse shape due to the finite switch time would then result in an effective kick strength that is better approximated by a Gaussian momentum dependence than a momentum dependence with the form of a sinc function. However, for longer pulse durations (250 ns and above) a square pulse shape may still be a good approximation. The shape

[5]Mini-Circuits, Mini-Circuits Europe, Dale House, Wharf Road, Frimley Green, Camberley, Surrey, GU16 6LF. www.minicircuits.com

[6]Thurlby Thandar Instruments Ltd., Glebe Road, Huntingdon, Cambridgeshire, PE29 7DR. www.tti-test.com

of the momentum dependence of the diffusion constant due to finite width kicks and the momentum boundary is explored experimentally in section 5.2.4.

The experiments require a coherent transfer of momentum from the pulsed optical lattice to the cold atoms. It was shown in section 2.5.1 that high laser powers are necessary to achieve suitable potential depths at negligible scattering rates. Given that the maximum output from the Ti:Sapphire laser is around 1W, it is possible to detune by several thousand linewidths and still fall within the required range for K. The laser is typically detuned by at least one thousand linewidths below the D2 cooling transition in caesium such that spontaneous scattering is made negligibly small. To get a feel for the acceptable rate of scattering, with the detuning set to 1000Γ and a typical intensity of $5000\mathrm{mWcm}^{-2}$ the scattering rate is around $2700\mathrm{s}^{-1}$ (see equation 2.7). For a typical kick duration of around 400ns this corresponds to 0.001 scatters per kick. The typical number of kicks per experiment is around 100, and so this corresponds to 0.1 scatters per experiment. While this has been found to be acceptable, reasonable kick strengths may still be obtained with the detuning set to 2000Δ which gives a scattering rate that is about four times less (around $675s^{-1}$, under 0.0003 scatters per kick or 0.03 scatters per typical experiment).

A portion of the optical power is lost through the AOMs, the maximum diffraction efficiency of which is approximately 70% into the first order beam at an RF power of 1W. A negligible fraction is lost to reflections from waveplates and lenses, and a negligibly small amount of power is also lost at mirror interfaces due to their high reflection efficiency.

From the experimental parameters the corresponding values of K and $\hbar_{eff}$, as well as the scattering rate, diffusion constant, break time, and so on, are calculated. A summary of caesium data and equations useful for experiment preparation and diagnostics is shown in appendix B.

5.1.4 Generating cold atoms with a non-zero initial momentum

For the investigation of atomic momentum diffusion in different regions of phase space it is useful to create a sample of atoms with a narrow momentum distribution centred at a non-zero momentum.

Using a uniform magnetic field it is possible to cool the atoms to a distribution about a non-zero velocity [90]. This is because the motion of atoms in a standing wave results in a modulation of the light intensity that induces a magnetic resonance at a particular velocity [91], $v_r = \omega_z/2k$, where $\omega_z = g_F \mu_B B/\hbar$ is the Larmor frequency. This is a stimulated Raman transition between the ground states that is resonant at $v = v_r$, and as a result of this velocity-selective resonance the atoms are cooled to nonzero velocity $\pm v_r$. The field is created by a large pair of current-carrying wire coils either side of the vacuum chamber in the Helmholtz configuration. However, as simple as it is to implement there are a number of disadvantages of this technique for the experimental requirements. The first is that after the cloud of atoms is released from the trap they quickly reach the edge of the field of view of the CCD camera, limiting in practice the range of momenta it is possible to investigate. By changing the magnification of the camera's zoom lens the field of view may be increased but at the expense of resolution. The

camera is also more sensitive in the middle of the field of view and so the signal to noise ratio falls as the cloud moves from the central starting position. Furthermore, it is very hard to align the experiment so that the atoms travel parallel to the optical lattice. The last disadvantage is that when cooling to a non-zero velocity it was found that the atomic momentum distribution is broader. This reduces the resolution by which features in phase space can be investigated.

Such complications are not an issue if instead the lattice is moved relative to the atoms. In this way, the atoms keep their narrow momentum distribution, centred at zero momentum in the laboratory rest frame, and remain at the centre of the field of view of the camera. In the rest frame of a moving lattice however, the atoms have a non-zero mean momentum.

The moving optical lattice is formed by counterpropagating laser beams with a controlled frequency difference. For this, the experimental arrangement described in the previous section (see figure 5.3) has to be modified slightly. The new experimental arrangement can be seen in figure 5.4. The beams for the kicking potential are derived, as previously, from the Ti:Sapphire laser. This is now split into two equal intensity beams using a half-wave plate and a polarising beam splitter and each sent through an AOM. Two RF synthesizers (phase-locked) at the carrier frequency (f=80MHz), controlled by separate fast RF switches, are now required to control the AOMs (see figure 5.5). Both switches are controlled by the same waveform generator that produces the kicks. This is programmed as before. A second waveplate is necessary to set the polarisations parallel so that, as before, atoms in different Zeeman states are affected by the same potential surface.

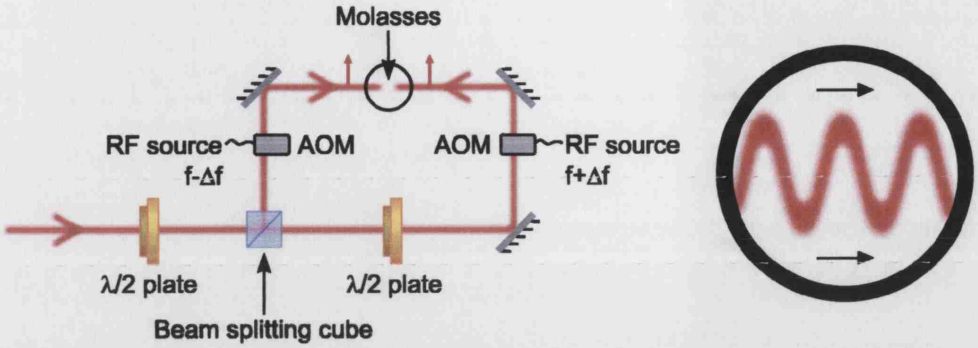

Figure 5.4: Experimental arrangement to generate a pulsed lattice that moves at a velocity $v_L = \lambda\Delta f$ ms^{-1}. The AOM are acousto-optic modulators that are used here to switch the lattice beams on and off and modulate the frequency of each of the beams by up to $\Delta f = \pm 0.5$ MHz. The polarisation of the beams must be parallel such that atoms in different Zeeman states are still affected by the same potential surface.

The two AOMs allow independent control over the frequency of each beam. For a frequency difference of $2\Delta f$ between the AOM RF sources, and hence the kicking beams, the lattice moves at a velocity $(\lambda\Delta f)$ms^{-1} in the laboratory frame of reference. In the frame of the moving potential, the distribution of atoms then has a non-zero mean momentum which is given by:

$$\langle p_L \rangle = M\lambda\Delta f \tag{5.3}$$

or in dimensionless units:

$$\langle \rho_L \rangle = \frac{M\lambda\Delta f\hbar_{eff}}{2\hbar k_L} = 4\pi T\Delta f \tag{5.4}$$

With this technique it is possible to vary the initial mean momentum of the cold atoms in the frame of the optical lattice, $\langle \rho_{L0} \rangle$, continuously over a wide range which is only limited by the intrinsic behaviour of the AOMs.

Given that the maximum frequency-modulated depth at a carrier fre-

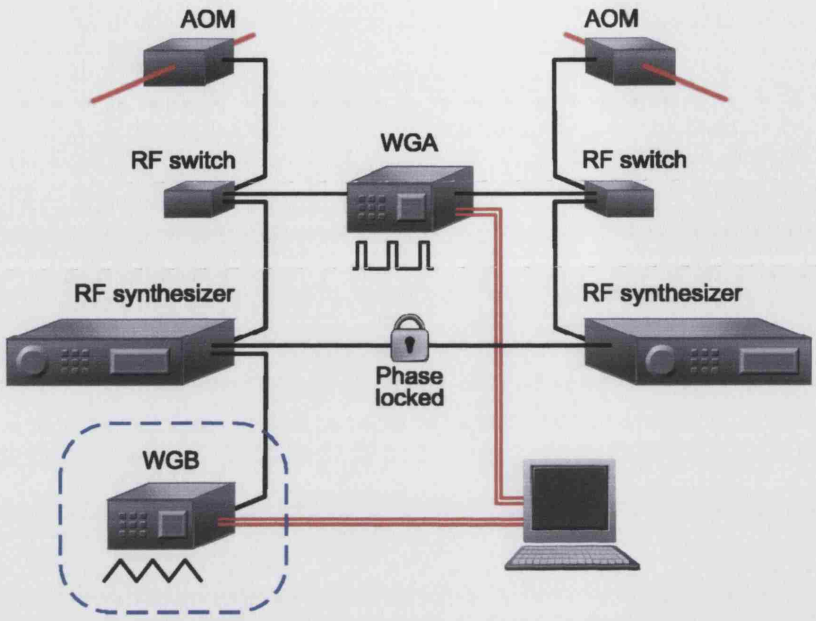

Figure 5.5: Apparatus configuration to to control the kick sequence. The waveform generator in the dashed blue frame, WGB, will not be referred to until later. In preparation, the kick sequence is drawn on a computer and downloaded to WGA. During the experimental cycle the computer is used to trigger WGA which controls the RF switches by a series of TTL pulses that represent the kick sequence. In turn, the RF switches pass the RF source from the RF synthesizers to the AOMs that the first order beams from the AOMs pulse on in synchrony to form the kicking optical lattice.

quency of 80MHz for the RF synthesizers is ± 1.25MHz, each AOM can potentially be driven through a range of 2.5MHz. However, as Δf is increased, the deflection angle of the first order beam changes ($\Delta\theta/\Delta f = 0.1°/\text{MHz}$). When the angle of deviation becomes too large the kicking becomes significantly misaligned from the atomic cloud, diminishing the kick strength, and realignment of the kicking beams is required. Experimentally, the effect of misalignment becomes noticeable at around $2\Delta f = 1$MHz, or $p_L/2\hbar k_L \approx 120$.

This method is a highly flexible tool when it comes to investigating phase space, as shall be seen in the results sections to follow. There is a large

experimental range over which the initial atomic distribution may be placed, and it is very easy to control the initial atomic momentum given that the frequency difference is easily set with the RF synthesizers.

5.2 Observations of quantum chaos

5.2.1 Dynamical Localization

Presented here are some results that illustrate the signature of dynamical localisation. As explained in section 3.3.2, dynamical localisation is the quantum suppression of the classical chaotic momentum diffusion, and the hallmark of this effect is a localized momentum distribution with an exponential profile.

The apparatus used is that described in section 5.1.3 for a symmetric, stationary kicking potential. The period of the kicks was set to $T = (9.47 \pm 0.02)\mu$s so that $\hbar_{eff} = 1.000 \pm 0.002$.

The pulse time $t_p = 417(\pm 20)$ns such that the duty cycle is small, $\eta = 4.4(\pm 0.2)\%$, in which way the effects due to the finite width of the kick can be neglected because the momentum boundary is relatively high: $p_b \approx 150 \pm 8$ (dimensionless units).

The radius of the beam is measured by monitoring the intensity of the beam through a 50μm diameter pinhole that is scanned across the beam profile. In this way, the beam was measured to have a $1/e$ radius of (1.36 ± 0.05)mm. The maximum power of the first order kicking beam from the AOM was measured to be (540 ± 30)mW. By limiting the RF level to the AOM, this was reduced by approximately 60% such that the beam was attenuated to an

intensity of approximately $(3500 \pm 200)\text{mWcm}^{-2}$.

The laser detuning was set to $(2000 \pm 100)\Gamma$. Given that the saturation intensity for caesium is 1.12mWcm^{-2} and the natural linewidth $\Gamma = 2\pi \times 5.22\text{MHz}$, one may calculate from the experimental parameters (see equation 2.5) that the resultant potential depth $V_0/\hbar = 8.5\text{MHz}$. From equation 4.8, the classical kick strength is thus $K = 3.5$. The error on V_0 and K is estimated to be around 10%, mainly a result in the difficulty in measuring the beam intensity and due to the power fluctuation and frequency drift of the Ti:S laser. During experimentation, the frequency is monitored typically every ten readings.

In preparation for subsequent experiments, an asymmetric kick sequence was used with a chirp parameter of $b = 0.2$. Values for $\hbar_{eff}$ and K were also chosen to approximate the values estimated to be used in subsequent experiments. In addition, considering the added effect of the chirp parameter, the kick strength was chosen so that atoms are not lost from the field of view of the imaging camera. The phase-space portraits for these values were shown in figure 4.4 in section 4.3. It was seen that stable structures became smaller as the time symmetry is broken, and their periodicity increased to 5π. We are hence looking at a regime that is almost completely chaotic with the exception of a few small cantori. The results are shown in figure 5.6.

Although the choice of a natural log scale results in the signal noise being amplified at low intensities, the graph clearly shows the characteristic exponential profile of dynamical localization.

One can see that the unkicked cloud of atoms has a relatively narrow and almost Gaussian distribution. This does not represent the initial momentum

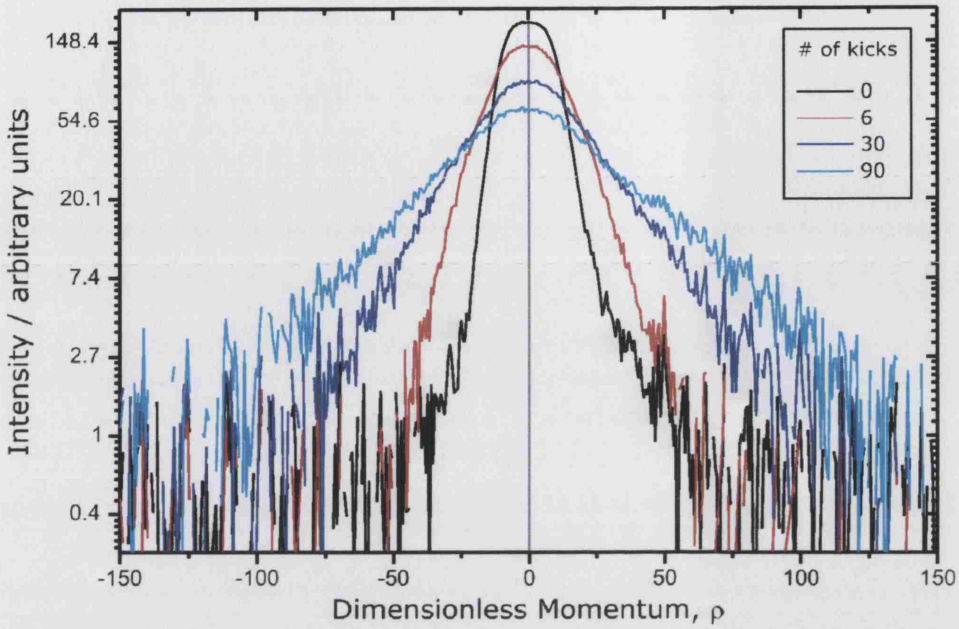

Figure 5.6: Results showing dynamical localisation for kicked and unkicked molasses on a logarithmic scale. Experimental parameters are $K = 3.5 \pm 0.35$, $\hbar_{eff} = 1.00 \pm 0.003$.

distribution, which is a lot narrower, but rather a convolution of the momentum distribution σ_ρ and the initial spatial distribution σ_ϕ which make the momentum profiles unreliable in the region of $\rho = 0$. As the number of kicks increases the distributions retain the rounded peak of the initial spatial distribution while they broaden and the wings become exponential. The result of even higher numbers of kicks were omitted from the graph because the distributions fall very close to that of 90 kicks. This is due to the onset of dynamical localisation, which is illustrated more clearly in graph 5.7 where the width of the distributions are plotted against the number of kicks. Although we see no definite halt to the energy growth of the system, the rate of energy growth is certainly slowing down.

The localisation length can be calculated from the gradient of a linear fit

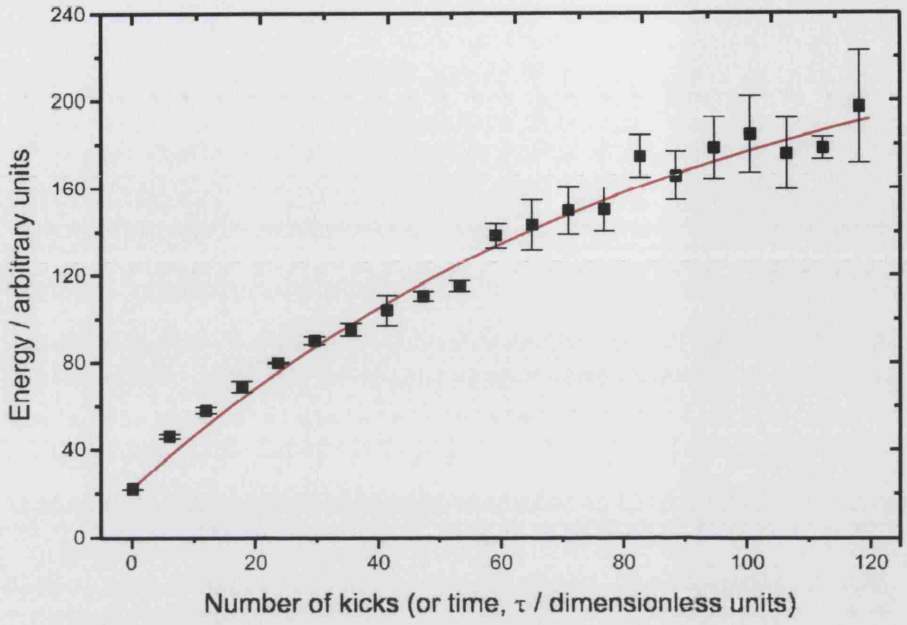

Figure 5.7: Results showing the energy growth of the chirped kicked rotor experiment against time. Experimental parameters are $K = 3.5 \pm 0.35$, $\hbar_{eff} = 1.00 \pm 0.003$. The red line of best fit is of the form $E = E_0(1 - e^{-\tau/\beta})$, where E_0 is the saturation energy and β is the characteristic exponential timescale.

to one of the wings of the broadest distribution in figure 5.6. By taking the average of the gradient from both wings of the plot we attempt to compensate for the slight asymmetry. This value was calculated to be $\langle g \rangle = (30 \pm 5) \times 10^{-3}$ and so the localisation length $L = 35 \pm 5$. By crossing an asymptote to an extended fit of the saturating energy growth in figure 5.7 and the classical linear growth ($E = D_{ql}\tau$), the break time is estimated to be $t^* = 90 \pm 20$. Calculated from equations 3.19 and 3.20, the localisation length and the break time for the equivalent Standard Map, that is a system with a symmetric kicking sequence, are estimated to be $L_{sm} = 6 \pm 1$ and $t^*_{sm} = 6 \pm 1$ respectively. It has not yet been shown theoretically how to estimate the localisation length or the break time for a chirped system, and we see that

the break time and the localisation length for a kicked ratchet system with an asymmetric kicking sequence are not well approximated by that calculated for the standard map.

In conclusion, the results confirm that the dynamical localisation, characteristic of quantum chaos, can be observed in our kicked rotor experiment with an asymmetric kicking sequence. A growth in momentum is seen for a finite number of kicks which changes to an exponential momentum distribution. The rate of absorption of energy has been observed to slow down.

5.2.2 Investigating mixed phase space

It was seen in section 3.2 that for small values of K there exist stable islands in phase space that significantly affect diffusion. In this section a moving lattice will be used to probe the diffusion at different momenta in mixed phase space. Providing the width of the initial atomic momentum distribution is comparable to the momentum width of these structures, it will be shown that it is possible to resolve the effect of stable islands on diffusion.

For this experiment a time-symmetric kicking sequence is employed. The apparatus used here is that described in section 5.1.4 for a symmetric kicking potential that can be moved at a constant velocity by applying a frequency difference between the two lattice beams, such that in the rest frame of the lattice the cloud of atoms start with a non-zero mean momentum, $\langle p_{L0} \rangle$. The results presented here are for two values of the effective Planck constant, $\hbar_{eff} = 0.250 \pm 0.002$ and $\hbar_{eff} = 1.000 \pm 0.002$, achieved by setting the period of the kick sequence to $T = (2.37 \pm 0.02)\mu s$ and $T = (9.47 \pm 0.02)\mu s$ respectively.

Remember that the standard map is 2π periodic. To investigate at least two periods the frequency difference between the beams is varied in small steps such that $\langle \rho_{L0} \rangle$ is scanned from at least $-\pi$ up to 5π. For example, in the case of $\hbar_{eff} = 1$, this requires the frequency difference to be varied from $\Delta f = -26.4$kHz to $\Delta f = 158.4$kHz.

For the data with $\hbar_{eff} = 0.25$, the kick duration $t_p = (379 \pm 20)$ns, and so the momentum boundary is at $\rho_b = (16 \pm 1)\pi$, high enough not to interfere with this experiment. For the experiment with $\hbar_{eff} = 1$, the pulse time $t_p = (296 \pm 20)$ns, and so the momentum boundary is at $\rho_b = (65 \pm 4)\pi$, which is also easily high enough to be neglected. The pulse times for both values of $\hbar_{eff}$ are different simply because of the restraint set by the pixelated way in which the pulse sequences are drawn (see section 5.1.3). Four representative values for K will be examined: 0.7, 1.5, 2.7 and 4.1 ($\pm 10\%$). Classical phase space portraits for these K are shown in figure 5.8, all of which exhibit a varying degree of regular and chaotic phase space. The portraits were generated by plotting 300 iterations from the starting conditions ($\theta_0 = \pi$, $l_0^m = -2\pi + m\pi/20$, $m = 0, 1, ..., 80$).

From the portraits it is seen that for $K = 0.7$ there are large regular islands centred in ρ at integer multiples of 2π and solid curves traversing ϕ that are centred in ρ about odd integer multiples of π. These should act to limit the absorption of energy by atomic distributions centred at these momenta as the majority of atoms remain bound to these stable trajectories. In between the regular structures there is very little chaotic phase space and so momentum diffusion, and hence energy growth, is expected to be small for all ρ.

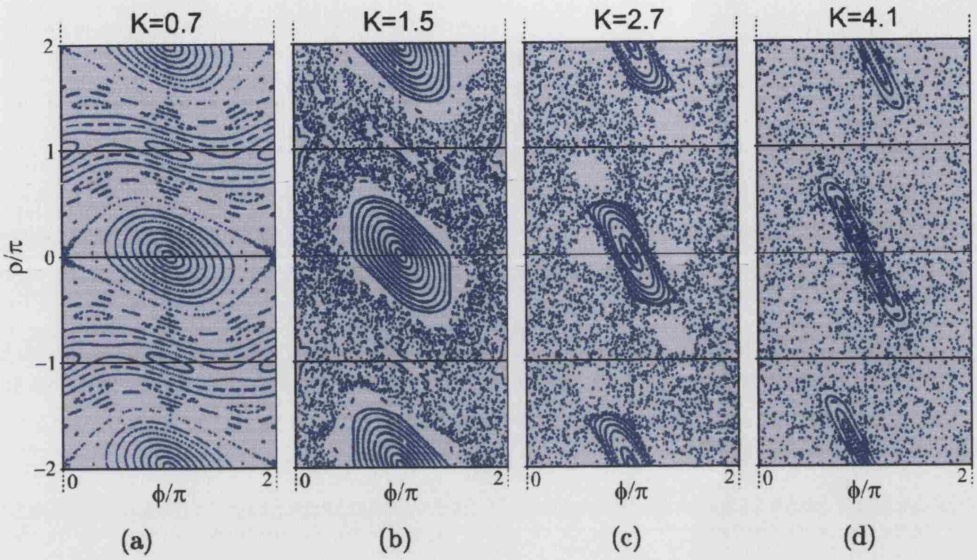

Figure 5.8: Classical phase-space portraits (Poincaré surface of sections) for the kicked rotor for the following kick strengths for which there is mixed regular and chaotic phase space: (a) $K = 0.7$, (b) $K = 1.5$, (c) $K = 2.7$ and (d) $K = 4.1$.

While the phase space portrait for $K = 1.5$ is globally chaotic there are still large stable islands centred in ρ at even integer multiples of π. These should also act to greatly limit the absorption of energy by atomic distributions centred at these momenta. Distributions centred in the chaotic space between the regular islands are expected to exhibit higher energy absorption.

For increasing K the stable islands are becoming smaller: there is increasingly more chaotic phase space and fewer regions of stability. While a modulation in energy absorption due to the stable islands may still be observed, the absorption of energy should in general become higher.

As has been said before, the typical starting temperature of the atomic sample is $(6.0 \pm 0.5)\mu K$, which corresponds to an rms dimensionless momentum width of $\sigma_\rho/\pi = 0.22 \pm 0.01$ for $\hbar_{eff} = 0.25$, and $\sigma_\rho/\pi = 0.87 \pm 0.04$

for $\hbar_{eff} = 1$. Figure 5.9 shows two Gaussian distributions corresponding to these parameters superimposed onto the Standard Map for $K = 0.7$. The

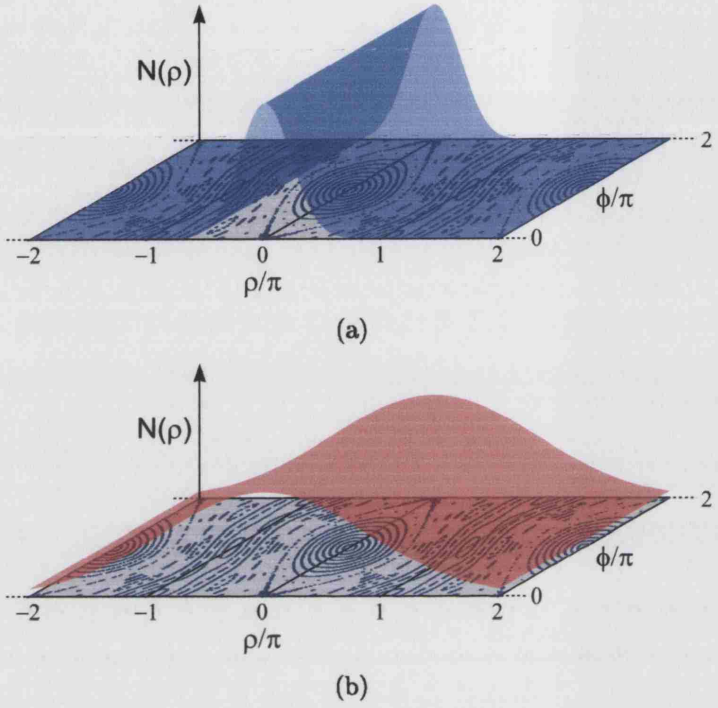

Figure 5.9: Atomic footprints for (a) $\hbar_{eff} = 0.25$, with a dimensionless $1/\sqrt{e}$ momentum width of $\sigma_\rho/\pi = 0.22$, and (b) $\hbar_{eff} = 1.00$, with $\sigma_\rho/\pi = 0.87$, both superimposed on the Standard Map for $K = 0.7$, $\langle\sigma_\rho\rangle = 0$. The wings of the blue distribution extend slightly beyond the central stable island while those of the red extend past the centres of the adjacent islands.

wings of the blue distribution with $\hbar_{eff} = 0.25$ extend slightly beyond the central islands while those of the red distribution for $\hbar_{eff} = 1.00$ extend past the centre of the adjacent islands. Comparing this to, for example, the phase space portrait for $K = 1.5$ in figure 5.8(b), the majority of an atomic distribution centred on the stable island at $\rho = 0$ would be expected to remain confined within the regular trajectories. The small portion of the population in the wings of the distribution that extend into the chaotic region of

phase space would be expected to gain energy. Now consider the distribution for $\hbar_{eff} = 1$. The wings reach beyond 2π in both directions. For a distribution centred, for example, at $\rho = 0$ in the phase space of figure 5.8(b), there would therefore be a significantly higher proportion of atoms residing in chaotic phase space than for $\hbar_{eff} = 0.25$. Because of the difference in size of these footprints it is therefore expected to observe differences regarding the resolution of the features as we investigate atomic diffusion about phase space with different values of $\hbar_{eff}$.

One can now appreciate the benefit of this experiment for testing many of the general relationships for the kicked rotor experiment and to check that the experimental mechanism to move the optical lattice is working as expected.

The first results that are displayed here compare three typical momentum distributions: two that result from starting the cloud of cold atoms at the centre of a stable island and one that results from beginning with the cloud of atoms in the chaotic phase space between islands. Presented are the results of an experiment performed with $K = 1.5$ such that the phase space contains quite large stable islands and chaotic phase space in between. Other parameters are $\hbar_{eff} = 0.25$, starting momenta $\langle \rho_{L0} \rangle / \pi = 0$, $\langle \rho_{L0} \rangle / \pi = 1$ and $\langle \rho_{L0} \rangle / \pi = 2$. The results are shown in figure 5.10.

The results are exactly as expected: the momentum diffusion for the atoms that are started within stable islands centred at $\rho/\pi = 0$ and $\rho/\pi = 2$ is greatly suppressed in comparison to that in which the atoms are started in the chaotic space between stable islands centred at $\rho/\pi = 1$. Note that although there are significant stable islands for $K = 1.5$ there are no observable

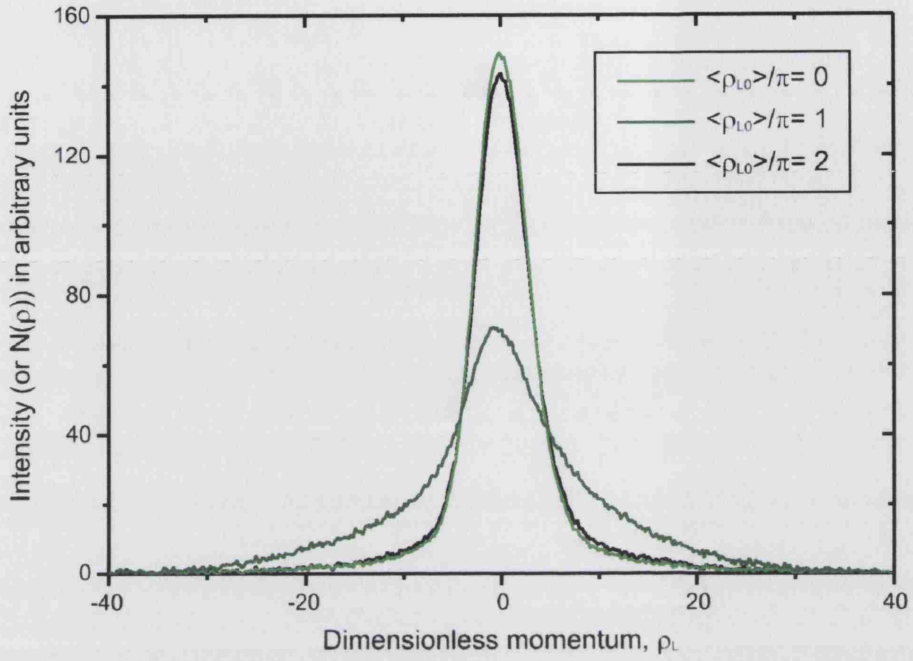

Figure 5.10: Momentum distributions for mixed phase space: comparing diffusion with atoms starting within and in-between stable islands. Here, $K = 1.5$ and $\hbar_{eff} = 0.25$. The narrower, light green and black results indicate a relatively small amount of diffusion as the atoms are initiated inside a stable island with $\langle \rho_{L0} \rangle / \pi = 0$ and 2 respectively. The wider, light green results indicate significantly more diffusion as the atoms begin within a chaotic region with $\langle \rho_{L0} \rangle / \pi = 1$.

corresponding features with 2π periodicity on the wings of the distributions.

The second set of results that are displayed are for the same parameters, but here the effect of starting the atomic cloud centred in ρ at half integer multiples of π is investigated by choosing $\langle \rho_{L0} \rangle / \pi = 0.5$ and $\langle \rho_{L0} \rangle / \pi = 1.5$. For this choice of parameters one would expect some asymmetric diffusion because the energy growth would be limited on the side of the distribution near the stable island and promoted on the chaotic side. The distributions are started on opposite sides of stable islands, and so the asymmetry is expected to be in opposite directions. The results are shown in figure 5.11.

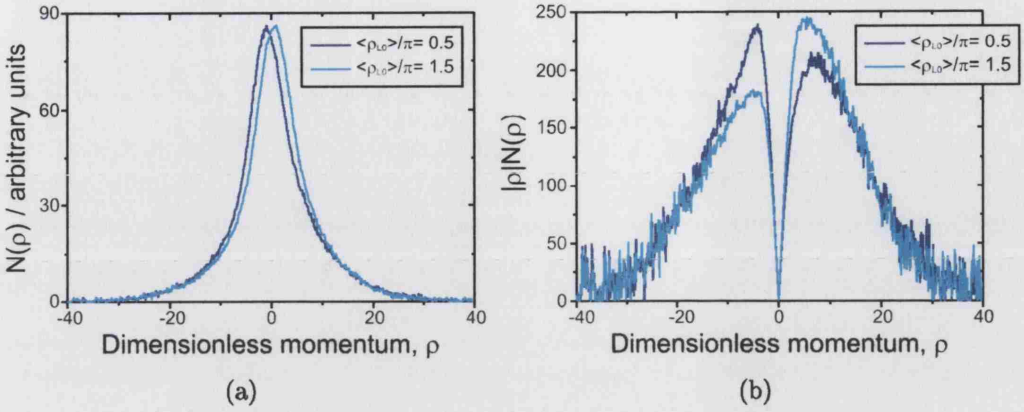

Figure 5.11: Momentum distributions for mixed phase space: comparing diffusion with atoms starting either side of a stable island. Here, $K = 1.5$ and $\hbar_{eff} = 0.25$. The light blue distribution with $\langle \rho_{L0} \rangle / \pi = 0.5$ is slightly asymmetric in favour of positive momentum, i.e. away from the closest stable island. The dark blue distribution with $\langle \rho_{L0} \rangle / \pi = 0.75\pi$ is asymmetric in favour of negative momentum because the closest stable island is on the other side.

Looking at the momentum distributions in figure 5.11(a) there is a small asymmetry about $\rho = 0$ for both distributions. A method used in [82, 87] to display the asymmetry more clearly is to plot the modulus of the first moment, $|\rho|N(\rho)$ against ρ. This is shown in figure 5.11(b). The difference in area under each half of the first moment plot is then proportional to the net current. From this it is seen that the asymmetry of the distributions are similar but in opposite directions, the plots almost looking like mirror images of each other. As expected, the diffusion, or energy growth, is thus limited in the direction of the nearby stable island.

Now consider the results of a collection of similar experiments for which the atomic energy $\langle \rho^2 \rangle / 2$ is plotted against $\langle \rho_{L0} \rangle$ for the various values of K and for $\hbar_{eff} = 0.25$ and $\hbar_{eff} = 1$. These are shown in figures 5.12 and 5.13 respectively. Energies extracted from the four example momentum dis-

tributions from the previous figures are highlighted with colour coordinated broken circles in graph 5.12.

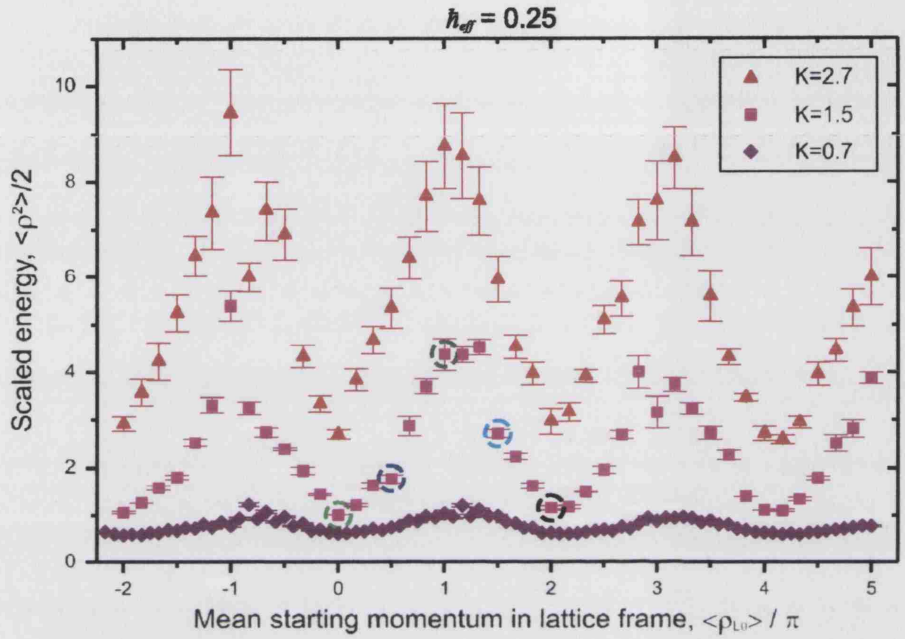

Figure 5.12: Resolving mixed phase space for $\hbar_{eff} = 0.25$. Energies are lower for $\langle \rho_{L0} \rangle = 2n\pi$ because diffusion is limited by stable islands in phase space. Energies are highest for $\langle \rho_{L0} \rangle = (2n+1)\pi$ because trajectories start in chaotic regions in phase space. Chaotic regions become larger and hence the energy increases with increasing K. The points highlighted with broken circles are colour coordinated with previous results.

The 2π periodicity of phase space is obvious from the graphs. In general, for initial momenta such that the atomic distribution is centred in ρ at odd integer multiples of π, the energy absorption is maximum because it is here that the chaotic regions are largest. This can even be seen with $\hbar_{eff} = 0.25$ with values of the stochasticity parameter as low as $K = 0.7$, whereby the momentum width of the initial distribution is narrow enough to resolve the small regions of chaotic space that there are. Features for $K = 1.5$ are barely resolvable with $\hbar_{eff} = 1$ because the initial distribution is so broad. Also

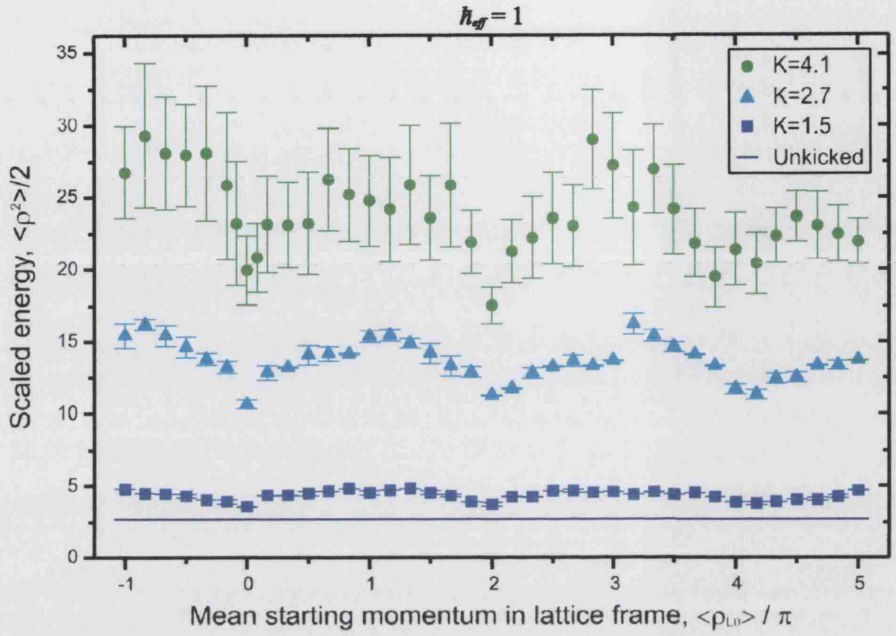

Figure 5.13: Resolving mixed phase space for $\hbar_{eff} = 1$. The resolution is less than for the results with $\hbar_{eff} = 1$ because the scaled momentum width of the initial distribution is higher. Initial distributions hence cover a greater mix of chaotic and regular phase space and the effects of each are diluted as a result.

observe that, in general, for initial momenta such that the atomic distribution is centred on an island in phase space (i.e. centred in ρ at even multiples of π), the energy absorption is a minimum. This is because the majority of the atoms are confined to the regular tori. Any diffusion that does occur at these points results from atoms that lie in the wings of the distribution that extend beyond the stable islands into chaotic phase space, thus making it possible for a fraction of atoms to pick up energy. Because of the increased width of the distribution for $\hbar_{eff} = 1$, this fraction is much higher and there is a marked decline in the resolution as a result.

As expected, average energies increase with K as the regular phase space gives way to chaos and as the atoms in the chaotic phase space are kicked

harder. For these small values of K the lowest energy growth is at odd integer multiples of $\langle p \rangle / \pi$. This must be because the stable islands are broad enough to confine the majority of the atoms. For this same reason, and because of the size of the surrounding chaotic sea, the best modulation in energy for these data is for $\hbar_{eff} = 0.25$, $K = 2.7$.

This simple investigation has allowed the verification of the structure of mixed phase space to be made and, as importantly, the demonstration of the utility of a moving lattice in order to do so. It has also been seen how stable islands in mixed phase space make a significant difference to the energy growth of the system, and that $\hbar_{eff}$ controls the resolution with which features in phase space are probed.

5.2.3 Investigating the momentum boundary

In this section the momentum boundary is investigated in the classically chaotic regime. Recall from section 4.2 that finite width kicks introduce to the diffusion constant a momentum dependent modulation which assumes the form of a sinc-squared function for square pulse kicks. By analogy to the two-kick correlation of an asymmetric kicking sequence (see section 4.2), this correlation is referred to as the "zero-kick" correlation. The sinc-squred function, and hence the diffusion constant and the kick strength, drops to zero at $p_b = 2\pi/\eta$ resulting in a momentum boundary past which atomic trajectories can not cross. Presented here are typical momentum distributions for experiments with finite width kicks which display a marked truncation at the momentum boundary.

For the experiment a time symmetric kick sequence is employed. The

apparatus used is that described in section 5.1.4, but for now the frequency of the kick beams are equal so the lattice is stationary. The kick period, and hence the effective Planck constant, is kept constant ($T = (18.94 \pm 0.02)\mu s \Rightarrow \hbar_{eff} = 2.000 \pm 0.002$), and the pulse time is increased until the momentum boundary can be observed. Of course the atomic momentum distributions should also broaden as the kick strength and the momentum diffusion constant increase with increasing kick duration. The value of $\hbar_{eff}$ is high so that a larger kick strength is possible. The value for $I/I_{sat} = 2850$ and $\Delta/\Gamma = 4000 \pm 100$ such that the potential depth $V_0/\hbar = (3.9 \pm 0.3)$MHz. This is not as high as previous experiments: it need not be because $\hbar_{eff}$ and t_p are larger.

For the atomic momentum distribution shown in black in figure 5.14, the pulse time $t_p = (379 \pm 20)$ns such that the duty cycle $\eta = (2.0 \pm 0.1)\%$ and the classical kick strength $K = 3.0 \pm 0.3$. Although for this kick strength the classical phase space is globally chaotic, there are still small stable islands. However, because $\hbar_{eff} = 2$ the atomic footprint has a dimensionless momentum width of $\sigma_p/\pi = 1.8 \pm 0.1$ and so any features in phase-space would not be expected to be resolved. Indeed, the distribution displays no observable sign of any 2π modulation, the stable features do not seem to have affected diffusion and the straight wings of the plot clearly display the exponential signature of dynamical localisation. The momentum boundary is calculated to be $p_b = \pm(320 \pm 17)$. This is outside the reach of the wings of the distribution which as a result is unaffected.

For the distribution shown in red, the pulse time $t_p = (947 \pm 20)$ns such that $\eta = (5.0 \pm 0.1)\%$, $K = 7.4 \pm 0.7$ and $p_b = \pm(128 \pm 3)$. Because

K is higher, the distribution is understandably wider than before. Again, the straight wings of the plot clearly display the exponential signature of dynamical localisation before they approach the momentum boundary, shown as a red dot-dash vertical line. There is a sharp drop in the wings of the momentum distribution at the momentum boundary.

The pulse time for the blue distribution is $t_p = (1894 \pm 20)$ns, for which $\eta = (10.0 \pm 0.1)\%$, $K = 15 \pm 2$ and $\rho_b = \pm(64 \pm 1)$. The distribution is also truncated at approximately the value calculated for the momentum boundary, as shown by the vertical blue dashed lines. Because the momentum boundary is so low it is thought to significantly influence the dynamics of the system, thus explaining why no experimental profile can be observed.

So it has been seen that the momentum boundary restricts diffusion and the atomic distribution does not spread far beyond the confines of the momentum boundary. However, a fraction of each distribution can be seen to diffuse past the boundary. This is thought to be due to phase noise, resulting from mechanical vibrations and air turbulence, which for a one-dimensional lattice made with two counterpropagating laser beams produces random fluctuations in the position of the potential. This phase noise results in a jitter and an uncertainty in the position of the momentum boundary which is why there is not a sharp cut-off in the momentum distribution.

In conclusion it has been demonstrated that a variation in the duration of the pulses used in a kicked rotor experiment translates to a change of the momentum boundary with a significant effect on atomic diffusion.

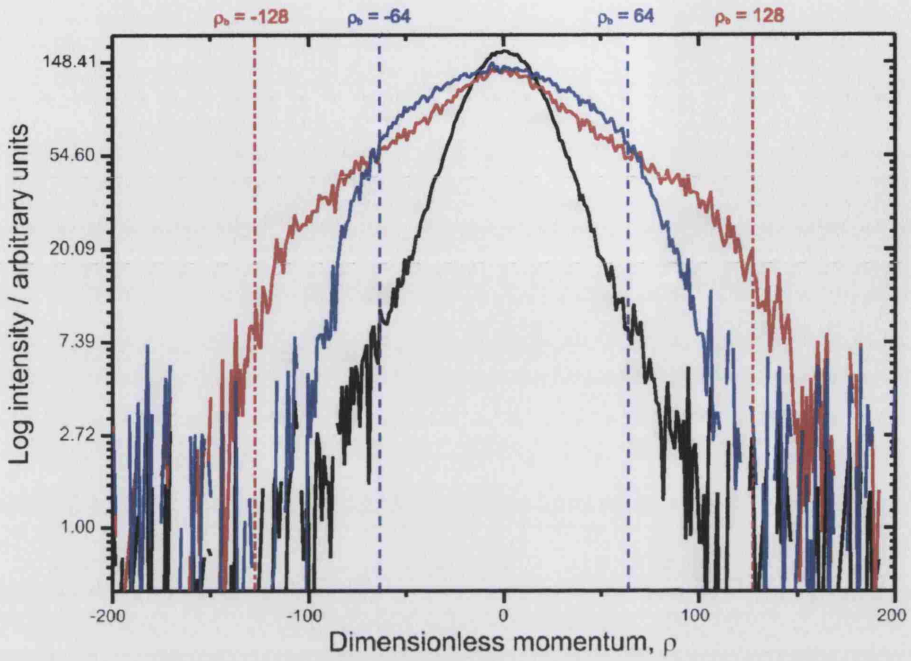

Figure 5.14: Results to show the effect of a finite pulse width. The black distribution (duty cycle $\eta = 2\%$, $K = 3$, and momentum boundary $\rho_b = \pm 320$) is well within the momentum boundary and is thus unaffected. The wings of the red distribution ($\eta = 5\%$, $K = 7.4$, $\rho_b = \pm 128$) fall off sharply at approximately the value given by the momentum boundary, shown by the dot-dash red line. The blue distribution ($\eta = 10\%$, $K = 15$, $\rho_b = \pm 64$), for which the momentum boundary is lower still, is also truncated at approximately ρ_b, as indicated by the dashed blue line.

5.2.4 Transport by restricting phase space

As a continuation of the previous experiment, here the atomic distribution is set to non-zero mean momenta in order to explore the momentum diffusion on either side of the momentum boundary. Using the technique described in section 5.1.4, the lattice is set at a constant velocity by applying a frequency difference between the beams such that in the rest frame of the lattice the cloud of atoms start with a non-zero mean momentum $\langle \rho_{L0} \rangle$. As a result of the sinc-squared modulation of the diffusion constant with ideal square-

pulse finite-width kicks, this can produce an asymmetry in the momentum distribution due to the gradient in $D(K, \rho)$. The effect is enhanced by the variation of the break time which, recall from section 3.3.2, is proportional to the diffusion constant. So, as the momentum of an atom approaches the momentum boundary, not only does the diffusion constant fall such that energy is absorbed more slowly, but the break time gets shorter such that the energy is absorbed for a shorter period of time. Due to the momentum boundaries, the space into which the atomic distribution can diffuse into is also restricted. It is hence a combination of the momentum boundary, $\partial D/\partial \rho$ and $\partial t^*/\partial \rho$ that causes asymmetric diffusion. A diagram to illustrate this is shown in figure 5.15.

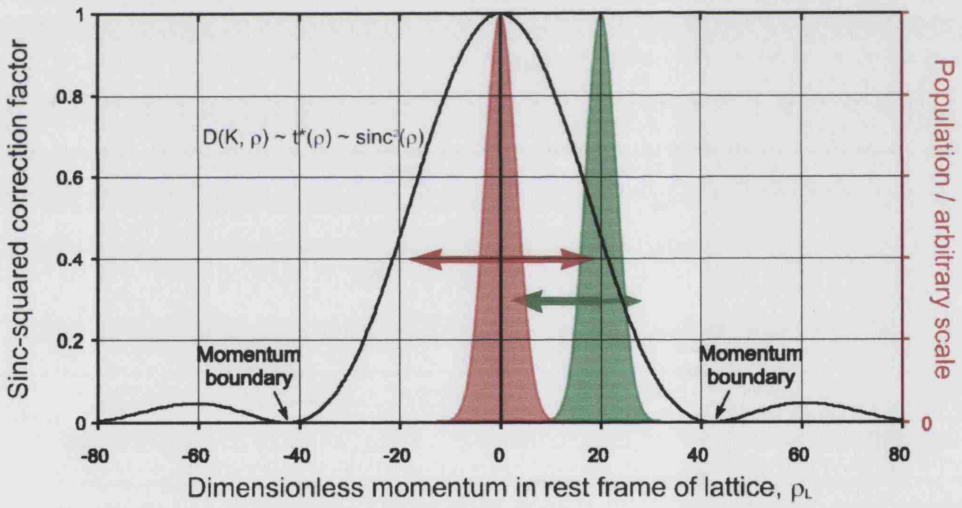

Figure 5.15: Sinc-squared modulation of the diffusion constant, $D(K, \rho)$ due to square-pulse finite-width kicks. The red atomic distribution with $\rho_{L0} = 0$ can expand symmetrically, whereas the green distribution with $\rho_{L0} = 20$ cannot. It can diffuse much further to the left than the $\rho_{L0} = 0$ case but is severely constrained on the right by the momentum boundary. The effect is enhanced by the variation of the break time t^* which is proportional to the diffusion constant.

Presented here are the results of an experiment performed with $T =$

$(9.47 \pm 0.02)\mu s$, so that $\hbar_{eff} = 1.000 \pm 0.002$. We have $t_p = (1.42 \pm 0.02)\mu s$ so that $\eta = (15.0 \pm 0.2)\%$ and a laser intensity and detuning such that $K = 5.3 \pm 0.5$. Because the pulse time is great with respect to the rise time of the AOM, the pulse shape does approximate a square-pulse function. A sinc-squared correction to the diffusion constant is thus believed to be realistic in this instance. For this value of η there is a relatively low momentum boundary: $\rho_b = 43 \pm 1$ (or $\rho_b/\pi = 13.5 \pm 0.6$). The width of the atomic footprint is $\sigma_\rho = 2.7 \pm 0.1$ (or $\sigma_\rho/\pi = 0.87 \pm 0.04$). Phase space diagrams for these parameters are shown in figure 4.2 of section 4.2. The starting momentum in the lattice frame was varied between 0 and 73 in order to explore the region past ρ_b.

Figure 5.16 shows some typical momentum profiles for atomic distributions centered at different starting momenta. Figure 5.16(a) is a plot of the intensity (or $N(\rho)$) against momentum. Figure 5.16(b) accentuates the asymmetry in the usual way by plotting $|\rho|N(\rho)$ against momentum. The momentum profiles are measured in the laboratory rest frame and so the momentum boundaries are offset by $\langle \rho_{L0} \rangle$. The symmetric, unkicked distribution is shown in black. For the red distribution $\langle \rho_{L0} \rangle = 0$ (with $\Delta f = 0$) and so the momentum boundary $\rho_b = \pm(43 \pm 2)$ in the laboratory frame. For the green distribution $\langle \rho_{L0} \rangle = 29.2 \pm 0.1$ (by setting $\Delta f = 245$kHz) and so the momentum boundary $\rho_b = 14 \pm 2$ and -72 ± 2 with respect to the laboratory frame of reference.

The results are in excellent agreement with the calculations for the momentum boundaries.

The red distribution has diffused in a way that is not quite symmetric.

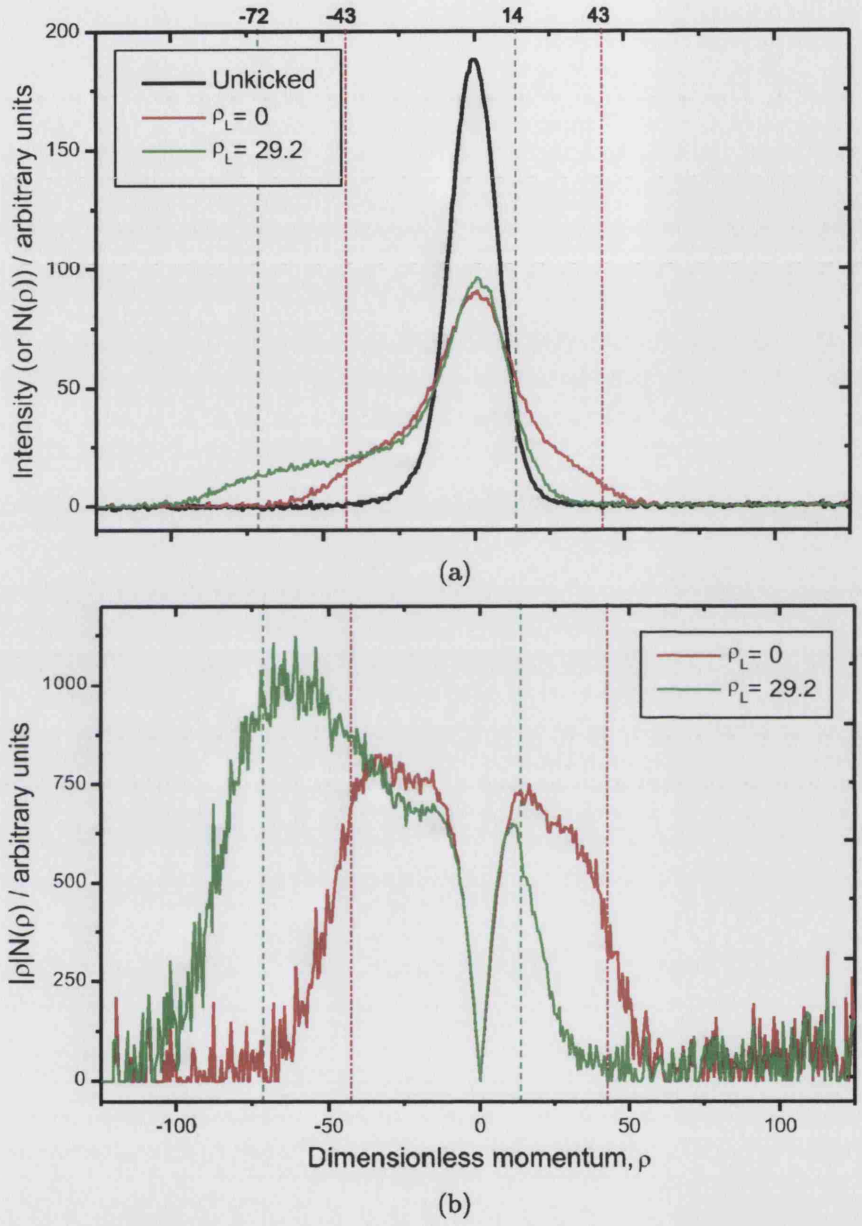

Figure 5.16: Asymmetric momentum profiles near momentum boundaries. The symmetric, un-kicked distribution is shown in black. Red and green profiles result from distributions centred at different starting momenta, $\langle \rho_{L0} \rangle = 0$ and $\langle \rho_{L0} \rangle = 29$ respectively. Their momentum boundaries (in the laboratory frame of reference) are indicated with broken lines.

This is most likely attributed a slight misalignment of the kicking beams on the atomic cloud. As a result the momentum boundary on the negative momentum side is more pronounced, at which point a clear shoulder can be seen in the wing of the distribution. Although no shoulder can be seen at the momentum boundary on the positive momentum side, diffusion does not continue far past it. The reason that this distribution diffuses a little beyond the momentum boundary is thought to be due to lattice phase noise and because of the finite width of the spatial distribution, as explained previously.

As expected, the green distribution is clearly very asymmetric. Because the centre of the momentum distribution of the atomic cloud is set close to the momentum boundary, diffusion is greatly inhibited in the positive momentum direction. Again, the apparent fraction of the population that is seen on the high side of the boundary is attributed to a combination of the initial spatial distribution in the region of $x = 0$ and diffusion past the boundary due to phase noise. Diffusion in the negative momentum direction is free up to the boundary at $\rho = -71.5$. At this point there is a shoulder in the distribution and the population falls away.

The above experiment was performed for various values of starting momentum, against which the resulting values for the asymmetry, or 'current', (see section 4.4) are plotted in figure 5.17.

It can be seen from the figure that as $\langle \rho_{L0} \rangle$ increases from zero a large negative asymmetry can be seen to accumulate as $\partial D/\partial \rho$ and $\partial t^*/\partial \rho$ increases and the diffusion to positive momenta becomes restricted by the presence of the momentum boundary. The asymmetry then sharply falls as $\langle \rho_{L0} \rangle$ approaches the momentum boundary, as the asymmetry of the diffusion con-

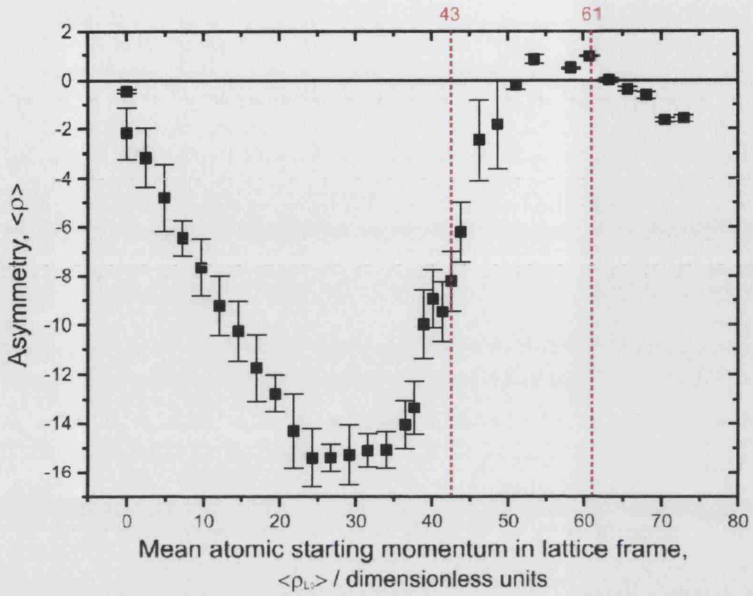

Figure 5.17: Results to show the variation of the ratchet current with increasing ρ_L up to and beyond the momentum boundary at $\rho_b = 43$. At $\rho_L = 61$, $dD/d\rho = 0$.

stant decreases and the value of the diffusion constant and the break time drops to zero. However, one can see that the asymmetry does not drop to zero until $\langle \rho_{L0} \rangle$ exceeds the momentum boundary. It is uncertain whether this is an effect caused by the finite momentum width of the atomic distribution and the asymmetry of the diffusion constant, or if it is due to an offset in the y-axis due to asymmetry in the initial momentum distribution.

The area of phase space past the boundary is inaccessible to conventional experiments that use a static potential. As the starting momenta pass the boundary there appears to be a small growth in momentum as D is small but non-zero. The asymmetry now grows in the opposite sense because the gradient of the diffusion constant has become positive and the momentum boundary inhibits diffusion in the opposite direction. The magnitude of this

asymmetry is less than before because the diffusion constant is lower and the break time is smaller in this region. The asymmetry then falls back to zero as the momentum approaches the next boundary at $\rho_L = 61$ where $dD/d\rho = 0$. This appears to suggest that square-function kicks are a good approximation to our experimental kicks (for long pulse times), and as a result the diffusion constant does indeed take on a sinc-squared momentum dependent correction. However, it may be that the reliability of the data at these momenta is questionable (possibly due to a misalignment of the kicking beams). It is clear that more data must be taken before results are conclusive, and it would also be interesting to investigate the effects that different kick shapes have on the diffusion constant.

In conclusion, by introducing a moving optical potential the momentum dependent diffusion constant due to finite-width kicks can be exploited to produce a strongly asymmetric momentum diffusion. Using the moving optical lattice has also enabled the investigation of diffusion in the normally inaccessible regions of phase space beyond the momentum boundaries imposed by the kicks of a finite temporal width. We believe this is the first time such a moving lattice technique has been used in quantum chaos experiments.

If continuous phase space is to be investigated it is important that the momentum boundary is as high as possible by making η as low as possible, to ensure that there is little modulation of the diffusion constant and no restrictions due to the momentum boundaries. This becomes particularly important in experiments presented in the next chapter because the momentum dependence of the diffusion constant due to broken time symmetry increases

from $\rho = 0$ with opposite sign to this experiment.

5.3 Conclusion

Presented in this chapter were results to show that dynamical localisation, the quantum effect that suppresses atomic diffusion, can be observed in our cold atom realisation of the kicked rotor with a time-asymmetric kicking sequence. It has been shown that, within the limit set by the maximum power of the Ti:Sapphire laser, the kick strength can easily be controlled. The moving lattice technique has been successfully demonstrated and proven to be a useful device to verify the structure of phase space for different kick strengths. It has also been shown that the effective Planck's constant can easily be controlled and that it sets the resolution with which phase space may be probed. The effect on atomic diffusion of varying the duration of the pulses has been successfully demonstrated and it has been shown that the combined effect of the local gradient in the modulation of the diffusion constant and the break-time, and the restriction imposed by the momentum boundary can be used with a moving lattice to generate asymmetric atomic diffusion. Finally, results have been presented that we believe to be the first to explore atomic diffusion in phase space beyond the momentum boundary.

The results in this chapter have been prepared for publication in [92,93].

CHAPTER 6

Asymmetric diffusion in a fully chaotic system

Presented in this chapter are results that we believe to be the first experimental realisation of directed transport in the kicked rotor that is due to chaotic dynamics alone.

Directed transport in the classically chaotic regime will be demonstrated in two ways, both of which use a time-asymmetric kicking sequence to break temporal symmetry with a pulsed sinusoidal potential. The first employs a moving lattice and the second uses a lattice that is accelerated in alternating directions from kick to kick.

6.1 Asymmetric diffusion with broken time symmetry

For this experiment an asymmetric kicking sequence is employed to induce a momentum dependence in the diffusion constant (see section 4.3). Using a moving lattice we investigate this momentum dependence and exploit it to create an asymmetry in the momentum diffusion that is entirely due to chaotic dynamics. In the first part of this section parameters are chosen such that the resulting momentum profiles display the clearest asymmetry. Results presented in the second part of this section use a different set of parameters to most clearly show the modulation of the diffusion constant and which tie-in with the theory by Monteiro *et al.* [89]. The last part of this section explores the evolution of the current for different values of the chirp parameter.

6.1.1 Asymmetric momentum profiles and time evolution

For the results presented here the period of the kick cycle was $T = (2.37 \pm 0.02)\mu$s so that $\hbar_{eff} = 0.250 \pm 0.002$ (as chosen by Jonckheere *et al.* [89]). The pulse duration, $t_p = (379 \pm 20)$ns, was chosen with the balance between the kick strength and the momentum boundary in mind. This was such that the kick strength ($K = 2.1 \pm 0.2$ for the given laser intensity and suitable detuning) and the momentum boundary ($\rho_b = 40 \pm 2$) were not too low. The chirp parameter $b = 1/8$ was chosen to maximise the asymmetry of the spatial distribution as viewed by eye on the computer screen.

Although the kick strength is fairly low it is seen from the classical phase portraits in figure 6.1 that the effect that a large chirp parameter has is to fracture the stable islands and leave phase space predominantly chaotic.

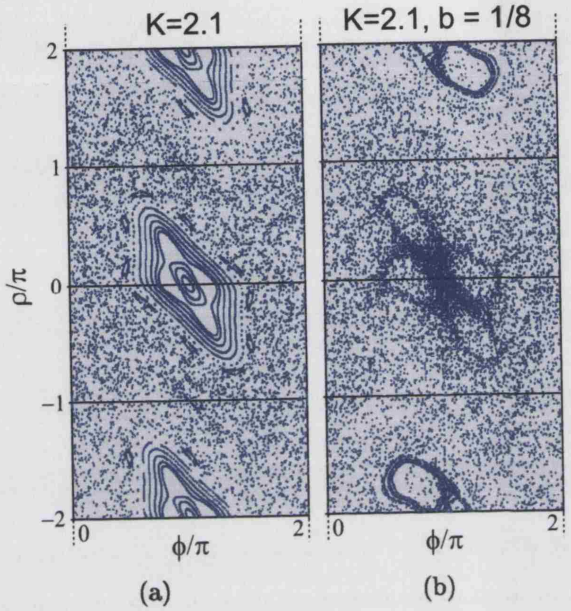

Figure 6.1: Phase-space portraits (Poincaré surface of sections) for the parameters used in the experiments. Diagram (a): $K = 2.1$, $b = 0$. Phase space is globally chaotic with relatively large stable islands. Diagram (b): $K = 2.1$, $b = 1/8$. The stable islands have broken up to leave phase space predominantly chaotic.

Recall from section 4.3 that by breaking the temporal symmetry with a chirped kick sequence a momentum dependence is imposed on the diffusion constant which varies as $D(K, \rho, b) \sim -K^2 J_2(K) \cos(2\rho b)$ (see equation 4.15). As before, the moving lattice technique is used to prepare the cloud of atoms with a non-zero mean momentum in the rest frame of the lattice. For $\langle \rho_{L0} \rangle = (2n+1)\pi/4b$, where $\partial D/\partial \rho$ is largest, one would therefore expect to observe maximum asymmetry in the diffusion of the cold atoms. The accumulation of asymmetry in the momentum distribution is, as explained

in the previous section, also enhanced by the variation of break time with momentum: the diffusion constant is lower on one side of the starting momentum distribution hence t^* is less and the growth of momentum is further suppressed (and vice-versa).

No asymmetry is expected when $\langle \rho_{L0} \rangle = n\pi/2b$, i.e. at $\partial D/\partial \rho = 0$, because the diffusion constant is locally symmetric. Given that the chirp parameter $b = 1/8$, the cosinusoidal correction to the diffusion constant has a period of 8π. In this case maximum symmetry should be observed by preparing the cold atoms with, for example, $\langle \rho_{L0} \rangle = \pm 2\pi$ (with $\Delta f = \pm 211$kHz). The resultant momentum distributions for these examples are shown in figure 6.2(a). The figures beneath the results show the modulation of the diffusion constant and the positions of the atomic distributions at $\langle \rho_{L0} \rangle = \pm 2\pi$ to illustrate the starting conditions. Because $\partial D/\partial \rho$ is of opposite sign for these examples, an asymmetry in the atomic diffusion in the opposite sense is expected. Conversely, no asymmetry is expected if the atoms are prepared with, for example, $\langle \rho_{L0} \rangle = \pm 4\pi$ (with $\Delta f = \pm 422$kHz).

The results are in qualitative agreement with the theory. The orange momentum distribution in figure 6.2, centred at a point of maximum positive gradient of the diffusion constant to begin with, is indeed skewed towards more positive momenta. Conversely, the green distribution, centred at a point of maximum negative gradient in the diffusion constant to begin with, is skewed towards more negative momenta. The distributions are almost mirror images of each other about $\rho = 0$. Any dissimilarity is most likely due to a small misalignment of the lattice beams.

The current (the mean atomic momentum $< \rho >$) is used to quantify the

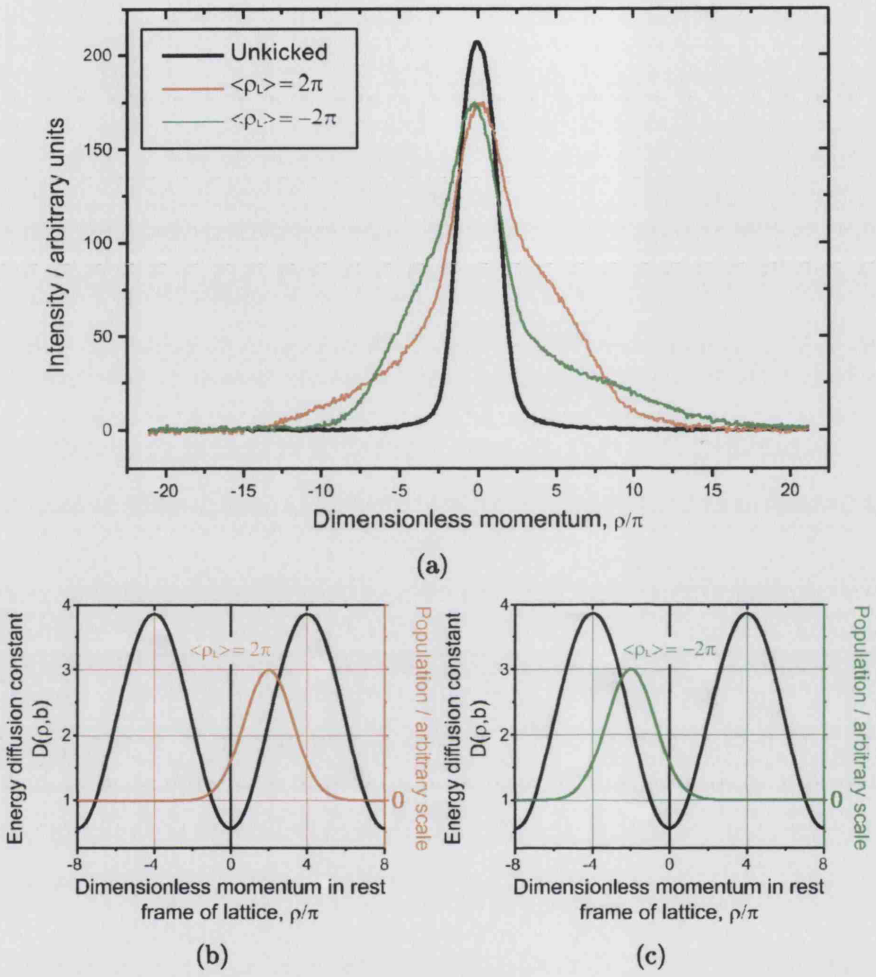

Figure 6.2: Asymmetric diffusion due to a time-asymmetric kicking sequence: example momentum distributions for $K = 2.1$, $\hbar_{eff} = 0.25$ and $b = 1/8$. Figures (b) and (c) show the modulation of the diffusion constant and the atomic distribution, both plotted against the dimensionless momentum in the frame of the moving lattice, for $\langle \rho_{L0} \rangle = 2\pi$ and $\langle \rho_{L0} \rangle = -2\pi$ respectively. For $\langle \rho_{L0} \rangle = 2\pi$, centred at maximum positive $\partial D / \partial \rho$, the diffusion constant (and the break time) is greater to the positive side of momentum and the momentum distribution in figure (a) is indeed skewed towards more positive momenta. The reverse is true for $\langle \rho_{L0} \rangle = -2\pi$.

asymmetry of the momentum distributions. For four values of $\langle \rho_{L0} \rangle$ the time evolution of the asymmetry will now be presented. The results are shown in

figure 6.3 with the current plotted against the number of two-kick cycles N.

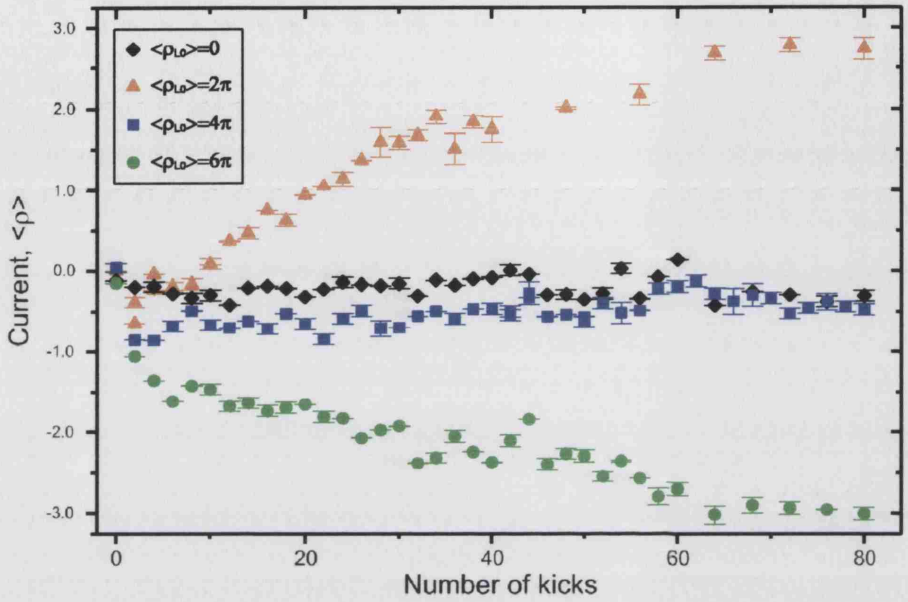

Figure 6.3: Time evolution for the asymmetric diffusion for different values of ρ_{L0}.

The results are very pleasing. It is seen from the graph that for $\langle \rho_{L0} \rangle = 0$ and $\langle \rho_{L0} \rangle = 4\pi$, about which momenta the diffusion constant is symmetric, as expected the current does not change.

The plots for $\langle \rho_{L0} \rangle = 2\pi$ and $\langle \rho_{L0} \rangle = 6\pi$ (with $\Delta f = 211$kHz and $\Delta f = 633$kHz respectively) grow in current in opposite senses, as expected from the gradient of the diffusion constant about their respective mean starting momenta, and to a similar magnitude.

6.1.2 Modulation of the diffusion constant

As a continuation of the previous experiment the results presented here display the modulation of the current against the scaled starting momentum in

the rest frame of the lattice for two values of the chirp parameter b.

The period of the kicks was $T = (9.47 \pm 0.02)\mu s$ so that $\hbar_{eff} = 1$. The pulse duration $t_p = 296$ns to give a momentum boundary at approximately $\rho_b \approx 200$, sufficiently high so that the effects due to a finite pulse width can be neglected for the range of momenta investigated. For the given laser power and suitable detuning the kick strength $K = 3.3 \pm 0.3$. The two values for the chirp parameter were $b = 1/16$ and $1/32$, and phase space portraits for these parameters are shown in figure 6.4 to check that diffusion is not inhibited by stable islands.

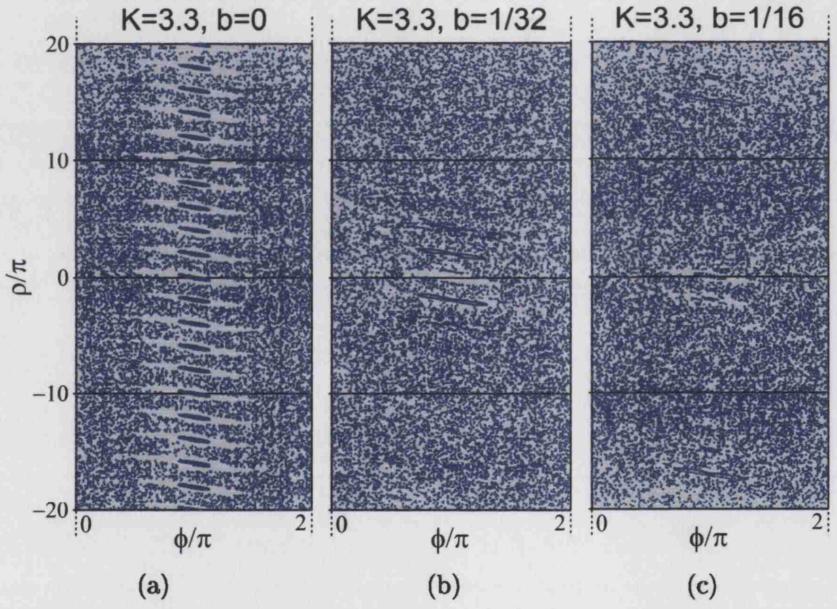

Figure 6.4: Phase-space portraits (Poincaré surface of sections) for the classical kicked rotor with $K = 3.3$. Diagram (a): $b = 0$. We see globally chaotic phase space containing stable structures with 2π periodicity in ρ. Diagram (b) and (c): $b = 1/32$ and $1/16$ respectively. The majority of regular structures have disappeared and phase space is predominantly chaotic.

One can see from the Standard Map ($b = 0$, figure 6.4(a)) that phase space is globally chaotic with evidence of stable structures of 2π periodicity.

This residual periodicity is destroyed for $b = 1/32$ and $b = 1/16$ as the system becomes sufficiently chaotic due to the broken time symmetry.

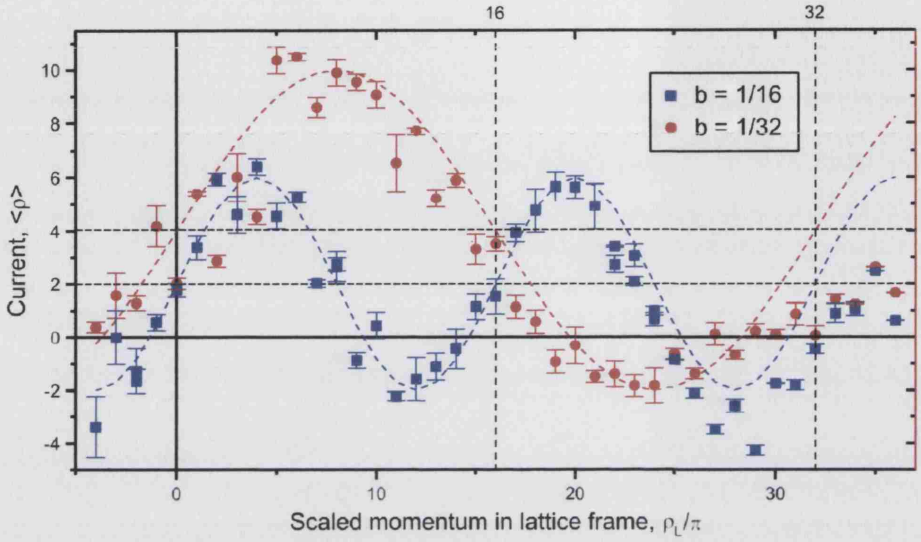

Figure 6.5: Ratchet current *vs* starting momentum in the lattice frame for $K = 3.3$, $\hbar_{eff} = 1$, 320 kicks, $b = 1/32$ (red circles) and $b = 1/16$ (blue squares).

Results are shown in figure 6.5. The figure clearly shows that the asymmetry of the momentum distributions for both values of b oscillate sinusoidally. This is in excellent agreement with the theory: the sinusoidal modulation is proportional to the local gradient of the cosinusoidal diffusion constant and the period of oscillation for both data sets is π/b. Although it can not be seen explicitly from any of the asymmetric diffusion data it is thought that the accumulation of asymmetry, and in this case the modulation of the current, is also enhanced by the variation of the break time with momentum.

The small offset from $\langle \rho \rangle = 0$ may be attributed to a small asymmetry in the initial momentum distribution.

The relative amplitudes of modulation are in qualitative agreement with

the theory. One can see from the graph that the amplitude of modulation for $b = 1/32$, let us label this A_{32}, is larger than that for $b = 1/16$, A_{16}. This is to be expected because, as seen in section 4.3, the ratchet time is inversely proportional to the square of the chirp parameter, $t_r \propto 1/b^2$. Systems with lower b will therefore accumulate asymmetry for a longer time: in this case four times longer for $b = 1/32$ than for $b = 1/16$. However, we see that A_{32} is not four times larger than A_{16}. This could be because, given that the break time is the same for both, the system with $b = 1/32$ becomes dynamically localised before the ratchet time is reached. This uncertainty motivated the experiment in the following section which investigates the time evolution of the current for various values of b.

6.1.3 Time evolution for varying b

Here we investigate the time evolution of the current for various values of the chirp parameter: $b = 1/32$, $1/16$ and $1/8$. The parameters used for the experiment presented are the same as in the previous section. To obtain the clearest results the asymmetry of the diffusion constant is maximised by shifting the phase of the diffusion constant by $\pi/2$. For $b = 1/32$, $1/16$ and $1/8$ this requires $\langle \rho_{L0} \rangle = 8\pi$, 4π and 2π, as achieved with $\Delta f = 211$kHz, 106kHz and 53kHz, respectively. Results showing the asymmetry against time for the different values of b are shown in figure 6.6.

For $b = 1/8$ (the black data in graph 6.6) the asymmetry grows quickly from $\tau = 0$ and dies away exponentially with a relatively low time constant. This is a very good demonstration of the finite lifetime of the corrections to the diffusion constant that result from the asymmetric kicking sequence.

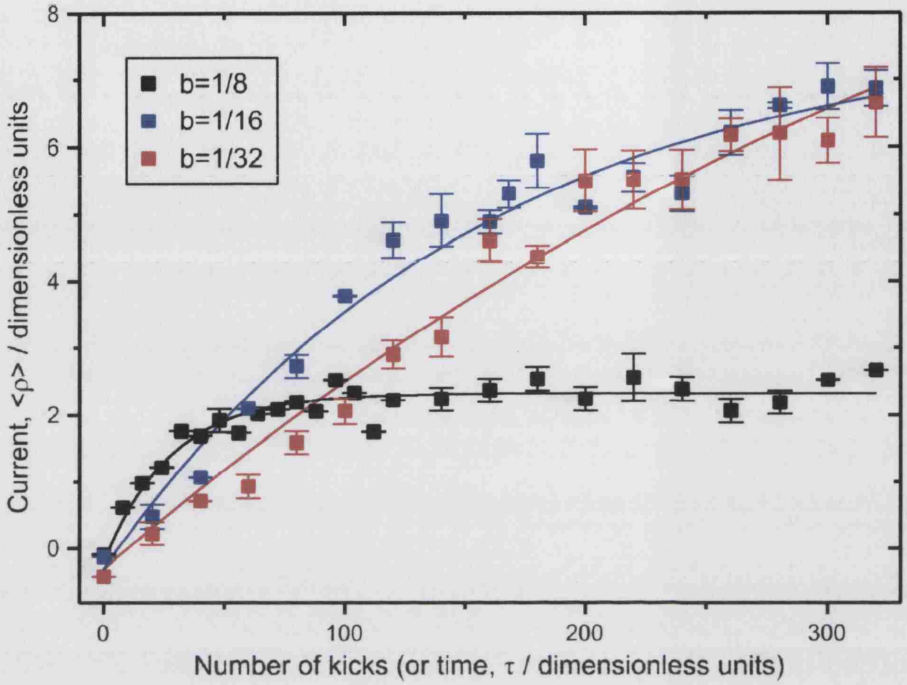

Figure 6.6: Graphs to show current growth for varying b. $K = 3.3$, $\hbar_{eff} = 1$, To maximise asymmetry, $\langle \rho_{L0} \rangle = 2\pi$, 4π and 8π for $b = 1/8$, $1/16$ and $1/32$ respectively. The fitted curves are exponential with the form $I_r(\tau) \sim 1 - e^{-\tau/\beta_r}$, where β_r is a characteristic timescale related to the ratchet time.

Interestingly it is seen from the other plots, with $b = 1/16$ and $b = 1/8$, that the initial rate of growth of asymmetry appears to decrease with b. The answer to the question of relative magnitudes raised in the previous section is therefore not as simple as considering only the ratchet time and the break time. However, this has certainly helped to give one qualitative explanation as to why the amplitude of modulation for the experiment in the previous section with $b = 1/32$ is not four times greater than that for $b = 1/16$.

Although the rate of growth in asymmetry appears to decrease for $b = 1/16$ and $b = 1/32$ (the blue and red plots respectively), they do not level out within the timeframe of this experiment. Unfortunately a longer kicking

duration is not possible because, as mentioned in section 5.1.1, the atomic cloud begins to fall out of the interaction region. Nevertheless, by fitting exponential curves to the data an approximation of the ratchet time can be made. The fitted curves are of the form $I_r(\tau) = I_{sat}(1 - e^{-\tau/\beta_r})$, where β_r is a characteristic timescale of saturation and I_{sat} is the projected saturation current. If we recall that the ratchet time, t_r, is defined as the time taken for the momentum to reach 95% of its saturation value, then it can easily be shown that t_r is related to β_r by the approximation $t_r = \beta_r \ln 20$. It can also easily be shown that the initial rate of growth in asymmetry of the exponential curves is given by $R_I = \frac{dI}{dt}|_{\tau=0} = \frac{I_{sat}}{\beta_r}$. Values of the projected saturation current, the time constant β_r, the initial rate of growth in asymmetry and the ratchet time for the different values of the chirp parameter are tabulated below.

b	I_{sat}	β	R_I	t_r
1/8	2.50 ± 0.05	31 ± 4	0.08 ± 0.01	93 ± 13
1/16	8.1 ± 0.5	145 ± 23	0.06 ± 0.01	434 ± 69
1/32	14 ± 4	414 ± 120	0.03 ± 0.01	1240 ± 360

Table 6.1: Values of the projected saturation current, the time constant β_r, the initial rate of growth and the ratchet current, calculated by the exponential fits in figure 6.6 for the different values of the chirp parameter.

From the calculated ratchet times we find the following ratios:

$$\frac{t_r(b = 1/16)}{t_r(b = 1/8)} = 4.7 \pm 1$$
$$\frac{t_r(b = 1/32)}{t_r(b = 1/16)} = 2.9 \pm 1$$

So within the calculated error, the relative ratchet times between data for $b =$

1/8 and $b = 1/16$ agree with the inverse-squared dependence of t_r on b (see equation 4.16). But the relative ratchet times between data for $b = 1/16$ and $b = 1/32$ do not. This is, as hypothesised before, possibly due to dynamical localisation affecting the energy growth at a timescale that is somewhere in between the ratchet times for $b = 1/16$ and $b = 1/32$. To investigate the timescales associated with dynamical localisation, the graphs in figure 6.7 display energy, $\langle p^2 \rangle / 2$, in dimensionless units against the number of kicks (the time in dimensionless units). In the same way as before, exponential curves of the form $E(\tau) = E_{sat}(1 - e^{-\tau/\beta^*})$ are fitted to the data, where E_{sat} is the saturation energy. It is obviously inconvenient to use the method described in section 3.3.2 to calculate a measure for the break time, especially for comparison with either measure of the ratchet time. It is more sensible to use the characteristic exponential timescale β^* as a measure of the quantum break time and compare this with the ratchet timescale β_r. Values are displayed in table 6.7(d).

From the table it can be seen that for $b = 1/8$ the break timescale is over twice as long as the ratchet timescale. We can therefore confirm that the growth of asymmetry observed for the black data in figure 6.6 is not likely to be affected to any great extent by the onset of dynamical localisation. The saturation of the current is, as expected, then a result of the finite lifetime of the momentum dependence of the diffusion constant alone. For $b = 1/16$ the ratchet timescale is fairly similar to the break timescale. Again, as expected, the growth of asymmetry observed for the blue data in figure 6.6 is not likely to be affected to a large extent by dynamical localisation. Indeed, it was shown that the relative magnitudes of saturation current for $b = 1/8$ and

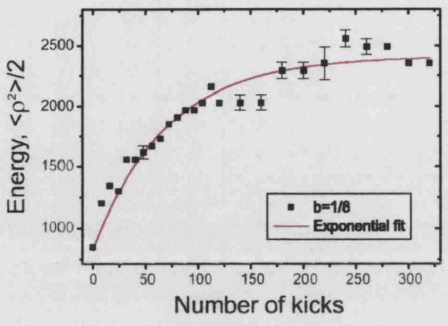

(a)

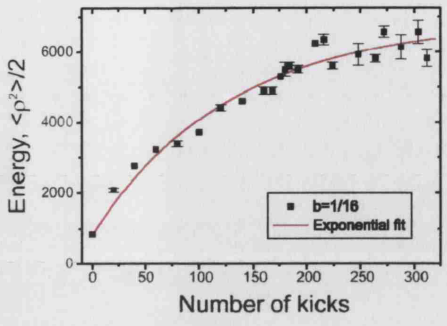

(b)

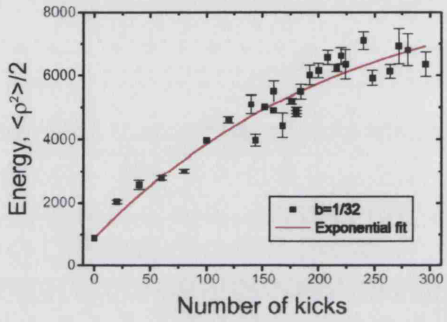

(c)

b	β_r	β^*
1/8	31 ± 4	69 ± 6
1/16	145 ± 23	131 ± 15
1/32	414 ± 120	220 ± 50

(d)

Figure 6.7: Energy growth for varying b. $K = 3.3$, $\hbar_{eff} = 1$, and $\langle \rho_{L0} \rangle$ is set to maximise asymmetry. The fitted curves are exponential with the form $E(\tau) \sim e^{-\tau/\beta^*}$, where β^* is a characteristic timescale related to the break time. The table compares β_r and β^* for the different values of b.

$b = 1/16$ were in agreement with the inverse-squared dependence of t_r on b, which only holds if the growth in asymmetry is not hampered by dynamical localisation.

Conversely, because the saturation current for $b = 1/32$ is not in agreement with the inverse-square dependence, it was hypothesised that the magnitude of saturation current for $b = 1/32$ *is* affected by dynamical localisation. This belief is reinforced here, given that the calculated break timescale is around half that of the ratchet timescale. The growth in asymmetry hence falls short of the inverse squared relationship because of the arrest of the

diffusion due to dynamical localisation.

In conclusion, it has been demonstrated that by breaking the time symmetry of the δ-kicked rotor the diffusion constant becomes momentum dependent as a result of the correlations between kicks. Using a moving lattice technique this cosinusoidal dependence has been verified and then exploited to produce an asymmetry in the diffusion of this fully chaotic system. We believe that this is the first demonstration of directed transport in a Hamiltonian system that results from chaotic dynamics alone.

We also believe that the initial rate of growth in asymmetry and the break timescale β^* are dependent on the chirp parameter. However, it is clear that much additional work will be required before a complete understanding of this is obtained.

6.2 Asymmetric diffusion with an accelerating lattice

In section 4.5 it was demonstrated that a temporally asymmetric system would produce asymmetric diffusion if the spatial symmetry was broken. This is done by introducing to the potential a linear term, a potential gradient, that alternates in sign between successive kicks. For this experiment we do exactly that, producing the 'rocking' action by alternating the acceleration of the optical lattice between kicks.

6.2.1 Preparation

An alternating acceleration of the kicking potential can be achieved by driving one of the AOMs in such a way that it "chirps" the frequency of one of the beams in a saw-toothed fashion. Using the experimental arrangement shown in figure 5.4 it was shown that a frequency difference of $2\Delta f$ between the RF sources produces a freqency difference of $2\Delta f$ between the lattice-forming laser beams and the resultant optical lattice moves at a speed $v_L = \lambda\Delta f$. However for this experiment a time-dependent frequency difference is used. The frequency $f(t)$ of one of the lattice beams (the "chirped" beam) is varied as a function of time so the resulting interference pattern between the chirped and stationary beam moves with an acceleration of $a = \frac{\lambda}{2}\frac{d\Delta f(t)}{dt}$. If the frequency difference is ramped linearly by an amount ν in a time T, then the acceleration becomes $a = \frac{\lambda}{2}\frac{\nu}{T}$, where $\nu = f_m - f_0$ is the maximum frequency difference (see figure 6.8).

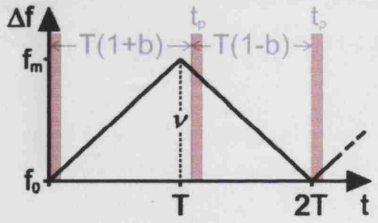

Figure 6.8: A saw-toothed RF frequency modulation to the AOMs to produce an alternating acceleration on the lattice from kick-to-kick.

Experimentally, the saw-toothed function for the frequency modulation is drawn in the WaveCad package on a computer and downloaded to a waveform generator (shown as WGB in figure 5.5). During the experimental cycle the waveform generator, triggered by the control computer, then feeds the

modulation input of one of the RF synthesizers to produce a saw-toothed RF signal for one of the AOMs.

As shown in [94–96], the effect of accelerating the optical lattice is to introduce an inertial term such that in the rest frame of the optical potential the unscaled Hamiltonian, omitting the kicking term, becomes

$$H = \frac{p^2}{2M} + V_0 \cos(2k_L x) + Max \tag{6.1}$$

Re-introducing the two-period asymmetric kicks the Hamiltonian in dimensionless units then becomes exactly that of equation 4.18 in section 4.5, with $A = 2k_L aTt_p$. This simplifies to $A = 2\pi\nu t_p$ for the symmetric, saw-toothed frequency modulation. It was seen that this system results in a diffusion constant that is dependent on A as well as ρ and b and varies as $D \sim -K^2 J_2(K)\cos(2\rho b - A)$. The cosinusoidal momentum dependence of the diffusion constant can therefore be made asymmetric about $\rho = 0$ by varying A, i.e. shifting the phase. Because the asymmetry of diffusion is related to the local gradient of the diffusion constant, for a sample of cold atoms centred at zero momentum this will result in asymmetric diffusion. The asymmetry of diffusion should vary with 2π periodicity in A.

This technique makes it possible to investigate the asymmetry of the momentum distribution as a function of A, simply by changing ν.

6.2.2 Results

The results presented here are for a set of parameters that are close to those in the last section. That is, the pulse sequence times are such that $\hbar_{eff} = 1$

and the momentum boundary $\rho_b \approx 200$. The value for the chirp parameter is $b = 1/16$. Below we show the phase portraits for these parameters, and briefly examine the effect of introducing a potential gradient A.

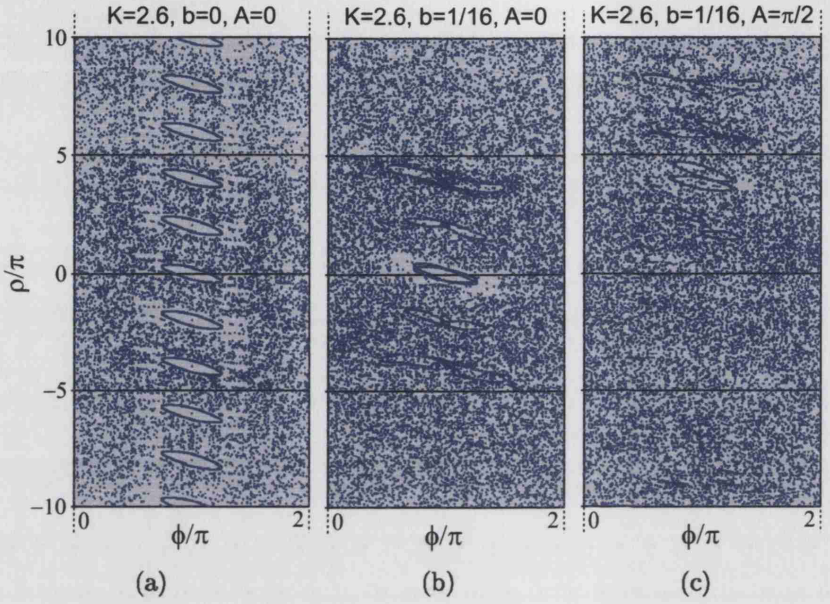

Figure 6.9: Phase-space portraits (Poincaré surface of sections) for the classical kicked rotor with $K = 2.6$. Diagram (a): $b = 0$, $A = 0$. Stable structures have 2π periodicity in ρ. Diagram (b): $b = 1/16$, $A = 0$. The effect of the chirped kicks alone breaks up the regular structures and phase space is sufficiently chaotic. Diagram (c): $b = 1/16$, $A = \pi/2$. The small structures evident in (b) have been shifted ρ by 4π.

It can be seen from the phase portraits that the effect of the chirp parameter, as seen previously, is to break up any regular structures to some extent and to alter the periodicity in ρ (see section 4.3). The broken features in figure 6.9(b) have a "super-periodicity" of 16π, and so the phase space is predominantly chaotic with small, widely spaced features that do not significantly affect atomic diffusion. Figure 6.9(c) shows the effect of introducing non-zero A. Phase space appears even more chaotic.

An example of some typical momentum distributions are shown in figure 6.10(a), the starting conditions for which are illustrated in the figures underneath.

The diffusion constant has a cosinusoidal momentum dependence of period $\rho/b = 16\pi$. Thus for $A = 0$, for which the diffusion constant is symmetric about $\rho = 0$ (see figure 6.10(b)), the distribution is symmetric. For $A = \pi/2$ the diffusion constant changes phase by $\pi/2$, as illustrated in figure 6.10(c) by a translation along ρ of 4π. A maximum negative gradient for the diffusion about $\rho = 0$ is expected and, accordingly, the distribution is skewed in the direction of negative momentum. The reverse is true for $A = -\pi/2$.

The same results are displayed again in figure 6.11. Here the dimensionless momentum is plotted against $|\rho|N(\rho)$ to highlight the asymmetry. The starting atomic distributions that are centred in momentum at an equal and opposite value of $\partial D/\partial\rho$ result in asymmetric distributions, the asymmetry of which are almost equal and opposite.

It was mentioned in section 5.1.4 that the maximum FM modulation amplitude through which the AOM could be scanned was ±1.25MHz. With the parameters in this experiment this corresponds to a value of A of $\pm 3\pi/4$. To increase the range over which the diffusion constant can be investigated, additional results can be taken with a constant frequency difference Δf_c applied in opposite sense to each of the lattice beams as well as frequency modulating the chirp beam. For $\Delta f_c = 211.193$kHz this has the effect of centering the atomic momentum distribution at $\rho_L = 4\pi T\Delta f = 8\pi$ in the rest frame of the lattice. Given that the period of the diffusion constant is 16π, two overlapping sets of data taken at $\langle\rho_{L0}\rangle = 0$ and $\langle\rho_{L0}\rangle = 8\pi$ demonstrate

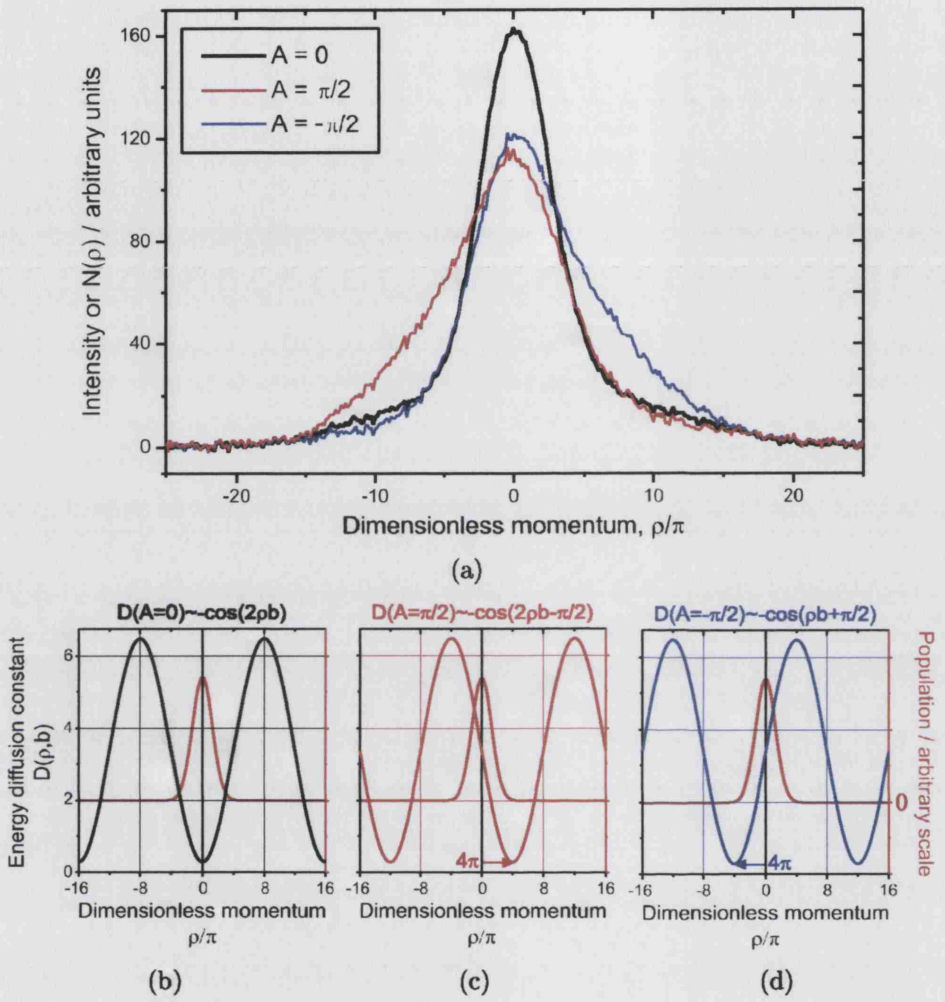

Figure 6.10: Figure (a) shows example momentum distributions for the accelerating lattice experiment with $K = 2.6$ and $b = 1/16$. Figures (b,c,d) illustrate the starting conditions. The bold black line shows symmetric diffusion for $A = 0$. There is preferential directional diffusion towards negative momenta for the thin red line with $A = +\pi/2$. The thin blue line, for which $A = -\pi/2$, is skewed towards positive momenta.

the modulation of the current over slightly more than a whole period in A. The current was calculated for each of the momentum distributions and plotted against the potential gradient. The results can be seen in figure 6.12.

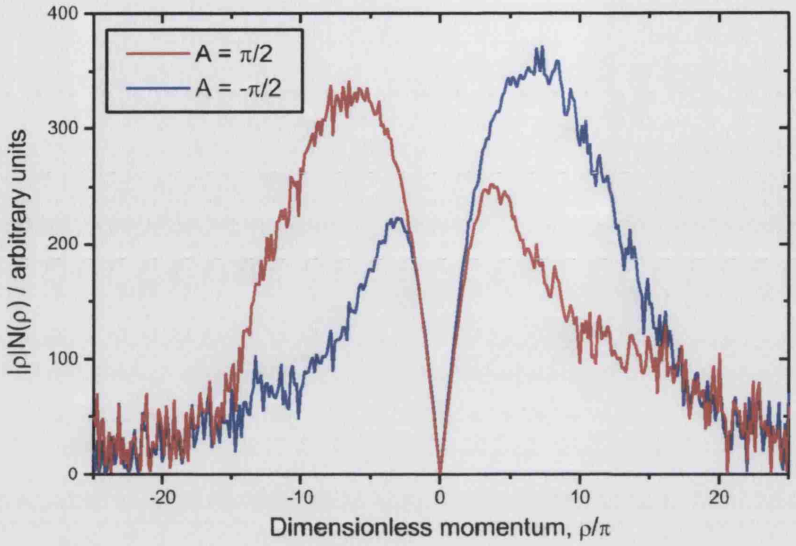

Figure 6.11: Plots of $|\rho|N(\rho)$ vs ρ for the accelerating lattice experiment, with $K = 2.6$ and $b = 1/16$. The asymmetric diffusion in opposite senses for $A = -\pi/2$ (blue) and $A = +\pi/2$ (red) is made very obvious.

It is clear that a phase shift can indeed be added to the variation of the momentum diffusion constant by varying A. As expected the asymmetry, or current, is proportional to the local gradient of the diffusion constant about the mean atomic starting momentum, and the current oscillates with a period of 2π. The accumulation of asymmetry in the momentum distribution is enhanced by the variation of break time with momentum [89].

The small offset from $\langle\rho\rangle$=0 is attributed to a small asymmetry in the initial momentum distribution, a systematic error in locating the centre of mass, or slightly misaligned kicking beams.

Also shown in figure 6.12 are the data from a numerical simulation shown in green (courtesy of Matthew Isherwood [82]). The agreement with the period is excellent, but there is a significant discrepency with the magnitude of the experimental result. This is not surprising given the approximations

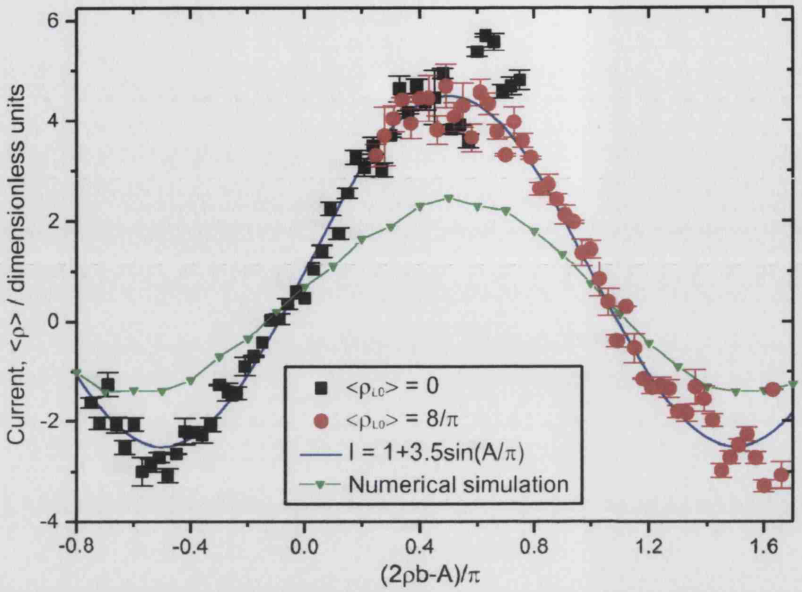

Figure 6.12: Results of the accelerating lattice experiment: graph to show the current I_r versus $(2\rho b - A)/\pi$. Results for the two values of the starting momentum, $\langle \rho_{L0} \rangle = 0$ and $\langle \rho_{L0} \rangle = 8\pi$ are shown in black and red respectively. The blue fit is the function $I_r = 1 + 3.5\sin(A/\pi)$. The green plot is the result of a numerical simulation.

that are made to simplify the numerical simulation. The numerical code considers the evolution of one (approximately) Gaussian wavepacket that is narrow in position and momentum, whereas, as has been discussed previously, the distribution is indeed narrow in momentum but has a fairly broad spatial distribution. A more accurate simulation is under construction, and it is hoped that this will demonstrate an even better correspondence with the experimental results.

6.3 Conclusion

In this chapter experimental results have been presented for two techniques that achieve directed atomic transport in a fully chaotic Hamiltonian system.

In the first section it was demonstrated that using a simple asymmetric kicking sequence to break temporal symmetry introduces a cosinusoidal momentum dependence into the diffusion constant. Employing an optical lattice moving at a constant velocity the symmetry of the diffusion constant was broken and directed transport followed as a result. With this technique it was proved that the period of the modulation of the diffusion constant with respect to the scaled momentum is exactly equal to the reciprocal of the chirp parameter. The effect of varying the chirp parameter was also briefly examined and new trends have been uncovered.

In the second section the modulation of the diffusion constant was exploited once again. An alternating accelerating kicking potential was used to introduce an inertial term into the Hamiltonian which enabled an asymmetry in the diffusion constant to be realised. The results showed directed current proportional to the gradient of the diffusion constant, the phase of which was dependent on the magnitude of the acceleration and in good agreement with calculations.

The results in this chapter are available on the e-Print archive [97] and will be submitted shortly.

CHAPTER 7

Future quantum chaos experiments

As the final chapter on experiments in quantum chaos we will discuss further experiments to investigate directed transport in a chaotic system. In particular, we will examine possible experimental set-ups to realise a stable ratchet-shaped optical lattice for which a three-kick cycle must be employed for asymmetric diffusion, and a rocking potential, obtained by applying an alternating intensity gradient.

7.1 Asymmetric diffusion with a double-well potential

7.1.1 Experimental arrangement

With the correct choice of phase a double-well potential of the following form:

$$V(x) = \cos x + a\cos(2x + \Phi) \tag{7.1}$$

is an approximation (to the second harmonic) of a 'saw-tooth' potential seen in many ratchet systems.

Such a potential can be created by using the configuration shown in figure 7.1. The retro-reflected beam pair $E_{1,2}$ will, as has been seen previously, create a standing wave in the direction of beam propagation of the form $\cos(2kx)$. The beam pair $E_{3,4}$ intersecting at 60° will create a standing wave in the x-direction with twice the period, of the form $\cos(kx)$. Given that the relative phase between the potentials are correct, the resultant potential will approximate a saw-tooth surface with a period of λ as shown in the figure inset. In fact it is not quite as simple as this as shall be seen below. First, however, it should be mentioned that the beam polarisations must all be parallel. As an example they are all shown in the diagram to be out of the plane. As explained before this means that atoms in different Zeeman states have the same light shift and are hence affected by the same potential surface.

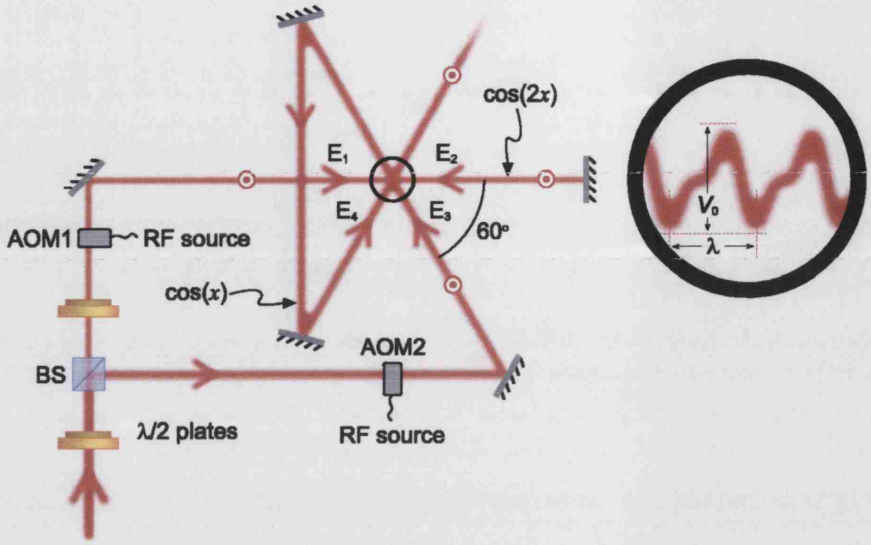

Figure 7.1: The double well lattice configuration. The beam from the Ti:Sapphire laser is split up into arbitrary proportions with a $\lambda/2$ waveplate and the beam-splitting cube BS. AOM are the acousto-optic modulators used to pulse the optical potential on and off and control the frequency of the lattice beam pairs. The four interacting beams (the two beam pairs) are designated E_1 through E_4. The second waveplate enables the beam polarisations to be made parallel such that atoms in different Zeeman states are affected by the same potential surface.

A small complication is that the optical potential is given by [98]:

$$\hat{U} \propto |E_1 + E_2 + E_3 + E_4|^2 \tag{7.2}$$

However, this results in unwanted cross-terms between E_1, E_2 and E_3, E_4. To circumvent this problem a frequency difference is applied between the beam pairs $E_{1,2}$ and $E_{3,4}$ using two acousto-optic modulators (AOM1 and AOM2). AOM1 is used to shift the frequency of $E_{1,2}$ up by 80MHz and AOM2 shifts the frequency of $E_{3,4}$ down by 80MHz. The interaction of the four beams is

averaged over a time $t = 6.25 \times 10^{-12}$s and the light field is then given by:

$$\begin{aligned} U &\propto |E_1 + E_2|^2 + |E_3 + E_4|^2 \\ &\propto a\cos(2kx + \Phi) + \cos(kx) \end{aligned} \tag{7.3}$$

where a is the relative amplitudes of the light fields and Φ is the spatial phase difference between the standing waves. For frequency shifted beam pairs and $\theta = 60°$ the desired form of the potential is thus achieved. This potential most closely resembles that of a saw-tooth if the relative amplitude $a = 1/2$ and the phase difference $\Phi = \pi/2$ (or any odd integer multiple of $\pi/2$).

It is important to note that because the periodicity of the optical structure, i.e. the characteristic length of the system, is now twice that of the simple retro-reflected beam configuration of former experiments, the scaled unit of position is now half of what it was. It can easily be shown that as a result the effective Planck's constant, and hence the kick strength for the system, are therefore four times less than before. The effects of this are discussed in the section 7.1.4.

It has been seen throughout that to achieve directed atomic transport in a fully chaotic Hamiltonian system it is necessary to break the system symmetries in some way. Here the spatial symmetry is broken by using an asymmetric optical lattice. The temporal symmetry has thus far been broken by introducing a small perturbation b into the sequence of otherwise equally spaced kicks to produce a two-period kick cycle. However, it is shown in [82, 85] that for a two-kick cycle the two-kick correlations which produce transport in the previously discussed system cancel out in the double-well

system because there is no longer an accelerating term. To achieve directed transport a kick cycle with a minimum of three periods, $N = 3$, is necessary: $T_1 = T(1+b) : T_2 = T : T_3 = T(1-b)$. In the same way the two-kick cycle was written in section 4.3, the three-kick cycle is represented by:

$$F_3(\tau) = \sum_{n=0}^{\infty} \sum_{M=1}^{3} f(\tau - nT_{tot} + \sum_{i=1}^{M} T_i) \tag{7.4}$$

This is illustrated in figure 7.2.

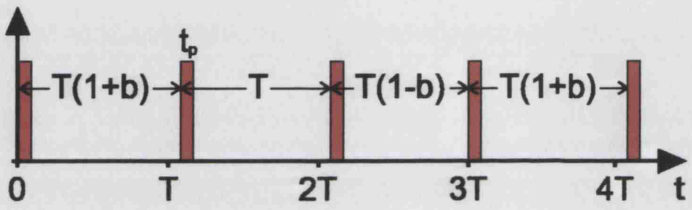

Figure 7.2: Three-period kicking cycle, $T(1+b) : T : T(1-b)$, where b is the chirp parameter

Finally, the scaled Hamiltonian for the double-well kicked rotor is written as follows:

$$\mathcal{H} = \frac{\rho^2}{2} + K\left[\cos(\phi) + a\cos(2\phi + \Phi)\right] F_3(\tau) \tag{7.5}$$

The mapping is now written:

$$\begin{aligned} \rho_{n+1} &= \rho_n + K[\sin(\phi_n) + 2a\sin(2\phi_n + \Phi)] \\ \phi_{n+1} &= \phi_n + \rho_{n+1}[1 + (j-1)b] \end{aligned} \tag{7.6}$$

where $j \in \mathbb{Z} \pmod 3$. The phase space portraits that result from these equations will be explored briefly in the next section.

In summary, it should be possible to construct a double-well potential

with which to perform chaotic ratchet experiments. The means by which the kick sequence is written and used to control the acousto-optic modulators is already in place from previous experiments. The kick strength may easily be set by changing the depth of the potential, V_0, the (average) time between kicks, T, or the kick duration t_p (recall equation 4.8). The level of quantum effects in the system may also be easily controlled with the average kick period. Thus, in principle, all of the tools to conduct a successful experiment are at hand.

7.1.2 Poincaré surfaces of section

The Matlab program to generate phase-space portraits was slightly modified to generate classical portraits for the double-well experiment with a three-kick sequence. The Poincare surfaces of section were generated by plotting 300 iterates from each point on a (5×21) grid of starting conditions: $(\phi_0^m = -\pi + 2m\pi/4,\ \rho_0^n = -n\pi/10)$, with $m = 0, 1, \ldots, 4$ and $n = 0, 1, \ldots, 20$. The portraits presented in figure 7.3 are for the parameters $b = 1/8$, $a = 0.5$ and $\Phi = \pi/2$rads, and for $K = 0.01$, 0.10, 0.50 and 2.00. It can be seen from the surfaces of section that as the kick strength is increased the invariant tori and islands break up and the system becomes globally chaotic at a value of K that is lower than that for the Standard Map. The last invariant tori breaks up at a value of K between $K = 0.10$ and $K = 0.50$, and the system appears completely chaotic for $K = 2.00$. Because the system is spatially and temporally asymmetric, the phase space is also asymmetric. This can be seen most clearly by looking at the small features at $\rho/\pi = \pm 1$ in panel 7.3(b). It is even more obvious in the phase portraits in the following figures,

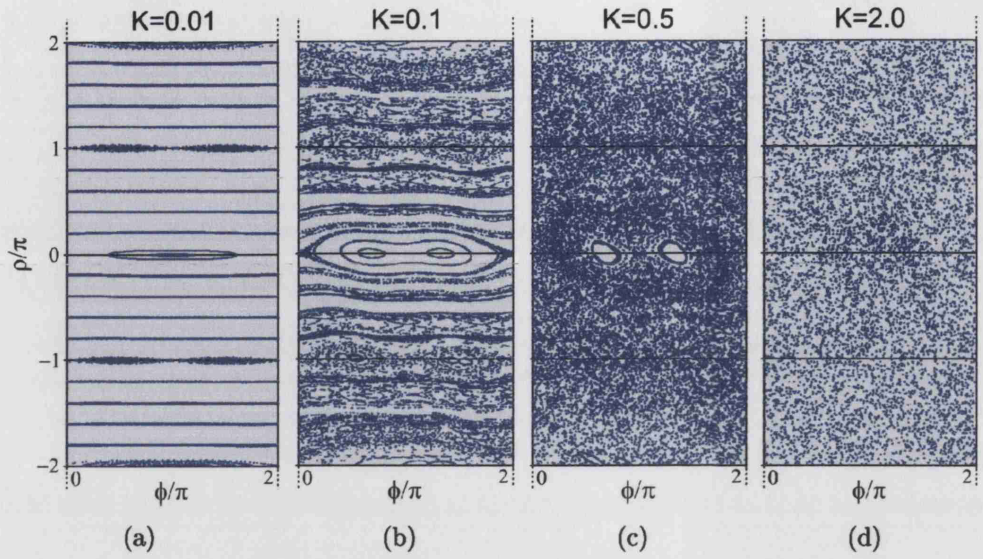

Figure 7.3: Classical phase-space portraits (Poincaré surface of sections) for the double-well delta kicked rotor for the following kick strengths (a) $K = 0.01$, (b) $K = 0.1$, (c) $K = 0.5$ and (d) $K = 2.0$. Other parameters are: $b = 1/8$, $a = 0.5$ and $\Phi = \pi/2$rads.

where the parameter b is varied and is shown to have an appreciable affect on the classical phase space.

As the chirp parameter is increased from zero to $b = 0.7$ the phase space becomes increasingly more chaotic, as was found before in the two-kick system.

Other parameters also have an effect on the nature of the classical phase space. By varying the ratio a of the two terms in the potential while keeping K constant it can be shown that one is effectively varying the symmetry of the system. As $a \to 0$ the potential becomes more like the standard map and phase space becomes more regular and symmetric.

An extensive theoretical study of the behaviour of the double-well ratchet as each of the system perameters is varied, and analytical forms for the

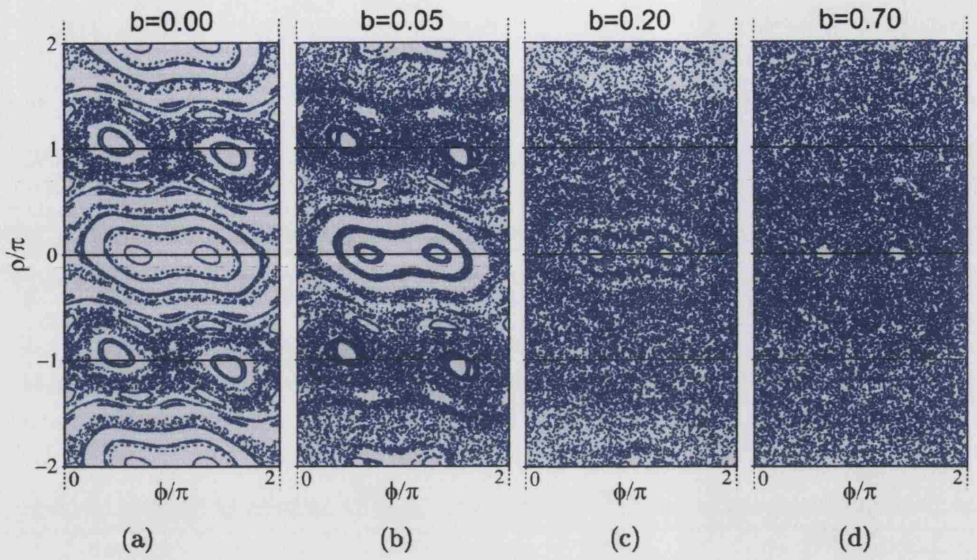

Figure 7.4: Classical phase-space portraits (Poincaré surface of sections) for the double-well delta kicked rotor for the following values of the kick parameter: (a) $b = 0$; (b) $b = 0.05$, (c) $b = 0.2$ and (d) $b = 0.7$. Other parameters are: $K_{eff} = 0.5$, $a = 0.5$ and $\Phi = \pi/2$rads.

diffusion rate and the average current can be found in [82].

7.1.3 Technical details

Phase stabilisation

For the double-well experiment two optical lattices must be superimposed with a phase difference of 0.5π rads in order for the resulting potential to best approximate a ratchet shape. As mentioned in section 5.2.3, phase noise on laser beams as a result of mechanical vibrations and air turbulence causes random fluctuations in the position of an optical potential. The relative position of the lattices must therefore be made stationary by locking their relative phase.

The relative phase of the lattice beams could be locked by using simple

interferometry if they were on constantly. Before the lattice beam enters the cell for the first time, a fraction could be taken with a beam-splitter to create a stable reference path. If, as the lattice beam emerges from the second pass through the vacuum cell, it were recombined with the reference beam (like an interferometer) a fringe pattern would be created. A phase shift in the lattice beam would then result in movement of the fringes: a shift of $\pi/2$ would make bright fringes dark and vice-versa. By monitoring a small part of the fringe pattern using a pinhole and a photodiode, small changes in phase can be detected electronically. By analysing the photodiode signal with simple electronics, the fluctuations in phase could then be actively compensated for by driving a piezo-electric driven mirror in the lattice beam arm of the interferometer. However, obvious problems would arise in keeping the phase stable from kick-to-kick as the beam is pulsed on and off. To overcome this the beam is overlapped with red light at a wavelength of 632.8nm from a Helium:Neon (He:Ne) laser. The red light is then used for the two arms of the interferometer: one that exactly follows the lattice beam and one for the stable reference path. Note that the red light does not interfere with the experiment and furthermore it may be left on constantly for the interferometric locking technique. Locking the phase of the He:Ne beams by using a piezo-electric driven mirror in the lattice-beam arm should then stabilise the phase of the lattice.

Optical configurations to implement this technique for the stabalisation of both $\cos(2kx)$ and $\cos(kx)$ components of the ratchet lattice are shown in figures 7.5 and 7.6 respectively. Note that (for continuity) the IR laser light from the Ti:Sapphire laser is drawn in red, and (somewhat counterintuitively)

the red laser light from the He:Ne is drawn in blue.

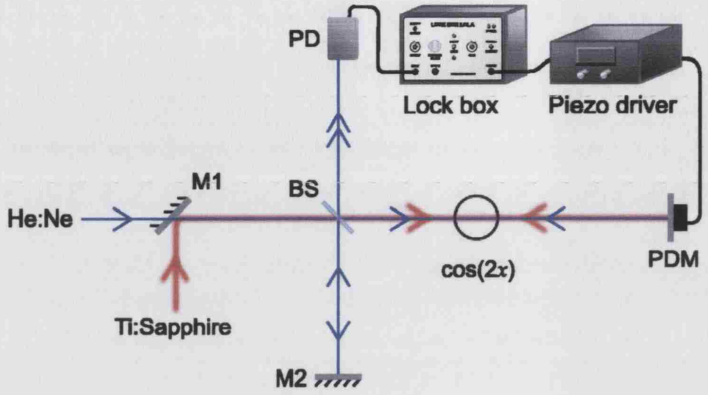

Figure 7.5: Optical configuration for locking the phase of the $\cos(2kx)$ lattice. Coated for the reflection of infra-red light, Mirror M1 is transparent to the visible light from the He:Ne laser allowing the two laser beams to be overlapped. The beam-splitter BS splits the He:Ne light into two arms of a Michelson interferometer, one of which follows the IR light from the Ti:Sapph laser (BS–PDM) and one for a stable reference path (BS–M2). Mirrors M2 and PDM are gold-coated to reflect both IR and visible light. The feedback circuit monitors the fringe pattern with a photodiode (PD) and drives the piezo-electric driven mirror PDM to actively compensate for phase jitter.

The mirrors labeled M1 in both figures, while of the type typically used for reflecting IR light throughout the laser cooling apparatus, transmit the visible light from the He:Ne laser and allow it to be overlapped with the beam from the Ti:Sapphire laser. Mirrors M2 and PDM are gold-coated and reflect both the IR and the visible laser light with approximately 99% efficiency. One beam-splitter is used in the setup in figure 7.5 to form a Michelson interferometer with the He:Ne light. For the setup in figure 7.6, a number of beam-splitters are used to make an interferometer with the He:Ne light similar to a Mach-Zehnder interferometer.

Although not shown in the diagrams, the interference pattern is magnified with a lens and the photodetector (PD) monitors a small section of the

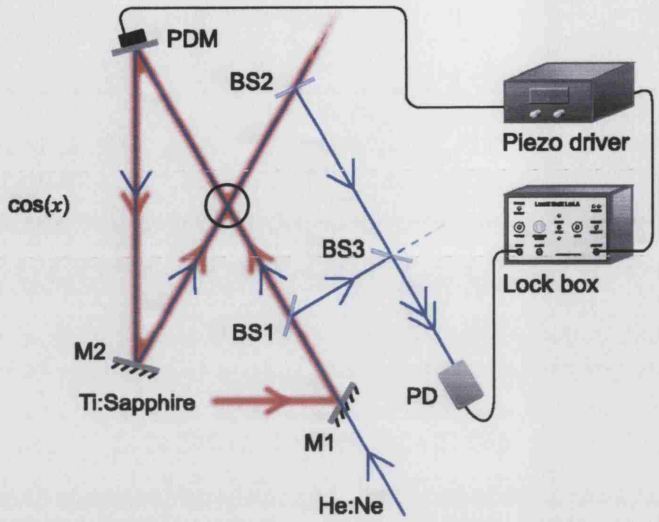

Figure 7.6: Optical configuration for locking the phase of the $\cos(kx)$ lattice. Reflection coated for the IR light shown in red, mirror M1 transmits the visible light from the He:Ne laser and mixes the two beams. The beams ghost each other around the bow-tie shaped arrangement with gold-coated mirrors M2 and PDM. Beam splitters (BS1, 2 and 3) are used to form a interferometer with the visible light to monitor the phase of the longer arm with reference to the phase of the light in the short, stable arm (BS1–BS3). The feedback circuit monitors the fringe pattern with a photodiode (PD) and drives the piezo-electric driven mirror PDM to actively compensate for phase jitter.

enlarged pattern through a pinhole. The homemade photodectectors each house a VTB8440B EG & G Vatec photodiode from RS. They have a peak spectral response at 580nm with a spectral response range from 330nm to 720nm. The diodes are operated under reverse bias for optimum response in a simple op-amp circuit that produces approximately $10\text{V}\mu\text{W}^{-1}\text{mm}^{-2}$. The signal is then sent to a homemade 'lock box'. The aim of the lock box is to monitor the signal from the photodetector and output a 'feedback' voltage to control the piezo-electric driven mirror (PDM) to actively compensate for any changes in intensity.

For far better mechanical response, homemade PDMs were replaced by

Str-35 Piezomechanik[1] actuators that travel 6μm with a maximum operating voltage of 150V. These are not driven directly from the lock box but via a MDT690 Thorlabs[2] piezo-electric driver. The lock box feeds the external input of the piezo driver which supplies an adjustable offset voltage (typically set to 50V to allow positive and negative feedback without distortion at the 0V and 100V rails) plus 10V to the PDM for every 1V from the lock box.

The developed circuit diagram for the lock box is shown in figure 7.7. The circuit uses two LF347N ICs, quad op-amp packages which save space.

The first module is an offset adder. This is to add an offset to the fluctuating signal from the photodiode so that it dithers about 0V. A switch allows the offset to be set to zero (bypass) for calibration purposes. The second module is a variable low-pass filter. Because the PDM can only be driven up to frequencies of around 10kHz it is pointless to try and compensate for changes in voltage (phase) that are any faster. The only caveat with simple low-pass filters such as this is that they can incur time-lag. The third module in the circuit is a non-inverting unity-gain buffer. This protects the value of signal amplification/attenuation in the fourth module from the variable RC value of the filter. The external potentiometer in the feedback loop of the op-amp of the 'gain' module scales the signal by a variable factor from approximately $0.05 \rightarrow 5$. The fifth module is the all-important unit that integrates the signal to provide a feedback voltage. This not only gets larger with signal deviation from zero (phase change), but also with time. Integration is started by opening the 'reset' switch, and is reset/turned off by

[1]Piezomechanik GmbH, Berg am Laim Str. 64, D-81673 Munchen, Germany, www.piezomechanik.com

[2]Thorlabs Ltd. 1 Saint Thomas Place, Ely, Cambridgeshire, CB7 4EX, UK, www.thorlabs.com.

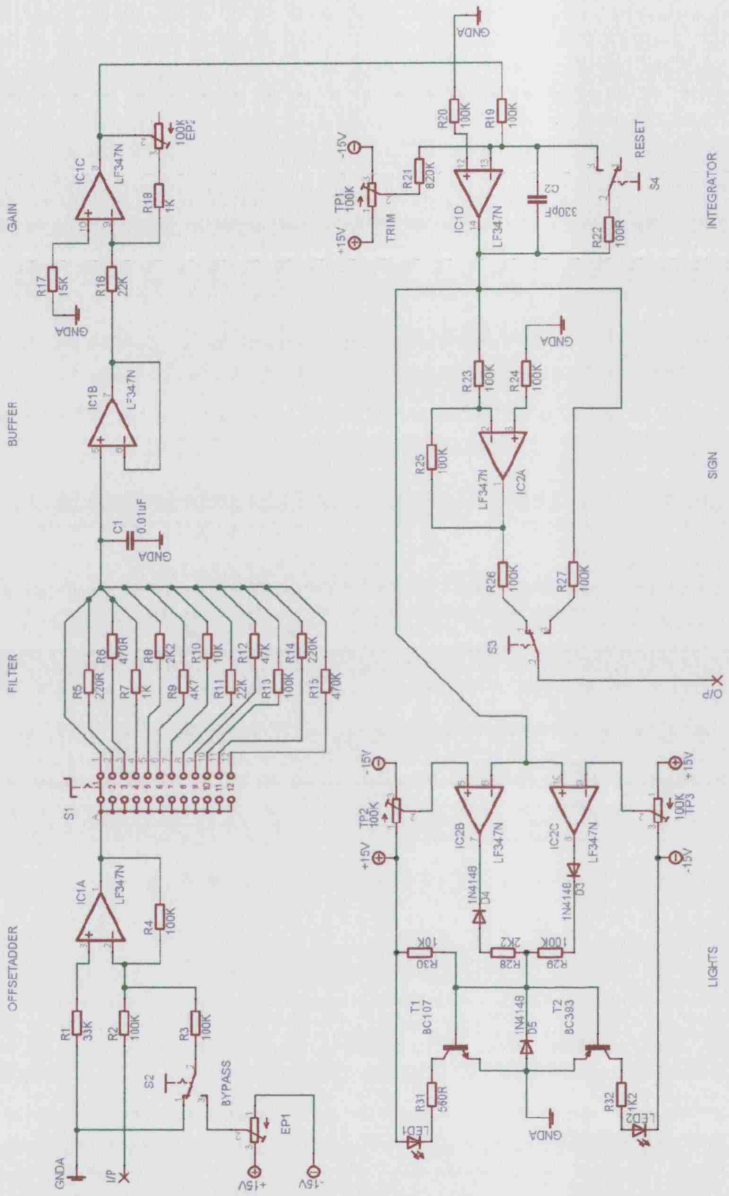

Figure 7.7: Schematic of the electronics for locking the phase of an optical lattice by monitoring interference fringes and actively compensating for phase jitter by driving a piezo-driven mirror. The input signal I/P is from the photodetector. The circuit will accept a maximum voltage input of just under 15V, but typical values from fringe-monitoring photodetectors is around 1V. The output signal O/P (0-15V) feeds the external input of the piezo-electric driver.

closing the switch. A trim potentiometer enables a small offset to be added to the inverting input of the IC for calibration. The sixth module is just a unity-gain inverting amplifier. A switch is used to select the output directly from the integrator or from the inverter so that the sense of the output can be changed if necessary. The last module, a useful extra, drives red and green LEDs to indicate whether the fringe pattern is locked or not. It is a basic window switch, the upper and lower voltage limits of which are set by the trim potentiometers TP2 and TP3 respectively.

The lock box was tested with a simple Michelson interferometer setup using a He:Ne laser, a beam-splitter and two gold-coated mirrors. The He:Ne laser available was a LASOS Lasertechnik[3] LGK 7650 laser from Lambda Photometrics[4] with a maximum output power of 5mW. One of the mirrors was firmly fixed to the optical bench and the other was mounted on the piezo-electric actuator. A lens was used to magnify the circular fringe pattern and a pinhole isolated an area of the light pattern that was narrower than one of the fringes. The fringes in the pattern could be seen to move in a fairly slow and random fashion. From time-to-time they were seen to shift by up to about 5 fringes (corresponding to the relative phase in the arms of the interferometer changing by 5π, or the effective length of one of the interferometer arms changing by 2.5λ). If the beam paths were blown into, the pattern could be seen to be significantly more erratic. Knocking or vibrating the optical bench also had a significant effect on the motion of the fringe pattern. The biggest effect was observed when either of the mirror mounts were tapped.

[3]LASOS Lasertechnik GmbH, Carl-Zeiss-Promenade 10, D-07745 Jena, www.lasos.com

[4]Lambda Photometrics Ltd., Batford Mill, Harpenden, Herts, AL5 5BZ, www.lambdaphoto.co.uk

This caused the fringe pattern to vibrate very quickly such that the moving pattern could not be resolved by eye. Monitoring the bright fringes, a typical high output from the photodetector is around 10V. As the phase jitters and the fringes move, the output signal from the detector typically fluctuates around 7V by about ±3V.

After calibrating and adjusting the offset and the gain of the lock box it was successfully shown to stabilise the position of the fringes. No amount of air turbulence could be found to visibly disturb the stationary state of the fringes. Only by hitting the optical bench quite hard, or tapping either mirror mount did the lock box fall out of lock for a brief period before snapping back into lock.

By introducing neutral-density filters to attenuate the laser light the lock-box was tested under increasingly worse signal-to-noise ratios. As the fringes become dimmer, the lock box becomes less adept at keeping the fringes stationary and can be thrown by increasingly smaller vibrations. The weakest signal from the photodetector that still enabled the fringes to be stably locked was a fluctuation of approximately 0.15V about a voltage of 0.25V.

Using the phase stabilisation technique under experimental conditions will be discussed in the next section.

7.1.4 Technical difficulties

Unfortunately there were a number of experimental challenges that, in the given timescale, were not quite met for the successful demonstration of the double-well chaotic Hamiltonian ratchet. One immediate and obvious worry was that of the reduced kick strength due to the shortened measure of dis-

tance for the new system. Another concern was, as mentioned, the stabilisation of the phase of the two lattice components that is necessary to obtain a stationary, isotropic ratchet-shaped potential. The last major consideration is the accuracy by which the 60° angle of the intersecting beams for the $\cos(kx)$ component of the potential must be set to obtain a uniform potential surface across the cold-atom region. Discussions of each of these issues are presented below.

Maximum kick strength for the double-well kicked rotor

It was shown in section 7.1.1 that because of the difference in period of the potential surface, the kick strength for the double-well experiment is only a quarter as much as that in previous experiments for a given beam intensity. Furthermore, power must be shared between the beams for each component of the lattice. The concern is that there may not be enough power available to kick the atoms hard enough so that experiments may be performed in the classically chaotic regime. Presented here is a calculation of the kick strength in the best-case scenario.

The kicking beam pairs are derived from the Ti:Sapphire laser which has a maximum output of approximately 1W. Given that the potential depth of the $\cos(kx)$ lattice must be twice that of the $\cos(2kx)$ lattice for the best shaped ratchet, the beam is split into two paths with an approximately 2:1 ratio of power between them. A maximum power of approximately 670mW is then available for the $\cos(kx)$ lattice, which becomes attenuated to approximately 470mW due to the efficiency of the AOM. The beam diameter is approximately 1.3mm, the minimum acceptable detuning is 1000 linewidths,

and so for typical values of the kick period and kick duration ($T = 9.47\mu$s and $t_p = 379$ns) this corresponds to a maximum kick strength of approximately $K^{max} = 3.7$ for the $\cos(kx)$ lattice. It is shown in [87] that the effective kick strength for the double-well lattice is given by $K_{eff} = K\sqrt{1+4a^2}$. Again, $a = 1/2$ for the best shaped potential surface and so the maximum effective kick strength for the double well potential is approximately $K_{eff}^{max} = 3.74$. Compared to a maximum kick strength of approximately $K^{max} = 16$ for the symmetric potential of previous experiments, the reduced kick strength available for the double-well experiment somewhat limits the accessible range of parameters. However, we saw in the previous section that phase space for the double-well kicked rotor is completely chaotic with, for example, $b = 0.7$ and $K = 0.35$ or $b = 0.125$ and $K = 2$. To explore asymmetric diffusion in a fully chaotic system should therefore be possible with parameters suggested by [87] (i.e. $K = 2$, $b = 0.1$). This is, however, provided that the Ti:Sapphire laser is working well and that the detuning is set to 1000Γ. To perform experiments with lower scattering rates, the detuning may be increased but only by a small amount because the kick strength becomes too weak. This may be compensated for by increasing the kick duration (although care must be taken such that the momentum boundary does not become too low) or by increasing the kick period (which will affect $\hbar_{eff}$).

In summary, to achieve desirable kick strengths in the double well kicked rotor experiment should be possible but the range of accessible parameters would be limited.

Phase stabilisation

Locking the phase of the IR kicking beams using the closed-loop interferometric technique proved to be a very difficult task. Unfortunately a lot of optical losses were incurred by the He:Ne laser light. To begin with the standard mirrors coated for the reflection of IR light that were used to overlap the Ti:Sapphire and the He:Ne beams (see figures 7.5 and 7.6) only transmit approximately 70% of the visible He:Ne light. Furthermore even greater losses were suffered at each air:glass interface at the vacuum cell. The cell has a dichroic anti-reflection coating for IR and is not designed for the optimum transmission of visible light. To make matters worse, the beam-splitters were fashioned from thin pieces of regular glass. Due to the losses this imposed on the kicking beams this also exacerbated concern over the kick strength.

As a result of the losses to the visible light the fringe patterns were very weak with a low signal-to-noise ratio. Because the resultant photodetector signals were so weak, and the signal-to-noise ratio high, the lock box was unable maintain a steady fringe pattern.

It may be practicable to overcome this problem by using more suitable optics. It should be possible to obtain a mirror that reflects IR light with great efficiency while transmitting the red He:Ne light with very little attenuation. This may be enough to overcome the signal-to-noise problems of phase-locking. Additionally, a higher- power He:Ne laser could be used and the locking circuitry could be improved. In conclusion, the phase-locking challenge certainly seems feasible.

Worries concerning the attenuation of the kicking beams due to the primitive glass beamsplitters could easily be thwarted by using beamsplitters that

reflect the red He:Ne light well and efficiently transmit the IR light.

Beam angle tolerance

It was shown that the lattice beams for the $\cos(kx)$ component of the optical potential must be at 60° in order for the period to be half that of the $\cos(2kx)$ component. Any deviation from exactly 60° and the period would not be exactly half that of the $\cos(2kx)$ component. This would result in the symmetry of the potential varying with position. The short calculation below determines the beam angle tolerance necessary to maintain the symmetry of the potential for a distance greater than the width of the cloud of cold atoms.

If the angle of the $\cos(kx)$ beams (see figure 7.1) is equal to 60° plus some small perturbation δ then equation 7.3 becomes

$$\hat{U} \propto a\cos(2kx + \Phi) + \cos(kx + 2k\delta x) \tag{7.7}$$

If $2k\delta x$ changes by $\pi/2$ across the width of the cloud then the symmetry of the double-well potential at side of the cloud will be opposite to that at the other. We shall then say that we require $2k\delta x \ll \pi/2$ over the extent of the cloud. Given that the cloud is approximately 1mm in diameter and the period of the lattice is equal to the wavelength of the laser light, this corresponds to a distance that spans approximately 1000 lattice sites. The

following condition is hence required:

$$\begin{aligned} 2k\delta \cdot 1000\lambda &\ll \pi/4 \\ \Rightarrow \delta &\ll \frac{1}{8000} \end{aligned} \tag{7.8}$$

The angular tolerance must therefore be greater than approximately 1mRad. This would be very difficult to achieve without some sort of guide for the laser beams to be aligned with. A simple solution would be to make a rigid frame with accurately drilled holes in it, as shown in figure 7.8. It can

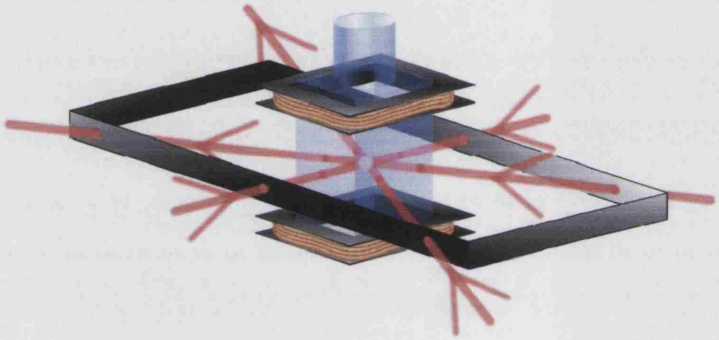

Figure 7.8: Frame for the alignment of the angular-dependent lattice beams. If the width of the frame and the position of the holes are accurate to within ±0.5mm then the frame has to be 35cm wide in order for the angular tolerance of the beams to be within 1mRad.

be calculated that if the width of the frame is accurate to within 0.5mm and the position of the holes are drilled to an accuracy of 0.5mm then the frame should be at least 35cm wide for the angular tolerance of the $\cos(kx)$ beams to be within 1mRad. The accuracy with which the frame must be constructed is reasonable and a frame this size ($\approx 35 \times 65$cm) could indeed be accomodated on the optical bench. In conclusion is is therefore plausible that if such a frame were made for the alignment purposes of the kicking

beams, then the angular tolerance would be met and the symmetry of the lattice should remain the same over the width of the cold atom cloud.

7.2 Asymmetric diffusion with a 'rocking' lattice

In section 4.5 a temporally asymmetric system was shown to produce directed motion if the spatial symmetry is broken by introducing to the potential a linear term, a potential gradient, that alternates in sign between successive kicks. For the results in section 6.2 the rocking action was produced by alternating the acceleration of the optical lattice between kicks. Proposed here is an alternative way of realising a similar system by applying an alternating intensity gradient.

7.2.1 Experimental arrangement

Consider a cloud of cold atoms subject to a pulsed stationary sinusoidal potential from the usual retroreflected beam configuration. An intensity gradient could be applied across the atoms by careful alignment of a perpendicular light field, as shown in figure 7.9. In the left inset we see the atom cloud subject to the almost linear part of the Gaussian intensity profile of the broad perpendicular beam. Given that the ac Stark shift is proportional to intensity, the resulting potential due to both light fields is a slanting sinusoid as shown in the right inset of the figure. The potential gradient can be made to alternate in sign between kicks by rocking the perpendicular beam

from side-to-side. This could easily be achieved by driving the AOM with an alternating RF source.

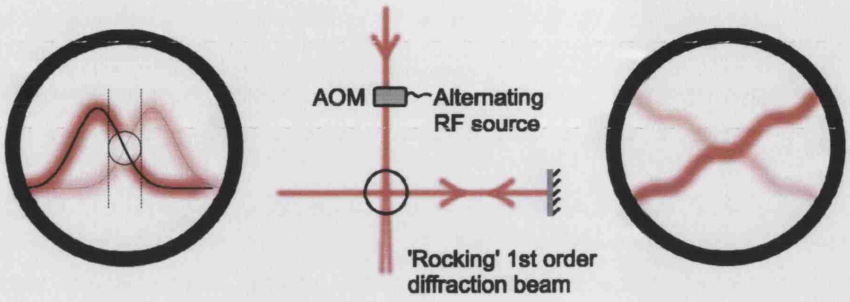

Figure 7.9: Beam configuration for the rocking lattice experiment. The beam from the acousto-optic modulator (AOM) rocks from side to side between successive kicks to realise a rocking potential as shown in the right inset.

Omitting the kicking term, the Hamiltonian for this new system includes the new potential gradient V':

$$H = \frac{p^2}{2m} + V\cos(2kx) + V'x \tag{7.9}$$

Re-introducing the two-period asymmetric kicks, the Hamiltonian in dimensionless units then becomes exactly that of equation 4.18 in section 4.5, with

$$A = \frac{\hbar_{eff} t_p V'}{2\hbar k} \tag{7.10}$$

Again, this enables the phase of the diffusion constant to be shifted by varying A: $D \propto -K^2 J_2(K)\cos(2\rho b - A)$. Maximum asymmetry is thus expected when $A = n\pi/2$, where n is any non-zero integer.

7.2.2 Feasibility

To check whether this experiment is feasible it is vital to calculate how much power is required in the rocking beam to produce directed transport. For this it is first necessary to calculate the required size of the rocking beam before looking at the light shift and calculating the necessary intensity.

Ideally the beam should be aligned such that the cloud of atoms is centred at the position of maximum intensity gradient and that the intensity gradient only changes by a small percentage across the width of the cloud. It is assumed that the beam intensity has a Gaussian profile with a central maximum intensity I_o and $\frac{1}{\sqrt{e}}$ width w:

$$I(x) = I_0 e^{-x^2/2w^2} \tag{7.11}$$

It can easily be shown that the maximum intensity gradient is located at $x = \pm w$, and that the maximum gradient is given by

$$I'_{max} = \left.\frac{dI(x)}{dx}\right|_{x=w} = \pm\frac{I_0}{w\sqrt{e}} \tag{7.12}$$

By expanding the intensity gradient (the first derivative of equation 7.11) with a Taylor series about $x = w$ and to second order in x gives the following approximation:

$$I'(x) = \frac{dI(x)}{dx} \approx \frac{I_0 x}{w^2\sqrt{e}}\left(\frac{x}{w} - 2\right) \tag{7.13}$$

To find the range about $x = w$ over which the gradient deviates from the maximum gradient by a certain fraction γ, simply equate equation 7.13 to

the product of $(1-\gamma)$ and equation 7.12. Solving the quadratic gives:

$$x_\gamma = w(1 \pm \sqrt{\gamma}) \tag{7.14}$$

It is estimated that a 10% variation in the intensity is acceptably small. By putting $\gamma = 0.1$ into the above equation it is calculated that this corresponds to a range about $x = w$ of $0.64w$. After kicking, the expanded cloud of atoms is typically around 2mm wide. The $\frac{1}{\sqrt{e}}$ width of the rocking beam must therefore be at least 3mm.

Now consider the light shift V_r caused by the rocking beam. For a detuning much greater than the natural linewidth, $\Delta \gg \Gamma$ it is given by:

$$V_r = \frac{\hbar(I/I_{sat})\Gamma}{8(\Delta/\Gamma)} \tag{7.15}$$

Using equation 7.11 this can be re-written as:

$$V_r(x) = \frac{\hbar\Gamma}{8(\Delta/\Gamma)} \frac{I_0}{I_{sat}} e^{-x^2/2w^2} \tag{7.16}$$

Proportional to the beam intensity, the light shift also has a gaussian form:

$$V_r = V_0 e^{-x^2/2w^2} \tag{7.17}$$

where V_0 is the on-axis light shift and w is the width of the distribution. By comparison with 7.16 the maximum light shift is thus:

$$V_0 = \frac{\hbar\Gamma}{8(\Delta/\Gamma)} \frac{I_0}{I_{sat}} \tag{7.18}$$

Next consider the energy gradient. With the same form as I'_{max} in equation 7.12, the maximum energy gradient can easily be shown to be:

$$V'_{max} = \left.\frac{dV(x)}{dx}\right|_{x=w} = \frac{V_0}{w\sqrt{e}} = \frac{\hbar\Gamma}{8w\sqrt{e}(\Delta/\Gamma)}\frac{I_0}{I_{sat}} \tag{7.19}$$

Another way to obtain the maximum energy gradient is to equate equation 7.10 to $\pi/2$ (for maximum asymmetry of the diffusion constant) and rearrange for V'_{max}:

$$V'_{max} = \frac{\pi\hbar k}{\hbar_{eff}t_p} \tag{7.20}$$

From equations 7.18 and 7.20 one finds that the on-axis intensity necessary to obtain maximum asymmetry of the diffusion constant is:

$$I_0 = \frac{8\pi k w\sqrt{e}(\Delta/\Gamma)I_{sat}}{\hbar_{eff}t_p\Gamma} \tag{7.21}$$

Since the power of a Gaussian beam is $P = 2\pi w^2 I_0$, the beam power necessary to maximise the rocking ratchet effect is finally estimated to be:

$$P = \frac{32\pi^3 w^3\sqrt{e}(\Delta/\Gamma)I_{sat}}{\hbar_{eff}\lambda t_p\Gamma} \tag{7.22}$$

By substituting the appropriate values for the parameters it is found that the required power is much larger than currently available in our set-up.

7.3 Summary

In this chapter we have discussed two future experiments to investigate directed transport in a chaotic Hamiltonian system. We have made a detailed

description of the necessary experimental set-ups and have discussed techniques to overcome experimental difficulties.

CHAPTER 8

The design and construction of a scanning beam laser tweezers

To complement the experiments with cold atoms in a pulsed far-detuned optical lattice it was thought that an optical tweezers could be built to perform experiments with microspheres in a pulsed optical potential. While the former has been focusing on asymmetric diffusion of a quantum system in the classically chaotic, non-dissipative regime, the latter could be used to investigate asymmetric diffusion of a classical macroscopic system in a heavily damped system. For example, laser tweezers were used in [8] to realise an optical thermal ratchet, and more recently in [99] to realise the rocking ratchet. Optical tweezers can be very versatile and it is planned to use the apparatus to diversify into biological applications. A review of the biological applications of optical forces can be found in [56].

This chapter discusses preparatory considerations that were made and the design and construction of the scanning beam optical tweezers.

8.1 Design considerations

The design and construction of any laser tweezers is an essential part of their operation, performance, versatility and efficiency. There are a handful of alternative ways that optical tweezers can be configured with any of the many combinations of different composite parts. It was essential to design with the experimental objectives in mind, but at the same time it was important to choose apparatus that would give the experiment the versatility to allow future exploration in other directions. It was also necessary to keep an eye on costs by making use of the equipment already available in the lab.

Design criteria are that the tweezers must be able to trap multiple objects, that the traps can be moved around independently in at least two dimensions, and that they facilitate the generation of tailored optical potentials, that is the ability, for example, to create a ratchet-shaped potential surface.

8.1.1 Methods for multiple trapping

This section discusses methods by which multiple particles can be trapped simultaneously and methods for rapidly scanning the laser beam for 'time-shared' multiple trapping.

Multiple beam trapping

Although costly, multiple tweezers could be constructed by simply increasing the number of laser light sources. The beams could be combined into a common optical path using polarising beam splitting cubes (each working as a beam merging cube). Prior to merging, using suitable beam-steering optics would allow each beam to be controlled individually for independently steerable traps. For multiple trapping experiments that are power hungry, this method has the advantage that each trap has access to the full power of each laser source. For lesser power-demanding tasks, a single light source could be split into two (or more) "arms" using refractive optics [100]. A beam splitter could be used to split the beam up into two orthogonally polarised beams which could then be individually controlled and merged as before. This approach becomes cumbersome for more than a few traps.

VCSEL array trapping

A very different technique to generate multiple-beam optical tweezers uses a vertical-cavity surface-emitting laser (VCSEL) array [101]. VCSELs, developed for telecommunication applications, are compact semiconductor micro-laser diodes that boast low threshold current, high efficiency, high-speed direct modulation, low cost, very low divergence and very symmetrical beams. Adapted for use in optical trapping, each VCSEL in an array can be controlled independently to achieve manipulation of multiple micro-objects by control of the spatial and temporal intensity distribution. The advantages of VCSEL array trapping appear to be in the compact hardware and simple control method. However, it would seem that independent manipulation of

particles in all dimensions may prove difficult to achieve.

Interferometric trapping and holographic optical tweezers

Another technique, ideal for multiple trapping in two or three dimensional regular arrays, is interferometric trapping. The method exploits interference patterns of Laguerre-Gaussian (LG) light beams [102] to create and rotate three dimensional trapped structures within an optical tweezers setup. The LG laser beam is generated from a holographic element. The interferometric pattern between two annular laser beams can be rotated controllably and continuously by introducing a frequency difference between the two beams. Rotating beams can also be created by interfering a Laguerre-Gaussian laser mode with a Gaussian laser mode [103]. The number of arms in the resultant spiral interference pattern can be tailored to fit the shape of the sample to be rotated. It is now possible to orient two, separately trapped particles and then dock them together in lock and-and-key assemblies. However, the structures adopted by the particles or the tailored traps are still essentially limited to simple interference fringe patterns.

As this trapping technique has developed, static glass holograms have been replaced with computer-generated holograms (CGH) encoded onto a spatial light modulator (SLM) [104]. Although capable of independent positioning of individual beams, real-time CGH-based manipulation of individual particles is limited because of the complex computation process involved and associated diffraction losses.

An even newer technique, and probably the most powerful approach to date, uses an optically addressed phase-only SLM to encode patterns directly

into the light. The phase-encoded information serves as the input for a generalised phase-contrast system in which a phase-contrast filter generates an intensity pattern of very high contrast. The combined benefits of the phase-only SLM and the straightforward phase-encoding procedure result in a efficient, real-time, individually addressable tweezer-beams [105].

Time-sharing trapping

An alternative approach that does not limit trapping patterns is a time-sharing method [106]. The key to this technique is the rapid and repetitive scanning of one focussed trapping beam between a set of positions in the plane of the sample. As a result of the damped motion of the particles due to the viscous drag of the suspending medium, if the scanning is fast enough the particles cannot follow the path of the trapping beam in between trap sites. Instead, the rapidly "blinking" individual traps mimic the effect of steady illumination, resulting in the steady trapping in all the positions at once. Trap sites with greatest potential depth are found where the scanning beam resides for longest. The potential depth could also be modulated by varying the laser intensity around the scanning path. Depending on the type of laser, this could readily be done by adjusting the operating current (easy with diode lasers) or by synchronising the scanning with the rotation of a neutral density filter wheel. The number of trapping sites is only limited by the power of the laser source and, unfortunately, the effective stiffness of each tweezing site is correspondingly diminished because of the reduced duty cycle. The steering or scanning of the laser beam can be done by various methods discussed in the next section, all of which can be computer controlled. The

shape of each trap or the configuration of traps and the ability to manipulate each trap individually or as a whole is only limited by the scanning control program.

8.1.2 Methods for beam steering

Unlike the holographic and VCSEL array trapping techniques, the multiple beam and time-sharing trapping methods are mechanically dependent and require exceptionally well-controlled beam deflections with accurate reproducibility. Presented here is a discussion of various computer-controllable beam steering alternatives.

Scanning galvanometer mirrors

The main advantages of moving magnet or moving coil galvanometer driven mirrors (SGMs) include very large deflection angles (commonly 40 degrees), negligible optical losses and low cost. Because they can have a very high torque-to-inertia ratio, the fast acceleration leads to step response times that can be as low as 0.3 ms. This is fast enough to produce multiple alternating traps but with relatively low roll-off frequencies (in the order of a few hundred Hz). Although without active feedback stabilization schemes the wobble, jitter, and repeatability figures (between 5 and 20 μrads) may not be good enough for tweezers that require nanometer-level positional stability, it should certainly be good enough for micrometer stability. SGMs can be very small and compact devices that are easy to operate (linear response to control voltage). Because the mirror is attached to the rotation shaft of the galvanometer actuator they provide only a single axis of rotation. A pair of

scanners, positioned to scan in perpendicular axes, is necessary for bi-axial beam-steering. Unfortunately this means that the pair, which should ideally only produce an angular displacement, can also produce a linear displacement because the rotation axes are not coplanar. This "displacement jitter" is minimised by keeping the scanner separation as small as possible or using optics to image the surface of the first scanner on to the second.

Galvanometer technology is well established and SGMs are readily available [107].

Piezoelectric actuated mirrors

Piezo-actuated mirrors are capable of producing extremely small and precise motions, they offer high response speeds, negligible optical losses and are capable of moving fairly large optics. They can offer two degrees of motion, therefore avoiding the displacement jitter inherent in glavanometer scanners. However, the major limitation of piezo-actuated mirrors is their severely restricted angular range which is typically in the order of a milliradian.

Fast steering mirrors

Fast steering mirrors (FSMs) offer bi-axial, high-bandwidth rotation with sub-microradian resolution [56]. Voice coil actuators, mounted behind or to the side of each quadrant of the mirror, work in push/pull pairs to produce orthogonal rotation. In most implementations the mirror pivots about the center of its front surface, making it a true gimbal mount. As a result, FSMs also avoid the displacement jitter found in a dual XY galvanometer scanner. The high force generated by four actuators enables them to move relatively

massive optics at high speed, while still maintaining excellent positional resolution and a large angular range (typically 60 *m*rads).

Acousto-optic modulators

In an acousto-optic modulator (AOM) the light is deflected by passing it through an acousto-optic crystal. Acoustic waves at ultrasound frequencies are generated by a piezoelectric crystal and applied across the crystal to create a density grating which diffracts the light. The deflection angle of the first order light is given by $\theta = \lambda f/v$, where λ is the wavelength of the incident light, f the acoustic wave frequency and v is the velocity of the sound wave. By tuning the acoustic frequency the angle of deflection and hence the position of the tweezers can be set. The tellurium oxide devices available in the laboratory operate within ±20MHz around a nominal centre frequency of 80MHz. This corresponds to an 8*m*rad deflection of the first order light (since v for $TeO_2 = 4.26$ km/sec).

The rise time of the AOMs is in the order of 100 ns, and the external modulation frequency range goes up to 2 MHz. This would give plenty of scope for multiple alternating traps with a high roll-off frequency.

The big disadvantage of using AOMs is the loss of light due to the low diffraction efficiency (the diffraction efficiency into the first order has been found to be around 65 percent [108, page 49]). This effect is exacerbated as two orthogonally mounted devices need to be used in series to achieve x and y deflections. Also, the diffraction efficiency varies over the acoustic bandwidth resulting in a variation in transmitted light levels for different beam deflections. Although this could be compensated for it would add

another degree of complexity to the computer control program.

Electro optic modulator

In an electro-optic modulator (EOM) the light is deflected by passing it through an electro-optic crystal. An applied electric field generates a linear refractive index gradient across the crystal that bends the light. The deflection angle is given by $\theta \propto LV/a^2$, where L is the length of the cell, V is the applied voltage, and a is the aperture diameter. The advantage of using an EOM is that the switching time is roughly 100 ns, far faster than any mechanically driven mirrors and faster than our AOMs. Also, the beam-angle stability, dependent mainly on the supply voltage noise levels, should be good enough for nanometer-level stability and the optical throughput is 90%. Unfortunately, EOMs can be large and the maximum angle of deflection of most EOMs is just 2 mrad: not enough for most applications.

8.2 Experimental design and setup

This first part of this section describes the apparatus used to construct the optical tweezers and briefly discusses why such apparatus was chosen. We then summarise the most important points made in the theory section (section 2.6) before discussing the optical setup in detail.

8.2.1 Apparatus

Laser diode

Optical trapping can be achieved using a large variety of CW lasers and laser diodes. Living specimens absorb light most weakly in the near infrared, so trapping lasers used for biological work are typically in the 800 to 1100 nm wavelength region to minimise photodamage. The laser available in the laboratory contained a laser diode, the SDL-5412-H1, from the SDL-5400 series[1]. This has a centre wavelength of 852 ± 4 nm, a maximum output power of 150 mW (at an operating current of 210 mA) and operates in a single spatial, TEM_{00}, mode. It has a threshold current of 14 mA, after which its power output goes up linearly with the driving current (see appendix C.2). The diode is mounted in a housing with a collimation lens on a very sturdy base plate. The containing box also houses an anamorphic prism pair that is used to turn the elliptical output from the laser diode into a Gaussian beam of roughly circular cross-section.

Figure 8.1 shows the mount and housing for the laser diode with the protective cover removed. In the eventuality of a voltage surge or reverse current across the diode a simple protection circuit is wired to the diode. To drive the diode an off-the-shelf power supply and temperature controller were purchased from Newport[2]. The Newport 505 Laser Diode Driver gives the diode an extra level of protection: redundant FET and relay shorting circuits and a slow turn-on sequence that gradually ramps the current up to operating level. It also offers an external analogue input which allows the modulation or

[1]SDL, Inc. 80 Rose Orchard Way, San Jose, CA 95134-1356, USA
[2]Newport, 1791 Deere Ave. Irvin, CA, 92606, www.newport.com

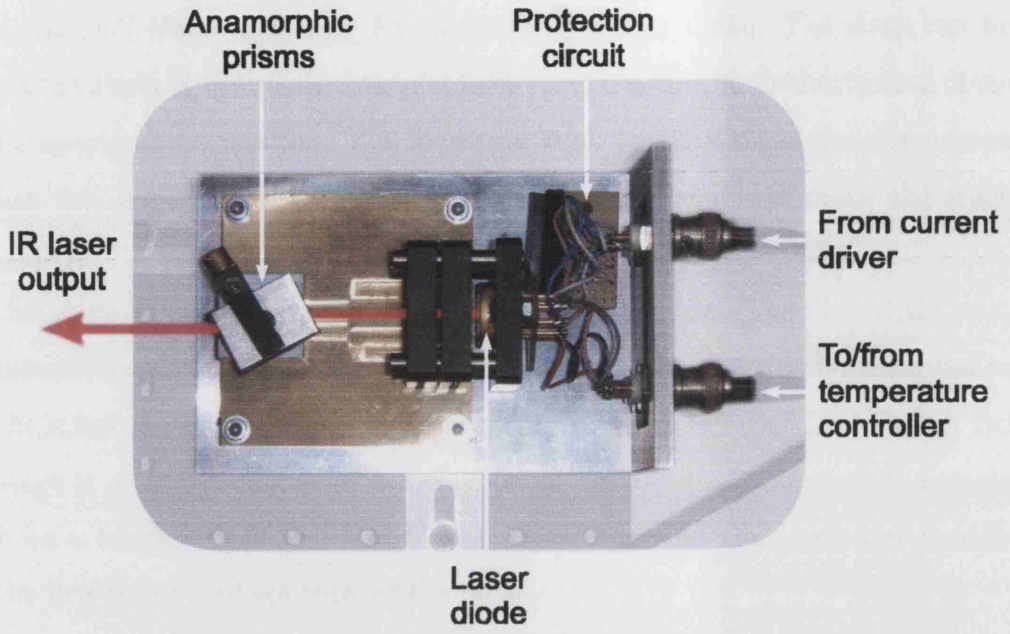

Figure 8.1: Laser diode setup used with laser tweezers

the remote control of the diode driving current by a external voltage (from DC to 500 kHz). The Newport 325 Temperature Controller monitors the diode's internal thermistor and adjusts the diode's in-built peltier element accordingly.

Microscope

The microscope available was a Galen III Compound Microscope made by Leica[3]. It is a traditional upright microscope with a tube length of 160mm. It is fitted with a trinocular head for the attachment of a CCD camera and was supplied with four objectives of different magnification. The microscope has

[3]Leica Microsystems (UK) Ltd, Davy Avenue Knowlhill, Milton Keynes, MK5 8LB, Bucks, UK, www.leica.com

a standard stage with a jig for clamping specimen slides. The stage can be moved finely in the vertical axis for focus, and coarsely in the horizontal plane for specimen translation. The focussing knob on the side of the microscope has two levels of adjustment. The coarse adjustment can move the stage through its entire range in under one revolution. It has no scale and moves the stage by approximately 20 cm in half a revolution. The fine adjustment moves the stage by 200 microns per revolution. It has a 1 micron scale and so the stage can be positioned to an accuracy of half a micron. Underneath the stage is a simple condenser which collects light and illuminates the sample from a tungsten halogen lamp. The adjustments on the condenser modify the brightness and contrast of the image.

Objectives The four objectives have magnifications of ×4, ×10, ×40 and ×100, and are all corrected for use with a 0.17mm cover slide. They are designed to operate in air, apart from the ×100 oil-immersion objective, which is designed to operate with a drop of specialized hydrocarbon-based oil between it and the cover slide. As plan achromat objectives they have a level of image correction higher than the least expensive (and most common) achromat objectives. This means that they are corrected for axial chromatic aberration in two wavelengths (at about 486 and 656 nm), which are focussed to the same point. They are corrected for spherical aberration in the green (546 nm), and in addition to achromats they provide flat-field corrections.

As has been said before, objectives with the highest numerical aperture create the strongest optical traps for dielectric particles. Some objectives are designed to be used with an immersion medium, such as water, oil or

glycerin, because it can dramatically increase the numerical aperture. This is because by using an immersion medium with a refractive index similar to that of a glass cover slip, rays of wide obliquity no longer undergo refraction and are more readily grasped by the objective. Also, image degradation due to thickness variations of the cover glass are practically eliminated.

The numerical aperture, NA, is the product of the sine of the angular aperture θ, and the refractive index, n, of the immersion medium:

$$\mathrm{NA} = n(\sin(\theta)) \tag{8.1}$$

The angular aperture of an objective is the maximum angle of image-forming light rays emanating from the specimen that the front lens of the objective can capture when the specimen is in focus. It has a practical upper limit of about 72 degrees. The value of n varies from 1 in air to 1.52 for most immersion oils. NA values are as small as 0.1 for very low magnification objectives (×1 to ×4), are lower than 1.0 for dry objectives, and are as much as 1.6 for high-performance immersion objectives. A very good source of information about objectives can be found in [109].

Our ×4, ×10, ×40 and ×100 objectives have a numerical aperture of 0.1, 0.25, 0.65 and 1.25 respectively. For best results, the ×100 oil-immmersion objective is chosen for optical trapping. The immersion oil used with our objective has a refractive index of 1.51.

Traditionally, microscope objectives were designed to operate at finite conjugates, producing an image of the sample plane at an arbitrary distance (typically 160mm) away from the back aperture of the objective. The only additional optic required for designs like this is an eyepiece or a camera, but

careful consideration must be taken if additional filters or light sources are to be incorporated. It is now common for objective lenses to produce an image at infinity. Such infinity corrected objectives necessitate the use of an additional tube lens to create an image, but the advantage is that there is no longer a restriction on the length of the optical system. This is particularly useful for laser tweezers since the focus of a collimated injected laser beam will fall on the sample plane (assuming the axial chromatic aberration is negligible).

Unfortunately, as a traditional microscope, the Leica Galen III uses finite conjugate objectives and the complimentary fixed tube length. Therefore care must be taken to ensure that the injected laser is focussed onto the sample plane. We shall see in section 8.2.3 that injected light at a specific angle of divergence is necessary to do this.

CCD camera and monitor

The camera is a black and white VBC-410 with a 1/3in CCD sensor made by InterM[4]. It has a Composite CCIR video output, a resolution of 768×494 pixels and a scanning frequency of 15.625kHz (H) × 50Hz (V).

The monitor is a standard 9 inch black and white Vista CCDTV supplied by RS[5]. A BNC cable is all that is necessary to connect the output of the camera to the video input on the monitor.

[4]InterM, 226-9, Dugjung-Li, Hoechun-Eub, Yangju-Kun, Kyungki-Do, Korea, www.inter-m.com

[5]RS Components Ltd. Birchington Road, Corby, Northants, NN17 9RS, UK, rswww.com

Camera attachment Depending on the model of microscope there are different ways that a laser beam can be coupled into the system for optical tweezers. Given the simplicity of our microscope, the easiest practical way to introduce the light was to modify the camera attachment to house a beam-splitting cube. This directs a horizontally incident laser beam down the trinocular head (see figures 8.3 and 8.4) while transmitting ascending light from the sample to the camera. As a traditional, fixed tube length system, the *length* of the camera attachment could not be modified for this would put the camera out of focus. The CAD design for the camera attachment modifications can be seen in Appendix C.1. It can be seen here that the length criterion is adhered to.

Laser light, scattered back from the sample, coverslip or from the slide, can enter the oculars and can also easily saturate the camera. For obvious safety reasons, special covers were placed on the eyepieces to block all emanating light (filters could have been used but the camera and TV screen make the oculars redundant anyway). An additional slot also had to be drilled into the camera attachment for the insertion of an infra-red filter (see designs in Appendix C.1). This gives the option to completely block the scattered laser light for a clear image of the sample.

Sample preparation

In the main, 2 micron polystyrene balls are used for experimentation because they have properties that are ideal for optical trapping, they are used a lot in biological applications and they are relatively cheap. They can be diluted and put into suspension in water-based solvents without sinking straight to

the bottom or floating to the top. Polystyrene has a refractive index of $n_b = 1.578 \pm 0.002$ at 852nm [110] and for water $n_m = 1.329$ at 850nm [111]. The microspheres thus have a high relative refractive index, $n_b/n_m \approx 1.2$, and are good for optical trapping.

The PS05N aqueous microspheres used in our experiment, made by Bangs Laboratories[6], come in a small container that is kept in the fridge (they should be stored at 2-8°C). They are $2(\pm 0.07)\mu$m in diameter and have a density of 1.05g/cu cm. Because they are at a concentration of approximately twenty thousand million beads per mililiter they must be significantly diluted before putting on a slide as a sample for trapping. As a rule of thumb, dilute one drop of bead solution with two or three glugs of distilled water (as a quantitative measure, one part bead solution to 125 - 150 parts of distilled water).

Using a pipette, one or two drops of diluted bead solution are put in the pit of a clean recessed microscope slide. A cover slip is gently placed on top of the solution filled recess and a lens cleaning tissue is used to mop up any excess. Regular slides with a piece of tape or film stuck to the surface are a good alternative. A hole is cut in the tape to make a reservoir for the solution on top of which a cover slip is placed, see figure 8.2.

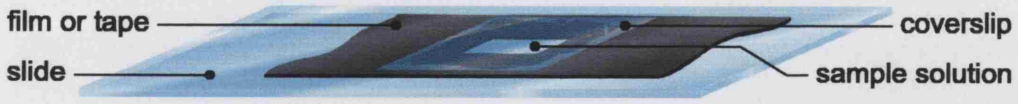

Figure 8.2: Slide preparation

Microsphere samples can coagulate and beads and clumps of beads can

[6]Bangs Laboratories Inc. 9025 Technology Drive, Fishers, IN 46038-2886, USA

stick to the slide and cover slip. These beads are called inactive because when stuck they no longer jostle around due to Brownian motion. Rarely can the inactive beads be pulled away from slide or cover slip with the tweezers. The best way to delay the onset of such an effect is to make sure everything is clean. Solutions containing soap, which was thought might stop beads sticking, do not help and can make the solution cloudy and bubbly. If the slide requires cleaning before use they are washed with a soft clean cloth soaked in water and detergent and rinsed thoroughly with water. They are then rinsed again with a small amount of distilled water and wiped with a methanol-soaked lens tissue.

Microspheres will gradually fall in solution to the bottom of the cell where they accumulate and eventually become inactive. Depending on the depth of the sample it can become completely inactive in as soon as twenty minutes. Axial trapping degrades with depth into the sample and beads can not be recovered below a certain depth. Within as little as two minutes the majority of beads can fall below this critical depth in a deep cell. For this reason when performing an experiment that requires many repetitions of the same measurement, to avoid having to re-load cells after every two or three measurements, it is useful to have a shallow cell. This allows the active beads that accumulate near the bottom of the cell to be recovered. A method adopted by [112] is to dilute the spheres in an 11% NaCl solution so that the beads come to rest just below the cover-slip surface.

It is important when performing sensitive measurements that the sample is not too turbulent. The best way to reduce turbulence is to place a tissue over the coverslip with which the edges of the coverslip are pushed down onto

the tape or thin film. This helps to keep the coverslip firmly in place and prevents fluid from escaping.

Different tapes and thin films were experimented with to compare cell depths and to see which produced the most stable samples. Table 8.1 summarises the findings.

Tape / film	Adhesive	Cell depth, D / um	Notes
Insulation tape	Self (acrylic)	140 ±15	Reliable, stable, longevity
Sellotape (polypropylene)	Self (acrylic)	90 ± 15	Reliable, stable, easy to replace
Thick mylar film	UV glue	230 ± 40	Turbulent, uneven
Thin mylar film	UV glue	10 ± 20	Turbulent
Thin mylar film	Super Glue	35 ± 12	Turbulent, dries out v. quickly

Table 8.1: Table to summarise cell depths and sample stability using various tapes and films

Insulation tape is easy to stick flat and so the cells are at a relatively uniform depth. Due to the robustness of insulation tape the cells can be re-used many times. Sellotape is also quite easy to stick flat and cell depth is fairly uniform. Because Sellotape is not waterproof, cells can only be used about three times. The water-logged Sellotape can be removed very easily. Because of the even surfaces of insulation tape and Sellotape, a pressed down cover slip will firmly stay in place, little fluid can escape and it takes a few days for the cell to dry up.

Mylar film is very tough and it can be permanently stuck to glass using a UV-curing glue. However, it is very difficult with this process to get the film to stick flat and as a result the cell depth is relatively uneven. Also, a pushed down cover slide will not make contact with the film all the way around the cut-out thus allowing fluid to escape. This makes mylar cell samples very turbulent and the cell can dry up within 30 minutes. Mylar film can be stuck to glass far more evenly with Super Glue. Although the adhesion is not very

strong (the mylar can easily be pulled away) the cells can be re-used many times with careful handling and, unlike UV adhesion, the glass slides can be re-used. Because a very thin layer of Super Glue can be applied, cells produced in this way can be very shallow. Cover slides sit far more securely on the evenly stuck film but, although this greatly reduces the turbulence, the shallow samples can still dry up within 30 minutes.

Scanning galvanometer driven mirrors

Given that the polystyrene beads are 2μm in diameter it was estimated that a scanning resolution in the sample plane of at least 0.5μm would be required. A preliminary experiment involved setting up the laser tweezers to trap one of the microspheres. Using the manual actuators on the higher periscope mirror a trapped bead can be walked about in the focal plane. Having calibrated on-screen distances using the 2μm spheres as a reference it was found that a mirror displacement of 14 arc minutes corresponds to a 6μm translation on the stage. This gave a rough estimate of the accuracy with which the scanning device must operate: it must have a repeatability of about 70 arc seconds to move the trap about with a 0.5μm resolution. Since the visible area on the CCDTV is approximately 40μm across the scanner should also have a range of at least 90 arc minutes. For suitability, versatility and for economic reasons, the obvious choice of beam scanning device is therefore the scanning galvanometer mirror (see section 8.1.2 for device comparison).

The Galvanometer Optical Scanner 6800HP, made by Cambridge Tech-

nology[7], was purchased from Laser2000[8]. The SGM is a moving magnet actuator, i.e. the rotor of the scanner is a magnet. The rotor is in suspension inside a stator coil which is glued to an iron case. This type of galvanometer allows high torques to be generated very quickly, and hence boasts short step times, because of the low electrical inductance of the magnet motor. The peak torque is only limited by the maximum stator current specification. The rms torque is limited by the maximum heat, generated from I^2R losses in the stator coil, that the scanner can conduct away. Very high levels of performance can be achieved because the peak torque limit, and the maximum power that the coil can dissipate, is very high. However, this does mean that attention must be given to the mounting of the SGM since it must provide an adequate path for conducting away this heat generated by the body of the scanner. Further details, and a good CAD drawing of a suitable mounting scheme for a single SGM, can be found in the instruction manual [113].

When the first SGM was set up and successfully scanning the optical trap in the x-axis, a second scanner (another 6800HP) was purchased for scanning in two dimensions. For obvious reasons the Y-axis scanner was supplied with a longer mirror (dimensions of X-scanning mirror: 5 × 6mm, dimensions of Y-scanning mirror: 5 × 10mm). For mounting both SGMs close to each other (to reduce displacement jitter) and in perpendicular axes, another mounting assembly was made. The CAD drawing supplied for this can also be found in the instruction manual [113]. The XY mount is designed to accept a 3mm

[7]Cambridge Technology, Inc, 109 Smith Place, Cambridge, MA, 02138, USA, www.camtech.com

[8]Laser 2000 (UK) Ltd, Britannia House, Denford Road Ringstead, Kettering, Northants, NN14 4DF, U.K., www.laser2000.co.uk

clear aperture and scan through an optical angle[9] of $\pm 30°$ in each axis. For smaller angles, the XY assembly will accept larger beam diameters.

The standard mirrors supplied with the SGMs are made from fused silica with a broad-band hard dielectric coating. They have a reflectance well above 99% for most of the laser lines from 480 to 700 nm [113]. Unfortunately, it was found that these mirrors were only 20% reflective at 852 nm. For this reason they had to be replaced with silver coated mirrors which are quoted to be 99% reflective at the IR wavelength of our diode (they were in fact found to be more like 94% reflective at 852nm). The replacement procedure is a very tricky job. The old mirrors must be carefully removed by using a soldering iron to heat up the glue that attaches them directly into the output shaft of the actuator. It is very important not to let any glue drip into the exposed front bearing of the motor. Excess glue is removed and fresh dabs of epoxy are applied to the shaft slot before fitting the new mirrors. Mirror alignment is ensured by close tolerancing of the size and position of the slot, and by a mirror alignment tool that was borrowed from Laser2000. The tool fits over the front of the motor and holds the mirror in position while gluing.

The frequency response of the SGMs was tested and found to roll off at around 1kHz. This is ample for our trapping requirements.

Drive electronics Supplied with each SGM is a servo drive circuit board which provides very fast and accurate mirror positioning. The basic operation of the servo is to take an analogue input signal and translate that into a stable and repeatable angular positioning of the shaft. It does this by monitoring

[9]The optical angle is the angular change of the beam. This is 2 x mechanical angle. The mechanical angle refers to the angular change of the scanner shaft.

the angular position of the scanner's shaft (detected by an optical sensor that is hard-wired to the position detector circuit board at the base of the scanner) and comparing this with the input signal to form an error signal. The servo then actively compensates for any error by rotating the rotor.

Each servo electronics board is tuned to the scanner's particular mirror inertia for best results. As supplied, the servo driver boards require mounting in suitable boxes and wiring to a ±28 V power supply and the input signal. The nominal input signal calibration for position out is 0.51V per mechanical degree of shaft rotation. Hence ±10.2V corresponds to a scan angle of ±20° mechanical (±40° optical). The input signal is limited to ±10.5V to keep from over-driving the scanner.

Computer control of scanning mirrors

The LabVIEW[10] graphical development environment was used to write various programs to control the operation of the two scanning mirrors and the laser power. The program drives the experiment through a 16-bit NI PCI 6733 High-Speed Analog Output expansion card. This device has 8 analogue output channels and 8 digital output channels. Through an NI BNC Connector Block, up to three analogue channels were used to feed the programmed voltage signals to both of the SGM drive electronics units and to the laser current driver external input.

The first programs written were very basic. Using one output they controlled only one SGM and had a very simple user interface. As the second

[10]Made by National Instruments (NI), National Instruments Corporation (U.K.) Limited, Measurement House, Newbury Business Park London Road Newbury, Berkshire RG14 2PS. www.ni.com

SGM was introduced it was necessary to use two channels and so the program had to be updated. Different programs, or 'virtual instruments' (VIs), were written to perform different tasks, some of which required the modulation of the laser power and so a third channel had to be programmed accordingly. Many sub-VIs were also written and integrated into the main program. For example, an automatic calibration wizard was written to speed up the calibration process necessary every time the optical apparatus was modified. Note that the program is calibrated against the size of the (2.00 ± 0.07) microspheres and the biggest source of error for most measurements stems from the accuracy to which the beads can be measured on the CCDTV screen. Taking into account the diffraction effects at the edges of the beads, their on-screen diameter is measured to be (9.00 ± 0.5)mm. When necessary, far more accurate calibration would be done by using a stage photomicrograph scale marker. They can be purchased with 1μm or 0.1μm rulings (or even 100Å rulings!) for under \$10 (for example see [114]).

As the programs evolved, the user interfaces became more sophisticated and intuitive. An example of the program and its user interfaces can be seen in appendix C.4.

8.2.2 Quick theory recap

Before going into the detail of the optical set-up, the most important points made in section 2.6 will be briefly reviewed.

- A laser beam, focussed strongly by, for example, a high powered objective, can provide a strong three-dimensional trap for dielectric particles of relative refractive index greater than one.

- Objectives with the highest numerical aperture focus light more sharply, thus creating a steeper intensity gradient and hence trap more strongly.

- The transverse trapping force is stronger than the axial trapping force because the intensity gradient is steeper in the transverse direction.

- The scattering force is in the direction of propagation of the laser light and a stable trap should exist as long as the axial trapping force is stronger than the scattering force.

- The back aperture of the objective must be filled (or even overfilled at the slight expense of the transverse trapping force) to ensure the most oblique rays are focussed onto the specimen plane thus producing a diffraction limited beam waist and the strongest axial trapping force.

8.2.3 Optical set-up

This section describes the optical manipulation of the laser beam to inject into the microscope for the maximum efficiency of the scanning optical tweezers.

The optical path includes a telescope to reduce the beam diameter for the moving mirrors and a periscope to elevate the beam to the level of the camera attachment porthole. The microscope, laser, and all the optics necessary for optical trapping were firmly mounted on a breadboard which was, in turn, securely fastened to a sturdy bench. As our practical knowledge of laser tweezers increased and as the experiment evolved from a single, stationary optical trap through a one-dimensional scanning trap to its current

state, a two-dimensional scanning trap, the optical configuration was modified significantly. Some of the earlier configurations yielded relatively poor trapping efficiencies due to, for example, configurations that made it very hard to align or those that made beam-clipping unavoidable, or because the choice of optics meant that the beam was under-filling the back aperture of the objective. The current configuration, and its careful alignment, produces the best trapping efficiency so far and the most even power distribution over the largest scanning area. A picture of the whole optical tweezers apparatus is shown in figure 8.3. An enlargement of the optics alone is shown in figure 8.4.

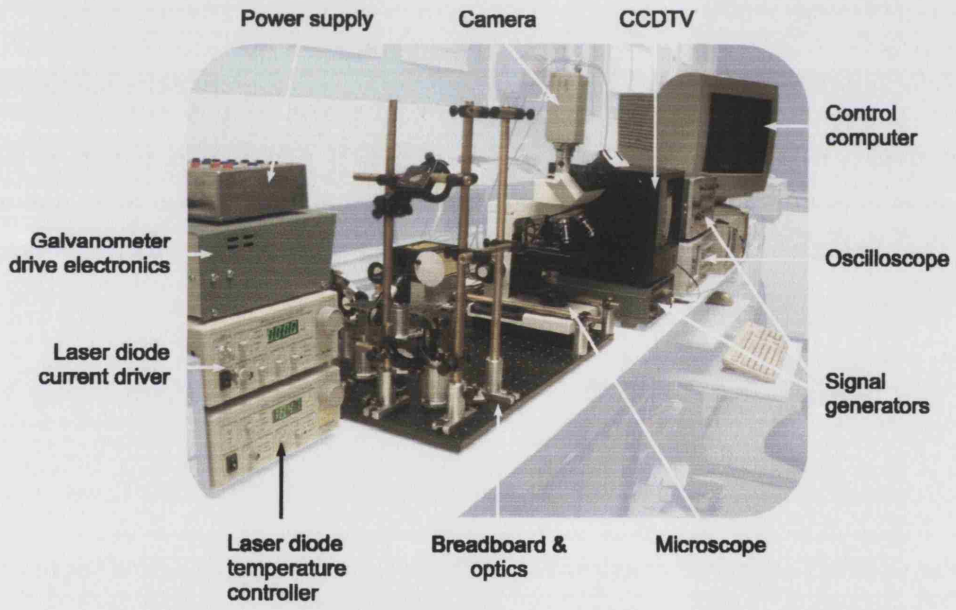

Figure 8.3: Photograph of laser tweezers setup

A schematic of the optical setup for the basic configuration is shown in figure 8.5. Following the laser output from the laser diode the first compo-

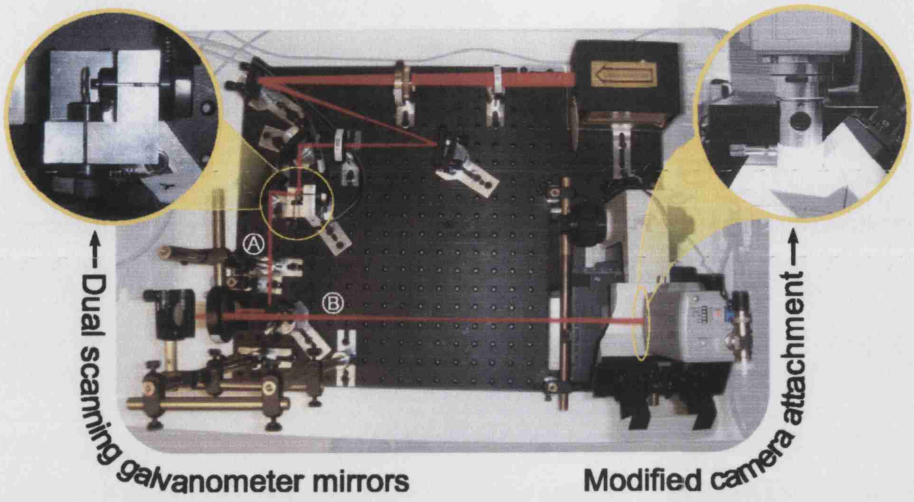

Figure 8.4: Photograph of laser tweezers optics configuration

nent in the optical path is a half wave plate, which could have been placed anywhere in the beam path. Its function is to set the polarisation of the beam so that it is reflected and not transmitted from the beam-splitting cube in the camera attachment. The second part is a telescope. This is to reduce the size of the collimated 10mm diameter laser diode output so that it does not overfill either of the 5mm wide mirrors of the SGM. Alignment of the beam onto the scanning mirrors is aided by adjustable mirrors. After the scanners a periscoping mirror pair raises the beam to the height of the porthole in the camera attachment. These mirrors are not shown in the schematic. The next optic is an "injection" lens which is essential for the operation of the tweezers. Given an infinity corrected microscope, this may not be necessary. However, since we have a traditional microscope with finite conjugate objectives and a fixed tube length (see section 8.2.1), the divergence of the injected beam has to be matched with that of the counter-propagating illuminating light.

Shown in figure 8.6 this is to ensure that the focus of the laser light is in the same plane as the optical focus. If it were not, the trapped beads would be out of focus on the CCDTV. The diagram shows how an injected beam that is collimated (shown in blue) comes to a focus in a different horizontal plane to the imaging light (shown in yellow). The matched divergence of the red beam, however, ensures that it comes to a focus in the same plane as the imaging light.

In order to calculate the focal length necessary for the injection lens to produce the correct beam divergence, the size of the back aperture of the objective needs to be known. Unfortunately Leica do not give out this information about their objectives so an attempt at physically measuring the size of the back aperture had to be made. It was estimated to be about 4 mm. Say, for example, that the diameter of the beam after being reduced for the SGM is 4mm then, given that the tube length or back focal distance is 160mm, simple calculation suggests that a lens with a focal length of 160mm should be used as the injection lens. The closest value focal length lens available is 150mm. In theory this should be ideal as it would produce a slight overfilling of the back aperture. The injection lens should be placed so that its focus is coincides with the back focal plane of the objective. Given that the microscope tube length is 160mm and the centre of the beam splitting cube is approximately 120mm up from the back aperture the focal plane of the injection lens should be about 40mm away from the centre of the camera attachment. The injection lens of focal length f should therefore be placed at $40 + f$ mm away from the centre of the camera attachment. Fine adjustment then has to be done to ensure the exact alignment of the laser and

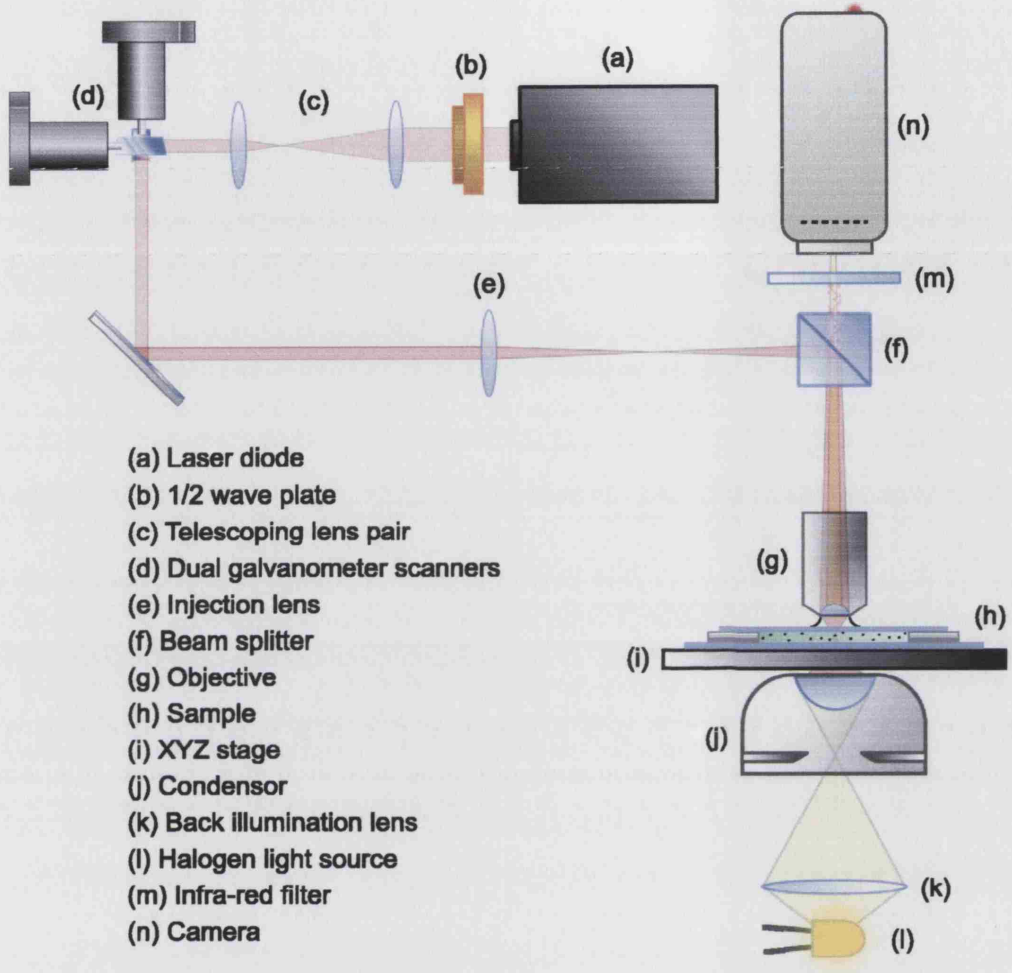

Figure 8.5: Laser tweezers schematic

optical focal planes. This will be addressed in the next section. Surprisingly it was found that for the two planes to coincide, the injection lens had to be positioned a considerable distance further away from the beam-splitter than expected. This may be due to axial chromatic aberration in the objective. With trial and error it was found that for infra-red light the back focal

distance of the objective is in fact about 250mm.

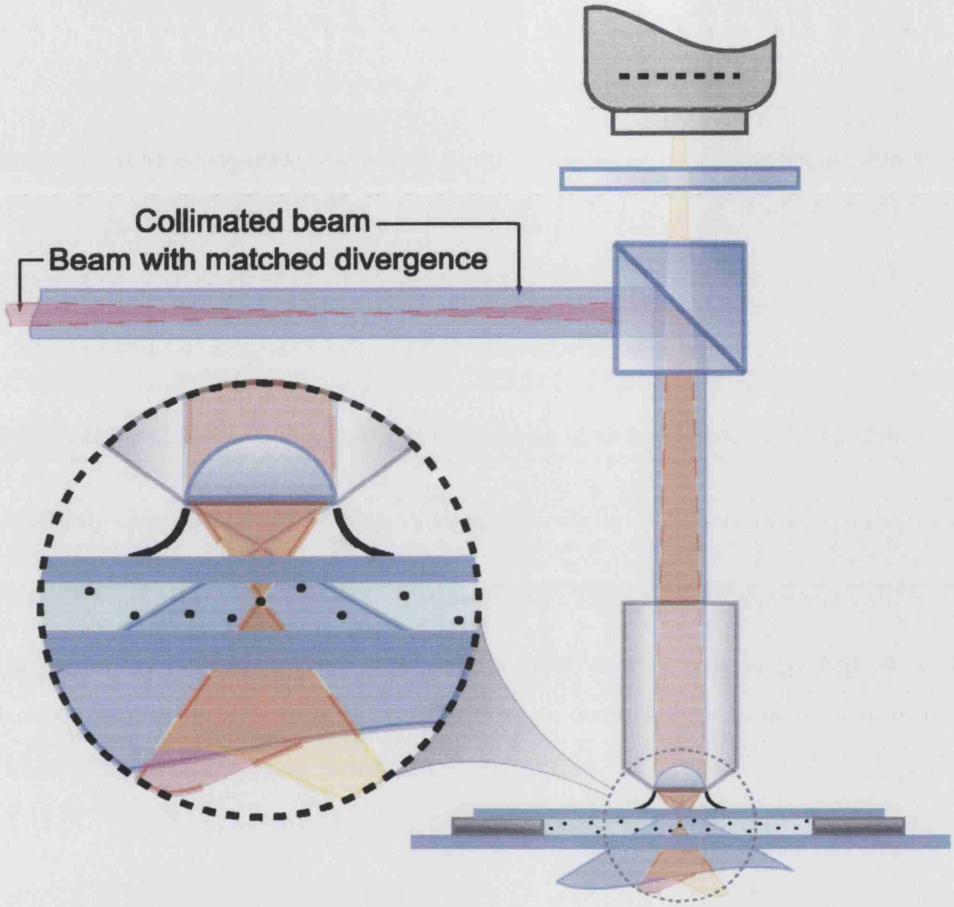

Figure 8.6: Collimated vs diverging injection beam. A collimated injection beam (shown in blue) comes to focus in a different horizontal plane to the imaging light (shown in yellow). The matched divergence of the red beam ensures that its focus is in the same plane as the imaging light.

For efficient laser tweezers, the beam steering mechanism is required to produce a laser beam that is always centred on the back aperture of the objective lens. An angular displacement about the back aperture then produces a lateral displacement of the focussed spot in the sample plane without any additional loss of light. It can easily be shown that, although it would be

convenient, lateral displacement in the sample plane can not be achieved by placing the galvanometer scanner at a focal plane of the laser beam. Instead the scanners must be placed in collimated laser light. It is possible to devise numerous optical configurations to meet these criteria and to begin with the simplest was used - as shown in diagram 8.5 and in the ray diagram 8.7. Here a collimated laser beam is incident on the scanning mirror. Angular displacement of the beam steering mirror then produces lateral displacement of the focussed spot in the sample plane.

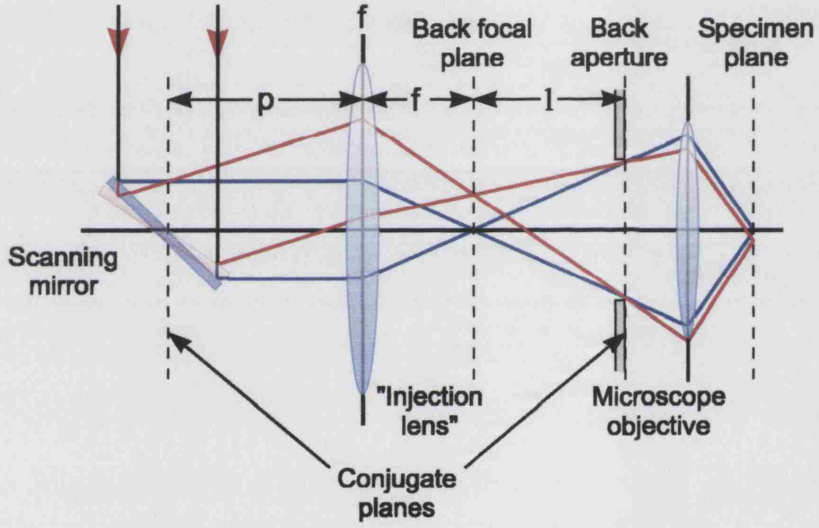

Figure 8.7: Ray diagram for the laser tweezers. For efficient trapping and scanning the optics must be positioned such that distances $f+l$ and p are correct, i.e. so that the scanning mirror and the back aperture are at conjugate planes. If the scanning mirror is placed incorrectly the beam will move laterally at the back aperture.

Unfortunately, with dual scanning mirrors there will always be a small amount of lateral displacement at the second mirror. This is minimised as much as possible with a carefully designed mount that holds the scanning mirrors at right-angles to each other and, importantly, as close as possible.

Another subtle but very important factor to consider is the distance p between the scanning mirror and the injection lens. By positioning the SGM so that it and the back aperture lie at conjugate planes, a purely angular displacement about the mirror leads to angular displacement about the back aperture with no lateral drift. From the thin lens formula it can easily be shown that

$$p = \frac{f}{l}(f + l). \tag{8.2}$$

For example, consider again a 150mm focal length injection lens: $f = 150\text{mm}$, $l = 250\text{mm}$ and so $p = 240\text{mm}$. It was very difficult to position and align the SGM this close to the injection mirror and so the tweezers were initially set up with no regard to the distance p. It will be shown in section 8.2.4 that while for small angles the effect of this is negligible, using a configuration that re-images the conjugate plane of the back aperture to the SGMs makes the scanning tweezers much more efficient at larger angles. Re-imaging the conjugate plane can be done with the insertion of a telescoping lens pair as shown in figure 8.8. The focal lengths of the lenses that make the additional

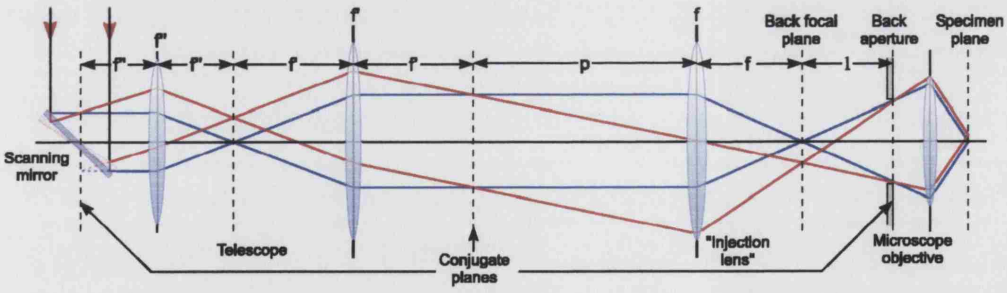

Figure 8.8: Ray diagram 2 for the laser tweezers. The conjugate plane of the back aperture is mapped back to the scanning mirror with a telescoping lens pair.

telescope can then be carefully chosen such that the distance $f' + p$ is long

enough to accommodate the periscope mentioned earlier.

After a lot of experimenting with different combinations of lenses and the degree to which the back aperture of the objective was overfilled, the scanning optical tweezers was found to work most efficiently with a configuration of components as summarised in figure C.7 in appendix C.

To conclude this section it has been seen that the positioning of the optical components is vital. The injection lens must be at the correct distance from the back aperture to ensure that the trapping and the imaging light come to focus at the same plane, and the scanning mirror and the back aperture must lie in conjugate planes to achieve efficient trapping throughout the scan area.

Beam alignment

To trap efficiently, delicate alignment of the laser beam through the microscope is essential. Because this can be a very fiddly and time-consuming procedure, the processes involved will be briefly described for useful future reference.

The first stage, with help using a spirit level and a steel rule, is to line up the plane of the periscope and, in particular, the centre of the higher mirror of the periscope with the porthole in the camera attachment as best as possible by eye. This should be done with the laser off and the injection lens removed. Looking through the porthole in the camera attachment towards the injection lens is a helpful trick, however, pay no attention to the circular light patterns reflecting from the beam splitting cube when the halogen lamp is on. Aligning the injection mirror with these patterns will not assure horizontal alignment.

If this is done well the mirrors should not need re-positioning at a later stage.

The second step is an iterative procedure to ensure that the beam is incident normal to the beam splitting cube and travels vertically down the microscope without being clipped. To see the beam with an IR card set the laser diode driving current to 20 - 30 mA. Adjust the mirrors so the beam is incident on the centre of the camera attachment porthole. With the objectives removed the IR card is used to view the beam on the stage and just above the back illumination lens of the microscope. Good alignment is achieved when the beam spot is seen to be neat, round, symmetrical and centred on the camera attachment porthole, the stage, and at the back illumination lens. This is done by the careful adjustment of the three mirrors nearest the porthole: the higher periscope mirror (HPM), the lower periscope mirror (LPM), and the third mirror (TM). The beam spot should be centred on the back illumination lens, the stage and on the porthole by adjusting HPM, LPM and TM respectively. This procedure has to be repeated several times before the three points are centred satisfactorily. If beam clipping or beam centring proves unavoidable, repeat stage one.

For the third stage insert the injection lens into the path of the injection beam at roughly the correct distance from the centre of the camera attachment. Align the lens so that it is normal to the beam path and so the beam falls in its centre, disrupting the direction of the beam as little as possible. Lens alignment is tricky without a translation stage and so the iterative alignment procedure of step two usually has to be repeated. The beam should now be aligned to travel straight down the centre of the microscope tube and incident in the centre of the back aperture of the objective.

The fourth step is to check and fine-tune the beam alignment and to finely adjust the position of the injection lens to ensure ensure the exact alignment of the laser and optical focal planes. This is done by viewing the quality, shape and size of the beam spot as seen on the CCDTV with the $\times 100$ oil-immersion objective in place. Prepare a slide by marking the upper surface with a permanent pen and placing a cover slip on top. Apply a drop of immersion oil between the objective and the cover slip and bring the ink into focus. Now remove the IR filter and turn the laser diode driving current up so the scattering of the laser light can be seen on the screen. Carefully adjust the position of the injection lens and the alignment mirrors so the scattered laser light becomes a small, centred, symmetric and focussed beam spot/pattern (see figure 8.9).

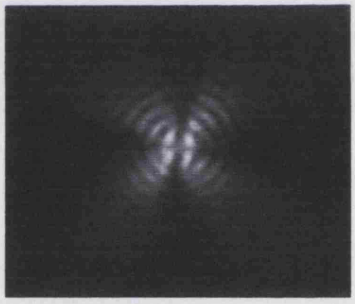

Figure 8.9: Picture of the beam spot being reflected from the surface of a slide. The centred, symmetrical spot and Airy ring pattern is a sign of good alignment.

The fifth and final step is to make sure that the beam spot can be translated in the horizontal sample plane with minimum distortion and power modulation. This can be done manually with the upper periscope mirror or by the electronic control of the scanning mirrors. If the beam becomes clipped, distorted, or if its intensity appears to change as it is walked about

in the area shown by the CCDTV then the whole alignment procedure may need repeating with optics adjusted accordingly. The final test to check the quality of alignment is to perform a 'power scan', the result of which is shown in the next section.

8.2.4 Alignment test

A useful feature that was included in the control program was a sub-VI to automatically scan the position of the trap in equal steps about a user-defined area with a user-defined step size and time between steps. With a power meter beneath the objective this semi-automates the process of measuring the power transmission as a function of position - very useful for accurately determining how well the optical tweezers are aligned transversely. Unfortunately the process could not be fully automated because the NI expansion card could not be used for data acquisition. Even still, this allowed these 'power scans' to be performed very quickly.

Example power scans can be seen in figure 8.10. They are all made with the laser-driver current set to 20mA. As detailed in section 8.2.3, an additional lens pair should be used in the optical setup to minimise transverse beam displacement at the back aperture. Here we compare power scans for optical arrangements with and without the 'compensating lens pair'. Both are aligned fairly well. Bad alignment can result in very asymmetric distributions that may be much more off-centre and may have sections missing due to beam clipping. The top pair of figures in the diagram show power scans for the optical setup without the compensating lens pair and the bottom figures are scans for the optical setup with the compensating lens pair.

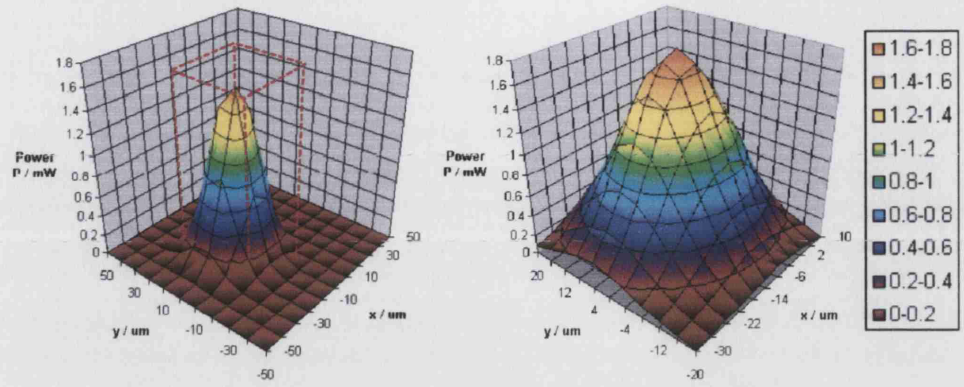

(a) Wide-area power scan. (b) CCTV-sized power scan.

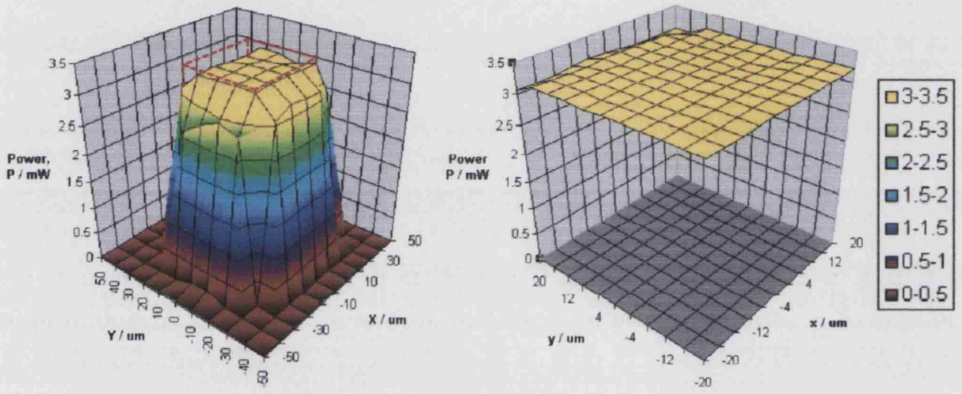

(c) Wide-area power scan (d) Central CCDV-sized power scan

Figure 8.10: Power transmission surface plots. Figures (a) and (b) are for an optical configuration that does not compensate for lateral beam displacement at the back aperture. Figures (c) and (d) are for an optical configuration that does.

Figures 8.10(a) and 8.10(c) are scans that correspond to a 50×50μm area in the trapping plane. The peak of the distribution in (a) is symmetric but slightly off centre, suggesting that while the alignment is good it could be a little better. The distribution in 8.10(c) is also very symmetric and very well centred. This indicates very good transverse alignment. Figures (b) and (d) are higher resolution scans of the central regions of figures (a) and

(a) respectively (the area of which are indicated by the red dotted lines). The size of these regions exactly match the size of the area viewed with the CCDTV. It is in this area that experiments are monitored and so it is here that it is desirable for the power distributions to be as flat as possible.

For the optical configuration without the compensating lens pair the distribution can be seen to fall away from the central maximum. This indicates that the beam moves transversely at the round back aperture of the objective and light is being lost as the mirrors scan away from the central position. Although the power loss could be compensated for electronically with feedback to the laser current controller it would make the laser tweezers very inefficient. Also the central maximum is not very high. This suggests that the degree of overfilling of the back aperture is too much and that the value of the focal length of the injection lens needs to be re-considered for this optical configuration. For the optical configuration *with* the compensating lens pair the distribution is higher, wider, and has a very flat central area. This indicates that the degree of overfilling of the back aperture is less and that the beam remains centred at the back aperture with little lateral displacement. Outside the flat central region the distribution drops off sharply. This is not because the beam is being displaced at the back aperture but because the displacement at the beam-splitting cube is causing the beam to be clipped. On closer examination of the central region it can be seen that the distribution remains almost entirely flat within the CCTV screen area. This is ideal. From the data of figure 8.10(d) it is calculated that the distribution has an average power of (3.20±0.04)mW.

8.3 Force calibration methods

The lateral trapping force on a spherical particle in a viscous medium can be calibrated against Stokes drag: $F_{drag} = 3\pi\eta dv$, where η is the coefficient of viscosity (0.001kg/ms for water at 20°C), d is the diameter of the sphere, and v is the relative velocity between the bead and the medium. This is done by trapping a particle in the optical tweezers and then accelerating the stage, or in our case the trap, until the particle is left behind. Using the control program the particles trapped in the laser tweezers can easily be made to oscillate in a sinusoidal or circular fashion. The maximum speed of the bead is then given by the amplitude a and frequency f of the oscillation: $v_{max} = 2a\pi f$. A feature in the program is used to increase a or f in arbitrarily small increments until the trapped particle falls away. Another feature of the program can then be used to calculate the lateral trapping force by the following equation:

$$F_{la} = 6\pi^2\eta daf k \tag{8.3}$$

where k is a factor that takes into account the increase in drag when a sphere is close to the upper or lower boundaries of the sample cell (see [115] and references therein). It is given by

$$k = 1 + \frac{9d}{32}\left(\frac{1}{D} - \frac{1}{H-D}\right) \tag{8.4}$$

where D is the distance of the sphere from the coverslip and H is the height of the specimen chamber. Higher order approximations can be found in [56,112] and references therein.

The axial trapping force can, in principle, be calibrated against the grav-

itational minus the buoyant force on the bead by reducing the laser power until the bead falls out of the trap. While being practical for particles that are large and dense enough to fall when the laser power is too weak to support them, the particles trapped in our experiments sediment in water on a time scale of several minutes and also exhibit strong Brownian motion. Nonetheless, the microspheres still appear to fall out of the trap when the laser power is reduced enough. The proposed mechanism is that the thermal energy pushes the beads over the potential energy barrier in the weakest direction of the trap: axially, and in our case downwards. Past the barrier it is pushed away from the trap by the scattering force such that it appears to fall away. From [115] the axial calibration force is shown to be

$$F_{ax} = \frac{2k_BT}{d} \tag{8.5}$$

For larger or denser beads the term from the initial proposal, the gravitational minus the buoyant force, may be added: $F_g = \frac{\pi}{6}(\rho_p - \rho_m)d^3g$, where ρ_p and ρ_m are the densities of the trapped particle and the suspending medium respectively, and g is the gravitational acceleration.

8.4 Summary

In this chapter we have described the design considerations, the apparatus, the construction, the alignment and the methods of force calibration for a scanning-beam optical tweezers. The system was designed to be cost effective and highly versatile, two requirements that have been successfully met. Other design criterion were that the tweezers must be able to trap multiple objects,

that the traps can be moved around independently in at least two dimensions and that they facilitate the generation of tailored optical potentials. Evidence of this shall be presented in the following chapter.

CHAPTER 9

Simple experiments with laser tweezers and future directions

In this chapter pictorial evidence is presented to demonstrate the 3D trapping and manipulation of polystyrene microspheres and albumin-coated microbubbles using the laser tweezers. The potential to utilise the ability of the optical tweezers to manipulate and act as a sensitive force transducer for micron-sized particles for statistical physics and biophysical research applications is also discussed.

9.1 Trapping microspheres

9.1.1 Single trap

The tweezers were successfully used to trap 2μm diameter polystyrene spheres in three dimensions. Figure 9.1 demonstrates a trapped bead being scanned in a sinusoidal fashion with the control program. The reference bead in the top right corner of the pictures in the sequence is untrapped and almost stationary apart from small random perturbations due to Brownian motion. For figure 9.2 the program was set to scan slowly around a circle and the trapped bead is shown to move clockwise around a 7μm diameter circular path.

For both figures the microspheres were trapped at a distance of 10μm below the coverslip and the laser current was set to 40mA (20mW light output). The amplitude of oscillation or the diameter of the circular path can, for example, be set to 10μm and the frequency can be turned up to around 3.5Hz before the bead falls away from the trap. This corresponds to a lateral trap force of about 2pN (see equation 8.3). Using higher laser powers trapping forces up to 15pN have been measured. A typical value for the lateral trap efficiency of our tweezers with a 2μm polystryene bead held in 3D at 10μm below the coverslip is $Q \approx 0.1$ (see equation 2.9). This is very similar to efficiency values of similar systems developed by other groups using different microscopes and objectives, for example [112, 115–117], and in qualititive agreement with the numerical calculations reported by [112, 116, 118].

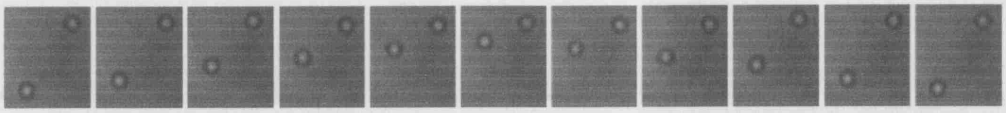

Figure 9.1: 3D trapping and sinusoidal manipulation of one microsphere. The reference bead in the top right of the pictures in the sequence is untrapped and almost stationary apart from small random perturbations due to Brownian motion.

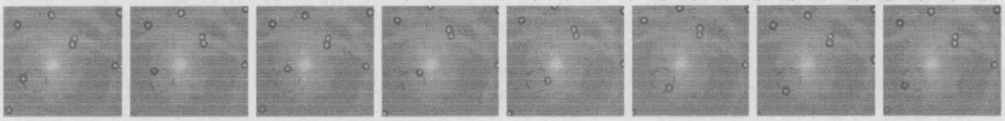

Figure 9.2: 3D trapping and circular manipulation of one microsphere. Here the bead is held in a circular path $7\mu m$ in diameter and can be driven at frequencies up to 2.5Hz before falling out.

9.1.2 Multiple trap

A simple control program was written to scan the optical trap at an arbitrary frequency between two points. Alternatively, creating a square wave with function generator to control one of the SGMs would have sufficed. As the frequency of oscillation becomes too high for a particle to respond, the two rapidly blinking sites behave as separate optical traps. The stiffness or the force exerted on the particles in each trap could easily be controlled by changing the duty cycle of the square wave to the SGM and hence the time spent at either of the trap locations.

Figure 9.3 shows two microspheres each trapped in three-dimensions in one of the time-shared trap sites. As the microscope stage is translated horizontally the two trapped beads remain stationary while the untrapped beads move in unison with the stage.

In the next example the control program is used to trap three microspheres by scanning quickly between three sites, the position of which can be

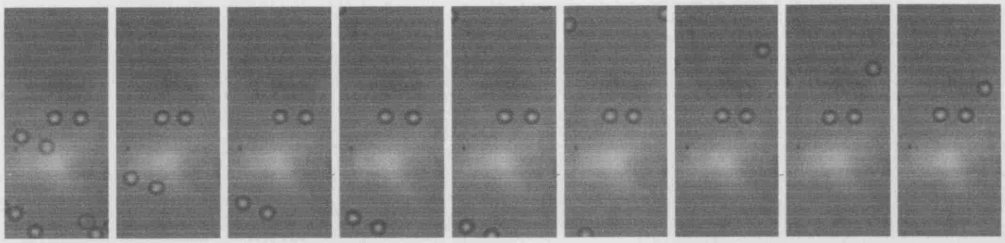

Figure 9.3: Dual trapping of microspheres by timeshared trapping. As the stage is moved the trapped beads remain stationary while the surrounding untrapped beads move by.

controlled separately. Figure 9.4 demonstrates the three-dimensional trapping of three beads. In turn, the outer microspheres are moved up close to and then back away from the trapped bead that is held stationary in the middle.

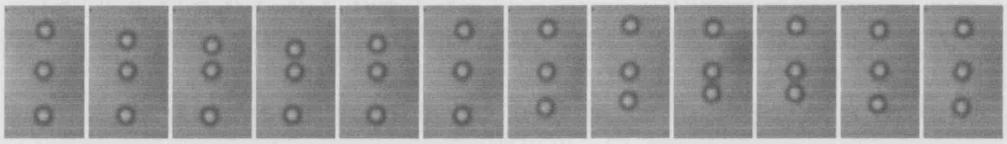

Figure 9.4: Three independently controlled laser tweezers trap sites. In turn both of the outside microspheres are brought towards and back from the trapped bead that is held stationary in the centre.

A slightly different technique is employed for multiple trapping in the final example. Instead of rapidly scanning to a trap site and residing here for a short time before moving to the next, the motion of the laser beam is kept constant while the laser power is modulated. For this the control program was modified to drive another analogue output channel to feed the external modulation input of the laser diode current controller. Code was written to control the laser power output in an arbitrary fashion, in synchrony with the sinusoidal or circular motion of the trap. This is demonstrated in figure 9.5 whereby the laser is pulsed on three times at equal intervals as the trap is

scanned around in a small circle. The first picture shows the resulting beam spots with the laser power turned down and the IR filter removed from the trinocular head of the microscope. The second picture shows three beads trapped in three dimensions in each of the trap locations. The third and fourth pictures demonstrate how the traps can be rotated by varying the duty cycle of the laser control pulses, or by varying the phase of the laser control pulses with respect to the phase of the circular scanning motion.

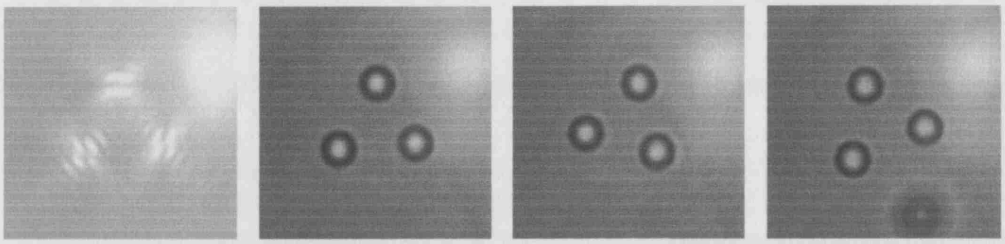

Figure 9.5: Three tweezers trap sites about a cirle. The laser is pulsed on three times each time the trap rapidly scans around the circular path. The configuration may be rotated by varying the duty cycle of the laser control pulses.

As explained in [119], the depth of the optical potential is proportional to the time-averaged intensity of the light, which is proportional to the trap intensity (and inversely proportional to the scanning velocity of the trap). Using the same control program, arbitrarily shaped potentials can therefore be created by modulating the power of the scanning beam in different ways (an alternative to modulating the trap velocity). By, for example, keeping the laser power constant as it is quickly scanned around a circular path a microsphere should in theory remain trapped radially, feel no net azimuthal force, and be confined to diffuse in the 'continuous' potential about the circle. Modulating the intensity should then induce a net drift of the Brownian particle towards the region of greatest intensity. A periodic, asymmetric

spatial modulation of the trap intensity can thus be used to make a saw-toothed shaped potential. The program has also been extended to enable the potential surface to be toggled between two different shapes. The usefulness of this will be explained in section 9.3. Another application of the circular scanning trap is to capture particles with lower refractive index than water. This will be addressed in the next section.

9.2 Trapping bubbles

In this section it will be shown that spherical micron-sized albumen bubbles (usually used as a contrast agent in ultrasound imaging) can be trapped in three-dimensions in the dark central region of a field formed by rapidly scanning the optical trap around a circular path. An impression of the vertical cross section of the 'bubble trap' can be seen in figure 9.6.

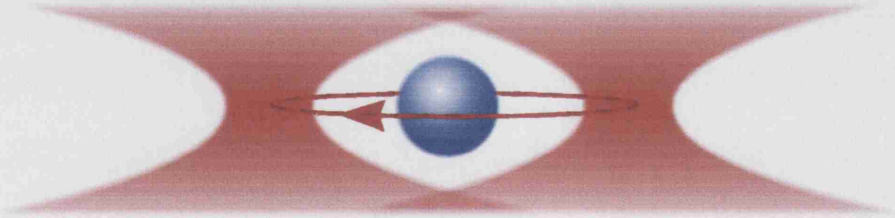

Figure 9.6: The bubble trap: optical trapping of particles with lower refractive index than the suspending medium. Repelled by the light, bubbles suspended in water will stay trapped in the dark region within a field formed by rapidly scanning a tightly focussed beam about a circle.

The bubbles were obtained from the UCL Ultrasonics Group[1]. They come

[1]Prof. Nader Saffari *et al.*, UCL Ultrasonics Group, Department of Mechanical Engineering, University College London, Torrington Place, London, WC1E 7JE.

in a suspension called Optison[2] which is a sterile injectable suspension of microspheres of human serum albumin with octafluoropropane for contrast enhancement during specific ultrasound imaging procedures. They have a mean diameter range between 2.0 and 4.5μm and a maximum diameter of 32.0μm, but over 90% are less than 10μm. The suspension is suitably diluted with sterile water.

To trap the bubbles the laser field must first be switched off. A bubble is located and the microscope translation stage is used to position it roughly at the trap location. The diameter of the bubble trap is then set to at least three microns larger than the size of the bubble and the laser is turned back on before the bubble has time to diffuse away. Once the bubble is confined the trap may be made smaller to hold the bubble more tightly. However, if the trap is made too small the bubble will suddenly pop out of the trap.

The control program was modified to produce two bubble traps of equal size. The sequence in figure 9.7 shows two bubbles of different sizes both trapped in separate 6μm diameter traps. As the stage is moved backwards and forwards the untrapped bubbles can be seen to move relative to the two central bubbles which remain trapped. The motion of one of the untrapped bubbles is marked in red. The traps are big enough to hold the larger $(4.3 \pm 0.2)\mu$m diameter bubble and this gives the smaller $(3.5 \pm 0.2)\mu$m diameter bubble room enough to visibly 'rattle around' within the trap. The trap force was measured against the viscous drag force as before. With the laser set to 20mW typical forces for example on a $(2 \pm 0.5)\mu$m bubble in a $(2.4 \pm 0.2)\mu$m trap are 0.8 ± 0.2pN.

[2]Optison (Human Albumin Microspheres) Injectable Suspension Octafluoropropane Formulation from Mallinckrodt Inc., St. Louis, MO 63042.

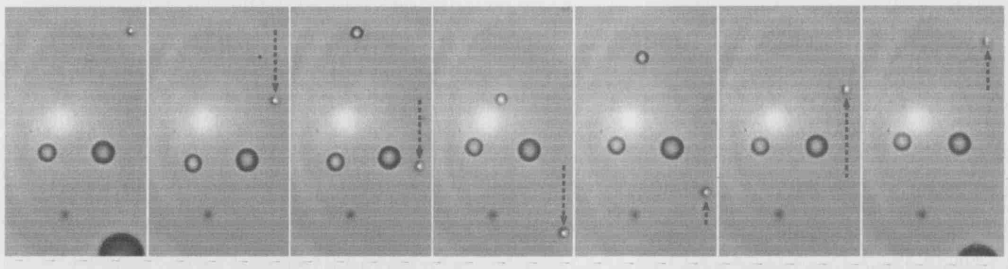

Figure 9.7: Dual trapping of micron-sized albumin bubbles in aqueous solution. The trapped bubbles remain stationary with respect to the untrapped bubbles that move with the translation of the stage.

For the next example a function called 'squeeze' was written to reduce the size of the traps at an arbitrary speed. The sequence in figure 9.8 begins with a $(3.4 \pm 0.2)\mu$m and a $(2.4 \pm 0.2)\mu$m bubble trapped in $(12 \pm 0.2)\mu$m traps.

Photographs of the traps and the bubbles were taken separately and superimposed. This is necessary because the intensity of the light required for trapping saturates the camera. The dimensions of the un-cropped images are all (659×589)pixels, which for superposition are aligned to the nearest pixel. The error in relative position of the image of the trap and the bead is therefore less than 0.2% (neglecting error due to stage vibration and laser beam jitter due to mechanical vibration of the optics).

As trap size is reduced very slowly the bubbles can be seen to become confined more tightly until they pop out of the trap. This process happens very suddenly. The bubbles are usually observed to go out of focus as they escape because the weakest part of the trap is at the top or the bottom (i.e. out of the plane of the paper).

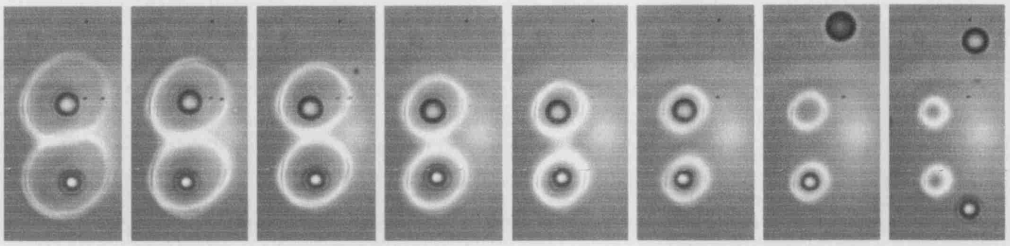

Figure 9.8: Squeezing bubbles: Using a dual circle trap to capture and squeeze the bubbles. When the trap becomes too small the bubbles 'pop' out.

9.3 Future directions

There are many exciting experiments planned for the near future with the optical tweezers, both in statistical physics and the emerging area of biophysics. One area of interest is that of Brownian ratchets. It has been explained that by moving the optical tweezers in a circular path while synchronously modulating the laser power, the time-averaged influence of the tweezers can be made to resemble a spatial saw-tooth potential. By switching between this asymmetric potential and a non-modulated circular potential, pulsed ratchet experiments could be realised in this heavily damped Brownian system. This represents the optical thermal ratchet and would constitute directed transport by noise as opposed to the cold atom realisation of the kicked rotor whereby directed diffusion resulted purely from chaos. By modulating the phase of the intensity profile in a sinusoidal manner, i.e. translating the potential surface backwards and forwards, rocking ratchet experiments could be realised as well. Such demonstrations of directed diffusion are also the thermally-driven processes believed responsible for directed motion in a wide range of biological molecular motors including actin/myosin and kinesin/tubulin.

A second proposed area of research is a collaboration with the Cellular and Molecular Biology group led by Prof. Anne Ridley at the Ludwig Institute for Cancer Reaearch at UCL in the study of the generation of force by migrating cells. Cell migration is central to animal development and physiological function, and also to biotechnological applications such as tissue engineering. It occurs in reaction to the detection of a gradient in chemical concentration (chemotaxis) or a gradient of extracellular matrix proteins (haptotaxis) that occurs during, for example, immune response and at sites of injury or trauma. However, the mechanisms by which the molecular components act together in a physically co-ordinated way to propel the cell are less well understood. The purpose of the experiments is to measure the forces involved in cell migration - bond strengths and traction - by calibrating them against the known force exerted by the laser light in the optical tweezers. Forces on migrating cells will be measured through the attachment of specially-coated, optically-trapped microspheres. Changes in forces made by genetic manipulation or pharmacological intervention for example may also be characterised in detail.

For this work it would be beneficial to replace the 'escape force method' of calculating the force required to pull a bead free of the trap by a method that allows the force on a bead to be measured continuously. One way that this may be done is by monitoring the bead displacement from the centre of the trap. For small displacements the restoring force is proportional to the displacement which means that the optical tweezers act like a Hookeian spring, characterised by a fixed stiffness at a given trap power. The stiffness would simply have to be calibrated against Stokes' drag force for a bead

moving at constant velocity. To accurately monitor the beam displacement the laser tweezers would have to be equipped with image-analysis software [117] or by imaging the trapped object at the focal plane of the microscope condenser using a split photodiode [120] or a quadrant photodiode [121]. An alternative arrangement is to use an optical trapping interferometer in which the same light serves to produce both the trapping and interferometer functions [122]. A good review of other force monitoring and position sensing methods and details of an experimental setup using a split photodiode can be found in [121].

The final proposed area of research is a collaboration with the UCL Ultrasonics Group in the Department of Mechanical Engineering. The project would involve investigating the properties of the aforementioned albumin microspheres, or 'bubbles', which have various medical applications. Their primary application is that of a contrast enhancement agent for ultrasound imaging. Ultrasound imaging has become an important clinical tool for assessing vascular structures and blood flow. However, help is necessary in many situations because not all patients yield optimal images, nor can such good images be obtained in all anatomical locations. To improve signal-to-noise ratios a small quantity of a water-based suspension of the gas microbubbles is intravenously injected with no physiological effects. A simple way to describe the action of an ultrasonic contrast agent is that it simply increases the amplitude of the echo returned from the blood. This happens because the acoustic impedance of the microspheres is much lower than that of the blood. Impinging ultrasound waves are scattered and reflected at the microsphere-blood interface and ultimately may be visualised in the ultra-

sound images. However, although there are various modes of imaging which can be used with the enhancement agent to build up an image, drawbacks such as angular dependency and flash artifacts in moving tissue still exist to reduce the signal-to-noise ratio.

It was found that at certain frequencies the microbubbles resonate and reflect signals containing second harmonic and multiples of the fundamental frequency to which they were exposed. By selectively receiving and enhancing harmonic signal components while suppressing the fundamental frequency, images with substantially improved spatial and contrast resolution can be obtained. The resonant phenomena are dependent on the incident ultrasound frequency, size of the microbubbles and the properties of their shells. However, the current development of harmonic imaging has been made without a comprehensive understanding of the behaviour of the bubbles and it is believed that the full potential of harmonic imaging is yet to be realised.

Another use of the bubbles is as a method for delivery of antitumoral agents into cancers. Sonoporation, as it is called, involves the use of the albumen bubbles being injected in vivo and illuminated with ultrasound in such a way that it leads to the bubble cavitating and causing poration of adjacent cells. Sonoporation promises a safer new alternative for enabling gene therapy but the mechnisms by which the poration of the cells is produced is complex and little understood.

To understand more about the bubbles and to quantify and optimise the useful effects, optical tweezers can be used as a gentle and almost non-contact tool with which to keep a certain bubble, or a trapped collection of specifically selected bubbles, localised while subjecting to ultrasound. By a special

method of subjecting a sample cell to sonic illumination we propose to measure the scattering response of a known number and known size of bubbles of known composition. By manipulating the distribution of the bubbles with the tweezers, effects due to bubble-bubble proximity and bubble-tissue proximity could also be investigated. Holding bubbles stationary with the laser tweezers also facilitates the observation of the deformation and cavitation of the bubbles with a fast camera. The deformation and the buckling of the shell of the bubbles could also be examined while squeezing with the optical trap. In vivo environment could be replicated by introducing suitable tissues and a bubble/bubbles could be manipulated to varying positions about the tissue. The effect of poration could be quantified and optimised for variables such as bubble size, illuminating frequency, pulse frequency, bubble composition, bubble-tissue separation and bubble distribution. With laser tweezers bubble traps, extremely accurate targeted delivery of agents contained within bubbles, the accurate poration of, for example, cancerous tissue, and the accurate protein transfection into cells is also made possible.

9.4 Summary

In this chapter the successful three-dimensional trapping of 2μm polystyrene beads in a water suspension has been demonstrated. Transverse trapping forces have shown to be on the order of pico-Newtons and a beam-sharing technique has been shown to enable multiple trapping and the individual and group manipulation of the microspheres. The progress of the work on the control program has been reported and it is now sophisticated enough to

enable certain shapes of pulsed or constant potential surfaces to be generated.

Albumen coated microspheres with a lower refractive index than their aqueous suspending medium have also been shown to be trapped in three-dimensions. This has been done by scanning the beam around a small circular path and trapping the bubble in the central dark cavity of the resulting light field. As expected, the transverse trapping forces are less than that for polystyrene microspheres, but still on the order of pico-Newtons. A special addition to the control program has also enabled the bubbles to be squeezed in a slowly shrinking circular trap.

The versatile system lends itself very well to a broad selection of future experimentation in various fields, and parallel development is already underway in preparation for the collaborative efforts in two exciting areas of biophysics.

CHAPTER 10

Conclusion

In the course of this thesis I have described examples of the interaction between matter and light, in particular the coherent manipulation and directed motion of cold atoms in a Hamiltonian system and the trapping and manipulation of neutral microparticles. In the former case the kicked rotor, a paradigm model for the study of quantum chaos, was realised in a laser cooling apparatus in which cold caesium atoms were 'kicked' by a far-detuned symmetrical optical lattice. Experiments demonstrate the quantum phenomenon of dynamical localisation which acts to suppress atomic momentum diffusion, and by preparing the sample at non-zero momenta relative to a moving optical potential asymmetric diffusion was achieved as a result of the asymmetry of features in the mixed (chaotic and regular) classical dynamics. Using the energy diffusion as a probe, the structure of mixed phase space was verified for increasing kick strength, i.e. completely regular to increasingly chaotic phase space. The resolution with which this was done was

shown to be dependent on the effective Planck constant, a measure of the strength of the quantum effects of the system. Further experiments made an exploration of phase space past the momentum boundary which is a consequence of finite-width kicks, and the location of the boundary was confirmed. By using an asymmetric kick sequence and a moving lattice, directed motion of the atoms was achieved in a fully chaotic system and the predicted cosinusoidal modulation of the diffusion constant was verified. Finally it was shown that a broken time symmetry and a 'rocking' lattice (accelerating with alternating sign between kicks) also gives rise to an asymmetric momentum diffusion in our fully chaotic Hamiltonian system. The effect of altering the inertial term is in good agreement with the theory.

The secondary topic within this thesis concerned the description, the design and the construction of a computer-controlled scanning-beam laser tweezers for the manipulation of dielectric microspheres and micron-sized protein-coated bubbles. Evidence for the three-dimensional trapping and the automated two-dimensional manipulation of these neutral particles in time-shared optical traps was presented. The preparation and plans for biological research applications was also detailed, the work of which marks the beginning of future biophysical collaborations.

"There is a single light of science, and to brighten it anywhere is to brighten it everywhere"

Isaac Asimov

APPENDIX A

Publications

1. P. H. Jones, H. Saunders-Singer, S. Bergamini and D. R. Meacher, "A moving-mirror frequency modulator for cold atom spectroscopy", *Rev. Sci. Instrum.* **73**:2549 (2002)

2. P. H. Jones, M. Goonasekera, H. E. Saunders-Singer and D. R. Meacher, "Shifting the boundaries: pulse-shape effects in the atom-optics kicked rotor", arXiv:quant-ph/0311120 (2003), submitted to *Europhys. Lett.*

3. P. H. Jones, M. Goonasekera, H. E. Saunders-Singer and D. R. Meacher, "Asymmetric diffusion in the delta-kicked rotor with broken time symmetry", arXiv:quant-ph/0309149 (2003), submitted to *Phys. Rev. Lett.*

4. M. Goonasekera, P. H. Jones, H. E. Saunders-Singer and D. R. Meacher, "Exploring the mixed phase space of the delta-kicked rotor with a moving optical lattice", manuscript in preparation (2004).

Appendix B

Chaos

B.1 Caesium data and useful equations

Useful data:

Quantity	Symbol	Value	Unit
mass	M	2.207×10^{-25}	kg
wavelength (vacuum)	λ	852.347	nm
wavevector	k_L	$2\pi \times 1.17 \times 10^{6}$	m^{-1}
excited state lifetime	τ	30.5	ns
natural linewidth	Γ	$2\pi \times 5.22$	MHz
saturation intensity	I_{sat}	1.12	$mWcm^{-2}$
recoil energy	E_R	1.37×10^{-30}	J
recoil frequency	ω_R	2.07	kHz
recoil velocity	v_R	3.5	mms^{-1}
recoil temperature	T_R	198	nK
Doppler temperature	T_D	125	μK
Planck's constant	h	6.626×10^{-34}	Js
Dirac constant	$\hbar$	1.05456×10^{-34}	Js

Table B.1: Useful physical properties of Caesuim and spectroscopic data for the $6^2S_{1/2} \rightarrow 6^2P_{3/2}$ transition

Useful equations:

The Effective unit of system action:

$$\hbar_{eff} = 8\omega_R T$$

where T is the kick period.

The potential depth, $V_0/\hbar$ (MHz):

$$\frac{V_0}{\hbar} = \frac{I}{I_{sat}} \frac{\Gamma^2}{6\Delta_L}$$

The momentum boundary, ρ_b (dimensionless units):

$$\rho_b = \pm \frac{M\lambda^2}{8\pi\hbar t_p} \hbar_{eff} = \pm 2\pi \frac{T}{t_p}$$

where t_p is the duration of a square kick.

The classical stochastisity parameter (kick strength) for the cold-atom realisation of the delta-kicked rotor:

$$K = \frac{\hbar_{eff} T V_0}{\hbar}$$

The classical stochastisity parameter for square kicks of duration t_p:

$$K = \frac{\hbar_{eff} t_p V_0}{\hbar}$$

The effective kick strength as a function of momentum for square kicks:

$$K_{eff} = K \frac{\sin(\pi\rho/\rho_b)}{\pi\rho/\rho_b}$$

The form of the energy diffusion constant with corrections that arise from kick-to-kick correlations [71,72]:

$$D = \frac{K^2}{2}\left[\frac{1}{2} - J_2(K) - J_1^2(K) + J_2^2(K) + \ldots\right] \tag{B.1}$$

to second order in the Bessel functions, $J_{1,2}(K)$.

The quasi-linear diffusion rate approximation in the limit of large K:

$$D_{ql} \approx \frac{K^2}{4}$$

The localisation length (standard map):

$$L \approx \frac{K^2}{2\hbar_{eff}}$$

The break time (standard map):

$$t^* \approx \frac{L}{\hbar_{eff}}$$

The diffusion rate approximation for a two-period kicking cycle defined by the chirp parameter b, with correlation terms that arise from next-but-one kicks (the 'two-kick' correlation):

$$D = \frac{K^2}{4}(1 - 2J_2(K)\cos(2\rho b) + \ldots)$$

The "ratchet time":

$$t_r \propto \frac{1}{Db^2}$$

The diffusion rate approximation for a system with an alternating potential gradient. The two-kick correlation term includes the potential gradient A:

$$D = \frac{K^2}{4}(1 - 2J_2(K)\cos(2\rho b - A) + \ldots)$$

Appendix C

Optical tweezers

C.1 Camera attachment modification: CAD drawings

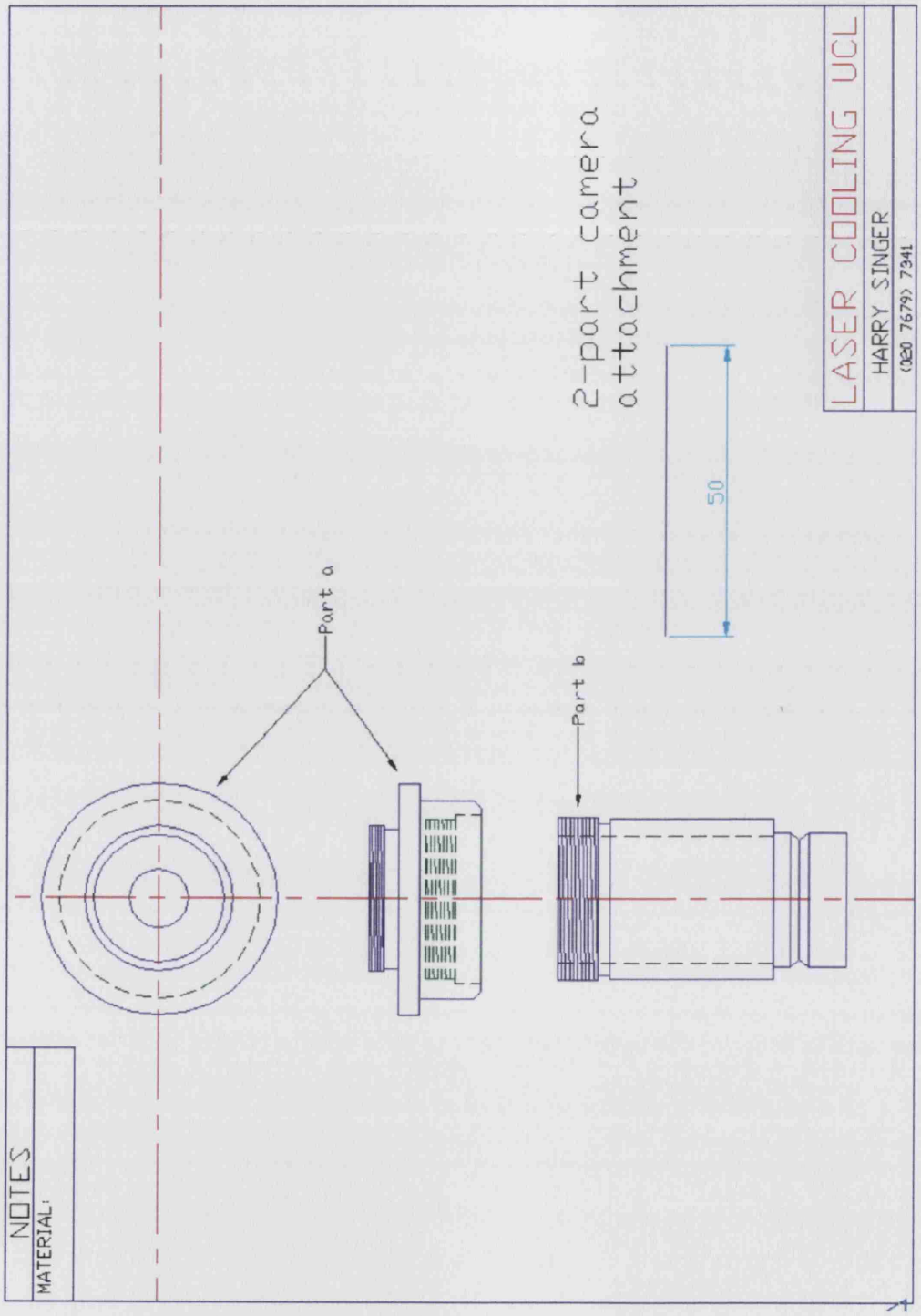

Figure C.1: CAD: Tweezers 2-part camera attachment.

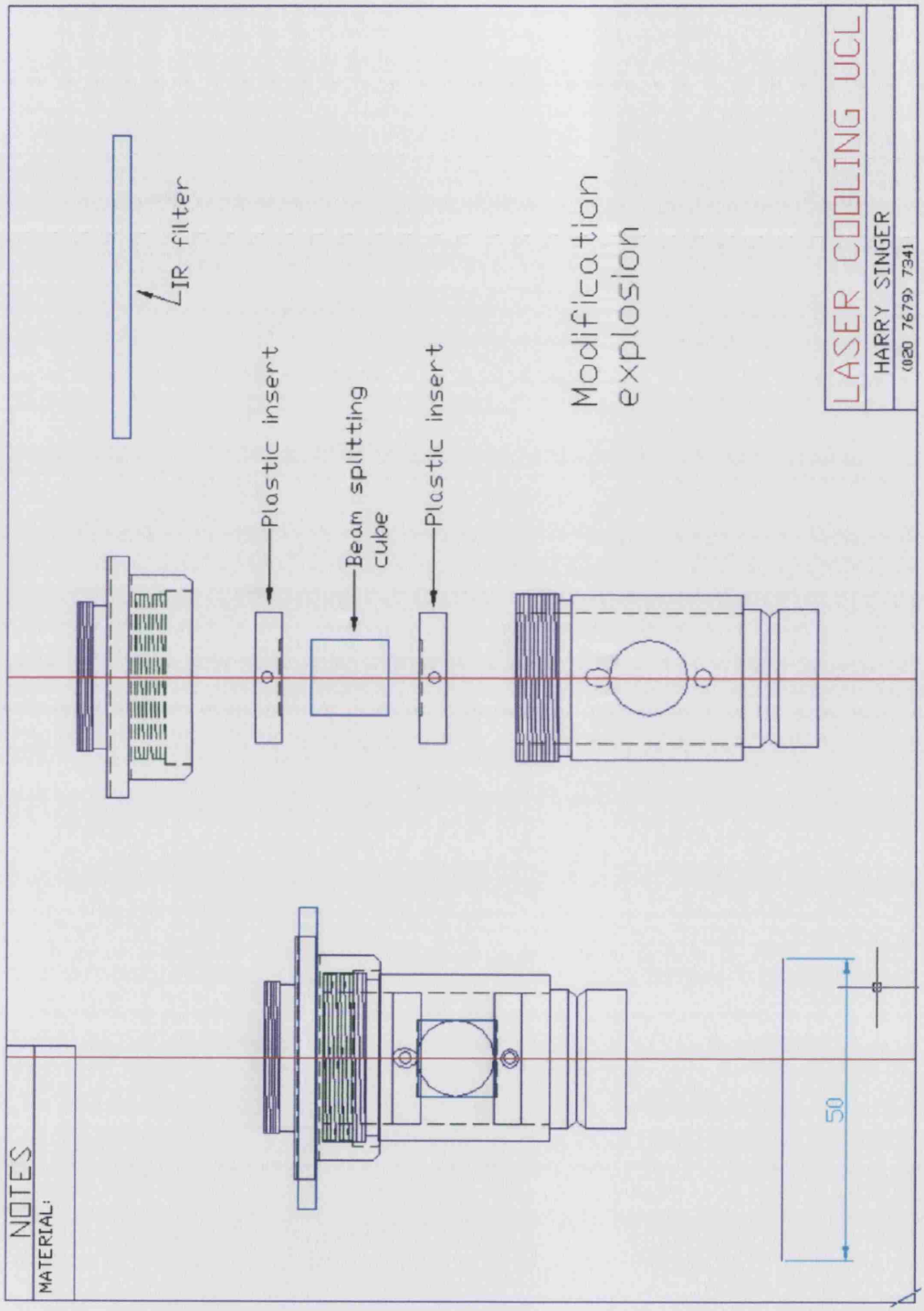

Figure C.2: CAD: Explosion of the camera attachment.

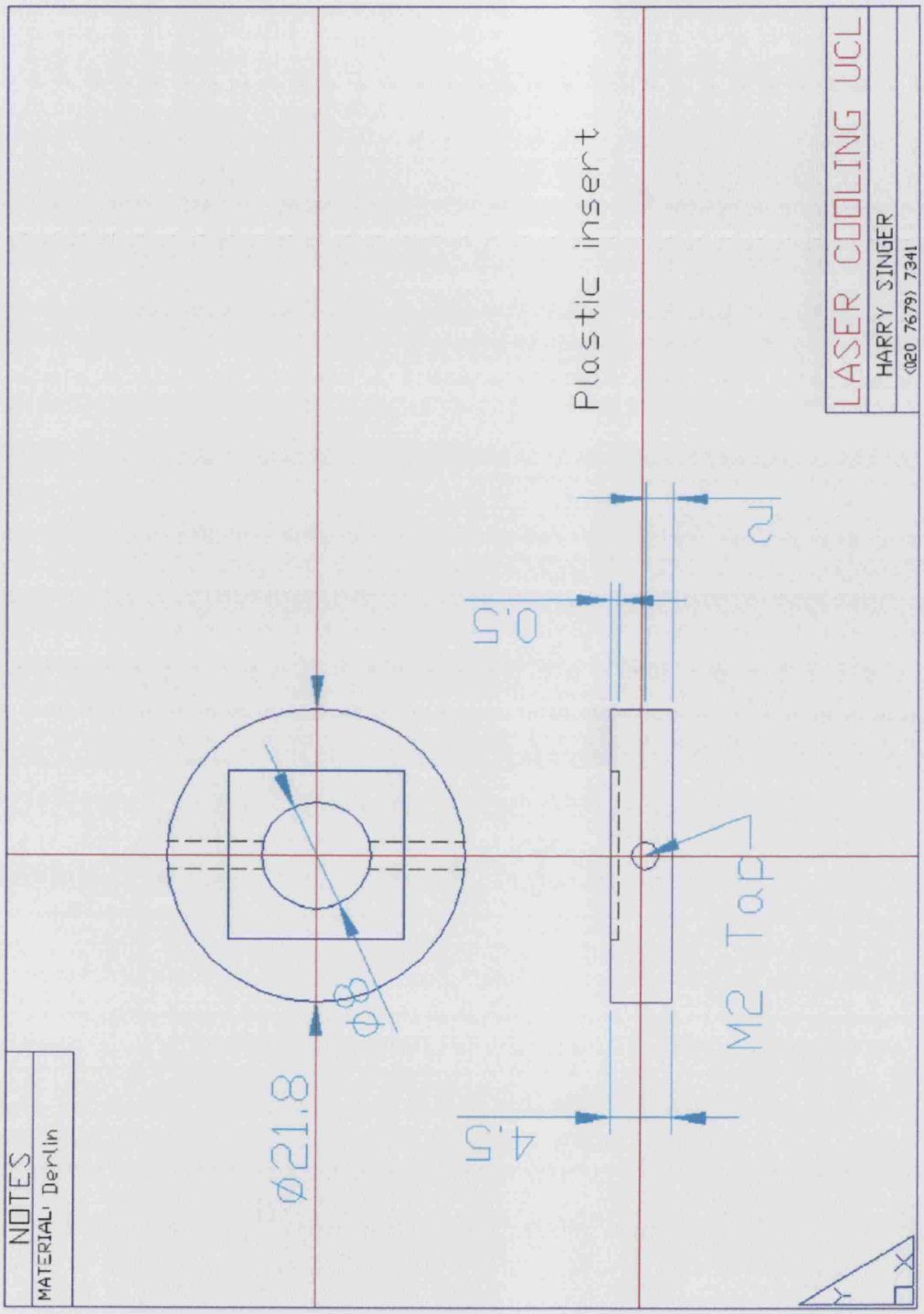

Figure C.3: CAD: Plastic insert to hold beam-splitting cube.

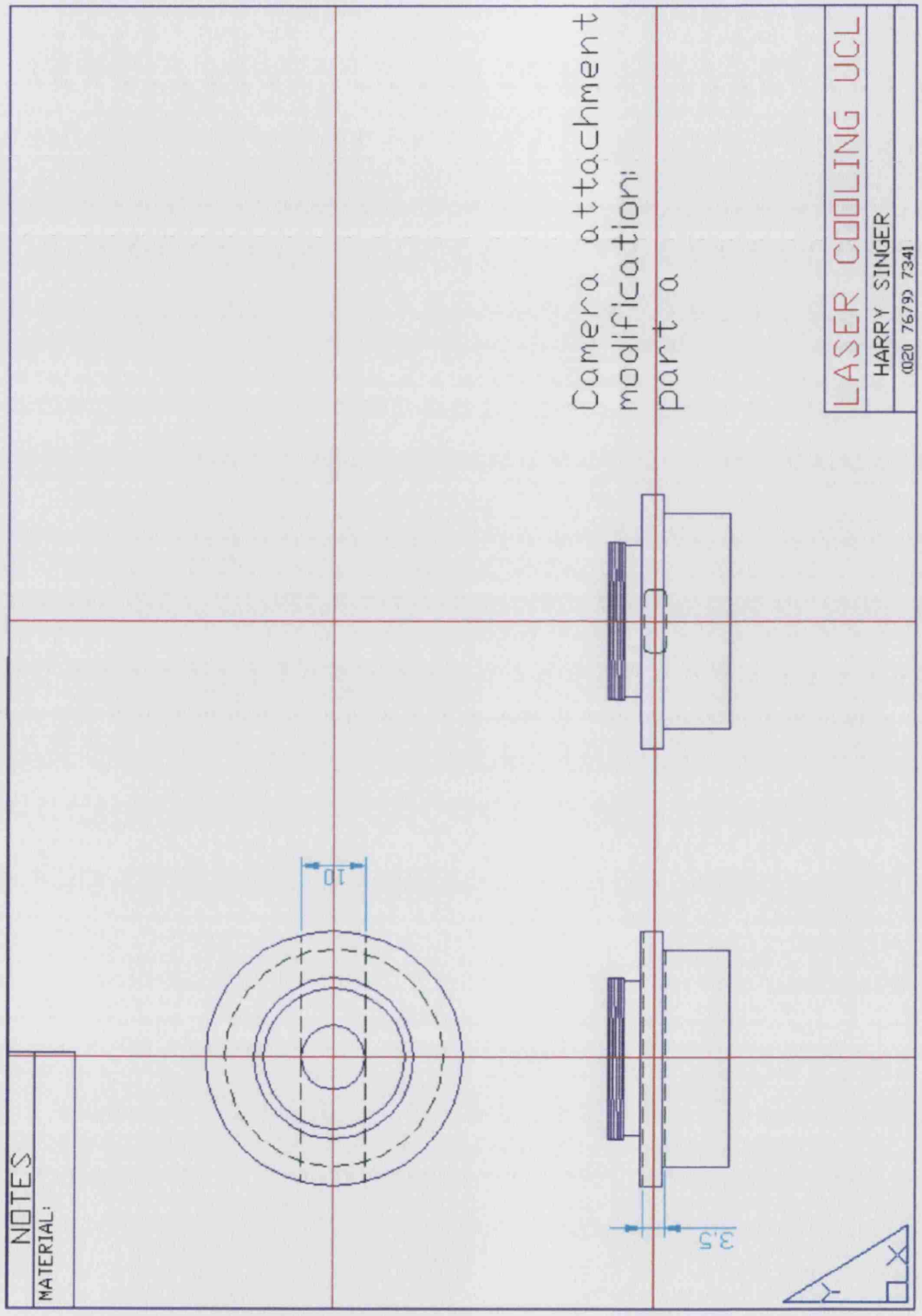

Figure C.4: CAD: Camera attachment modification part A.

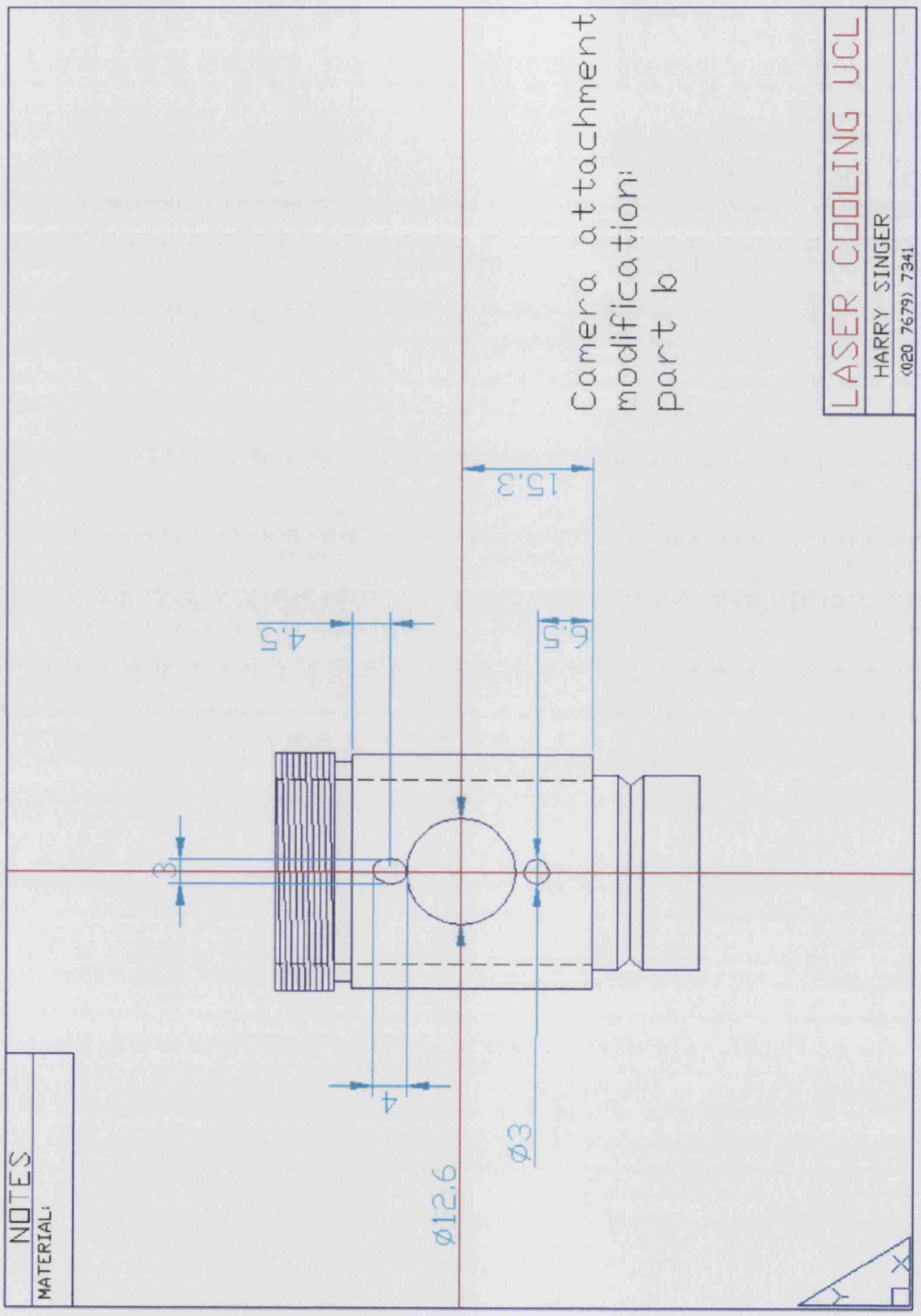

Figure C.5: CAD: Camera attachment modification part B.

C.2 Laser diode

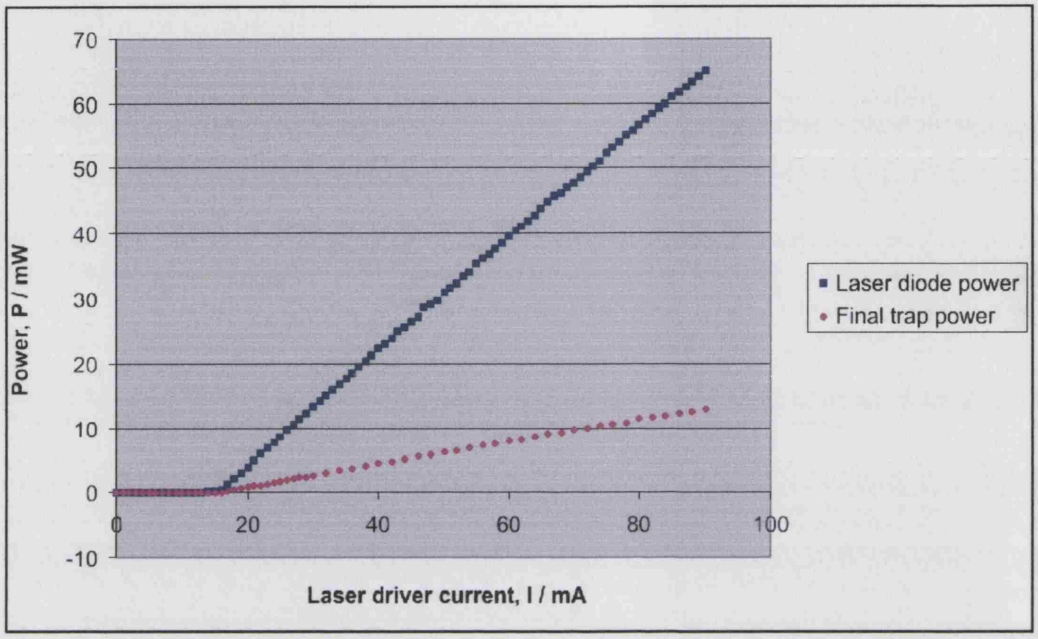

Figure C.6: Graph of power vs current for the laser diode used with the optical tweezers. The blue data is the unattenuated laser power, whilst the pink data is the beam power measured directly after the microscope objective

C.3 The optimum configuration for the laser tweezers

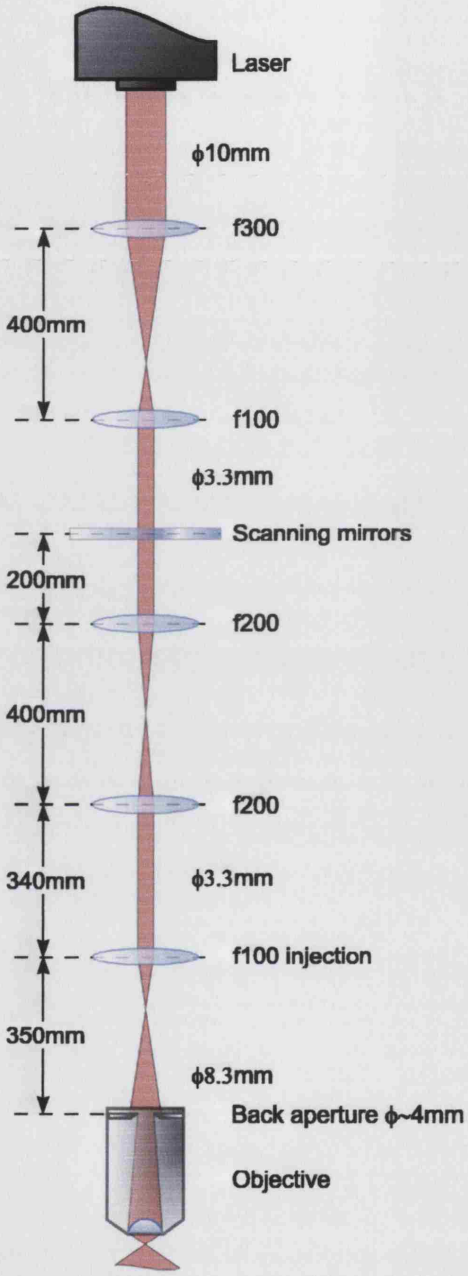

Figure C.7: Optimum tweezers configuration. The scanning mirror and the back aperture are at conjugate planes. The injection lens provides the correct beam divergence such that optical and trapping foci are in the same plane. The high degree of overfilling of the back aperture has led to the highest trapping forces.

C.4 Example LabView program for scanning tweezers operation

Presented here is one of the user interfaces and the LabView programs to control the two galvanometers produce various single moving trap or multiple scanning trap configurations. A similar program was written to produce a pulsed circular ratchet potential surface by modulating the laser diode current-driver. This program is slightly more complicated and is not presented here.

To summarise the code, there is a main file which writes data to a buffer that outputs analogue signals through the PCI bus. The main file continuously calls on sub-programs (sub-VIs) to generate this data. These sub-VIs may be interrupted by other sub-VIs that generate different data for when the user is calibrating, or performing a power-scan. Other small programs work in parallel with the main code, for example the function that is used for squeezing bubbles by slowly reducing the size of a circular trap. There are a few other sub-VIs that are used frequently, for example the reset module. These neaten-up and reduce the overall size of the code.

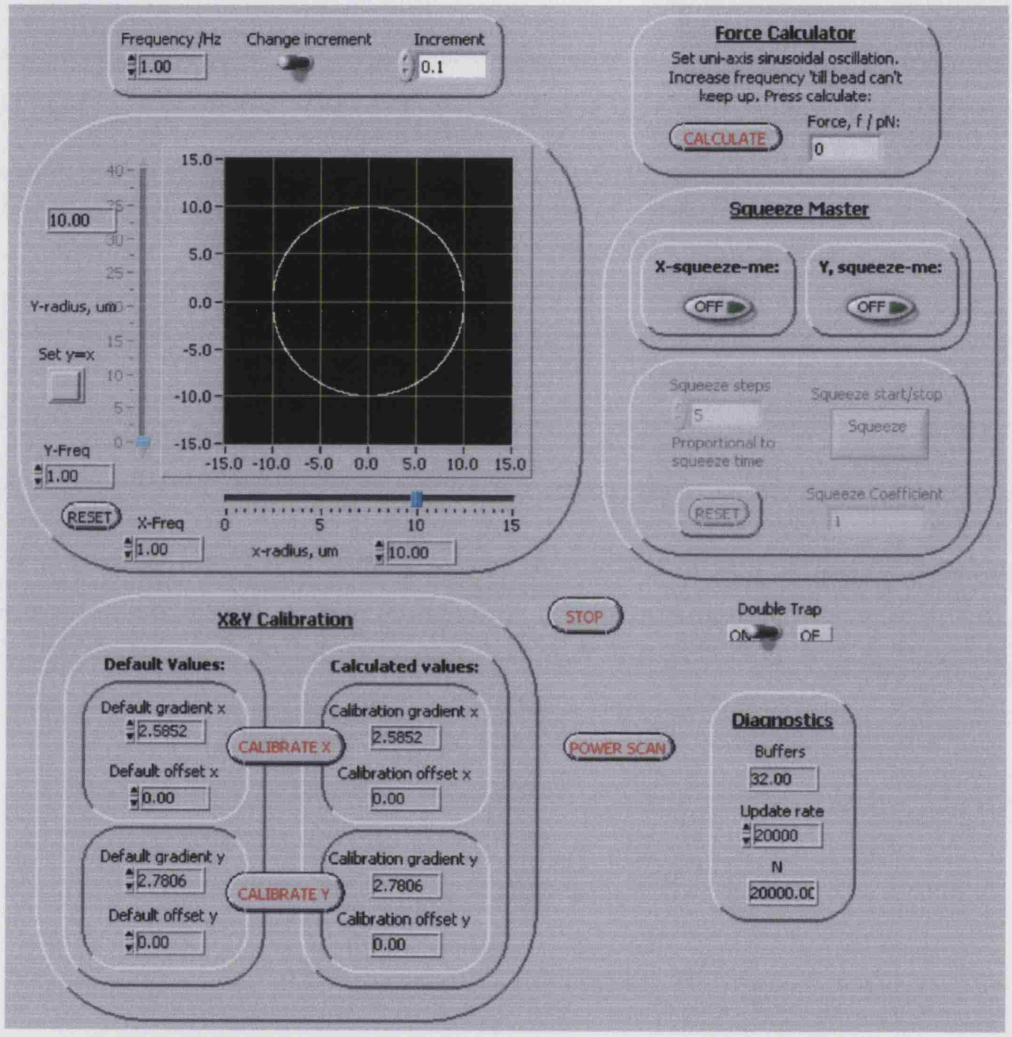

Figure C.8: Tweezers control program: Main user interface.

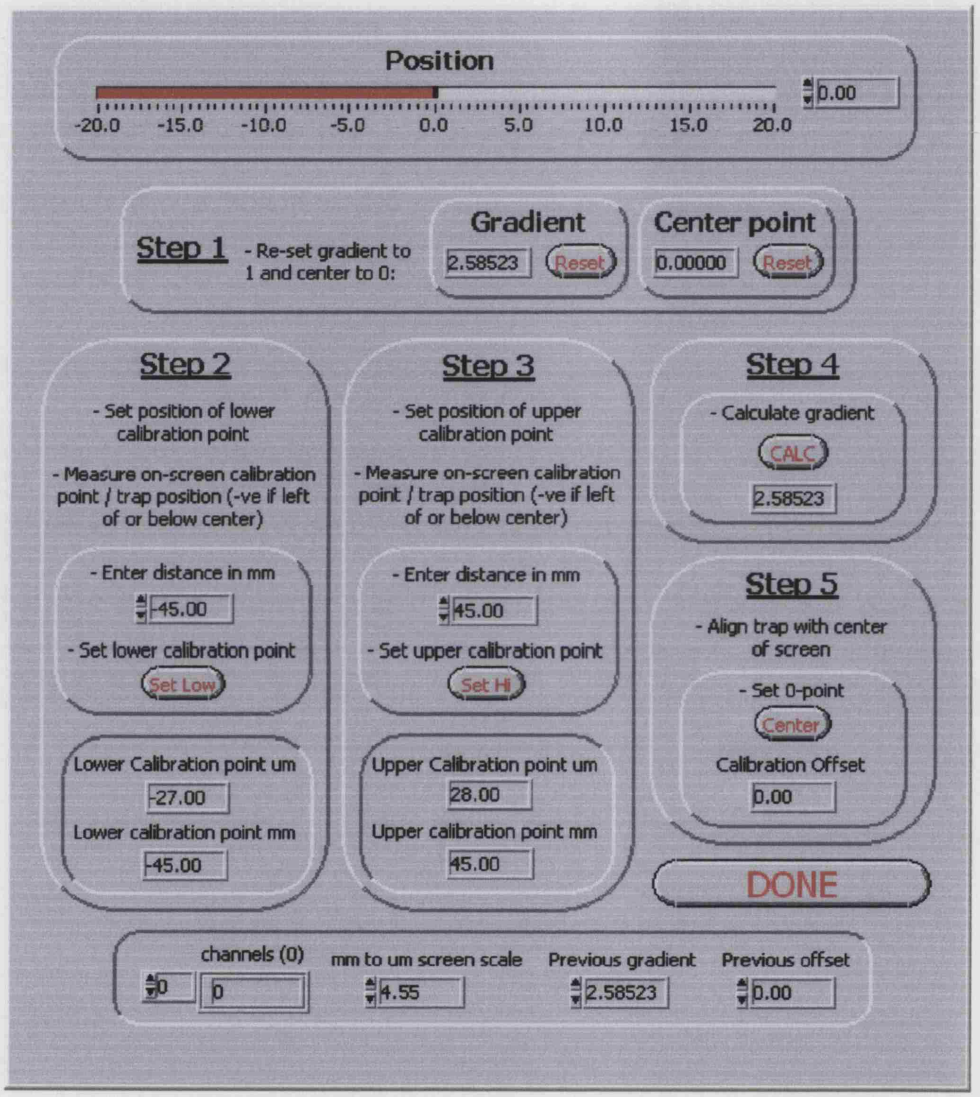

Figure C.9: Tweezers control program: Single axis calibration pop-up window.

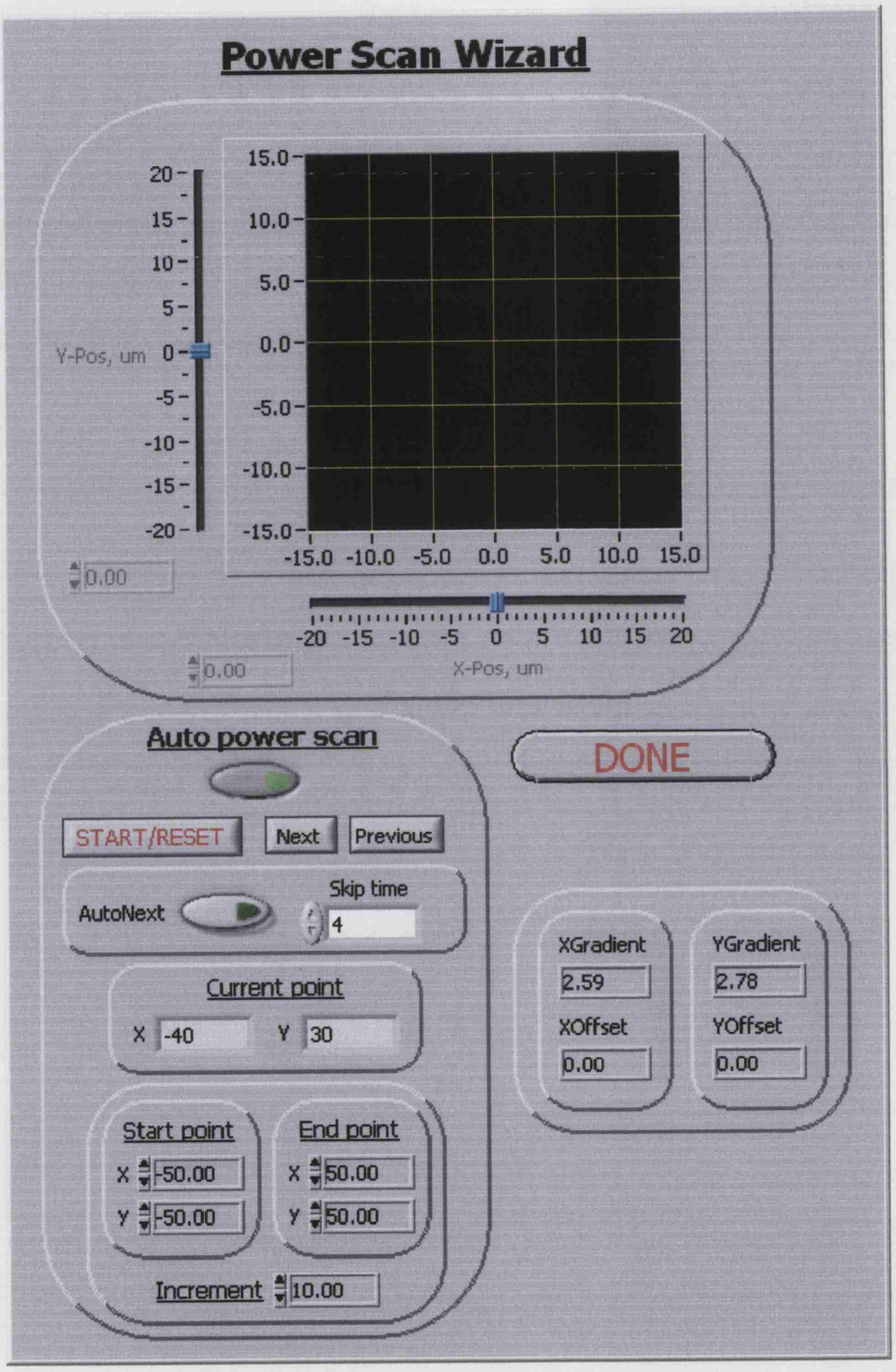

Figure C.10: Tweezers control program: Power scan pop-up interface.

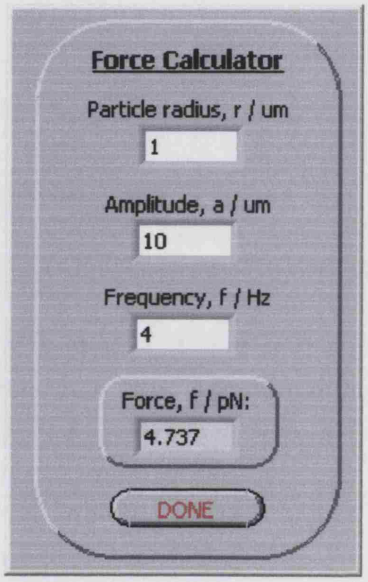

Figure C.11: Tweezers control program: Force calculator pop-up window.

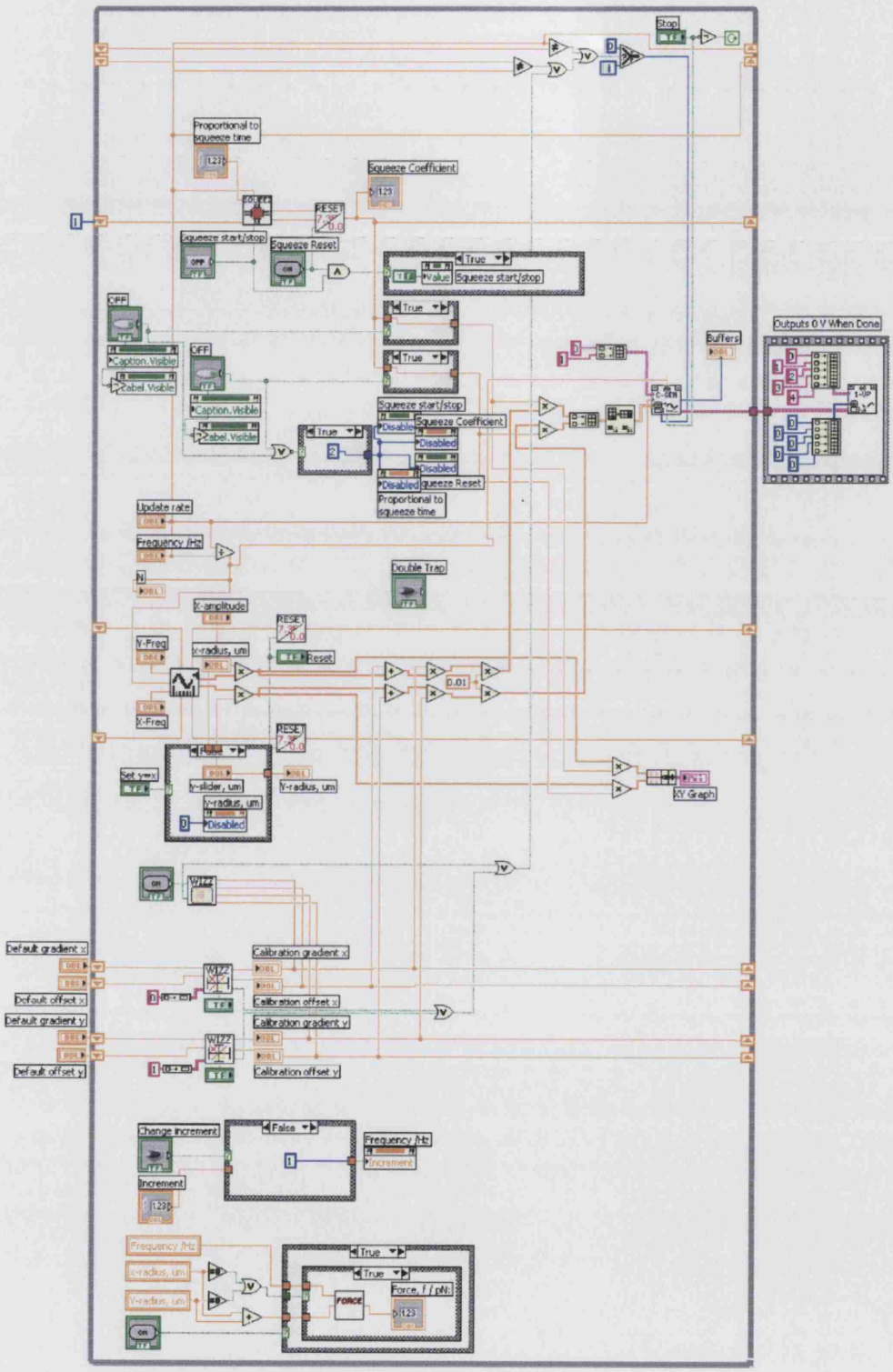

Figure C.12: Tweezers control program: Main programming code.

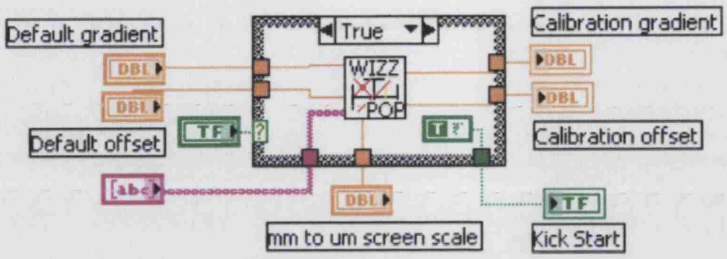

Figure C.13: Tweezers control program: Calibration code.

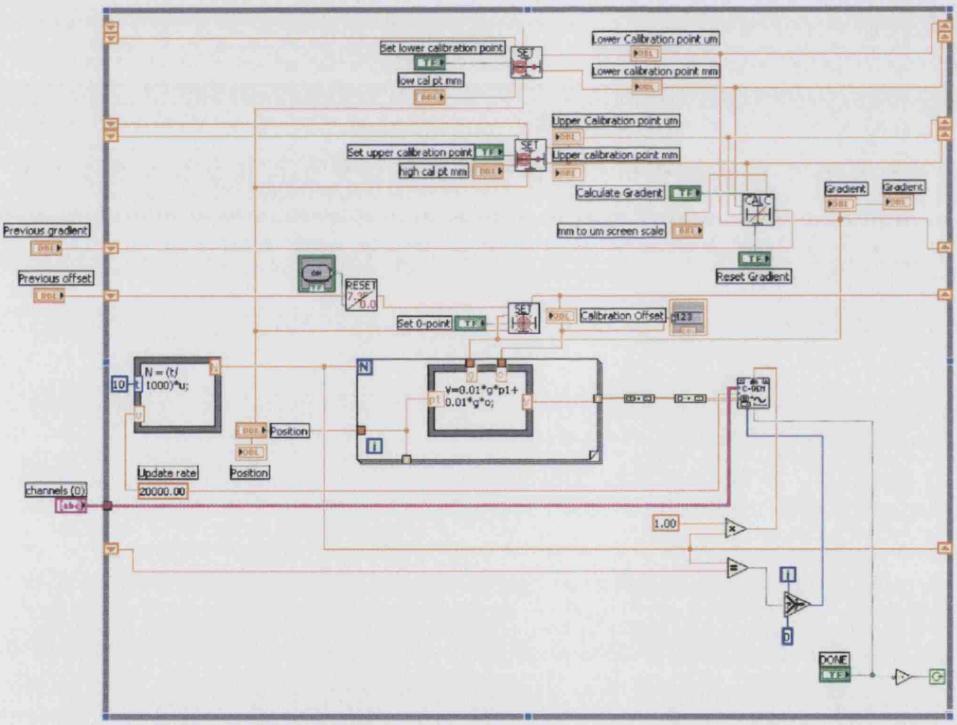

Figure C.14: Tweezers control program: Code for the calibration pop-up window.

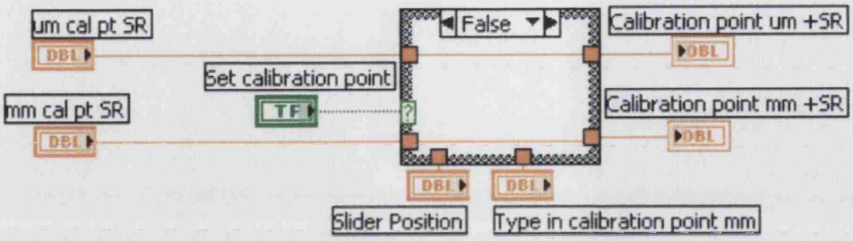

Figure C.15: Tweezers control program: Calibration set point code.

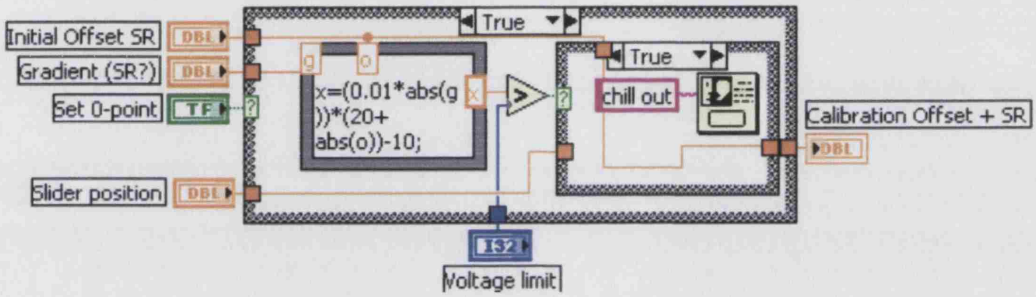

Figure C.16: Tweezers control program: Calibration set centre code.

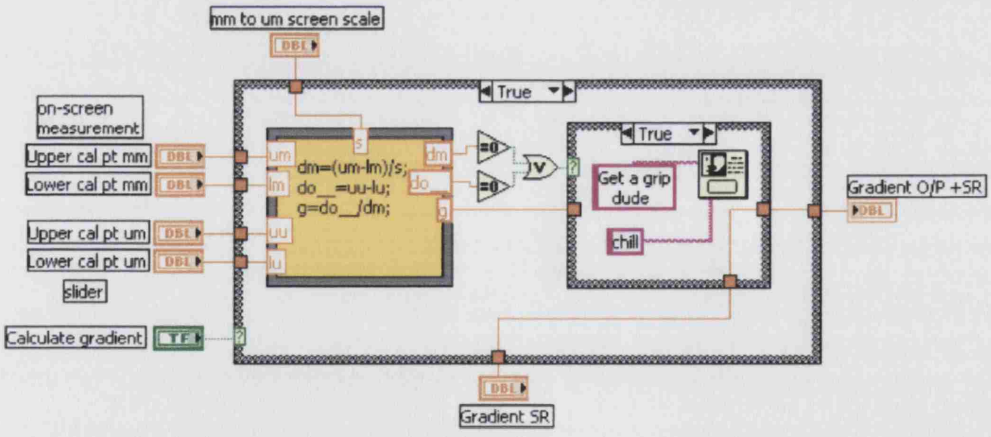

Figure C.17: Tweezers control program: Calibration calculate gradient code.

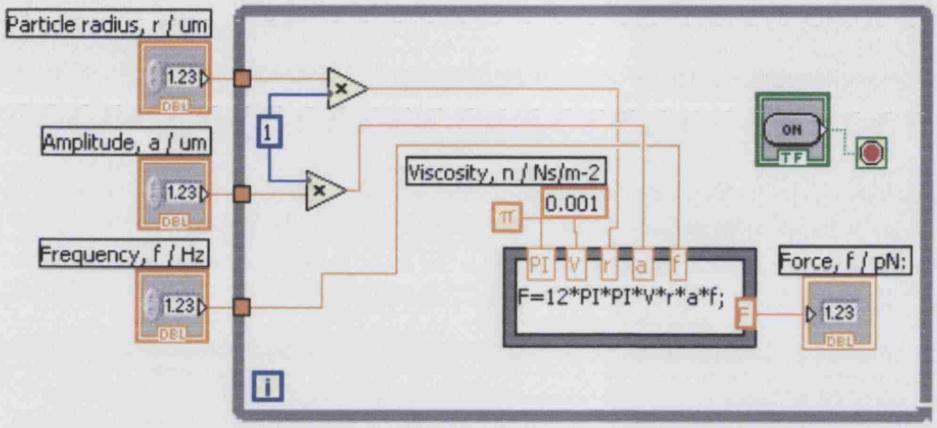

Figure C.18: Tweezers control program: Code for the force calculator pop-up window.

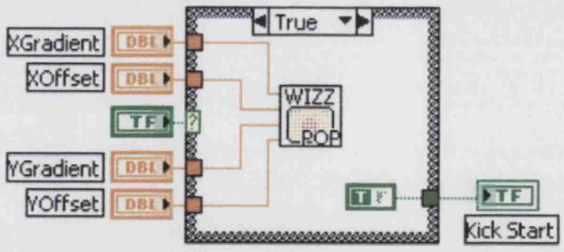

Figure C.19: Tweezers control program: Power scan code.

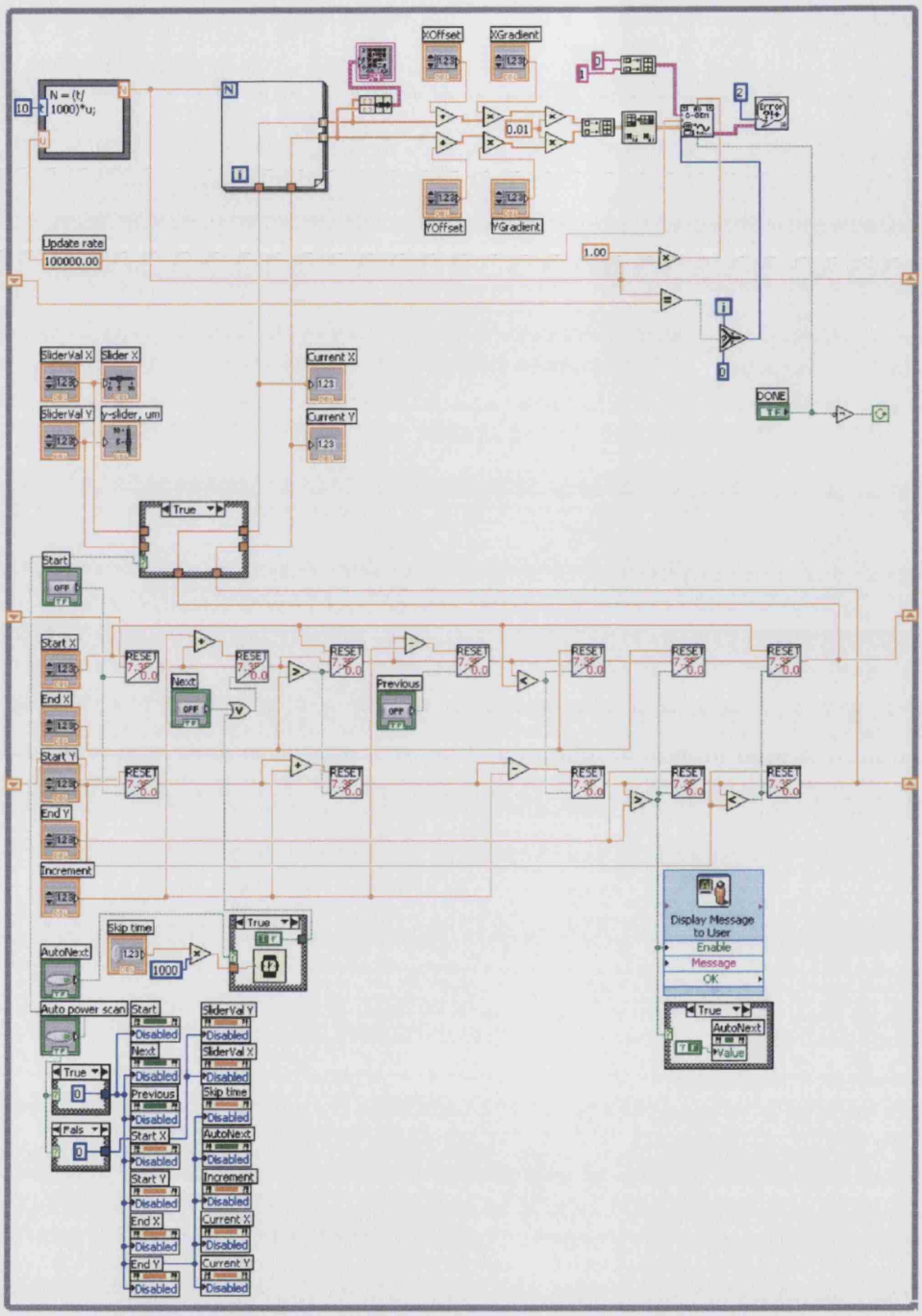

Figure C.20: Tweezers control program: Code for the power-scan pop-up window.

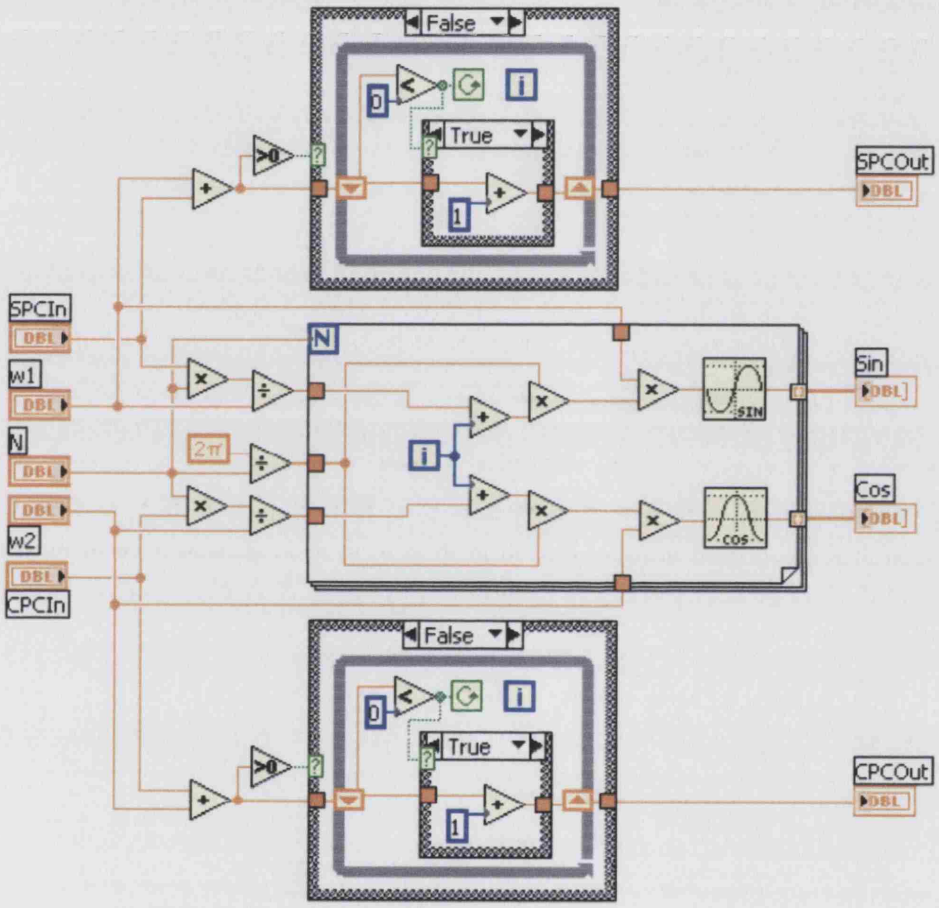

Figure C.21: Tweezers control program: Circular scanning code.

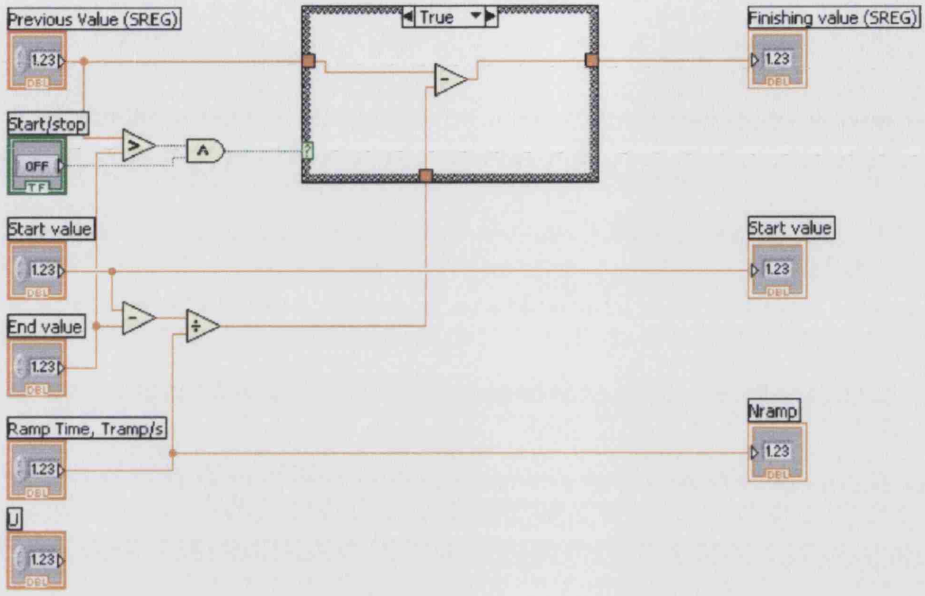

Figure C.22: Tweezers control program: Code to reduce the size of an elliptical trap so that bubbles can be squeezed.

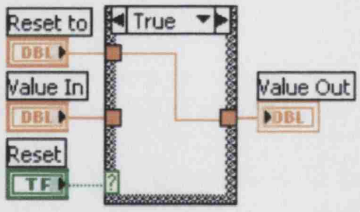

Figure C.23: Tweezers control program: Reset code.

Bibliography

[1] P. Reimann. Brownian motors: noisy transport far from equilibrium. *Phys. Rep.*, 361:57, 2002.

[2] M. Bier. Brownian ratchets in physics and biology. *Contemp. Phys.*, 38:371, 1997.

[3] R. D. Astumian. Thermodynamics and kinetics of a Brownian motor. *Science*, 276:917, 1997.

[4] F. Jülicher, A. Ajdari, and J. Prost. Modelling molecular motors. *Rev. Mod. Phys.*, 69:1269, 1997.

[5] P. Reimann and P. Hänggi. Quantum features of Brownian motors and stochastic resonance. *Chaos*, 8:629, 1998.

[6] L. Darnell. *Molecular cell biology.* W. H. Freeman, San Fransisco, 1990.

[7] R. P. Feynman, R. B. Leighton, and M. Sands. *The Feynman lectures on physics.* Addison-Wesley, Reading MA, 1963.

[8] L. P. Faucheux, L. S. Bourdieu, P. D. Kaplan, and A. J. Libchaber. Optical thermal ratchet. *Phys. Rev. Lett.*, 74:1504, 1995.

[9] P. Reimann, M. Grifoni, and P. Hänggi. Quantum ratchets. *Phys. Rev. Lett.*, 79:10, 1997.

[10] H. Linke, T. E. Humphrey, A. Löfgren, A. O. Sushkov, R. Newbury, R. P. Taylor, and P. Omling. Experimental tunneling ratchets. *Science*, 286:2314, 1999.

[11] P. Jung, J. G Kissner, and P. Hänggi. Regular and chaotic transport in asymmetric periodic potentials: inertia ratchets. *Phys. Rev. Lett.*, 76:3436, 1996.

[12] F. L. Moore, J. C. Robinson, C. Bharucha, P. E. Williams, and M. G. Raizen. Observation of dynamical localization in atomic momentum transfer: A new testing ground for quantum chaos. *Phys. Rev. Lett.*, 73:2974, 1994.

[13] F. L. Moore, J. C. Robinson, C. F. Bharucha, Bala Sundaram, and M. G. Raizen. Atom optics realization of the quantum delta-kicked rotor. *Phys. Rev. Lett.*, 75:4958, 1995.

[14] C. Mennerat-Robilliard, D. Lucas, S. Guibal, J. Tabosa, C. Jurczak, J.-Y. Courtois, and G. Grynberg. Ratchet for cold rubidium atoms: The asymmetric optical lattice. *Phys. Rev. Lett.*, 82:851, 1999.

[15] M. Schiavoni, L. Sanchez-Palencia, F. Renzoni, and G. Grynberg. Phase control of directed diffusion in a symmetric optical lattice. *Phys. Rev. Lett.*, 90:094101, 2003.

[16] S. Flach, O. Yevtushenko, and Y. Zolotaryuk. Directed current due to broken time space symmetry. *Phys. Rev. Lett.*, 84:2358, 2000.

[17] H. Schanz, M.-F. Otto, R. Ketzmerick, and T. Dittrich. Classical and quantum Hamiltonian ratchets. *Phys. Rev. Lett.*, 87:070601, 2001.

[18] T. Dittrich, R. Ketzmerick, M.-F. Otto, and H. Schanz. Classical and quantum transport in deterministic Hamiltonian ratchets. *Ann. Phys.*, 9:755, 2000.

[19] V. G. Minogin and V. S. Letokhov. *Laser light pressure on atoms.* Gordon and Breach, NY, 1987.

[20] E. F. Nichols and G. F. Hull. A preliminary communication of the pressure of heat and radiation. *Phys. Rep.*, 13:307, 1901.

[21] D. J. Wineland and W. M. Itano. Laser cooling. *Physics Today*, page 2, June 1987.

[22] J. L. Bromberg. The birth of the laser. *Physics Today*, page 26, Oct 1988.

[23] A. Ashkin. Acceleration and trapping of particles by radiation pressure. *Phys. Rev. Lett.*, 24:156, 1970.

[24] D. Wineland and H. Dehmelt. Proposed $10^{14}\delta\nu < \nu$ laser fluorescence spectroscopy on Tl^+ mono-ion oscillator III. *Bull. Am. Phys. Soc.*, 20:637, 1975.

[25] T. Hänsch and A. Schawlow. Cooling of gases by laser radiation. *Optics. Commun.*, 13:68, 1975.

[26] W. D. Phillips and H. Metcalf. Laser deceleration of an atomic beam. *Phys. Rev. Lett.*, 48:596, 1982.

[27] J. Prodan, L. Migdall, and W. D. Phillips. Stopping atoms with laser light. *Phys. Rev. Lett.*, 54:992, 1985.

[28] S. Chu, J. E. Bjorkholm, A. Cable, and A. Ashkin. Three-dimensional viscous confinement and cooling of atoms by resonance radiation pressure. *Phys. Rev. Lett.*, 55:48, 1985.

[29] J. E. Bjorkholm, R. R. Freeman, A. Ashkin, and D. B. Pearson. Observation of focussing of neutral atoms by the dipole forces of resonance radiation pressure. *Phys. Rev. Lett.*, 41:1361, 1978.

[30] E. L. Raab, M. Prentiss, A. Cable, S. Chu, and D. E. Pritchard. Trapping of neutral sodium atoms with radiation pressure. *Phys. Rev. Lett.*, 59:2631, 1987.

[31] C. Monroe, W. Swann, H. Robinson, and C. Wieman. Very cold trapped atoms in a vapor cell. *Phys. Rev. Lett.*, 65:1571, 1990.

[32] C. S. Adams and E. Riis. Laser cooling and trapping of neutral atoms. *Prog. Quant. Electr.*, 21:1, 1997.

[33] P. H. Jones. *Ultra-cold atoms in far-detuned optical lattices.* PhD thesis, University of Oxford, 2001.

[34] P. D. Lett, R. N. Watts, C. I. Westbrook, W. D. Phillips, P. L. Gould, and H. J. Metcalf. Observation of atoms laser cooled below the Doppler limit. *Phys. Rev. Lett.*, 61:169, 1988.

[35] H. J. Metcalf and P. van der Straten. *Laser cooling and trapping of neutral atoms.* Springer-Verlag, NY, 1999.

[36] H. Metcalf and P. van der Straten. Cooling and trapping of neutral atoms. *Phys. Rep.*, 244:203, 1994.

[37] C. Cohen-Tannoudji. Laser cooling and trapping of neutral atoms: theory. *Phys. Rep.*, 219:153, 1992.

[38] D. J. Wineland and W. M. Itano. Laser cooling of atoms. *Phys. Rev. A*, 20:1521, 1979.

[39] S. Stenholm. The semiclassical theory of laser cooling. *Rev. Mod. Phys.*, 58:699, 1986.

[40] V. I. Balykin, V. G. Minogin, and V. S. Letokhov. Electromagnetic trapping of cold atoms. *Rep. Prog. Phys.*, 63:1429, 2000.

[41] S. L. Gilbert and C. E. Wieman. Laser cooling and trapping for the masses. *Opt. & Photon. News*, 4(7):8, 1993.

[42] C. Cohen-Tannoudji and W. D. Phillips. New mechanisms for laser cooling. *Physics Today*, 43:33, 1990.

[43] J. Dalibard and C. Cohen-Tannoudji. Laser cooling below the Doppler limit by polarization gradients: simple theoretical models. *J. Opt. Soc. Am. B*, 6:2023, 1989.

[44] P. Verkerk, D. R. Meacher, A. B. Coates, J.-Y. Courtois, S. Guibal, B. Lounis, C. Salomon, and G. Grynberg. Designing optical lattices: an investigation with caesium atoms. *Europhys. Lett.*, 26:171, 1994.

[45] H. Perrin, A. Kuhn, I. Bouchoule, and C. Salomon. Sideband cooling of neutral atoms in a far-detuned optical lattice. *Europhys. Lett.*, 42:395, 1998.

[46] S. E Hamann, D. L. Haycock, G. Klose, P. H. Pax, I. H. Deutsch, and P. S. Jessen. Resolved-sideband Raman cooling to the ground state of an optical lattice. *Phys. Rev. Lett.*, 80:4149, 1998.

[47] A. Ashkin. Atomic beam deflection by resonance-radiation pressure. *Phys. Rev. Lett.*, 25:1321, 1970.

[48] D. A. Steck. Cesium D_2 line data. *http://george.ph.utexas.edu/~dsteck/alkalidata/cesiumnumbers.pdf*, Los Alamos National Laboratory, 1998.

[49] K. Lindquist, M. Stephens, and C. Wieman. Experimental and theoretical study of the vapor-cell Zeeman optical trap. *Phys. Rev. A*, 46:4082, 1992.

[50] A. L. Migdall, J. V. Prodan, W. D. Phillips, T. H. Bergeman, and H. J. Metcalf. First observation of magnetically trapped neutral atoms. *Phys. Rev. Lett.*, 54:2596, 1985.

[51] O. Morsch. *Optical lattices for ultra-cold atoms.* PhD thesis, University of Oxford, 1999.

[52] Homer (trans. E. V. Rieu). *The Odyssey, Book XI: The book of the dead (Nekuia).* Penguin Books Inc., Harmondsworth, Middlesex, England, 14th edition, 1959.

[53] I. H. Deutsch, J. Grondalski, and P. M. Alsing. Local dynamics of laser cooling in an optical lattice. *Phys. Rev. A*, 56:R1705, 1997.

[54] S. A. Hopkins and A. V. Durrant. Parameters for polarization gradients in three-dimensional electromagnetic standing waves. *Phys. Rev. A*, 56:4012, 1997.

[55] A. Ashkin. Forces of a single-beam gradient laser trap on a dielectric sphere in the ray optics regime. *Biophys. J.*, 61:569, 1992.

[56] K. Svoboda and S. M. Block. Biological applications of optical forces. *Annu. Rev. Biophys. Biomol. Struct.*, 23:247, 1994.

[57] A. Ashkin, J. M. Dziedzic, J. E. Bjorkholm, and S. Chu. Observation of a single-beam gradient force optical trap for dielectric particles. *Opt. Lett.*, 11:288, 1986.

[58] J. E. Molloy and M. J. Padgett. Lights, action: optical tweezers. *Chem. Phys.*, 43:241, 2002.

[59] A. Ashkin and J. M. Dziedzic. Stability of optical levitation by radiation pressure. *Appl. Phys. Lett.*, 24:586, 1974.

[60] G. Roosen and C. Imbert. The TEM_{01}^{*} mode laser beam – A powerful tool for optical levitation of various types of spheres. *Optics. Commun.*, 26:432, 1978.

[61] J. Moser. Is the solar system stable? *Math. Intell.*, 1:65, 1978.

[62] I. Peterson. *Newton's clock: chaos in the solar system.* W. H. Freeman, NY, 1993.

[63] H. W. Broer. KAM theory: the legacy of Kolmogorov's 1954 paper. *Bull. Am. Math. Soc.*, S 0273-0979(04)01009-2, 2004.

[64] E. N. Lorenz. Deterministic nonperiodic flow. *J. Atmos. Sci.*, 20:130, 1963.

[65] Book and lyrics by A. J. Lerner. *My Fair Lady.* Penguin Books, 2001.

[66] T.-Y. Li and J. A. Yorke. Period three implies chaos. *Am. Math. Monthly*, 82:985, 1975.

[67] B. V. Chirikov. A universal instability of many-dimensional oscillator systems. *Phys. Rep.*, 52:263, 1979.

[68] B. V. Chirikov. Time-dependent quantum systems. In *Chaos and Quantum Physics: Proceedings of the Les Houches Summer School*, 1989. Session L11.

[69] E. Ott. *Chaos in Dynamical systems.* Cambridge University Press, Cambridge, 1993.

[70] A. J. Lichtenberg and M. A. Lieberman. *Regular and Chaotic Dynamics.* Springer-Verlag, NY, 1992.

[71] A. B. Rechester and R. B. White. Calculation of turbulent diffusion for the Chirikov-Taylor model. *Phys. Rev. Lett.*, 44:1586, 1980.

[72] A. B. Rechester, M. N. Rosenbluth, and R. B. White. Fourier-space paths applied to the calculation of diffusion for the Chirikov-Taylor model. *Phys. Rev. A*, 23:2664, 1981.

[73] M. V. Berry. Quantum chaology. *Proc. R. Soc. Lond. A*, 413:183, 1987.

[74] J. C. Robinson, F. L. Moore, R. Jahnke, G. A. Georgakis, Q. Niu, M. G. Raizen, and B. Sundaram. Study of quantum dynamics in the transition from classical stability to chaos. *Phys. Rev. Lett.*, 74:3693, 1995.

[75] M. V. Berry, N. L. Balazs, M. Tabor, and A. Voros. Quantum maps. *Ann. Phys.*, 122:26, 1979.

[76] D. L. Shepelyansky. Localization of quasienergy eigenfunctions in action space. *Phys. Rev. Lett.*, 56:677, 1986.

[77] S. Fishman, D. R. Grempel, and R. E. Prange. Chaos, quantum recurrences, and Anderson localization. *Phys. Rev. Lett.*, 49:509, 1982.

[78] F. F. Bharucha, J. C. Robinson, F. L. Moore, B. Sundaram, Q. Niu, and M. G. Raizen. Dynamical localization of ultracold sodium atoms. *Phys. Rev. E*, 60:3881, 1999.

[79] G. Casati, B. V. Chirikov, F. M. Izralev, and J. Ford. Stochastic behaviour in classical and quantum Hamiltonian systems. In G. Casati and J. Ford, editors, *Lecture notes in physics*, volume 93, page 334, Springer, Berlin, 1979.

[80] P. W. Anderson. Absence of diffusion in certain random lattices. *Phys. Rep.*, 109:1492, 1958.

[81] P. W. Anderson. Local moments and localised states. *Rev. Mod. Phys.*, 50:191, 1978.

[82] M. Isherwood. *Chaotic Hamiltonian ratchets in optical lattices.* PhD thesis, University College London, 2004.

[83] B. G. Klappauf, W. H. Oskay, D. A. Steck, and M. G. Raizen. Quantum chaos with cesium atoms: pushing the boundaries. *Physica D*, 131:78, 1999.

[84] B. G. Klappauf, W. H. Oskay, D. A. Steck, and M. G. Raizen. Experimental study of quantum dynamics in a regime of classical anomalous diffusion. *Phys. Rev. Lett.*, 81:4044, 1998.

[85] N. Hutchings. *Chaotic Hamiltonian ratchets with cold atoms.* PhD thesis, University College London, 2003.

[86] T. Cheon, P. Exner, and P. Šeba. Extended standard map with spatio-temporal asymmetry. *J. Phys. Soc. Japan*, 72:1087, 2003.

[87] T. S. Monteiro, P. A. Dando, N. A. C. Hutchings, and M. R. Isherwood. Proposal for a chaotic ratchet using cold atoms in optical lattices. *Phys. Rev. Lett.*, 89:194102, 2002.

[88] F. Haake. *Quantum signiatures of chaos.* Springer-Verlag, Berlin, 1991.

[89] T. Jonckheere, M. R. Isherwood, and T. S. Monteiro. Chaotic filtering of moving atoms in pulsed optical lattices. *Phys. Rev. Lett.*, 91:253003, 2003.

[90] S.-Q. Shang, B. Sheehy, P. van der Straten, and H. Metcalf. Velocity-selective magnetic-resonance laser cooling. *Phys. Rev. Lett.*, 65:317, 1990.

[91] W. Bell and A. Bloom. Optically driven spin precession. *Phys. Rev. Lett.*, 6:280, 1961.

[92] P. H. Jones, M. Goonasekera, H. E. Saunders-Singer, and D. R. Meacher. Shifting the boundaries: pulse-shape effects in the atom-optics kicked rotor. *arXiv:quant-ph/0311120.* Submitted to *Europhys. Lett.*

[93] M. Goonasekera, P. Jones, H. E. Saunders-Singer, and D. R. Meacher. Exploring the mixed phase space of the delta-kicked rotor with a moving optical lattice. 2004. Manuscript in preparation.

[94] E. Peik, M. Ben Dahan, I. Bouchoule, Y. Castin, and C. Salomon. Bloch oscillations and an accelerator for cold atoms. *Appl. Phys. B*, 65:685, 1997.

[95] K. W. Madison, C. F. Bharucha, P. R. Morrow, S. R. Wilkinson, Q. Niu, B. Sundaram, and M. G. Raizen. Quantum transport of ultracold atoms in an accelerating optical potential. *Appl. Phys. B*, 65:693, 1997.

[96] C. F. Bharucha, K. W. Madison, P. R. Morrow, S. R. Wilkinson, B. Sundaram, and M. G. Raizen. Observation of atomic tunneling from an accelerating optical potential. *Phys. Rev. A*, 55:R857, 1997.

[97] P. H. Jones, M. Goonasekera, H. E. Saunders-Singer, and D. R. Meacher. Asymmetric diffusion in the delta-kicked rotor with broken time symmetry. *arXiv:Quant-ph/0309149*, 2003.

[98] I. H. Deutsch and P. S. Jessen. Quantum-state control in optical lattices. *Phys. Rev. A*, 57:1972, 1998.

[99] T. Harada and K. Yoshikawa. Fluctuation-response relation in a rocking ratchet. *Phys. Rev. E*, 69:031113, 2004.

[100] E. Fällman and O. Axner. Design for fully steerable dual-trap optical tweezers. *Appl. Opt.*, 36:2107, 1997.

[101] Y. Ogura, K. Kagawa, and J. Tanida. Optical manipulation of microscopic objects by means of vertical-cavity surface-emitting laser array sources. *Appl. Opt.*, 40:5430, 2001.

[102] M. P. MacDonald, L. Paterson, K. Volke-Sepulveda, J. Arlt, W. Sibbett, and K. Dholakia. Creation and manipulation of three-dimensional optically trapped structures. *Science*, 296:1101, 2002.

[103] L. Paterson, M. P. MacDonald, J. Arlt, W. Sibbett, P. E. Bryant, and K. Dholakia. Controlled rotation of optically trapped microscopic particles. *Science*, 292:912, 2001.

[104] E. R. Dufresne, G. C. Spalding, M. T. Dearing, S. A. Sheets, and D. G. Grier. Computer-generated holographic optical tweezer arrays. *Rev. Sci. Instrum.*, 72:1810, 2001.

[105] R. L. Eriksen, V. R. Daria, and J. Glückstad. Fully dynamic multiple-beam optical tweezers. *Opt. Express*, 10:597, 2002.

[106] K. Sasaki, M. Koshioka, H. Misawa, N. Kitamury, and H. Masuhara.

Pattern formation and flow control of fine particles by laser-scanning micromanipulation. *Opt. Lett.*, 16:1463, 1991.

[107] *Moving magnet optical scanners.* Laser2000. http://www.laser2000.co.uk/lasers/accsry/magnet.htm.

[108] O. Morch. *Optical lattices for ultra cold atoms.* PhD thesis, Magdalen College, University of Oxford, 1999.

[109] K. R. Spring, H. E. Keller, and M. W. Davidson. *Anatomy of the microscope: Microscope objectives.* Molecular Expressions. http://micro.magnet.fsu.edu/primer/anatomy/objectives.html.

[110] X. Ma, J. Lu, R Brock, K. Jacobs, P. Yang, and X.-H. Hu. Determination of complex refractive index of polystyrene microspheres from 370 to 1610 nm. *Phys. Med. Biol.*, 48:4165, 2003.

[111] G. Hale and M. Querry. Optical constants of water in the 200-nm to 200-μm wavelength region. *Appl. Opt.*, 12:555, 1973.

[112] W. Wright, G. Sonek, and M. Berns. Parametric study of the forces on microspheres held by optical tweezers. *Appl. Opt.*, 33:1735, 1994.

[113] *Model 6800HP Galvanometer Optical Scanner.* Cambridge Technology, revision 1 edition, Nov 1996.

[114] *Product no. 251, Photomicrograph scale marker.* Ted Pella, Inc., P.O. Box 492477, Redding, CA 96049-2477. www.tedpella.com.

[115] H. Felgner, O. Müller, and M. Schliwa. Calibration of light forces in optical tweezers. *Appl. Opt.*, 34:977, 1995.

[116] Z. Ulanowski and I. K. Ludlow. Compact optical trapping microscope using a diode laser. *Meas. Sci. Technol.*, 11:1778, 2000.

[117] N. Malagnino, G. Pesce, A. Sasso, and E. Arimondo. Measurements of trapping efficiency and stiffness in optical tweezers. *Optics. Commun.*, 214:15, 2002.

[118] Y. Harada and T. Asakura. Radiation forces on a dielectric sphere in the Rayleigh scattering regime. *Optics. Commun.*, 124:529, 1996.

[119] T. Tlusty, A. Meller, and R. Bar-Ziv. Optical gradient forces of strongly localized fields. *Phys. Rev. Lett.*, 81:1738, 1998.

[120] S. Kamimura. Direct measurements of nanometric displacements under an optical microscope. *Appl. Opt.*, 26:3425, 1987.

[121] K. Visscher, S. P. Gross, and S. M. Block. Construction of multiple-beam optical traps with nanometer-resolution position sensing. *IEEE Journal of Selected Topics in Quantum Electronics*, 2:1066, 1996.

[122] K. Svoboda, C. F. Schmidt, B. J. Schnapp, and S. M. Block. Direct observation of kinesin stepping by optical trapping interferometry. *Nature*, 365:721, 1993.

Index